Downloaded from orbit.dtu.dk on: Apr 10, 2024

DTU Library

Aerodynamic and Aeroelastic Shape Optimization of Aircraft Wings

Conlan-Smith, Cian

Publication date:
2020

Document Version
Publisher's PDF, also known as Version of record

Link back to DTU Orbit

Citation (APA):
Conlan-Smith, C. (2020). *Aerodynamic and Aeroelastic Shape Optimization of Aircraft Wings*. Technical University of Denmark. DCAMM Special Report No. S282

General rights
Copyright and moral rights for the publications made accessible in the public portal are retained by the authors and/or other copyright owners and it is a condition of accessing publications that users recognise and abide by the legal requirements associated with these rights.

- Users may download and print one copy of any publication from the public portal for the purpose of private study or research.
- You may not further distribute the material or use it for any profit-making activity or commercial gain
- You may freely distribute the URL identifying the publication in the public portal

If you believe that this document breaches copyright please contact us providing details, and we will remove access to the work immediately and investigate your claim.

DTU Mechanical Engineering
Department of Mechanical Engineering

Aerodynamic and Aeroelastic Shape Optimization of Aircraft Wings

Cian Conlan-Smith

PhD Thesis

AERODYNAMIC AND AEROELASTIC SHAPE OPTIMIZATION OF AIRCRAFT WINGS

CIAN CONLAN-SMITH

Department of Mechanical Engineering,
Technical University of Denmark,
Kgs. Lyngby, 2020.
DCAMM Special Report No. S282

Thesis Title:
Aerodynamic and Aeroelastic Shape Optimization of Aircraft Wings

Author:
Cian Conlan-Smith
Department of Mechanical Engineering,
Technical University of Denmark
Nils Koppels Allé, Building 404, DK-2800 Lyngby, Denmark
cicosm@mek.dtu.dk

Supervisors:
Associate Professor Casper Schousboe Andreasen
Department of Mechanical Engineering,
Technical University of Denmark
Nils Koppels Allé, Building 404, DK-2800 Lyngby, Denmark

Professor Ole Sigmund
Department of Mechanical Engineering
Technical University of Denmark
Nils Koppels Allé, Building 404, DK-2800 Lyngby, Denmark

Senior Researcher Néstor Ramos-García
Department of Wind Energy,
Technical University of Denmark
Nils Koppels Allé, Building 403, DK-2800 Lyngby, Denmark

Ph.D. Assessment Committee:
Professor Mathias Stolpe
Department of Wind Energy,
Technical University of Denmark

Associate Professor Carlos Simão Ferreira
Department of Wind Energy,
Delft University of Technology

Professor Anders Klabring
Department of Management and Engineering,
Linköping University

© 2020 Cian Conlan-Smith
MEK-PHD: ISSN 0903-1685, ISBN 978-87-7475-628-6

Preface

This thesis is submitted in partial fulfillment of the requirements for obtaining the degree of Ph.D. in Mechanical Engineering at the Technical University of Denmark (DTU). The Ph.D. project titled, *Aerodynamic and Aeroelastic Shape Optimization of Aircraft Wings*, is funded by the Villum Foundation under the *InnoTop Villum Investigator project.* The work was conducted in the Section of Solid Mechanics within the Department of Mechanical Engineering at DTU during the period from the 15th of November 2017 to the 14th of November 2020. The main supervisor has been Associate Professor Casper Schousboe Andreasen with co-supervisors Professor Ole Sigmund and Senior Researcher Néstor Ramos-García.

There are many people I would like to acknowledge for their support over the past three years. Firstly, I would like to thank Casper for all his guidance, advice, and discussions. I would also like to thank my other supervisors, Ole and Néstor for their discussions and feedback. Thanks to my co-workers, Lukas and Erik, who have been working on extending methods presented in this thesis to 3D continuum elements for topology optimization problems. Thanks also to my colleagues within the Solid Mechanics Section, both past and present, for their scientific discussions and for the great company throughout my Ph.D. studies.

Finally, thanks to Maria and my parents for your encouragement, always believing in me, helping with proof reading, and always supporting me whenever I needed you.

Kongens Lyngby, November 2020

Cian Conlan-Smith

Abstract

The goal of this thesis is to develop an efficient framework for aerodynamic and aeroelastic shape optimization. The framework includes coupled aerodynamic and structural analysis, where a multidisciplinary formulation is used in order to create optimized trade-offs between structural and aerodynamic performance. A primary challenge with these problems is the computational expense of solving the coupled problem on each design iteration. In order to help overcome this expense, panel methods are used to calculate the aerodynamic loads which are an efficient alternative to conventional CFD methods. Beam finite element models are used in this thesis to capture structural deformations, but extensions to 3D continuum finite elements are also discussed. All optimization problems are solved using gradient-based methods, where gradients are derived analytically and implemented using a discrete adjoint approach. The methodology developed throughout this thesis has been applied to the design of aircraft wings. Results demonstrate the applicability of the methods, and the framework is used to explore the potential of unconventional aircraft wing designs such as curved wall spars and drooped wings.

The specific details of the thesis are covered by four journal publications which contain the following topics:

P1. The aerodynamic optimization framework is introduced which lays out the main considerations for solving aerodynamic optimization problems with panel methods, namely: choice of boundary conditions; drag calculation methods; parameterization methods; regularization; and wake modeling.

P2. The coupled panel-beam framework for aeroelastic optimization is introduced. The publication includes a general panel-beam load-displacement transfer scheme, parameterizations that define both the external wing geometry and internal structural geometry, and investigations conducted on the benefits of curved wall spars in wingbox design.

P3. A parameterization is presented for aerodynamic optimization of non-planar wings. The method is able to improve upon reference designs taken from the literature, and is used to investigate the potential performance benefits of drooped wings compared to more traditional raised wing designs with winglets.

P4. The coupled aeroelastic framework is extended to include a non-linear co-rotating beam model. The results demonstrate the importance of capturing non-linear deformations in aeroelastic optimization problems, and presents aeroelastic comparisons of solid foam core wings with raised and drooped geometry.

Resumé (in Danish)

Målet med denne afhandling er at udvikle et effektivt beregningsværktøj til aerodynamisk og aeroelastisk formoptimering. Beregningsværktøjet inkluderer en koblet aerodynamisk og strukturel analyse kombineret i en multidisciplinær formulering for at optimere strukturel og aerodynamisk ydeevne. En umiddelbar udfordring ved disse problemer er de beregningsmæssige omkostning forbundet med at løse det koblede problem i hver designiteration. For at afhjælpe dette benyttes panelmetoder til beregning af de aerodynamiske laster, hvilket er et effektivt alternativt til konventionelle CFD metoder. Bjælkeelementmetoder benyttes til beregning af de strukturelle deformationer herudover diskuteres mulige udvidelser i form af 3D kontinuum metoder også. Alle optimeringsproblemer er løst ved brug af gradientbaserede optimeringsalgoritmer, hvor gradienterne er beregnet analytisk og implementeret ved brug af en diskret adjoint formulering. Metoderne udviklet i dette arbejde er blevet anvendt til design af flyvinger. Resultaterne demonstrerer metodernes anvendelighed og beregningsværktøjet er anvendt til at undersøge potentialet ved ukonventionelle vingedesigns så som krumme vingespær og nedad-buende vinger.

De konkrete detaljer er beskrevet i fire videnskabelige artikler der dækker de følgende emner:

P1. Det aerodynamiske optimeringsværktøj introduceres og beskriver de grundlæggende overvejelser for løsning af aerodynamiske optimeringsproblem ved brug af panel metoder, herunder: valg af randbetingelser, metoder til beregning af luftmodstand, parametriseringsmetoder, regularisering og modellering af hækbølge.

P2. Det koblede panel-bjælke beregningsværktøj til aeroelastisk optimering introduceres. Artiklen inkluderer en generel panel-bjælke last- og deformations-overførsels procedure, parametrisering af såvel ydre vingegeometri som indre strukturelle geometri samt undersøgelser af fordele ved brug af krumme vingespær i vingeboksen.

P3. En parameterisering for aerodynamisk optimering af ikke-plane vinger. Metoden kan forbedre referencedesigns fra litteraturen og benyttes til afdækning af potentielle ydelsesforbedringer for nedad-buende vinger i forhold til mere traditionelle winglet designs.

P4. Det koblede aeroelastiske beregningsværktøj udvides til at inkludere en ikke-lineær med-roterende bjælkemodel. Resultaterne understreger vigtigheden af at medtage ikke-lineære deformationer i aeroelastiske optimeringsproblemer og sammenligninger det aeroelastiske respons for vinger med skumkerne og hhv. opad- og nedadbuende vingespidser.

List of Publications

The following journal publications are submitted as part of this thesis:

[P1] **Cian Conlan-Smith**, Néstor Ramos-García, Ole Sigmund, and Casper Schousboe Andreasen. "Aerodynamic Shape Optimization of Aircraft Wings Using Panel Methods". In: *AIAA Journal* 58.9 (2020), pp. 3765–3776. DOI: `https://doi.org/10.2514/1.J058979`

[P2] **Cian Conlan-Smith** and Casper Schousboe Andreasen. "A coupled 3D panel-beam model for aeroelastic optimization of aircraft wings". In: *AIAA Journal* (2020). Accepted/In press.

[P3] **Cian Conlan-Smith**, Néstor Ramos-García, and Casper Schousboe Andreasen. "Aerodynamic shape optimization of non-planar wings". In: *Journal of Aircraft* (2020). Submitted/under review.

[P4] **Cian Conlan-Smith** and Casper Schousboe Andreasen. "Aeroelastic optimization of solid foam core wings subject to large deformations". In: *AIAA Journal* (2020). To be submitted.

The following journal publication was published during the Ph.D. studies; however is not considered part of this thesis:

[P5] **Cian Conlan-Smith** and Kai A. James. "A stress-based topology optimization method for heterogeneous structures". In: *Structural and Multidisciplinary Optimization* 60.1 (2019), pp. 167–183. DOI: `https://doi.org/10.1007/s00158-019-02207-9`

Contents

List of Publications v

Part 1. Description of Methods, Results, and Outcomes 1

1 Introduction 3
- 1.1 Motivation & Goals 3
- 1.2 A Reader's Guide 4
- 1.3 An Overview of Aircraft Design 4

2 Numerical Methods 11
- 2.1 Design Optimization 11
- 2.2 Panel Methods 14
- 2.3 Beam Finite Element Analysis 22
- 2.4 Multidisciplinary Analysis 26

3 Aerodynamic Shape Optimization 28
- 3.1 Wing Parameterization and Discretization 28
- 3.2 A Discussion on Choice of Methods 29
- 3.3 Shape Optimization of Planar Wings 33
- 3.4 Shape Optimization of Non-Planar Wings 36

4 Aeroelastic Shape Optimization 41
- 4.1 Panel-Beam Discretization 41
- 4.2 Panel-Beam Load-Displacement Transfer 41
- 4.3 An Investigation of Curved Wall Spars 43
- 4.4 Shape Optimization of Solid Foam Core Wings 49

5 Conclusions 53
- 5.1 Summary of Outcomes and Contributions 53
- 5.2 Future Work 54

Bibliography 56

Appendices 63
- A Topology Optimization of Aircraft Wings 64
- B Compressibility Correction 67
- C A Comparison of Coupling Methods 68
- D NACA Airfoil Parameterizations 70
- E B-Spline Airfoil Parameterization 72
- F Higher Order Panel Methods 74

Part 2. Publications **77**
Publication [P1] 79
Publication [P2] 109
Publication [P3] 141
Publication [P4] 167

Part 1. Description of Methods, Results, and Outcomes

1 Introduction

Aircraft wings are complex engineering structures that demand low-weight with a strong aerodynamic performance. These two attributes are linked by the fact that low-weight is usually associated with flexible structures where large deformations can cause large changes in aerodynamic loading. Because of the coupling between these two physics regimes it is important to consider both in the design of aircraft wings, and the end design will usually require trade-offs between structural and aerodynamic performance. It is not always obvious how to create these trade-offs in a manner that leads to a well-performing design overall. Numerical optimization can be a powerful method for the design of any engineering system, but is particularly useful in such cases where the design requires trade-offs between different physical attributes. This thesis details the development of shape optimization methods which are applied to the aerodynamic and aeroelastic design of aircraft wings. This chapter will outline the specific goals of the thesis and provide a general overview of aircraft design to familiarize the reader with some of the basic practical concepts.

1.1 Motivation & Goals

This Ph.D. thesis is part of a larger six-year project called the *InnoTop Villum Investigator Project*. The goal of the *InnoTop* project is to create an interactive software that produces optimized designs for multiscale and multiphysics problems. The software will have the capability to design aerodynamic form, structural members, and microstructure designs simultaneously. This Ph.D. project will focus specifically on the development of aerodynamic and aeroelastic optimization methods, and conduct investigations on the applicability of the developed methods.

The primary goal of this Ph.D. project is to develop an efficient aerodynamic and aeroelastic optimization framework for applications such as aircraft wings, windturbines, and propeller blades. Requirements of the framework include: maintaining a low computational cost; allowing large geometric changes to the design; and include the capability to interface with different structural models. From a practical perspective, the project aims to apply the subsequent framework to explore the potential gains of non-traditional aircraft wing designs.

1.2 A Reader's Guide

This thesis is divided into two parts. The first part describes the methods implemented throughout the Ph.D. project, the subsequent studies conducted, and the resulting contributions. The second part includes the author's relevant publications to the methods described in Part 1. For clarity, the first part of the thesis will refer to studies detailed in these publications, however notation and definition of variables may vary between Parts 1 and 2.

The thesis is written to be somewhat self-contained whereby general introductions to concepts are included, but specific details may be excluded – in which case, references will be provided for the reader to pursue further details. However, it is recommended that the reader have some basic knowledge of the following areas and are referred to the respective texts: numerical optimization [1], potential flow theory [2] and finite element methods [3, 4].

Part 1 of this thesis is structured as follows. The remainder of this introduction will give an overview of aircraft design. Chapter 2 will introduce the numerical methods used throughout the Ph.D. project. Chapter 3 will present methods specific to aerodynamic optimization, accompanied by relevant studies and findings. Methods are extended to aeroelastic shape optimization studies in Chapter 4. Chapter 5 concludes the thesis, highlights the important contributions, and discusses recommendations for future work. Additionally, the Appendices contain further information on methods and a number of smaller unpublished studies which aid the discussions throughout Part 1.

1.3 An Overview of Aircraft Design

1.3.1 A Short History of the Modern Aircraft

It is of no doubt common knowledge to most readers that the first self-propelled flight was conducted by the Wright brothers in 1903. This marked a historic day in human history, but with the flight lasting only twelve seconds and spanning a distance of 37 meters, their *Wright Flyer* (shown in Figure 1.1a) was far from the modern aircraft in use today. However, both the *Wright Flyer* and modern aircraft designs have the same principle components. In fact, it was Cayley [5] who had outlined the principle components of modern aircraft roughly a century before the Wright brothers took flight. More specifically, Cayley introduced the concept of fixed-wing aircrafts with separate systems for lift, propulsion, control, and payload. Today we know these systems as the wing, engine, tail, and fuselage respectively, which can be seen for each aircraft in Figure 1.1. Cayley also identified the four aerodynamic forces of flight: lift, drag, weight, and thrust (which are detailed in the next subsection).

Aircraft designs rapidly improved throughout the 20th century aided by significant developments in aerodynamic theory during the first half of the century, large investments in new technologies during two world wars, and the gains in computational power in the latter half of the century. A timeline of

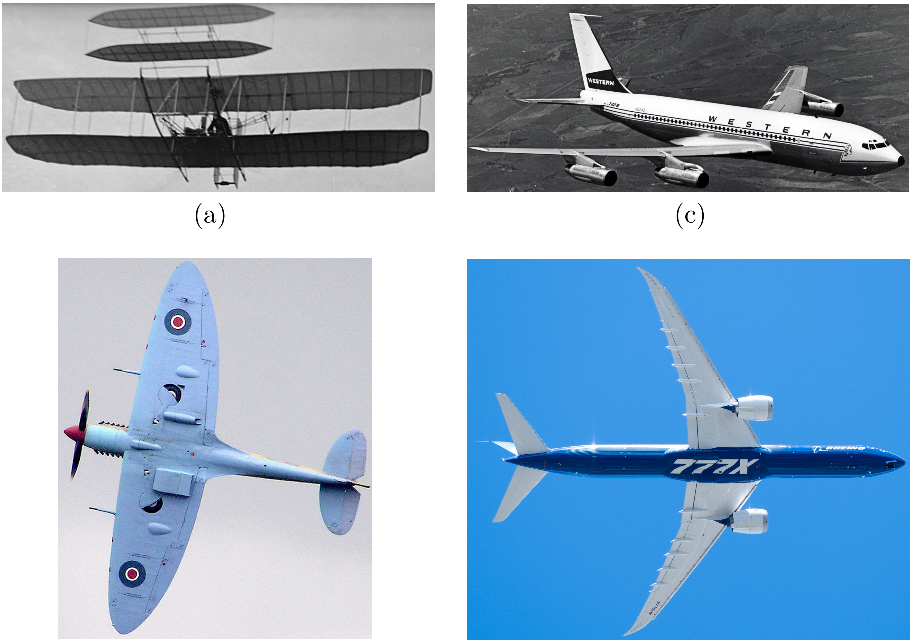

(a)

(c)

(b)

(d)

Figure 1.1: Aircraft of different periods: (a) *Wright flyer* 1903 [6], (b) *Spitfire* 1938 [7], (c) *Boeing 707* 1958 [8], and (d) *Boeing 777X* 2022 [9].

these developments is shown in Figure 1.2, along with some notable milestones in aviation. A major early contribution of particular relevance is the development of lift circulation theory and the Kutta-Joukowski theorem. The theory relates the lift generated by two-dimensional bodies to a circulation defined as a closed-loop integral of the velocity tangential to a path enclosing the body [10]. The theory laid the groundwork for Prandtl's lifting line theory, the first 3D method for modeling the aerodynamics of aircraft wings. In 1923, Munk [11] developed a criteria for defining the aerodynamic efficiency of aircraft wings and proved an optimal planar wing will have an elliptic circulation distribution along the span, which by the Kutta-Joukowski theorem corresponds to an elliptic lift distribution. These findings inspired the elliptic planform designs of World War II era planes such as the *Spitfire* (shown in 1.1b). World War II also saw the start of mass production of aircraft and after the war, many of these production lines continued producing aircraft for civilian use, leading to reduced manufacturing costs and increases in the number of operational aircraft worldwide.

Comparing Boeing's first passenger jet aircraft, the *707* which launched in 1958 (in Figure 1.1c), to their latest aircraft, the *777X* scheduled for 2022 (in Figure 1.1d), there has been an increase in efficiency from 45 passenger miles

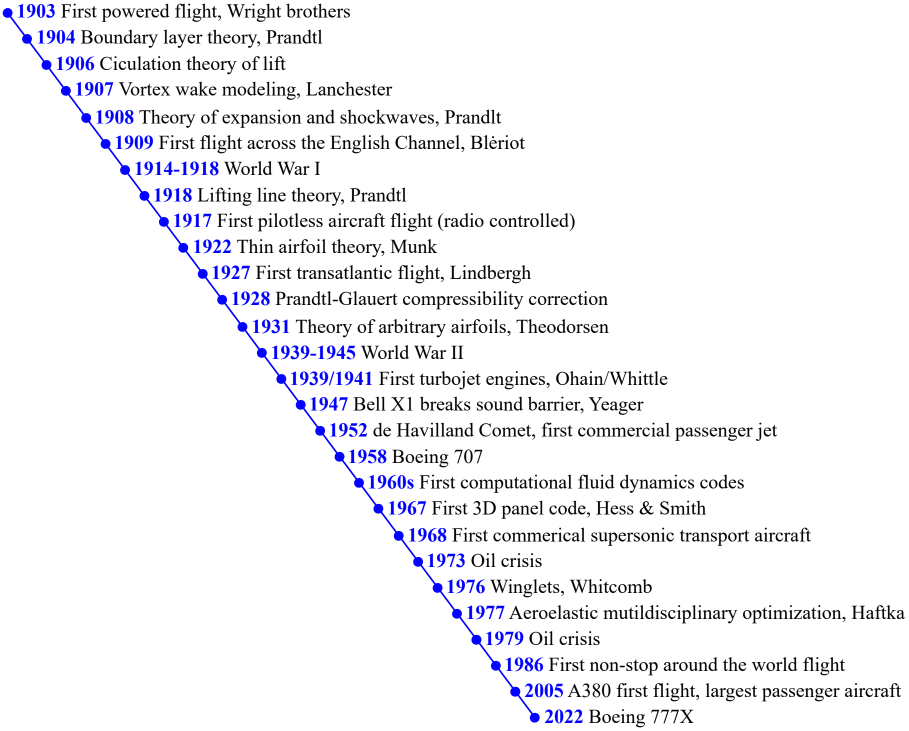
1903 First powered flight, Wright brothers
1904 Boundary layer theory, Prandtl
1906 Ciculation theory of lift
1907 Vortex wake modeling, Lanchester
1908 Theory of expansion and shockwaves, Prandtl
1909 First flight across the English Channel, Blėriot
1914-1918 World War I
1918 Lifting line theory, Prandtl
1917 First pilotless aircraft flight (radio controlled)
1922 Thin airfoil theory, Munk
1927 First transatlantic flight, Lindbergh
1928 Prandtl-Glauert compressibility correction
1931 Theory of arbitrary airfoils, Theodorsen
1939-1945 World War II
1939/1941 First turbojet engines, Ohain/Whittle
1947 Bell X1 breaks sound barrier, Yeager
1952 de Havilland Comet, first commercial passenger jet
1958 Boeing 707
1960s First computational fluid dynamics codes
1967 First 3D panel code, Hess & Smith
1968 First commerical supersonic transport aircraft
1973 Oil crisis
1976 Winglets, Whitcomb
1977 Aeroelastic mutildisciplinary optimization, Haftka
1979 Oil crisis
1986 First non-stop around the world flight
2005 A380 first flight, largest passenger aircraft
2022 Boeing 777X

Figure 1.2: Timeline of the advancements in aviation and modeling methods since the first powered flight in 1903.

per gallon (p-mpg) to an expected 97 p-mpg [12, 13]. This gain in efficiency is due to increases in passenger-to-aircraft weight ratios, engine efficiency, and lift-to-drag ratios. The largest impact in improving aerodynamic performance is undoubtedly from the advances in computational technology and computational methods for aircraft design. Computational fluid dynamics (CFD) codes were first developed in the 1960s and have since become a pivotal part of aircraft design. The main advantage of CFD is that it provides the ability to simulate a number of cases in a short time frame and at a low cost compared to wind tunnel experiments. In the early days of computers, potential flow models played the largest role in aircraft design [14]. Advancements in computational power has made more advanced CFD models viable, where potential flow solvers are now predominately only used at the preliminary design phase. Section 2.2.1 provides more detail on the differences between aerodynamic models.

The 1970s saw two oil crises which forced the price of aviation fuel to drastically inflate and inspired aircraft engineers to seek methods of improving efficiency. Motivated by this, Whitcomb began experimenting with winglet designs, where the wing geometry is curved upward towards the wingtip. Whitcomb documented increases in lift-to-drag ratios of up to 9% [15], which is due to a reduction in the induced drag, a concept discussed later in this section. It took almost three decades for winglets to become a common feature on commercial airliners, and other than winglets, there are very few noticeable differences in aerodynamic form between the commercial airliners of the 1950s, like the *Boeing 707*, and the airliners of today. As stated previously, these designs use a configuration that is based on Cayley's interpretation of flying machines from 1809. It is already a popular opinion that a large potential for increased efficiency can be achieved by exploring unconventional aircraft configurations and wing designs, such as a blended wing-body [16, 17, 18], lifting fuselage [19, 20, 21], drooped wings [22, 23], and morphing wings [24, 25, 26]. Similar to the aerodynamic form, the internal structural designs of wings have not changed much since the early days of flight where wings are usually constructed from rib-spar configurations. This type of structural design is discussed later in this section, and was used in both the *Wright flyer* from 1903 and the modern aircrafts of today. However, it is worth noting that advancements in material technology has had a large impact. For example, the ribs and spars of the *Wright flyer* were made of wood, the *707* used aluminum, and the *777X* will use composite materials – where each development has offered a greater strength-to-weight ratio.

The challenge of reducing fuel consumption is just as prominent today. From a commercial perspective, reducing fuel consumption is directly related to cost savings and profit. From an environmental perspective, the aviation sector currently accounts for 2.5% of the world's CO_2 emissions [27], and has been forecast to triple by 2045 due to increases in passenger air traffic. For context, Denmark accounts for around 0.09% of the world's CO_2 emissions, and if the aviation industry were a country they would be the fifth largest contributer. Trends in air traffic have been steadily rising for decades with less than half a billion passengers transported worldwide in 1975, to just over one billion in 1990, and over 4 billion in 2019 [28]. If these trends were to continue they would exceed 11 billion by 2039, but in light of the recent pandemic and expected efforts to reduce air travel due to environmental concerns, a rise to 8 billion in 2039 is more likely [29]. Regardless, air traffic will continue to increase, which will create a further need for reducing emissions and fuel consumption. Improvements in aerodynamic performance and weight savings will be crucial in achieving this goal.

1.3.2 Aircraft Terminology

Throughout this thesis and the accompanying publications, terminology may be used which is unfamiliar to the reader. For completeness, terminology with regard to aircraft design will be outlined here. Consider the typical aircraft configuration shown in Figure 1.3a, with the main wing design features labeled. The wing is typically defined by either a leading and trailing edge or by the quarter chord line and chord distribution, with cross sections defined by airfoils. Figure 1.3b shows the section view, X-X, with typical airfoil geometry

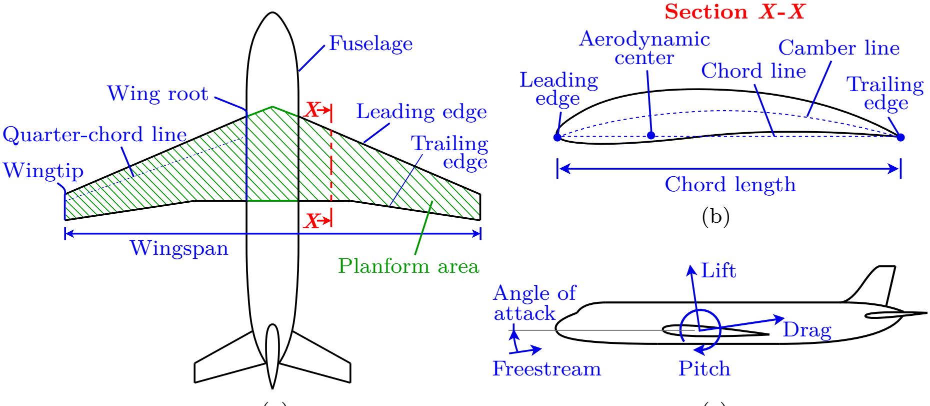
Section X-X
Fuselage
Wing root
Quarter-chord line
Wingtip
Leading edge
Trailing edge
X
X
Wingspan
Planform area
Aerodynamic center
Camber line
Leading edge
Chord line
Trailing edge
Chord length
Lift
Angle of attack
Drag
Freestream
Pitch

(a) (b) (c)

Figure 1.3: Aircraft terminology: (a) planform view with wing geometry terminology, (b) cross section X-X with airfoil terminology, (c) side view with aerodynamic force terminology.

labeled. The aerodynamic center is defined as the point where the pitching moment does not change with angle of attack and is located approximately at the quarter chord point. Because the aerodynamic center is fixed, it is convenient for design purposes to assume the aerodynamic forces act through this point. The aerodynamic forces acting the aircraft are shown in Figure 1.3c where lift and drag are defined perpendicular and parallel to the freestream. Another important parameter that is not labeled in Figure 1.3 is the aspect ratio, which is defined as the ratio of the wingspan squared to the planform area.

A typical internal wing structure is shown in Figure 1.4. The wing's structure has four main components: spars, ribs, skin, and stringers. Spars run along the span of the wing and carry the majority of the load. Ribs are a series of parallel structures that maintain the aerodynamic profile, protect the skin against buckling, and are attached to the spars. The skin gives the wing its aerodynamic shape and is attached to stringers. Stringers are additional stiffeners running spanwise along the wing between the ribs and skin. Forward and aft spars together with their flanges or parts of the ribs form a box-like structure known as a wingbox (whose cross section is labeled in Figure 1.4). Because the skin of the *Wright Flyer* is made of a translucent fabric, the wing's rib-spar structure can also be seen in Figure 1.1a.

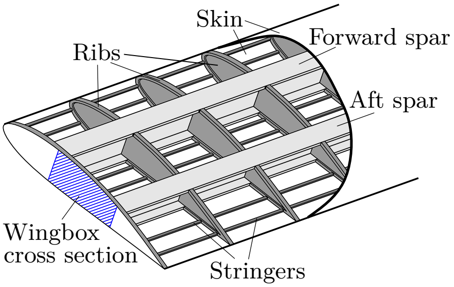
Skin
Forward spar
Ribs
Aft spar
Wingbox cross section
Stringers

Figure 1.4: A typical internal structure of a wing with the main components labeled.

1.3.3 Induced Drag

There are three types of drag that affect aircraft: parasitic drag, lift-induced drag, and wave drag. Wave drag is produced by the pressure variation caused by shockwaves, where flow across the surface becomes locally supersonic, and as such can only take effect in transonic speeds (Mach 0.7-1.3). Parasitic drag accounts for viscous effects relating to the shape of the aircraft and skin friction between the fluid and aircraft surface. Induced drag results from an induced down-wash in the wake of the wing. Parasitic drag is proportional to the square of the freestream velocity whereas induced drag is inversely proportional to square of the freestream velocity. This means that the total drag (assuming no wave drag) is usually dominated by the induced drag at low speeds and parasitic drag at high speeds. The optimization problems presented in this will seek to minimize induced drag as the focus is on aircraft in low-speed subsonic flow where induced drag is dominant. But even for commercial aircraft, which typically operate at Mach 0.7-0.75 during cruise, induced drag accounts for 40% of the total drag in cruise and up to 90% during climb and take-off [30].

Induced drag affects all 3D lifting bodies and is a side effect of lift generation. There are many explanations on how lift is produced, and many factors that contribute to lift. In the most general sense, lift is produced by turning an incoming flow in one direction, resulting in a reaction force in the opposite direction as according to Newton's third law. The component of this reaction force perpendicular to the incoming flow is called lift.

Figure 1.5 is used to explain how induced drag is formed and its relation to lift. To create lift, there needs to be a pressure differential between the upper and lower surfaces of the wing i.e. the lower surface pressure is increased and the upper surface pressure is decreased (refer to Figure 1.5a). This means

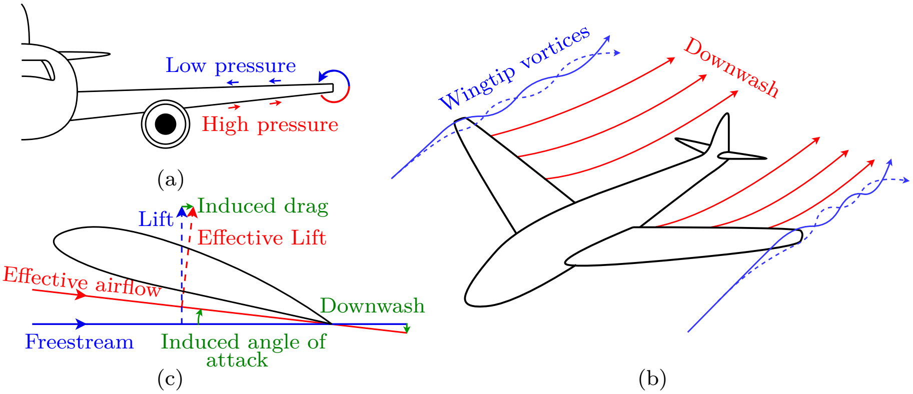

Figure 1.5: Theory of induced drag: (a) pressure differences between the upper and lower surface creates spanwise flow leading to formation of trailing vortices, (b) vortices induce a downwash in the wake, and (c) downwash changes the effective angle of attack leading to a loss in lift and creates induced drag.

the lower surface pressure is higher than the pressure outboard of the wingtip, creating a tendency for outward spanwise flow across the wing's lower surface. Conversely, the upper surface pressure is lower than the pressure outboard of the wingtip, creating a tendency for inward spanwise flow on the upper surface. When upper and lower surface flows meet at the trailing edge their differences in spanwise flow causes vortices to form. These vortices are unstable and combine to produce a wingtip vortex which induces a downwash in the wake of the wing, as shown to Figure 1.5b. The downwash in the wake changes the effective incoming angle of attack and the direction of the aerodynamic load, resulting in a loss in lift and increase in drag as depicted in Figure 1.5c. This additional drag is known as induced drag.

Three important design philosophies for reducing induced drag include:

1. Creating an elliptic spanwise circulation/lift distribution, which in turn creates a constant downwash along the span and the minimum induced drag for a planar wing with a specified wingspan.
2. Maximizing the wingspan (or aspect ratio) which reduces the downwash in the wake for a specified lift. This technique is usually limited by the fact that large wingspans will lead to increased weight (and bending moments), where induced drag is inversely proportional the wingspan squared, but the weight is proportional the wingspan cubed [31].
3. Creating a tailored wingtip geometry, such as winglets or raked wingtips, which reduce spanwise flow leading to a reduction in vortex strength.

2

Numerical Methods

This chapter introduces the numerical methods used in publications [P1-P4]. In the broadest sense these methods are distinguished by 3 distinct areas: design optimization, computational aerodynamics, and structural mechanics. Each of the following sections will include general overviews of the methods implemented with relevant references for further reading. Within the section *design optimization*, readers are introduced to how the optimization problems are formulated. The aerodynamic model used throughout this thesis is based on panel methods which are detailed in the succeeding section. The structural analysis used in [P2,P4] is based on beam finite element (FE) models which are described in Section 2.3. The final section of this chapter is on multidisciplinary analysis which discusses the methods used to solve coupled aeroelastic problems.

2.1 Design Optimization

2.1.1 Background

Design optimization applies numerical optimization techniques to the design of engineering systems whose physics can be captured by a numerical model (typically in the form of a discretized PDE). The goal is to find a design that minimizes an objective function subject to constraints on the physics and/or design. The design is defined by a parameterization method which is controlled by a set of design variables. Typically, methods of parameterizing designs for optimization problems are classified with respect to three techniques: sizing optimization, shape optimization, and topology optimization. These methods are illustrated in Figure 2.1. All techniques involve an initial design which is modified by perturbing design variables. Sizing optimization scales the design but does not allow any changes to the initial shape. Shape optimization modifies the external border of the design, allowing changes in shape, but does not permit changes to internal geometry such as the creation of holes. Topology optimization has full design freedom, allowing both changes to the external shape and creation of internal features.

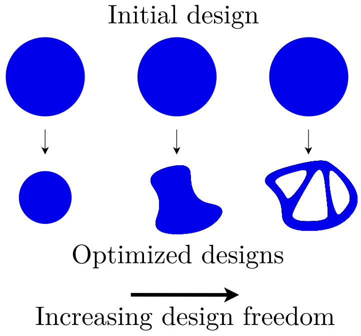

Figure 2.1: Parameterization methods for design optimization: sizing (left), shape (middle), and topology (right) optimization.

In posing a design optimization problem it is important to choose an appropriate parameterization technique for the specific goal of the study or the available physics in the numerical model. Sizing optimization offers the least design freedom but is usually the simplest to implement and is very efficient in ground-structure type approaches [32, 33, 34, 35] where some geometry is prescribed. On the other extreme, topology optimization offers the largest design space and is very versatile making the method applicable to a wide range of problems in different disciplines including structural mechanics [36, 37, 38, 39], fluid dynamics [40, 41, 42], and various multi-physics applications [37, 43, 44, 45]. Shape optimization also offers a large design space but is limited to applications where internal voids are not required. With respect to purely aerodynamic optimization internal voids are usually of little interest and shape optimization is the most commonly adopted method. For shape optimization of airfoil geometries there are some key components to the shape which must be maintained, for example a sharp trailing edge and blunt leading edge. Most parameterizations for these types of problems will include restrictions to ensure such features in geometry. The airfoil parameterization methods used in this thesis are discussed in detail in Section 3.3.1, and further details on topology optimization methods are provided in Appendix A.

2.1.2 The Design Problem

Once the parameterization and physics models are defined, the optimization problem can be expressed in terms of design variables, **d**, and state variables, **s**. The optimization problem is generally defined as

$$
\begin{array}{llll}
\min\limits_{\mathbf{d}\,\in\,\mathbb{R}^{N_d}} & : \; f(\mathbf{d},\mathbf{s}) & & \\
\text{subject to} & : \; \mathbf{R}(\mathbf{d},\mathbf{s}) = 0 & & \text{state equations} \\
 & \quad g_i(\mathbf{d},\mathbf{s}) \leq 0 & \text{for } i = 1, ..., N_g & \text{inequality constraints} \\
 & \quad h_i(\mathbf{d},\mathbf{s}) = 0 & \text{for } i = 1, ..., N_h & \text{equality constraints} \\
 & \quad \underline{d} \leq d_i \leq \bar{d} & \text{for } i = 1, ..., N_d & \text{box constraints}
\end{array}
\tag{2.1}
$$

where f denotes the objective function to be minimized, **R** is the residual of the state equations, g and h are inequality and equality constraint functions. Each of these functions may depend on some or all of the state variables and/or design variables, which are constrained to be within the lower and upper bounds, $\underline{d}$ and $\bar{d}$. In this thesis a nested formulation is used where the state equations are always converged, and as such are often not included in the problem definition. The optimization problem is solved using gradient-based methods where the design is updated iteratively by making small perturbations to **d** in a direction dependent on the gradients of the objective and constraint functions. The process of calculating these gradients is known as sensitivity analysis.

2.1.3 Sensitivity Analysis

Gradients for optimization problems are usually calculated using one of four methods: finite difference, complex step, direct or adjoint analysis. A finite difference approximation is the easiest to implement but can be inaccurate and does not scale well to problems with many design variables. The complex step method can be used to improve the accuracy but also does not scale well. Direct and adjoint methods are accurate to machine precision where direct methods scale with the number of design variables and adjoint methods with number of constraint/objective functions. It follows that an adjoint approach is more efficient when the number of functions is less than the number of design variables, i.e. $N_g + N_h + 1 < N_d$. This is the case for each problem in this thesis and as such a discrete adjoint approach is implemented. Gradients are derived by first expressing the objective/constraint function in augmented Lagrangian form as

$$\tilde{f} = f + \boldsymbol{\lambda}^{\mathrm{T}}\mathbf{R} \tag{2.2}$$

where $\boldsymbol{\lambda}$ is a Lagrangian multiplier, and left- and right-hand sides are equal because $\mathbf{R} = \mathbf{0}$ (as implied from (2.1)). Differentiating (2.2) and applying the chain rule yields

$$\frac{d\tilde{f}}{d\mathbf{d}} = \frac{\partial f}{\partial \mathbf{d}} + \frac{\partial f}{\partial \mathbf{s}}\frac{d\mathbf{s}}{d\mathbf{d}} + \boldsymbol{\lambda}^{\mathrm{T}}\left(\frac{\partial \mathbf{R}}{\partial \mathbf{d}} + \frac{\partial \mathbf{R}}{\partial \mathbf{s}}\frac{d\mathbf{s}}{d\mathbf{d}}\right) \tag{2.3}$$

where partial derivatives capture only explicit dependence (without resolving the state equation) and total derivatives capture the implicit dependence also. The aim now is to find a value of $\boldsymbol{\lambda}$ such that all total derivatives are eliminated. This is achieved through solving the adjoint equation

$$\frac{\partial \mathbf{R}}{\partial \mathbf{s}}^{\mathrm{T}}\boldsymbol{\lambda} = -\frac{\partial f}{\partial \mathbf{s}}^{\mathrm{T}} \tag{2.4}$$

which yields the final form

$$\frac{d\tilde{f}}{d\mathbf{d}} = \frac{\partial f}{\partial \mathbf{d}} + \boldsymbol{\lambda}^{\mathrm{T}}\frac{\partial \mathbf{R}}{\partial \mathbf{d}} \tag{2.5}$$

It is important to note that the methods discussed here are also applicable to multidisciplinary design optimization (MDO) where the physics problem contains multiple disciplines or subsystems (such as aerodynamic and structural analysis). In the case of MDO problems, (2.4) and (2.5) are solved with respect to the global multidisciplinary system which is expressed as an augmented residual, $\mathbf{R} = \{\mathbf{R}_a(\mathbf{d},\mathbf{s}), \mathbf{R}_b(\mathbf{d},\mathbf{s}), ...\}^{\mathrm{T}}$, with state variables, $\mathbf{s} = \{\mathbf{s}_a, \mathbf{s}_b, ...\}^{\mathrm{T}}$, where subscripts represent different subsystems. Readers are referred to [46] for a detailed overview of sensitivity analysis for MDO problems.

2.2 Panel Methods

Throughout this thesis, aerodynamic characteristics and loads are calculated using a panel method. This section first outlines the motivation for using panel methods, then introduces the numerical methods including the problem formulation, boundary conditions, model discretization, and force calculations.

2.2.1 Why Panel Methods?

The Navier-Stokes equations provide the most general description of fluid flow, but direct simulation of these equations for complete aircraft configurations would be extremely expensive or even impossible with today's computational power. This requires some simplifications and assumptions about the flow. When more assumptions are made about the flow, the fidelity of the aerodynamic model will reduce but so will the required computational cost. In the aircraft industry, flow of complete configurations is typically resolved by solving the Reynolds-averaged Navier-Stokes (RANS) equations, Euler equations, or potential flow models [14]. Figure 2.2 ranks these models in terms of fidelity and computational cost. The following gives descriptions of each model's capabilities and examples from literature of their applications to aerodynamic and/or aeroelastic optimization.

- RANS models achieve time averaged solutions, are applicable to turbulent flows, capture viscous effects, and require a volume mesh of the entire fluid domain [47, 48, 49].

- The Euler equations neglect viscosity, are applicable to compressible laminar flow, and also require a volume mesh [50, 51, 52, 53].

- The full potential flow equation is applicable to inviscid compressible flow and requires a volume mesh [54, 55]. However, potential flow models are often linearized, where they are only applicable to incompressible flow, and can be implemented as panel methods (3D surface mesh) [56, 57, 58], vortex lattice methods (2D surface mesh) [59, 60, 61], or lifting line methods (1D mesh) [62, 63].

As discussed in the introduction, the main goal of this thesis is to create an optimization framework that can produce optimized aerodynamic and structural designs in a relatively fast time frame (from a couple of hours up to a day). This rules out many of the high fidelity methods as the physics models alone come with a large computational cost which must be solved on each design iteration of the optimization procedure. The potential flow models shown in Figure 2.2 are low- to mid-fidelity methods that differ mainly due to the model's representation and varying degrees of freedom in the mesh (as described above). Another requirement is that the framework can be interfaced with different structural models. By representing the actual surface of the wing, 3D pressure distributions can be achieved and applied directly to 3D finite element models

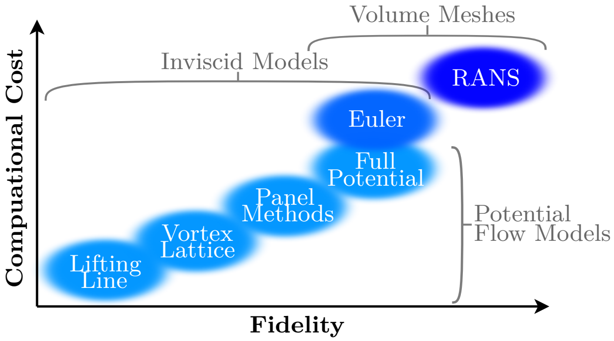

Figure 2.2: Common aerodynamic models ranked in terms of computational cost and fidelity. Axes are representative and are not to scale.

such as continuum or shell elements. With a simplified representation such as a lifting line or vortex lattice, pressure distributions are not immediately available for application to 3D finite elements. A third requirement is to allow large geometric changes to the design, which is of course possible with any of the methods. However, with a volume mesh, elements can easily become distorted as the geometry changes which may require regular remeshing during the optimization procedure, and subsequently increase the computational cost. Allowing large shape changes is much simpler with a surface mesh as elements are not so easily distorted. Considering all of the above, panel methods offer an excellent option to achieve all requirements of the framework. The panel code used in this thesis is based on MIRAS [64], where the methods have been extended to include different boundary conditions, far-field calculations, and sensitivity analysis using a discrete adjoint approach.

2.2.2 Background

The panel method is a numerical approach to solving inviscid, irrotational and fully subsonic or supersonic flow based on linearized potential flow theory. In potential flow theory, the flow can be described at any point in a domain, p, by a potential function, $\phi(x, y, z)$ where the velocity at p is given by the gradient of the potential function, $\boldsymbol{U}_p = \nabla\phi_p$, and ϕ satisfies the Laplace equation

$$\nabla^2\phi = 0 \tag{2.6}$$

Now consider the wing shown in Figure 2.3a with a surface, S. There are two boundary conditions associated with this potential flow problem: the velocity normal to the surface must be 0 (i.e. no penetration), and the disturbance of the flow due to the wing must decay when p is far from S i.e. $r \to \infty$.

$$\nabla\phi_p \cdot \boldsymbol{n}_p = 0 \quad \text{for } p \text{ on } S \tag{2.7a}$$

$$\lim_{r\to\infty}(\nabla\phi_p - \boldsymbol{U}_\infty) = 0 \tag{2.7b}$$

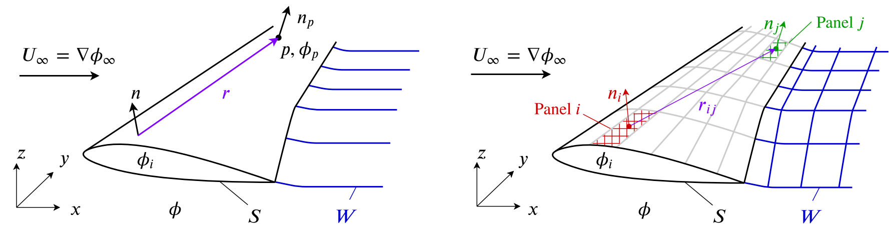

(a) (b)

Figure 2.3: Potential flow problem for a wing with surface, S, and wake, W in (a) continuous and (b) discrete form.

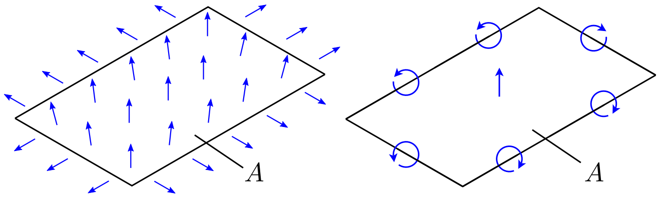

(a) (b)

Figure 2.4: Flow patterns for distributed constant-strength (a) sources and (b) doublets.

The first condition, given in (2.7a), is known as the Neumann condition and there are a number of elementary solutions to (2.6) that naturally satisfy the second condition in (2.7b), of which the most relevant are sources and doublets. The flow associated with constant-strength source and doublets distributed over a surface, A, is depicted in Figure 2.4 where the distributed sources project flow outward in all directions from the surface and the distributed doublets circulate flow around the surface edges. The potential functions associated with distributed constant-strength source and doublets are defined in [2] as

$$\phi_\sigma = -\frac{\sigma}{4\pi}\int_A \frac{1}{r} dA \quad , \quad \phi_\mu = \frac{\mu}{4\pi}\int_A \frac{\partial}{\partial \boldsymbol{n}}\left(\frac{1}{r}\right) dA \tag{2.8}$$

where σ is the source strength, μ is the doublet strength, $\boldsymbol{n}$ is the surface's normal vector, and r is the distance from the source/doublet. Referring back to Figure 2.3a, sources and doublets are distributed over the surface, S, and doublets only over the wake, W. The potential at point p can then be expressed as the sum of influences from the surface, wake, and freestream as

$$\phi_p = -\frac{1}{4\pi}\int_S \left[\sigma\frac{1}{r} - \mu\frac{\partial}{\partial \boldsymbol{n}}\left(\frac{1}{r}\right)\right] dS + \frac{1}{4\pi}\int_W \left[\mu\frac{\partial}{\partial \boldsymbol{n}}\left(\frac{1}{r}\right)\right] dW + \phi_{\infty,p} \tag{2.9}$$

where ϕ_∞ is the freestream potential.

An important property of the Laplace equation is the principle of superposition, which states that if ϕ_σ, ϕ_μ, and ϕ_∞ are all solutions to the Laplace equation, then their sum, $\phi_\sigma + \phi_\mu + \phi_\infty$, is also a solution, which means (2.9) satisfies (2.6). Equation (2.9) holds anywhere in the domain and can be used to form expressions for the potential on S in order to satisfy (2.7a). These expressions in turn will form the governing equation for the panel method where (2.7a) can be satisfied explicitly in terms of the velocity, or implicitly in terms of the potential function. These two methods are known as Neumann and Dirichlet boundary conditions (BC), respectively. Depending on the problem, one BC may be advantageous over the other and as such it is important to understand the differences between formulations.

2.2.3 Neumann Boundary Condition

The Neumann BC satisfies the non-penetration boundary condition explicitly by combining (2.9) and (2.7a) to yield the following state equation for a point on S

$$\left[-\frac{1}{4\pi}\int_S\left[\sigma\nabla\left[\frac{1}{r}\right]-\mu\nabla\left[\frac{\partial}{\partial\boldsymbol{n}}\left(\frac{1}{r}\right)\right]\right]dS+\frac{1}{4\pi}\int_W\mu\nabla\left[\frac{\partial}{\partial\boldsymbol{n}}\left(\frac{1}{r}\right)\right]dW\right]\cdot\boldsymbol{n}_p=-\boldsymbol{U}_\infty\cdot\boldsymbol{n}_p \tag{2.10}$$

The source strength, σ, is defined using the derivatives of the potential on the external, ϕ, and internal, ϕ_I, surface of the wing

$$-\sigma=\frac{\partial\phi}{\partial\boldsymbol{n}}-\frac{\partial\phi_I}{\partial\boldsymbol{n}} \tag{2.11}$$

The first derivative on the right hand side is equivalent to $\nabla\phi\cdot\boldsymbol{n}$, which is equal to 0 by (2.7a). This means the source strength is equal to the derivative of the internal potential. A zero internal perturbation formulation [65, 66] is used where the internal potential is set to be equal to the freestream potential, $\phi_I=\phi_\infty$, yielding

$$\sigma=\boldsymbol{U}_\infty\cdot\boldsymbol{n} \tag{2.12}$$

The surface, S, and wake, W, are discretized into a number of panels as shown in Figure 2.3b, where each panel on the wing has a constant-strength source and doublet, and each panel in the wake has a constant-strength doublet. The Neumann BC in (2.10), is expressed using a discrete set of collocation points at the center of each panel, which yields the following set of algebraic equations

$$\mathbf{R}_a=\mathbf{A}_N\boldsymbol{\mu}+(\mathbf{B}_N+\mathbf{I})\boldsymbol{\sigma}=\mathbf{0} \tag{2.13}$$

where $\mathbf{A}_N$ is the aerodynamic influence coefficient (AIC) for doublet distributions on both the wing and wake with a Neumann BC, and $\mathbf{B}_N$ is the AIC for source distributions along the wing with a Neumann BC. Figure 2.3b shows the discretized form of the wing shown in Figure 2.3a, where the $\{i,j\}$ entry of $\mathbf{A}_N$ and $\mathbf{B}_N$ is the influence panel i has on panel j. AICs for the Neumann

BC are derived using the methods outlined in [2]. Each panel will influence every other point in the domain meaning that $\mathbf{A}_N$ and $\mathbf{B}_N$ are dense matrices. Equation (2.13) defines the governing equation when a Neumann BC is used, where the doublet strengths $\boldsymbol{\mu}$ are the unknowns and source strengths $\boldsymbol{\sigma}$ are calculated using (2.12).

2.2.4 Dirichlet Boundary Condition

The second option is to apply a Dirichlet BC which is an implicit formulation of (2.7a). It has been shown that to satisfy (2.7a), it is required that $\frac{\partial \phi}{\partial \boldsymbol{n}} = 0$ which means the internal potential must be constant [67]. The constant value is arbitrary, however if one were to set ϕ_I equal to the freestream potential, as done previously, then (2.9) for any point enclosed by the wing is simplified to

$$-\frac{1}{4\pi}\int_S \left[\sigma\frac{1}{r} - \mu\frac{\partial}{\partial \boldsymbol{n}}\left(\frac{1}{r}\right)\right] dS + \frac{1}{4\pi}\int_W \mu\frac{\partial}{\partial \boldsymbol{n}}\left(\frac{1}{r}\right) dW = 0 \tag{2.14}$$

The surface and wake are discretized into panels in the same manner as for a Neumann BC, and (2.14) is enforced at collocation points just underneath each panel center (inside the wing). This creates the governing equation for the Dirichlet problem.

$$\mathbf{R}_a = \mathbf{A}_D\boldsymbol{\mu} + \mathbf{B}_D\boldsymbol{\sigma} = \mathbf{0} \tag{2.15}$$

where $\mathbf{A}_D$ is the AIC for doublet distributions on the wing and wake with a Dirichlet BC, and $\mathbf{B}_D$ is the AIC for source distributions on the wing with a Dirichlet BC. These terms are defined for quadrilateral panels in [2]. Similar to the Neumann problem, $\mathbf{A}_D$ and $\mathbf{B}_D$ are dense matrices, and (2.15) is solved for $\boldsymbol{\mu}$, where $\boldsymbol{\sigma}$ is calculated using (2.12).

At this point it is important to emphasize the key differences between Neumann and Dirichlet BCs. Firstly, the Neumann BC is expressed in terms of velocity where $\mathbf{A}_N$ and $\mathbf{B}_N$ are formed from the dot product of the velocity influence coefficient in three dimensions and a normal vector, whereas the Dirichlet BC is expressed in terms of the potential function, which is a scalar. Secondly, the Dirichlet BC is formulated based on separated external and internal domains, whereas the Neumann BC makes no explicit assumptions about the internal domain (however the source terms do).

2.2.5 Wake Model

In previous discussions on the problem formulation the wake was included in the model, but so far the discussion has been mainly on the wing itself. The wake model is included in order to satisfy the Kutta condition and to calculate induced drag. These principles will be discussed later in this section, whereas the focus here is on the wake model itself. The simplest wake model is a vortex sheet projected in the freestream direction from the trailing edge of the wing, as shown in Figure 2.5a. This freestream model can be implemented using a

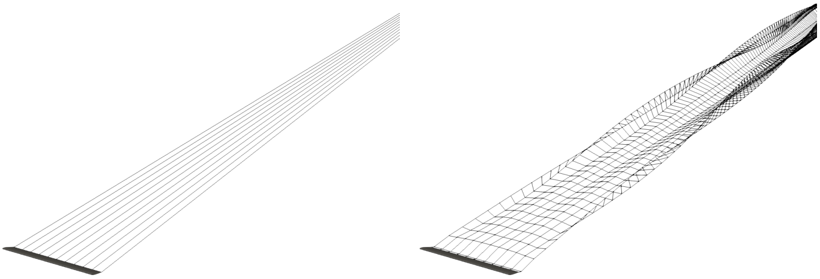

(a) (b)

Figure 2.5: Two different wake models for panel methods: (a) a fixed freestream wake, and (b) an iterative wake model.

single panel at each spanwise section of the wake. The low number of wake panels makes the freestream model computationally efficient but may become inaccurate for wing geometries that create a large variance in the structure of the wake. To increase accuracy, multiple wake panels can be used to capture the correct wake geometry, but this requires prior knowledge of the wake shape in order to position panels appropriately. In optimization problems the wing geometry is unpredictable during the optimization procedure and the wake geometry is unknown. Iterative wake models can be used to capture complex wake structures as shown in Figure 2.5b. However on each iteration the AIC's are recalculated to account for the influence from the new wake shape, and the governing equations need to be resolved. This creates a large computational cost for iterative methods and as such a freestream model will be used in each case presented in this thesis. For more information on implementing iterative wake models readers are referred to [64, 68, 69, 70].

2.2.6 Kutta Condition

As stated previously, the wake model allows the Kutta condition to be enforced which is required to ensure the model remains physical. The Kutta condition states that flow must leave the surface of the wing at the trailing edge (TE) with a finite velocity. This can be enforced by ensuring there is no circulation at the TE. From Figure 2.6b we see that this condition corresponds to

$$\boldsymbol{\mu}_W - \boldsymbol{\mu}_U + \boldsymbol{\mu}_L = 0 \tag{2.16}$$

The Kutta condition must be applied to each TE section. This condition can be enforced explicitly by adding (2.16) to our system of equations, (2.13) or (2.15), and solving for $\boldsymbol{\mu}_W$ directly, or enforced implicitly by modifying the

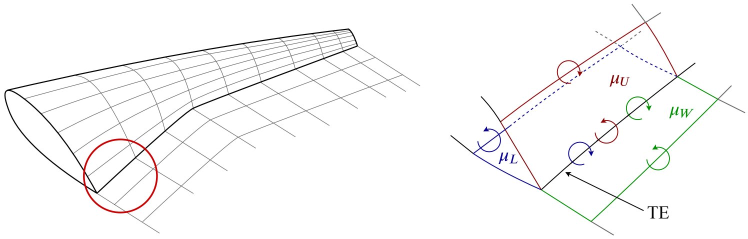

(a) (b)

Figure 2.6: Wing and wake panels extending from trailing edge (TE). The red circle in (a) marks the detail shown in (b) where doublet strengths and directions are shown.

doublet influence coefficients of the TE panels as follows

$$\begin{aligned} A_{i,U} &= A_{i,U} + A_{i,W} \\ A_{i,L} &= A_{i,L} - A_{i,W} \end{aligned} \tag{2.17}$$

2.2.7 *Post-Processing*

After solving (2.13) or (2.15), $\boldsymbol{\sigma}$ and $\boldsymbol{\mu}$ distributions can be used to achieve surface pressures on the wing and velocities anywhere in the domain. Because the velocity at any point is defined as the gradient of the potential function, numerical differentiation methods can be used to achieve the velocity over the surface of the panel. The velocity over panel i is expressed in local coordinates (l,m,n) as

$$\boldsymbol{U}_i = \left\{ \frac{\partial \phi}{\partial l}, \frac{\partial \phi}{\partial m}, \frac{\partial \phi}{\partial n} \right\}_i^{\mathrm{T}} = \left\{ \frac{\partial \mu}{\partial l}, \frac{\partial \mu}{\partial m}, 0 \right\}_i^{\mathrm{T}} + \{U_{\infty,l}, U_{\infty,m}, U_{\infty,n}\}_i^{\mathrm{T}} \tag{2.18}$$

The Bernoulli equation uses the panel velocities to calculate the pressure coefficient, C_P, which is integrated over the wing to find the total force, $\boldsymbol{F}$, and moments, $\boldsymbol{M}$, via the following

$$C_{P,i} = 1 - \frac{\|\boldsymbol{U}_i\|^2}{U_\infty^2} \tag{2.19}$$

$$\boldsymbol{F} = q_\infty \sum_{i=1}^{N_P} C_{P,i} S_i \boldsymbol{n}_i \quad , \quad \boldsymbol{M} = q_\infty \sum_{i=1}^{N_P} C_{P,i} S_i (\boldsymbol{r}_i \times \boldsymbol{n}_i) \tag{2.20}$$

where q_∞ is the dynamic pressure defined as $q_\infty = \frac{1}{2}\rho_\infty U_\infty^2$, N_P is the number of panels on the wing surface, and $\boldsymbol{r}_i$ is a spatial vector from a reference point, about which moments are calculated, to panel i's collocation point. Moment calculations can be used to obtain pitching and bending moments, and projecting $\boldsymbol{F}$ perpendicular and parallel to the freestream direction yields the following expressions for lift and induced drag

$$L_{C_P} = \frac{1}{U_\infty}\{-U_{\infty,z}\ ,\ 0\ ,\ U_{\infty,x}\}\boldsymbol{F} \quad , \quad D_{C_P} = \frac{1}{U_\infty}\{U_{\infty,x}\ ,\ 0\ ,\ U_{\infty,z}\}\boldsymbol{F} \tag{2.21}$$

where it is assumed the y velocity of the freestream is 0. The subscripts of D_{C_P} and L_{C_P} indicate that the forces are calculated via C_P-integration. Aerodynamic forces can also be calculated through far-field calculations within a Trefftz plane. The Trefftz plane is represented in Figure 2.7 where it is defined perpendicular to the freestream and far enough downstream that perturbations to the flow in the freestream direction are negligible. Applying the conservation of momentum yields expressions for lift, L_{TP}, induced drag, D_{TP}, and root bending moment, M_r, in terms of a 2D integral along the intersection of the wake and Trefftz plane [71, 72].

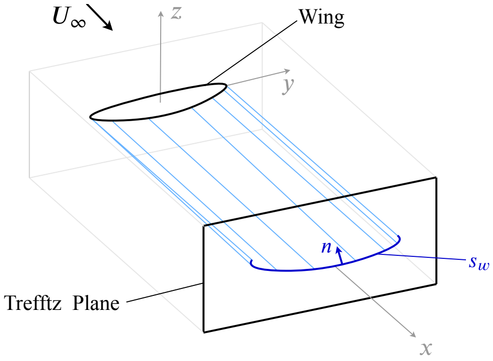

Figure 2.7: Definition of the Trefftz plane. Figure retrieved from [P1].

$$L_{TP} = \rho_\infty U_\infty \int_{s_w} \Delta\phi dy \simeq \rho_\infty U_\infty \sum_{i=1}^{N_w} \mu_i s_i \cos(\theta_i) \tag{2.22}$$

$$D_{TP} = -\frac{1}{2}\rho_\infty \int_{s_w} \Delta\phi \frac{\partial \phi}{\partial n} ds_w \simeq -\frac{1}{2}\rho_\infty \sum_{i=1}^{N_w} \mu_i s_i \boldsymbol{u}_i.\boldsymbol{n}_i \tag{2.23}$$

$$M_r = \rho_\infty U_\infty \int_{s_w} r_w \Delta\phi ds \simeq \rho_\infty U_\infty \sum_{i=1}^{N_w} \mu_i s_i |y_i \cos(\theta_i) + z_i \sin(\theta_i)| \tag{2.24}$$

where s_w is the 2D curve representing the wake-Trefftz plane intersection, $\Delta\phi$ is the difference in potential over s_w, and r_w is the distance from the origin in the Trefftz plane. In discrete form, s_i, θ_i, $\boldsymbol{n}_i$, and (y_i, z_i) represent the length, orientation, normal vector, and center point of wake panel i in the Trefftz plane.

Finally, aerodynamic forces can be normalized to give lift and drag coefficients, $C_L = \frac{L}{q_\infty S}$ and $C_D = \frac{D}{q_\infty S}$, where L and D may represent lift or drag via either integration method, and S represents the planform area of the wing. In some cases, compressibility effects will be included by solving the Prandtl-Glauret equation rather than the Laplace equation in (2.6). This can be achieved by performing a simple coordinate transformation in a preprocessing step, and applying a correction to physical quantities in post-processing to invert the transformation. Further details are supplied in Appendix B.

2.3 Beam Finite Element Analysis

Loads calculated in the panel method will be applied to a structural model to capture deformations of the wing. Structural models considered in this thesis are based on beam finite element (FE) analysis. Methods have also been extended to 3D continuum elements, which is discussed in Appendix A, but is not considered here. This section introduces beam theory and the application to FE models.

2.3.1 Background

Beam models are applicable to slender structures whose length is relatively larger than the cross section. The model is represented with respect to a one dimensional reference axis along the length of the beam, and two dimensional cross sections at arbitrary points along the axis. Figure 2.8 shows a typical beam of length l subject to an external load $\mathbf{q}$.

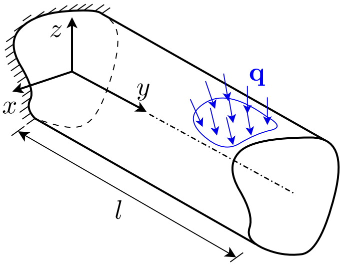

Figure 2.8: An arbitrary beam of length l with its reference axis co-linear to the y-axis, and subject to an external load, $\mathbf{q}$.

The beam is assumed to maintain continuity along the reference line and static equilibrium is ensured through the principle of virtual work which states that the total internal and external virtual work must be balanced, i.e.

$$V = \underbrace{\int_l \{\mathbf{F}^{\mathrm{T}}, \mathbf{M}^{\mathrm{T}}\} \begin{Bmatrix} \delta\boldsymbol{\gamma} \\ \delta\boldsymbol{\kappa} \end{Bmatrix} dl}_{\text{internal}} - \underbrace{\int_l \mathbf{q}^{\mathrm{T}} \delta\mathbf{u} dl}_{\text{external}} = 0 \tag{2.25}$$

The external load, $\mathbf{q}$, is applied in the form of distributed forces and moments which cause the beam to deform through virtual displacements and rotations $\delta\mathbf{u}$. External loads are balanced by the internal forces $\mathbf{F} = \{F_x, F_y, F_z\}^{\mathrm{T}}$, composed of shear and axial forces, and moments $\mathbf{M} = \{M_x, M_y, M_z\}^{\mathrm{T}}$, composed of bending and torsional moments. These vectors act on the beam cross section at a reference point as shown in Figure 2.9a. The internal forces and moments are statically equivalent to the stresses in the cross section which are defined by

$$\begin{gathered} F_x = \int_A \sigma_{yx} dA, \quad F_y = \int_A \sigma_{yy} dA, \quad F_z = \int_A \sigma_{yz} dA \\ M_x = \int_A z\sigma_{yy} dA, \quad M_y = \int_A (\sigma_{yz} x - \sigma_{yx} z) dA, \quad M_z = -\int_A x\sigma_{yy} dA \end{gathered} \tag{2.26}$$

Figure 2.9b shows the generalized strains, $\boldsymbol{\gamma} = \{\gamma_x, \gamma_y, \gamma_z\}^{\mathrm{T}}$, and curvatures, $\boldsymbol{\kappa} = \{\kappa_x, \kappa_y, \kappa_z\}^{\mathrm{T}}$ which also act on the cross section. These strains and

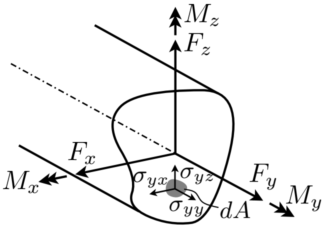

(a) (b)

Figure 2.9: Components of (a) forces and moments, and (b) generalized strains and curvatures, for a given cross-section of a beam.

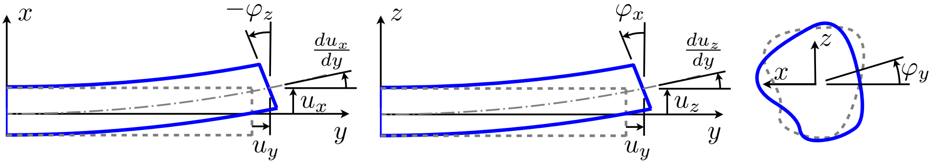

(a) (b) (c)

Figure 2.10: Beam kinematics: (a) deformations in the x-y plane, (a) deformations in the y-z plane, and (c) deformations in the x-z plane

curvatures are defined by the beam kinematics shown in Figure 2.10. Beam cross sections are assumed to remain in-plane and undergo rigid body displacements, $\boldsymbol{u} = \{u_x, u_y, u_z\}^{\mathrm{T}}$, and rotations, $\boldsymbol{\varphi} = \{\varphi_x, \varphi_y, \varphi_z\}^{\mathrm{T}}$. Assuming small rotations, the contributions shown in Figure 2.10 can be summed and differentiated to yield the generalized strains and curvatures

$$\boldsymbol{\gamma} = \left\{ \frac{du_x}{dy} + \varphi_z \ , \ \frac{du_y}{dy} \ , \ \frac{du_z}{dy} - \varphi_x \right\}^{\mathrm{T}} \quad , \quad \boldsymbol{\kappa} = \left\{ \frac{d\varphi_x}{dy} \ , \ \frac{d\varphi_y}{dy} \ , \ \frac{d\varphi_z}{dy} \right\}^{\mathrm{T}} \tag{2.27}$$

The generalized strains and curvatures hold a linear relationship to the cross sectional stresses via a constitutive model and can be related to the internal forces and moments by

$$\begin{Bmatrix} \mathbf{F} \\ \mathbf{M} \end{Bmatrix} = \mathbf{K}_{cs} \begin{Bmatrix} \boldsymbol{\gamma} \\ \boldsymbol{\kappa} \end{Bmatrix} \tag{2.28}$$

where $\mathbf{K}_{cs}$ is the cross sectional constitutive matrix.

2.3.2 Constitutive Model

The constitutive model is derived using the stress relations in (2.26). Assuming linear elasticity, isotropic materials, and that cross sections remain in-plane, the three stress states that exist in the beam cross section are

$$\begin{aligned}\sigma_{yy} &= E\varepsilon_{yy} = E\left(\frac{du_y}{dy} - z\frac{d\varphi_x}{dy} + x\frac{d\varphi_z}{dy}\right) = E(\gamma_y - z\kappa_x + x\kappa_z)\\ \sigma_{yx} &= G\tau_{yx} = G\left(\frac{du_x}{dy} + \varphi_z + z\frac{d\varphi_y}{dy}\right) = G(\gamma_x + z\kappa_y)\\ \sigma_{yz} &= G\tau_{yz} = G\left(\frac{du_z}{dy} - \varphi_x - x\frac{d\varphi_y}{dy}\right) = G(\gamma_z + x\kappa_y)\end{aligned} \tag{2.29}$$

where ε_{yy} is the axial strain and τ is shear strain. The constitutive matrix, $\mathbf{K}_{cs}$, is defined by integrating these stresses over the cross section in accordance with (2.26) and expressing in the form of (2.28)

$$\begin{Bmatrix} F_x\\ F_y\\ F_z\\ M_x\\ M_y\\ M_z \end{Bmatrix} = \underbrace{\begin{bmatrix} GA & 0 & 0 & 0 & -GAs_z & 0\\ 0 & EA & 0 & EAe_z & 0 & -EAe_x\\ 0 & 0 & GA & 0 & GAs_x & 0\\ 0 & EAe_z & 0 & E(I_{xx}+Ae_z^2) & 0 & -EI_{xz}\\ -GAs_z & 0 & GAs_x & 0 & G(K+A(s_x^2+s_z^2)) & 0\\ 0 & -EAe_x & 0 & -EI_{xz} & 0 & E(I_{xz}+Ae_x^2) \end{bmatrix}}_{\mathbf{K}_{cs}} \begin{Bmatrix} \gamma_x\\ \gamma_y\\ \gamma_z\\ \kappa_x\\ \kappa_y\\ \kappa_z \end{Bmatrix} \tag{2.30}$$

where (e_x, e_z) and (s_x, s_z) are the elastic and shear centers of the cross section, and by definition the area and second moments of area are

$$A = \int_A dA \quad , \quad I_{xx} = \int_A z^2 dA \quad , \quad I_{zz} = \int_A x^2 dA \quad , \quad I_{xz} = \int_A xz dA \tag{2.31}$$

There is no explicit analytical function for the torsional constant, K, of arbitrary cross sections. However, there are some explicit functions for K of specific cross sections. One relevant case is that of closed thin-walled cross sections with K defined in [73] as

$$K = \frac{4A}{\oint_s \frac{ds}{t}} \tag{2.32}$$

where the denominator is an integral around the circumference of the cross section defined by the wall's median line, with a wall thickness, t. A second relevant case is that of a solid airfoil section which can be approximated as [74]

$$K \simeq 0.15ct_{\max}^3 \tag{2.33}$$

where c and $t_{\max}$ are the airfoil's chord length and maximum thickness respectively.

An important special case for $\mathbf{K}_{cs}$ is when the cross section is doubly symmetric about x- and z-axes. In such a case the elastic and shear center are coincident to the origin (i.e. $s_x = s_z = e_x = e_z = 0$) and all off-diagonal terms of $\mathbf{K}_{cs}$ are 0.

2.3.3 Problem Formulation

With the kinematics and constitutive relations defined, the beam can now be discretized into one dimensional finite elements of length l_e, which represent the reference axis. The displacements and rotations are achieved along the element via $\mathbf{N}\mathbf{u}_e$ where $\mathbf{u}_e$ are the displacements and rotations at the element nodes, and $\mathbf{N}$ contains interpolation functions. Similarly, the generalized strains and curvatures can be achieved by $\mathbf{B}\mathbf{u}_e$, where $\mathbf{B}$ is the strain-displacement matrix containing derivatives of the shape functions and off-diagonal terms to account for rotation of the cross section (refer to (2.27)).

The problem is first derived in terms of a non-linear co-rotating formulation which is then reduced to a linear form. The term co-rotating is used to describe a system where the reference frame continuously rotates with the elements which are locally subject to the constitutive relationship in (2.28). A transformation matrix, $\mathbf{T}$, is used to map local strains and internal forces to the global coordinate system by

$$\begin{Bmatrix} \gamma \\ \boldsymbol{\kappa} \end{Bmatrix} = \mathbf{T}(\mathbf{u})^{\mathrm{T}} \begin{Bmatrix} \gamma_l \\ \boldsymbol{\kappa}_l \end{Bmatrix} \quad , \quad \mathbf{f}_{i,e}(\mathbf{u}) = \mathbf{T}(\mathbf{u})^{\mathrm{T}} \mathbf{K}_{cs} \begin{Bmatrix} \gamma_l \\ \boldsymbol{\kappa}_l \end{Bmatrix} \tag{2.34}$$

where $\mathbf{f}_{i,e}$ is the element's internal forces defined from (2.28), and the subscript l represents a local quantity. Static equilibrium can be ensured by satisfying the residual equation

$$\mathbf{R}_b(\mathbf{u}) = \mathbf{f}_i(\mathbf{u}) - \mathbf{f} = \mathbf{0} \tag{2.35}$$

where $\mathbf{f}_i$ is the global internal force vector formed from assembling $\mathbf{f}_{i,e}$, and $\mathbf{f}$ is the global external force vector formed by assembling

$$\mathbf{f}_e = \int_{l_e} \mathbf{N}^{\mathrm{T}} \mathbf{q} \, dl_e \tag{2.36}$$

Note that the external virtual work is assumed to be independent of geometric variation, i.e. $\mathbf{f}$ has no dependence on $\mathbf{u}$. However, in aeroelastic problems the load will change as the wing deforms. This will be accounted for in the multidisciplinary analysis formulation (discussed in Section 2.4), and is not considered as part of the FE formulation.

A Newton-Raphson scheme is used to satisfy (2.35) with updates in $\mathbf{u}$ calculated by solving

$$\mathbf{K}(\mathbf{u}) \Delta \mathbf{u} = -\mathbf{R}_b(\mathbf{u}) \tag{2.37}$$

where $\mathbf{K}$ is the tangent stiffness matrix formed by assembling element stiffness matrices, $\mathbf{K}_e$. The derivation of the element stiffness is achieved by taking the variation of the internal virtual work, defined in (2.25), which can be expressed as combination of constitutive and geometric terms by

$$dV_i = \int_l \big(\underbrace{d\mathbf{F}^{\mathrm{T}} \delta\boldsymbol{\gamma} + d\mathbf{M}^{\mathrm{T}} \delta\boldsymbol{\kappa}}_{\text{constitutive}} + \underbrace{\mathbf{F}^{\mathrm{T}} d(\delta\boldsymbol{\gamma}) + \mathbf{M}^{\mathrm{T}} d(\delta\boldsymbol{\kappa})}_{\text{geometric}} \big) dl = \delta\mathbf{u}_e^{\mathrm{T}} \mathbf{K}_e \mathbf{u}_e \tag{2.38}$$

$$\mathbf{K}_e(\mathbf{u}) = \int_{l_e} \underbrace{\mathbf{T}(\mathbf{u})^{\mathrm{T}}\mathbf{B}^{\mathrm{T}}\mathbf{K}_{cs}\mathbf{B}\mathbf{T}(\mathbf{u})}_{\text{constitutive}}\, dl_e + \underbrace{\mathbf{K}_g(\mathbf{u})}_{\text{geometric}} \tag{2.39}$$

where $\mathbf{K}_g$ is the geometric stiffness defined by the variation of the virtual strains as implied in (2.38). The specific definition of $\mathbf{K}_g$ depends on the choice of element and local deformation modes. In order to ensure consistency, $\mathbf{K}_g$ must also account for the variation of the transformation matrix. Some methods may choose to simplify the calculation by excluding these terms. However, this can lead to slower convergence rates in the FE analysis and large errors in the sensitivity analysis. For the formulation used in this thesis, the definition of $\mathbf{K}_g$ can be found in [P4].

Alternatively, the problem can be linearized by neglecting the geometric terms in (2.39), where $\mathbf{T}$ then represents the orientation in the undeformed configuration, i.e. $\mathbf{T}$ is not dependent on $\mathbf{u}$. It then follows that $\mathbf{K}_e$ is independent of $\mathbf{u}$, and with no geometric dependence, the governing equation becomes

$$\mathbf{R}_b = \mathbf{K}\mathbf{u} - \mathbf{f} = \mathbf{0} \tag{2.40}$$

2.4 Multidisciplinary Analysis

Multidisciplinary analysis involves coupling multiple physics disciplines into a single engineering system. The global system is defined by a combination of residual vectors and state variables from each subsystem. The focus in this thesis is coupling panel and FE methods where the global system is defined by

$$\mathbf{R}(\mathbf{d},\mathbf{s}) = \begin{Bmatrix} \mathbf{R}_a(\mathbf{d},\mathbf{s}) \\ \mathbf{R}_b(\mathbf{d},\mathbf{s}) \end{Bmatrix} = \mathbf{0} \quad , \quad \mathbf{s} = \begin{Bmatrix} \mathbf{s}_a \\ \mathbf{s}_b \end{Bmatrix} = \begin{Bmatrix} \boldsymbol{\mu} \\ \mathbf{u} \end{Bmatrix} \tag{2.41}$$

where $\mathbf{R}_a$ is defined in (2.13) or (2.15) depending on the boundary condition, and $\mathbf{R}_b$ is defined in (2.40) or (2.35) depending on whether linear or non-linear analysis is implemented.

Two coupling methods are considered in this thesis: 1- and 2-way coupling. For the 1-way coupling procedure each subsystem is solved once where the aerodynamic loads calculated in the panel method are used to solve the FE problem. When using this coupling method the finite element formulation ($\mathbf{R}_b$), holds a dependence on the panel method state variables, $\boldsymbol{\mu}$, through the external force vector, $\mathbf{f}$. As information is only transferred one way (panel to FE) the panel method ($\mathbf{R}_a$) has no dependence on the state variables of the FE problem, $\mathbf{u}$. When the problem is 2-way coupled, aerodynamic loads are still applied to the FE problem, but the displacements are then used to deform the panel geometry. The panel method ($\mathbf{R}_a$) is then dependent on the FE state variables $\mathbf{u}$, through AIC's $\mathbf{A}$ and $\mathbf{B}$ as well as source terms $\boldsymbol{\sigma}$. This creates a 2-way dependence as each subsystem is dependent on the others state variables, and a non-linear solver is required to satisfy the global system in (2.41).

Two methods have been trialled for computing 2-way coupled solutions – fixed-point iterations and a Newton method. The Newton method experiences second order convergence which allows the method to converge in fewer iterations than the fixed-point iterations. However, fixed-point iterations only require the calculation of AICs, and not their derivatives. The derivatives of AICs are needed to form the Jacobian matrix on each iteration of the Newton method, and this calculation dominates the analysis as the cost is roughly 8 times that of the AIC calculation [P1]. Because of this large computational cost, fixed-point iterations are instead used to solve the 2-way coupled problems presented in this thesis. Appendix C contains algorithms for each method and a comparison that demonstrates the differences in computational cost and stability.

3 Aerodynamic Shape Optimization

This chapter discusses the results of [P1] which introduces a framework that uses panel methods for aerodynamic shape optimization of planar wings, and [P3] which extends these methods to shape optimization of non-planar wing configurations. The aerodynamic modeling is discussed in Section 2.2, whereas this chapter focuses on the details specific to [P1] and [P3]. The first section describes the wing parameterization and discretization, and is followed by studies that highlight some of the differences in calculation methods when using panel methods for shape optimization problems. The third section will present optimization studies on planar wings and the final section explores the potential benefits of non-planar wings.

3.1 Wing Parameterization and Discretization

The wing parameterization and discretization is shown in Figure 3.1. The model represents a delta wing configuration where the effect of both wings are considered but without a fuselage. The wing coordinates are achieved by assembling airfoil sections on a quarter chord curve defined in 3D space by a set of control points that are on the curve, and represent the airfoil quarter chord points. The freestream wake geometry introduced in Section 2.2.5 is used with

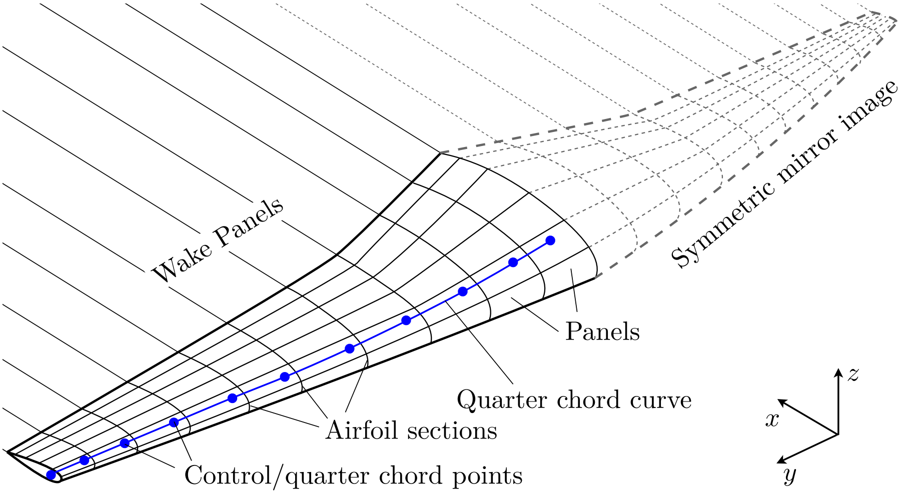

Figure 3.1: Wing parameterization and panel discretization with symmetry about the x-z plane.

a single wake panel per spanwise section. One wing is defined where symmetry is enforced by calculating the influence from a mirror image of the wing and wake about the root.

Design variables are used to control the airfoil shape and control points of the quarter chord curve. In order to ensure smoothly varying geometry and avoid numerical artifacts, the design variables are filtered in the spanwise direction. The filtering technique is shown in Figure 3.2 and is defined as

$$\tilde{\mathbf{d}} = \boldsymbol{\mathcal{W}}\mathbf{d} \quad \text{where} \quad \mathcal{W}_{i,j} = \frac{1}{\sum_{k=1}^{N_S} w_{i,k}} w_{i,j} \quad \text{and} \quad w_{i,j} = \max(0, R - r_{i,j}) \tag{3.1}$$

where $\tilde{\mathbf{d}}$ are filtered design variables and $\boldsymbol{\mathcal{W}}$ is a filter matrix containing weights w, for neighboring sections' design variables. There is an inverse-linear relationship between an airfoil section's weight and the distance between sections, $r_{i,j}$. If $r_{i,j}$ is greater than a filter radius, R, then there is no weight associated with these sections.

Airfoil parameterization techniques are discussed in Section 3.3.1, where Section 3.2 uses constant NACA 0012 airfoils throughout the span. Sections 3.2 and 3.3 only consider unswept planar wings where the quarter chord curve is co-linear with the y-axis.

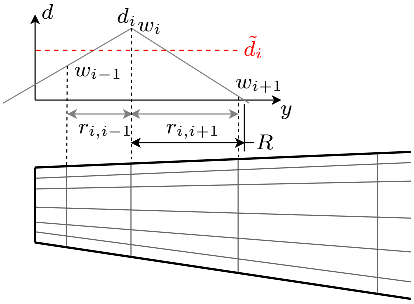

Figure 3.2: Representation of the filtering method defined in (3.1).

3.2 A Discussion on Choice of Methods

This section discusses the applicability of different calculation methods within the panel method when used for shape optimization problems. More specifically, choice of boundary conditions and drag calculation methods are compared based on their computational cost and the resulting optimized designs.

3.2.1 Boundary Conditions

As discussed in Section 2.2, the 3D panel method can be solved with either Neumann or Dircihlet boundary conditions (BC). This section investigates the differences in BCs through solving shape optimization problems. Consider the following drag minimization problem which is subject to a lift constraint and defined with respect to twist variables at N_S airfoil sections.

$$\begin{aligned} \min_{\boldsymbol{\alpha} \,\in\, \mathbb{R}^{N_s}} \quad & : D(\boldsymbol{\alpha}) \\ \text{subject to} \quad & : \underline{L} - L(\boldsymbol{\alpha}) \leq 0 \\ & \quad \underline{\alpha} \leq \alpha_i \leq \bar{\alpha} \quad \text{for} \quad i = 1, ..., N_S \end{aligned} \tag{3.2}$$

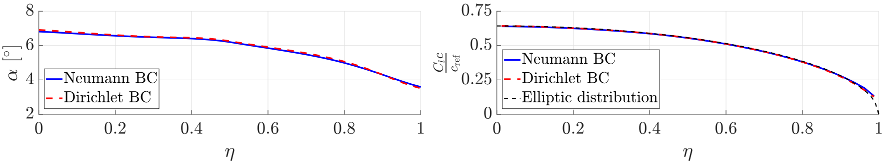

(a) (b)

Figure 3.3: Twist optimization results with different boundary conditions: (a) twist distribution and (b) lift distribution along the half-span. Figure retrieved from [P1].

Figure 3.3 shows the twist and lift distribution for optimized designs with a rectangular planform of aspect ratio 6, where η represents the normalized spanwise location. Both problems converge to designs with negligible differences in sectional lift and twist distributions. The sectional lift distribution closely approximates the elliptic distribution which is the known optimal solution for a planar wing. These results show that choice of BC is not crucial for analyzing the aerodynamic performance or solving the optimization problem.

Even though this demonstrates that choice of BC does not effect the outcome of the optimization problem, choice of BC is important for reducing computational cost. A timing comparison between BCs is shown in Figure 3.4a, where for the same mesh size, a Dirichlet BC takes half the time of a Neumann BC. The reason for this results from the formulation of the problem. To understand why, it is first noted that as panel methods are dense systems the majority of the computational time is spent assembling the system, i.e. calculating AICs. The AICs for a Neumann BC require the calculation of the influence on velocity in three dimensions, whereas the Dirichlet BC requires the calculation of the influence on the potential which is a scalar. This becomes crucial when the gradients are required, as the gradient calculation takes roughly 8 times longer than the physics problem, which in turn will now dominate the computational time. The factor of 8 arises from the fact that gradients are required for each influence coefficient between any two panels with respect to 8 nodes (4 per panel). Because AIC calculations for a Neumann BC comes at twice the cost of a Dirichlet BC, calculating the derivative of AICs is also twice as expensive.

Another major difference between the boundary conditions is the discretization error. Figure 3.4b shows a mesh convergence study for a rectangular wing of aspect ratio 4. Using a Dirichlet BC, the induced drag (calculated via C_P integration) converges faster than it does for a Neumann BC. This means that accurate results can be achieved on coarser meshes with a Dirichlet BC leading to further reductions in cost. The difference in numerical error arises from the nature of the boundary conditions. A Dirichlet BC specifies that the internal flow must be constant anywhere inside the wing, whereas a Neumann BC makes no assumptions about the internal flow. Because the panel method enforces

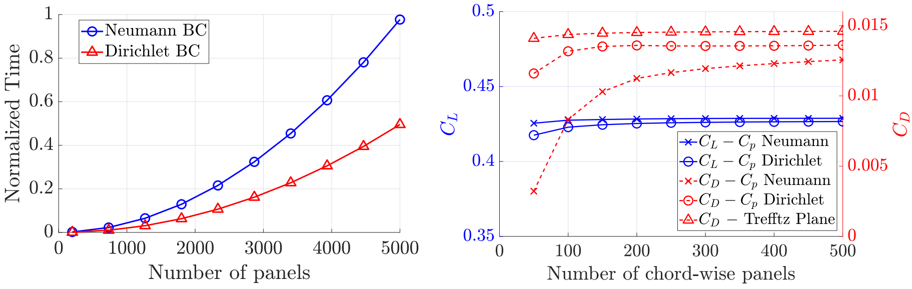

(a) (b)

Figure 3.4: Comparisons between different methods: (a) timing comparison between Neumann and Dirichlet BCs and (b) mesh convergence study for a rectangular wing of aspect ratio 4.

BCs at discrete points, there is some *leaked flow* from the external to internal regions, which contributes to discretization errors. By explicitly forcing a constant velocity inside the wing, *leaked flow* is reduced [75].

3.2.2 Induced Drag Calculation

Section 2.2 introduced two ways of calculating the lift and induced drag – through C_P integration or Trefftz plane integration. When the wing geometry is well defined both methods can produce similar results. However, it is known that C_P integration can be susceptible to numerical errors resulting from the discretization [71, 76]. These numerical errors can become very large for non-conventional wing geometries, leading to non-physical values of drag. This is demonstrated through solving the following optimization problem where the objective is to minimize drag subject to a minimum lift constraint with respect to a sectional chord distribution and at a fixed angle of attack.

$$\begin{aligned} \min_{\boldsymbol{c}\,\in\,\mathbb{R}^{N_S}} \quad &: D(\boldsymbol{c}) \\ \text{subject to} \quad &: \underline{L} - L(\boldsymbol{c}) \leq 0 \\ & \quad \underline{c} \leq c_i \leq \bar{c} \quad \text{for} \quad i = 1, \ldots, N_S \end{aligned} \tag{3.3}$$

The optimization problem is solved twice, once where drag is calculated using C_P integration and once with Trefftz plane integration. Converged designs are compared to a rectangular wing with equal span and aspect ratio of 6. Each design is shown in Figure 3.5 with sectional drag distributions calculated using both methods.

The optimization problem in (3.3) has a known optimal solution – the elliptic wing. This design is achieved when drag is calculated via Trefftz plane integration predicting a reduction in drag of 1.4% compared to the reference wing. When using C_P integration the design converges to an non-conventional

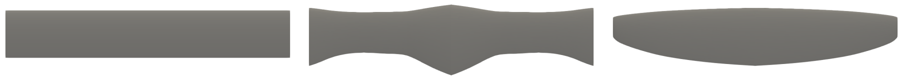

(a) Initial design/reference (b) min D_{C_P} (c) min D_{TP}

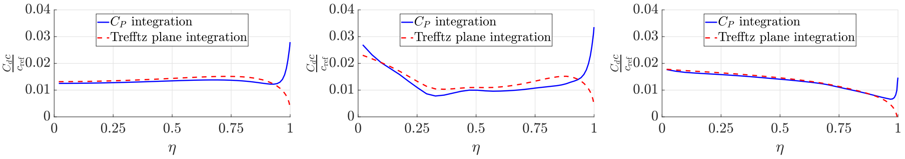

(d) Initial design/reference (e) min D_{C_P} (f) min D_{TP}

Figure 3.5: Wing planforms and sectional drag distributions for reference design, optimized design with C_P integration, and optimized design with Trefftz plane integration. Figure retrieved from [P1].

wing shape that predicts a reduction of 2.4%. The C_P optimized wing has been able to create a larger reduction in drag by exploiting numerical errors in the drag calculation. Resolving the problem using Trefftz plane integration shows that the optimized wing actually creates an increase in drag of 0.5%. These errors are most obvious at the wingtip as seen from the drag distributions in Figures 3.5d-3.5f, where the drag should tend to zero at $\eta = 1$ (wingtip). The large numerical errors in C_P integration can also have large sensitivities that will push the optimizer to more non-conventional designs. The results presented here suggest that C_P integration is unsuitable for optimization problems when the parameterization allows a large change in geometry.

Numerical errors from C_P integration have a large impact on the induced drag because the error is of a similar order in magnitude to the induced drag. Lift is usually much greater than the induced drag (and magnitude of numerical errors) which means that reasonable results can still be predicted for lift. However, it is still recommended to calculate both lift and drag from Trefftz integration. This is because the optimizer may try to exploit the inviscid pressure distributions by creating irregular airfoil geometries with unphysical C_P values. Section 3.3.1 discusses this point in more detail.

Figure 3.4b presented mesh convergence studies for different BCs with C_P and Trefftz plane integration methods, where the convergence has negligible differences with choice in BC when drag is calculated in the Trefftz plane. The Trefftz plane calculations converge much faster than the C_P integrations as they are not susceptible to discretization error. Because similar results can be predicted on a coarser mesh the computational cost can also be reduced.

3.3 Shape Optimization of Planar Wings

In the previous studies only one design variable per section was used with a fixed airfoil profile throughout the span. In this section, airfoil parameterization methods are used to allow changes in airfoil shape throughout wing. The section is divided into two subsections where the first introduces airfoil parameterization methods which are compared based on their performance and robustness for inviscid shape optimization problems. The second study explores the effect of wingspan in induced drag minimization problems.

3.3.1 A Comparison of Airfoil Parameterization Methods

For the purpose of this study, two airfoil parameterization methods are introduced and are represented in Figures 3.6a and 3.6b. The first is based on the definition of NACA 4- and 5-digit airfoils which have a well defined airfoil shape, and the second uses a B-spline representation which is a free-form parameterization that can represent a large range of geometries.

NACA airfoils are defined using 4 parameters (refer to Figure 3.6a): chord length c, maximum thickness t, maximum camber m, and position of maximum camber p. The airfoil coordinates are achieved by summing a thickness and camber distributions which are defined as polynomial equations based on these 4 parameters. For optimization problems these parameters are controlled by design variables. The twist, α, is included as an additional variable, giving the NACA parameterization a possible 5 design variables per airfoil section. For more details on the NACA parameterization readers are referred to Appendix D.

When a B-spline parameterization is used the airfoil is represented by a B-spline curve whose control points are defined by design variables, refer to Figure 3.6b. Each control point can move vertically within specified bounds, and there is a fixed relative spacing in the horizontal direction which scales with a single design variable. If a control point is near a bound and the corresponding control point at the same horizontal location is sufficiently far away, the bounds are updated to allow more freedom to the control point. Updating the bounds in

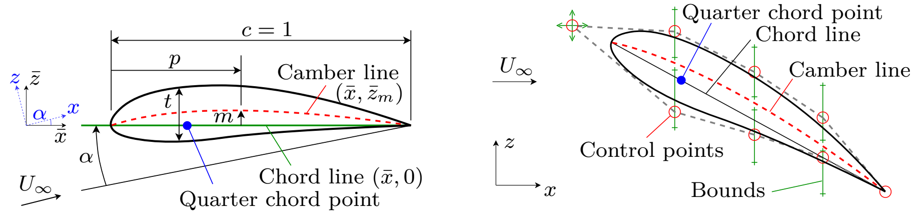

(a) (b)

Figure 3.6: Airfoil parameterization methods: (a) NACA and (b) B-spline parameterization. Figures are adapted from [P1].

this way ensures that the B-spline cannot self-intersect. For more details on the B-spline parameterization readers are referred to Appendix E.

Both parameterizations include the spanwise filtering discussed in Section 3.1, where each set of design variables are filtered separately, i.e. $\mathbf{d}$ in (3.1) may represent any of the 5 NACA airfoil parameters or any corresponding set of B-spline control points. To compare the different parameterization methods consider the following optimization problem where the objective is to minimize the induced drag with respect to constraints on lift, pitching moment, twist, and maximum curvature.

$$\begin{aligned}
\min_{\mathbf{d}\,\in\,\mathbb{R}^{N_d}} \quad &: D(\mathbf{d}) \\
\text{subject to} \quad &: \underline{L} - L(\mathbf{d}) \leq 0 \\
&\quad M_p(\mathbf{d}) = 0 \\
&\quad \alpha_i - \bar{\alpha} \leq 0 \qquad \text{for} \;\; i = 1, ..., N_S \\
&\quad \hat{\kappa}_i - \bar{\hat{\kappa}} = 0 \qquad \text{for} \;\; i = 1, ..., N_S \\
&\quad \underline{d} \leq d_i \leq \bar{d} \qquad \text{for} \;\; i = 1, ..., N_d
\end{aligned} \tag{3.4}$$

Both the twist and maximum curvature constraints are enforced to ensure that the flow remains physical as the aerodynamic model cannot predict flow separation which can occur with high angles of attack or sharp geometries. The maximum curvature of a NACA airfoil is approximated as $\kappa = 0.9075\frac{c}{t^2}$, and for a B-spline it is approximated using a p-norm function as described in [P1], where curvature calculations are detailed in Appendix E.

The problem in (3.4) is solved with both NACA 5-digit and B-spline parameterizations, where design variables are defined as $\mathbf{d} = \{\boldsymbol{c}, \boldsymbol{t}, \boldsymbol{p}, \boldsymbol{\alpha}\}$ for the NACA airfoils, and $\mathbf{d} = \{\mathbf{P}_1, \mathbf{P}_2, ..., \mathbf{P}_{N_S}\}$ for B-spline airfoils. Results for both cases are shown in Figure 3.7. Both airfoil parameterization methods produce optimized designs with similar planforms, the same induced drag, and negligible differences in lift distributions which closely approximate the optimal elliptic distribution. The aspect ratio is higher for the NACA parameterization due to differences in the airfoils. The NACA 5-digit airfoils have a larger camber than B-spline airfoils, which creates a flatter region towards the leading edge on the lower surface of the airfoils, and corresponds to a larger pressure in that region. This difference can be seen in airfoils and C_P distributions at each section (refer to Figures 3.7c-3.7e). The lower surface pressure in B-spline designs leads to a lower C_l which is compensated for by a larger chord length. This highlights an important fact about shape optimization problems for minimizing induced drag: the minimum drag and corresponding optimum lift distribution, can be achieved by a number of combinations of chord, twist, and camber, which creates many possible solutions with the same performance.

B-spline results presented in this study have been able to produce realistic designs. However, from experience, the B-spline parameterization has proven not to be as robust for all cases of inviscid optimization problems. The additional freedom provided by the B-spline parameterization can produce non-

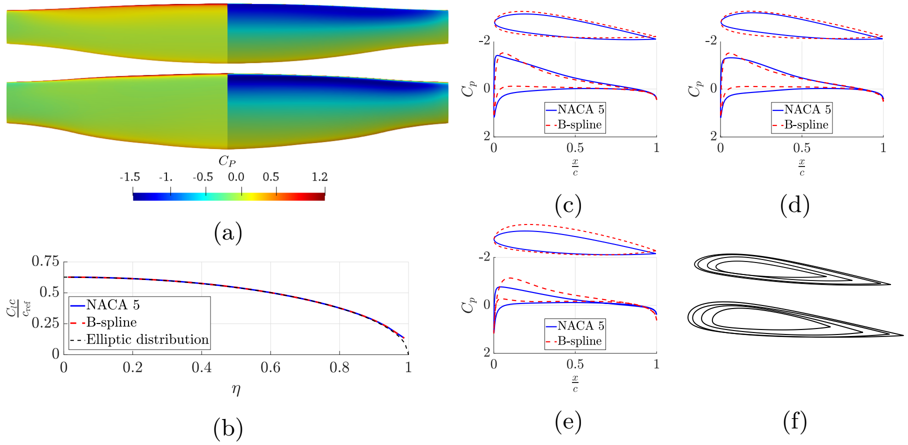

Figure 3.7: Optimized designs with different airfoil parameterization methods: (a) Wing planforms with lower and upper surface C_P (NACA 5 above, B-spline below), (b) spanwise lift distributions, airfoil sections with C_P distributions at (c) $\eta = 0.05$, (d) $\eta = 0.50$, (e) $\eta = 0.95$, and (f) airfoil stacks (NACA 5 above, B-spline below). Figure retrieved from [P1].

conventional geometries that take advantage of the inviscid nature of the problem. This issue can also get worse when the optimization problem is posed in terms of quantities calculated via C_P integration. The motivation of the B-spline parameterization was to allow more design freedom to the optimizer, but in doing so it has been able to exploit the assumptions of the physics model. In order to prevent this, further geometry constraints are enforced on quantities such as curvature, which has the effect of restricting the design space again. As discussed, there are many solutions to the optimization problem that can produce the same value of minimized induced drag, and this has been achieved with the simpler NACA parameterization. Ultimately, incorporating free-form parameterizations, such as those defined by splines, requires more regularization, increases complexity, and has not demonstrated any advantage over the NACA parameterization which always produces well defined airfoil geometries.

3.3.2 The Effect of Wingspan

The opening chapter of this thesis discussed design philosophies for reducing induced drag (Section 1.3.3). The first method was to create an elliptic lift distribution, which was achieved by the optimized designs in the previous examples. This section demonstrates the second method which is to increase the wingspan. The optimization problem in (3.4) is solved again using a NACA 5-digit parameterization and with small perturbations to the wingspan of 0.1 m, where the original wingspan was 6 m. Optimized designs are shown in Figure 3.8 and are compared to the reference design from Figure 3.5a in Table 3.1.

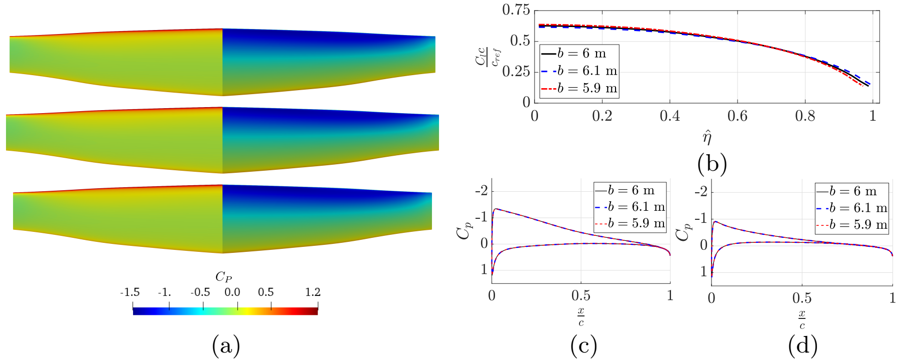

(a) (b) (c) (d)

Figure 3.8: Optimized designs with perturbations to the wingspan: (a) Wing planforms with lower and upper surface C_P ($b = 6$ m above, $b = 6.1$ m middle, $b = 5.9$ m below), (b) spanwise lift distributions where η is normalized with $b = 6$, airfoil sections with C_P distributions at (c) $\eta = 0.05$, (d) $\eta = 0.95$.

Each of the optimization problems converged to similar designs with negligible differences in planform, airfoil sections or pressure distributions. The optimized design from the previous example creates a reduction in drag of 1.5% compared to the reference wing, whereas with a slightly larger wingspan, a reduction in drag of 4.7% is produced. Conversely, if the wingspan was slightly shorter, the optimized design increases the drag by 1.9% compared to the reference wing. This result shows that even small reductions to the wingspan can cause a large increase in induced drag. Additionally, the results demonstrate just how effective increasing the wingspan is at reducing induced drag. This is an important discussion point for optimization problems that minimize induced drag, and is relevant to many of the discussions on examples presented later in this thesis.

Table 3.1: Drag of optimized designs with perturbed wingspans, normalized by the drag of the reference wing. Table retrieved from [P1].

Design	D/D_{ref}
Reference	1.000
min D, $b = 6$ m	0.985
min D, $b = 6.1$ m	0.953
min D, $b = 5.9$ m	1.019

3.4 Shape Optimization of Non-Planar Wings

The previous section demonstrated that optimizing airfoil sections for minimum induced drag grants very little performance gains compared with varying the wingspan. This section explores the potential of optimizing non-planar wing geometry rather than the airfoil sections. As such, all studies maintain constant NACA 0012 airfoil profiles. Results are presented in two subsections, where the first creates comparisons to designs from literature and explores the effect of sweep and droop. The second investigates the differences between raised and drooped wing designs. The studies presented in this section relate to the third design philosophy for induced drag reduction outlined in Section 1.3.3, which is to specifically tailor the wingtip design.

3.4.1 The Effect of Sweep and Droop

In recent years there has been a growing interest in unconventional wing designs such as drooped wings. These designs are usually bio-inspired with many citing the drooped shape of a seagull wings in gliding flight. To demonstrate the potential for optimizing non-planar wings, a comparison is created between optimized designs and designs taken from literature. Consider the following optimization problem to maximize the efficiency factor, e, where the aspect ratio, $A\!\!\!R$, is prescribed as $A\!\!\!R_0 = 7$.

$$\begin{aligned} \min_{\mathbf{d}\,\in\,\mathbb{R}^{N_d}} \quad &: \; -e(\mathbf{d},\boldsymbol{\mu}) = -\frac{C_L^2(\mathbf{d},\boldsymbol{\mu})}{\pi A\!\!\!R(\mathbf{d})C_D(\mathbf{d},\boldsymbol{\mu})} \\ \text{subject to} \quad &: \; A\!\!\!R(\mathbf{d}) = A\!\!\!R_0 \\ &\quad |\hat{x}_t(\mathbf{d})| \leq \bar{\hat{x}}_t \\ &\quad |\hat{z}_t(\mathbf{d})| \leq \bar{\hat{z}}_t \\ &\quad \underline{d} \leq d_i \leq \bar{d} \quad \text{for} \;\; i = 1, ..., N_d \end{aligned} \tag{3.5}$$

The terms $\hat{x}$ and $\hat{z}$ refer to the x and z coordinates of the quarter chord curve at the control points, and the subscript t is associated with the values at the wingtip. The coordinates $\hat{x}$ and $\hat{z}$ are included in the parameterization where design variables define the change in parameters, i.e. $\delta\hat{x}$, such that they are monotonically increasing/decreasing, as described in [P3]. Three reference designs are taken from literature – a traditional elliptic wing, a planar crescent wing introduced in [77], and a hyper elliptic cambered span (HECS) wing introduced in [78]. By solving (3.5) with specific design variables, appropriate optimized designs can be created for comparisons to the reference designs. The elliptic wing is comparable to $\mathbf{d} = \delta\boldsymbol{c}$, the crescent wing to $\mathbf{d} = \{\delta\boldsymbol{c}, \delta\hat{\boldsymbol{x}}\}$ and, HECS wing to $\mathbf{d} = \{\delta\boldsymbol{c}, \delta\hat{\boldsymbol{x}}, \delta\hat{\boldsymbol{z}}\}$. Reference and optimized designs are shown in Figure 3.9.

The converged design in Figure 3.9d closely matches the elliptic wing in Figure 3.9a. This is expected as the elliptic wing is the known optimal design for a straight planar untwisted wing. An elliptic wing should have efficiency factor, $e = 1$, and the model closely approximates this with $e = 1.004$ in both wings in Figures 3.9a and 3.9d. When allowing changes in $\hat{x}$, the design converges to a wing which remains straight until $\eta \simeq 0.75$ then sweeps backward creating raked wingtips. This design is quite different from the crescent wing in Figure 3.9b, but has larger efficiency of 1.027 compared to 1.019. The converged design with sweep and droop (Figure 3.9f) is also very different from the reference design. The HECS wing has a gradual change in sweep and droop starting from the wing's root. The optimized design begins to sweep at $\eta \simeq 0.55$

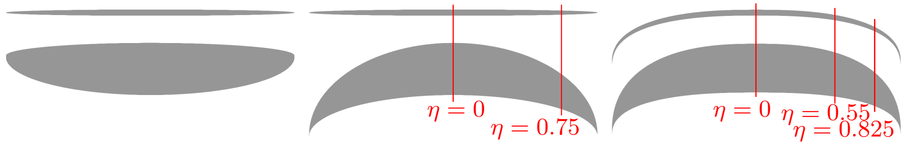

(a) Elliptic (b) Crescent (c) HECS

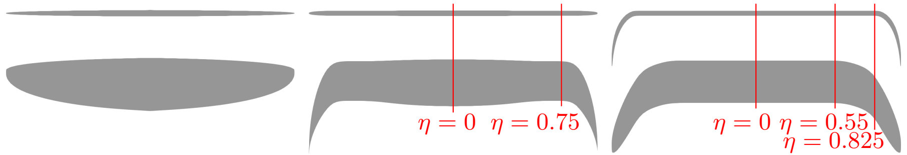

(d) $\mathbf{d} = \delta\mathbf{c}$ (e) $\mathbf{d} = \{\delta\mathbf{c}, \delta\hat{\boldsymbol{x}}\}$ (f) $\mathbf{d} = \{\delta\mathbf{c}, \delta\hat{\boldsymbol{x}}, \delta\hat{\boldsymbol{z}}\}$

Figure 3.9: Elevation and planform views for (a)-(c) reference wings and (d)-(f) optimized designs. η locations represent when wings begin to sweep and droop. Figure retrieved from [P3]

and droop at $\eta \simeq 0.825$. Because of the additional freedom to create different c, $\hat{x}$, and $\hat{z}$ distributions the optimized design has increased the efficiency factor from 1.178 to 1.291. In each case, optimized results have matched or improved upon the performance of reference designs. Including sweep has allowed small gains in efficiency of roughly 2% compared to the elliptic wing, whereas allowing the wing to both sweep and droop has created large gains of almost 30%.

3.4.2 A Comparison of Raised and Drooped Wings

The previous study demonstrated that a large aerodynamic benefit can be achieved from drooped wings. But there is a common discussion point in the literature on whether drooped wings can outperform traditional raised wing designs such as those with winglets. Within the literature there is no general consensus on whether this is true, with different studies presenting contradictory results (refer to [P3] for literature review). In an effort to explore this, consider the following optimization problem where the only design variables are $\hat{\boldsymbol{z}}$ and the planform is a rectangular wing of aspect ratio 7.

$$\begin{aligned} \min_{\mathbf{d}\,\in\,\mathbb{R}^{N_d}} \quad &: \; -e(\mathbf{d},\boldsymbol{\mu}) = -\frac{C_L^2(\mathbf{d},\boldsymbol{\mu})}{\pi \mathcal{R}(\mathbf{d}) C_D(\mathbf{d},\boldsymbol{\mu})} \\ \text{subject to} \quad &: \; |\hat{z}_t(\mathbf{d})| \leq \bar{\hat{z}}_t \\ & \quad\; \underline{d} \leq d_i \leq \bar{d} \qquad \text{for} \quad i = 1, ..., N_d \end{aligned} \tag{3.6}$$

Raised and drooped wings are considered by constraining designs for $\hat{\boldsymbol{z}} > \mathbf{0}$ and $\hat{\boldsymbol{z}} < \mathbf{0}$, respectively. The optimized designs are shown in Figure 3.10 and are compared to a planar wing of the same aspect ratio. The optimized designs for raised and drooped wings have similar trends in $\hat{z}$ where one is roughly the mirror image of the other. However, there are differences in efficiency factors

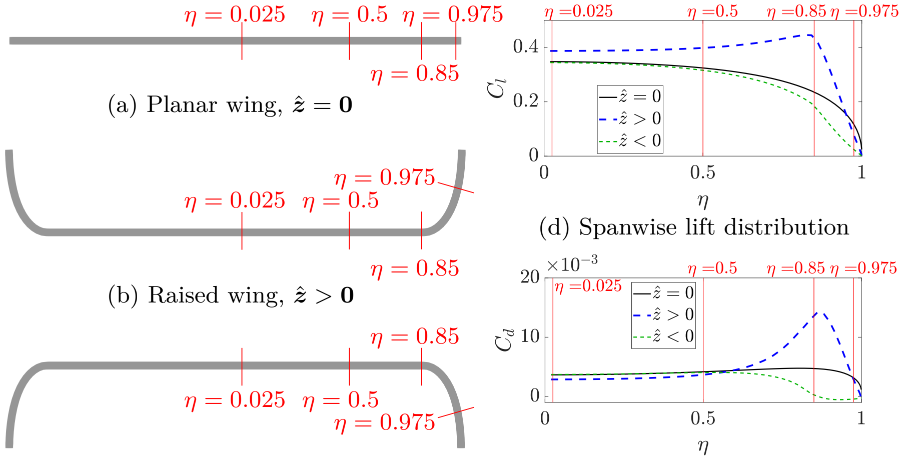

(a) Planar wing, $\hat{\boldsymbol{z}} = \boldsymbol{0}$

(b) Raised wing, $\hat{\boldsymbol{z}} > \boldsymbol{0}$

(c) Drooped wing, $\hat{\boldsymbol{z}} < \boldsymbol{0}$

(d) Spanwise lift distribution

(e) Spanwise drag distribution

Figure 3.10: Comparison of planar, raised, and drooped wings with a rectangular planform of aspect ratio 7. (a)-(c) show front views of the wings with spanwise markers corresponding to markers in (d) and (e). Figures adapted from [P3].

where the raised wing produces an efficiency of 1.14 compared to 1.22 for the drooped wing, and 0.98 for the planar wing.

Figure 3.10 also shows the lift and drag distributions along the span of the wing, which gives some insight into the differences in performance between these designs. The raised wing design has induced a lift along the entire span of the wing, but there is also a large peak in drag at the base of the winglet. The drooped wing has a large reduction in drag towards the wingtip which also corresponds with a reduction in lift. The increase in lift by the raised wing and the reduction in drag from the drooped wing is what provides the increase in efficiency in each respective design. From lift or drag distributions alone it is not clear how these changes in lift and drag are produced, but Figure 3.11 can provide more insight.

Figures 3.11a-3.11c plots the normalized velocity in the freestream direction, $\bar{U} = \frac{\boldsymbol{U}\cdot\boldsymbol{U}_\infty}{\|\boldsymbol{U}_\infty\|^2}$, within a plane at the quarter chord point (refer to [P3] for more on $\bar{U}$ definition). Comparing the raised and planar wings, there has been an increase in the induced velocity in the freestream direction on the upper surface when a winglet is created. This increase in velocity corresponds to a lower pressure on the upper surface which generates more lift, as was seen in Figure 3.10d. The drooped wing design has reduced the velocity on the upper surface towards the wingtip, and increased the velocity on the lower surface. This leads to a smaller pressure differential between upper and lower surfaces, and hence a reduction in the lift.

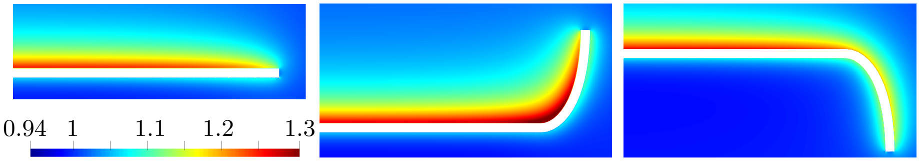

(a) $\bar{U}$, $\hat{\boldsymbol{z}} = \mathbf{0}$ (b) $\bar{U}$, $\hat{\boldsymbol{z}} > \mathbf{0}$ (c) $\bar{U}$, $\hat{\boldsymbol{z}} < \mathbf{0}$

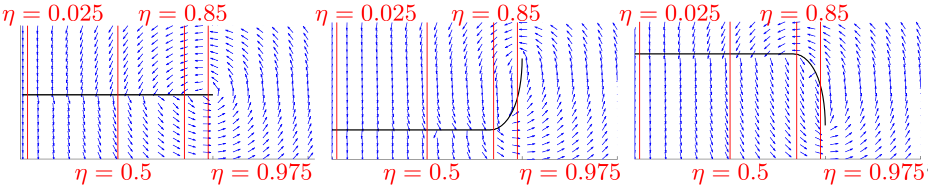

(d) U_{TP}, $\hat{\boldsymbol{z}} = \mathbf{0}$ (e) U_{TP}, $\hat{\boldsymbol{z}} > \mathbf{0}$ (f) U_{TP}, $\hat{\boldsymbol{z}} < \mathbf{0}$

Figure 3.11: Induced velocities for planar, raised, and drooped wings. (a)-(c) Normalized velocities in the freestream direction within a plane at the quarter chord point, and (d)-(f) directions of induced velocities within the Trefftz plane. Figures adapted from [P3].

Figures 3.11d-3.11f plots the direction of induced velocities within the Trefftz plane, U_{TP}, which gives a greater insight into the drag distributions. Induced velocities above the wake for the planar and raised wings have a negative component for $\eta < 1$, i.e. a downwash. However, the induced velocities above the wake for the drooped wing have a positive component in the region $0.85 < \eta < 1$. In the same region, they are negative below the wake meaning the potential jump over the wake must be close to zero, resulting in very low drag within this region, as was seen in Figure 3.10e. Note that vectors in Figures 3.11d-3.11f represent the direction of the induced velocities only and their length is not indicative of the velocity magnitude.

Results presented in this section would suggest that drooped wings are more efficient than raised wings. However, the studies here have a restricted design space as the only $\hat{\boldsymbol{z}}$ can vary. Results presented in [P3] demonstrate that comparative studies on raised and drooped wings can have different outcomes depending on how the design space is restricted. With a large enough design space both raised and drooped wings should be able to converge to designs with the same performance, when only inviscid analysis is considered. [P3] also presents studies which include viscous approximations, where drooped wings are not beneficial, and do not form during the optimization procedure as to do so will increase the viscous drag.

4 Aeroelastic Shape Optimization

This chapter extends methods discussed in the previous chapter on aerodynamic shape optimization to account for structural deformations using beam finite element (FE) models. The specific details will draw from studies discussed in [P2] which applies a linear beam FE model to investigate the performance of curved wall spars, and [P4] where a non-linear co-rotating beam formulation is used to investigate the performance of non-planar wings subject to large deformations. The chapter will only include details specific to [P2] and [P4], where readers are referred to Section 2.3 for an overview of beam finite element methods, Section 2.4 for an overview on multidisciplinary analysis, and Chapter 3 for concepts of aerodynamic shape optimization using panel methods. The following section describes the discretization of the panel-beam problem. The second section introduces a generalized load-displacement transfer method for coupled 3D panel-beam models. The third section includes investigations on the performance gains of curved wall spars. The final section presents studies on aeroelastic shape optimization of solid foam core wings subject to large deformations.

4.1 Panel-Beam Discretization

The discretization of the coupled panel-beam problem is shown in Figure 4.1. The external wing geometry and panel discretization is defined in the same manner as presented in Section 3.1, and is represented in planform in Figure 4.1a. Figure 4.1a also shows the beam finite element discretization where a beam node is defined at each airfoil section, with elements inside the wing. Each beam finite element has a local orientation notated by the coordinate system (x_b, y_b, z_b), where nodes are defined at a fraction of the chord length, κc, refer to Figure 4.1b. Depending on the application, the beam node will either be defined on the camber line (as shown in Figure 4.1) or on the chord line.

4.2 Panel-Beam Load-Displacement Transfer

Once the discretization is defined the next step is to define the load-displacement transfer. This section introduces a generalized load-displacement transfer method for coupled panel-beam problems. There are two criteria that must be satisfied in defining a load-displacement transfer method: consistency and conservativeness [79]. For consistency the total load calculated via the aerodynamic model must be equal to the total load applied in the structural model. For a method to be conservative the virtual work experienced in the structural model under

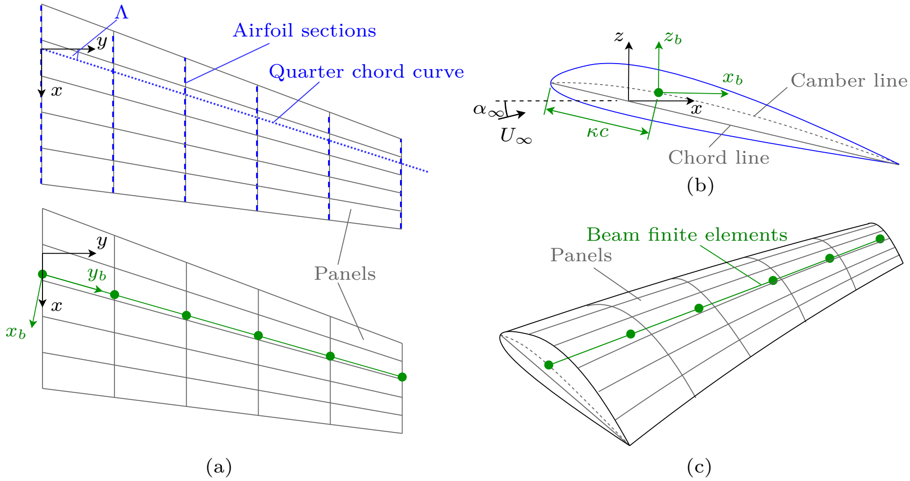

Figure 4.1: Panel-beam discretization with wing parameterization shown in blue and beam finite elements shown in green: (a) planforms detailing wing geometry (top) and beam finite elements (below), (b) root airfoil, and (c) 3D view. Figure adapted from [P2].

virtual displacements and rotations must be equal to the virtual work of the aerodynamic model. The load displacement transfer scheme is depicted in Figure 4.2. The beam finite element model assumes that sections remain in-plane and undergo rigid body displacements and rotations. As each beam node is defined at an airfoil section, the displacement transfer can be defined by

$$\delta \boldsymbol{X}_a = \delta \boldsymbol{u}_b + \delta \boldsymbol{\varphi}_b \times \boldsymbol{r} \tag{4.1}$$

where $\delta \boldsymbol{X}_a$ are displacements to the panel nodes, $\delta \boldsymbol{u}_b$ and $\delta \boldsymbol{\varphi}_b$ are displacements and rotations of the beam finite element node at the same spanwise location, and r is a spatial vector from the finite element to the panel node. The applied external load on a single finite element can be expressed as the sum of integrated distributed loads across N panels at the same spanwise section.

$$\mathbf{f}_e = \sum_{i=1}^{N} \int_0^{l_e} \begin{Bmatrix} \mathbf{p} \\ \mathbf{m} \end{Bmatrix} dl \tag{4.2}$$

where the moments arise from transferring the pressure load $\mathbf{p}$, from the panel to the beam element, i.e. $\mathbf{m} = \boldsymbol{r} \times \mathbf{p}$. The virtual work of the beam finite element from the loading of a single panel is then

$$\delta \boldsymbol{W}_b = \int_0^{l_e} \{\mathbf{p}^{\mathrm{T}}, \mathbf{m}^{\mathrm{T}}\} \begin{Bmatrix} \delta \boldsymbol{u} \\ \delta \boldsymbol{\varphi} \end{Bmatrix} dl = \int_0^{l_e} (\mathbf{p}^{\mathrm{T}} \delta \boldsymbol{u} + (\boldsymbol{r} \times \mathbf{p})^{\mathrm{T}} \delta \boldsymbol{\varphi}) dl \tag{4.3}$$

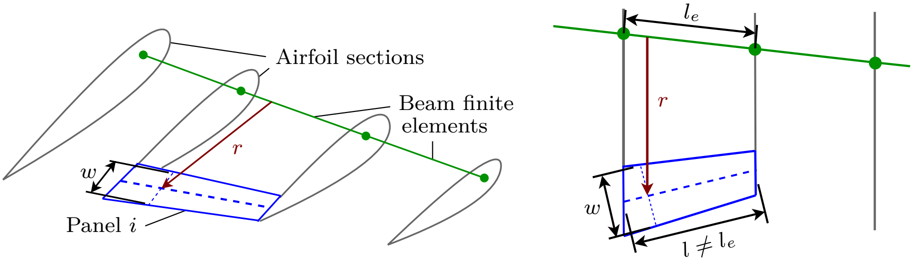

(a) **(b)**

Figure 4.2: A generalized load displacement transfer method for panel-beam models. A single panel to beam finite element load transfer shown in (a) 3D and (b) planform views. Figure adapted from [P2].

The virtual work by the panel method is expressed as

$$\delta \boldsymbol{W}_a = \int_S q_\infty C_P \boldsymbol{n}^{\mathrm{T}} \delta \boldsymbol{X}_a dS = q_\infty C_P J_l \boldsymbol{n}^{\mathrm{T}} \int_0^{l_e} w(\delta \boldsymbol{u} + \delta \boldsymbol{\varphi} \times \boldsymbol{r}) dl \tag{4.4}$$

where (4.1) has been used to expand the expression, and J_l is a linear mapping that accounts for cases where the panel length is not equal to beam finite element length (refer to Figure 4.2b). With some algebraic manipulation of (4.3) and equating to (4.4) yields a consistent and conservative expression for $\mathbf{p}$ as

$$\mathbf{p} = q_\infty C_P J_l w \boldsymbol{n} \tag{4.5}$$

4.3 An Investigation of Curved Wall Spars

The first aeroelastic studies will investigate the potential benefits of curved wall spars. The motivation for this comes from a study by Aage et al [80] who conducted topology optimization studies on the common research model (CRM) wing [81] with over 1 billion finite elements. The ultra-high resolution of this study allowed design features to form that did not appear in previous topology optimization studies of aircraft wings. One such feature was curved wall spars that create an increased torsional stiffness at the cost of decreasing bending stiffness. This design feature can easily be modeled with beam finite elements, and is used here to create optimized trade-offs between torsional and bending stiffness in aeroelastic design.

The beam is defined by a wingbox where the stiffness of the airfoil skin and additional structures is neglected. Figure 4.3 shows the parameterization of the beam cross section which is defined at each airfoil profile by 5 parameters: the height and width of the wingbox (h and w); the spar and flange thicknesses

(s and a); and the center offset of the curved spar walls (e). The offset e is defined such that it can tend from $e = 0$ where spar walls are straight and at 90° to the flanges, to $e = \frac{h}{2}$ where spar walls are semi-circular. The intermediate values of e are defined to give an elliptic curve.

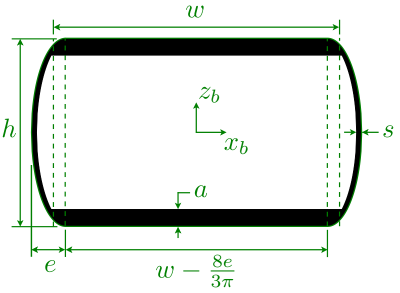

Figure 4.3: Curved wall wingbox parameterization with dimensions labeled. Figure retrieved from [P2].

This section is divided into two subsections. The first subsection investigates the performance benefits of curved wall spars for a fixed outer wing geometry, whereas the second combines the beam and airfoil parameterizations to achieve designs that are optimized for both external wing and internal structural geometries. Throughout this section a linear finite element model is used where the analysis assumes thin-walled cross sections.

4.3.1 Wingbox Structural Optimization for the CRM Wing

As an initial study consider the CRM wing geometry with an internal structure described by the wingbox parameterization in Figure 4.3 at each airfoil section. The optimization problem is defined in (4.6) where the objective is to minimize the sum of compliance over three loads cases with angles of attack, $\alpha_\infty = \{0°, 5°, 10°\}$. The design is subject to a constraint on volume and the physics are 1-way coupled.

$$\begin{aligned} \min_{\mathbf{d}\,\in\,\mathbb{R}^{N_d}} \quad & : f = \sum_{\alpha_\infty} C_{\alpha_\infty}(\mathbf{d}, \mathbf{u}) \\ \text{subject to} \quad & : V(\mathbf{d}) - \bar{V} \leq 0 \\ & \quad \underline{d} \leq d_i \leq \bar{d} \qquad\qquad \text{for} \quad i = 1, \ldots, N_d \end{aligned} \tag{4.6}$$

The problem is first solved for straight wall spars where the design variables are defined by $\mathbf{d} = \{\boldsymbol{w}, \boldsymbol{h}, \boldsymbol{a}, \boldsymbol{s}\}$. The optimized design is then taken as the initial condition for a second optimization problem where only $\boldsymbol{e}$ can vary, i.e. $\mathbf{d} = \boldsymbol{e}$. The change in stiffness properties between the optimized designs with straight and curved spar walls is shown in Figure 4.4 for different upper bounds on volume fraction. Low volume fractions have experienced the largest changes in stiffness properties, where the torsional stiffness has been increased and bending stiffness reduced. The change in stiffness corresponds to the curving of spar walls where sections with no change maintain straight walls. For high volume fractions the wingbox dimensions are larger giving a higher torsional stiffness and less incentive to curve the spar walls. Curved wall spars predominantly form towards wingtip where torsional loads are dominant, and bending loads tend to zero. A gain of over 10% in torsional stiffness was achieved by implementing curved spars for low volume fractions, leading to

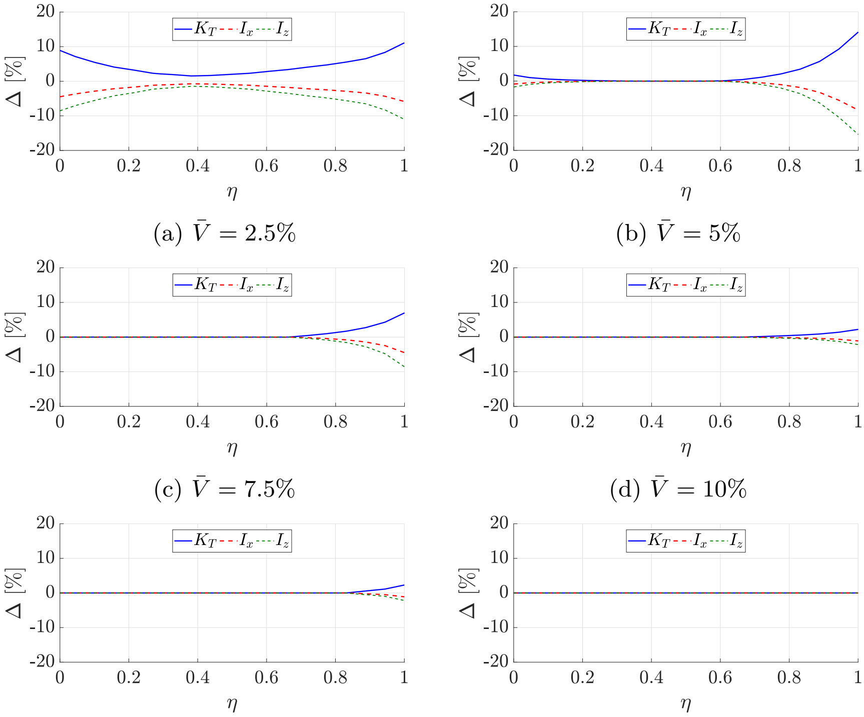

(a) $\bar{V} = 2.5\%$ (b) $\bar{V} = 5\%$

(c) $\bar{V} = 7.5\%$ (d) $\bar{V} = 10\%$

(e) $\bar{V} = 12.5\%$ (f) $\bar{V} = 15\%$

Figure 4.4: Relative difference in cross sectional stiffness properties for optimized curved wall spars for different volume fractions, $\bar{V}$. Figure retrieved from [P2].

reductions in compliance of up to 9%. This finding is then in keeping with the prediction made in [80], that the curved wall spars reduce compliance by producing optimized trade-offs between torsion and bending stiffness.

The previous example presented compliance minimization problems where the goal is to produce stiff structures that experience small deflections under a prescribed load. However, in an effort to reduce weight, wing structures are commonly designed to experience large deformations. A more natural formulation for the structural optimization of an aircraft wing is to minimize mass subject to stress constraints, defined as

$$\begin{aligned} \min_{\mathbf{d} \,\in\, \mathbb{R}^{N_d}} \quad & : m(\mathbf{d}) \\ \text{subject to} \quad & : \frac{\hat{\sigma}_i(\mathbf{d}, \mathbf{u})}{\bar{\sigma}} - \beta \leq 0 \quad \text{for} \quad i = 1, ..., N_\sigma \\ & \quad \underline{d} \leq d_i \leq \bar{d} \qquad\quad\; \text{for} \quad i = 1, ..., N_d \end{aligned} \tag{4.7}$$

where $\hat{\sigma}$ is the maximum von Mises stress which is approximated using a p-

norm function as described in [P2]. Rather than a single constraint, stress constraints are enforced on N_σ regions to improve the accuracy of the p-norm approximation. The term β in (4.7) acts as a safety factor for the design when $\beta \leq 1$. The optimization problem is solved for different values of β with both 1- and 2-way coupling. The external geometry is again defined as the CRM wing, and two cases are considered where only straight wall spars are allowed and where curved spar walls are able to form, i.e. $\mathbf{d} = \{\boldsymbol{w}, \boldsymbol{h}, \boldsymbol{s}, \boldsymbol{a}\}$ and $\mathbf{d} = \{\boldsymbol{w}, \boldsymbol{h}, \boldsymbol{s}, \boldsymbol{a}, \boldsymbol{e}\}$. The maximum stress ratio in each section is plotted in Figure 4.5 against the normalized span for each design problem.

With a high value of β, the stress constraint is active at each section along the wing in each case. As β decreases, the stress constraint eventually becomes inactive for sections near the root in 2-way coupled designs. To understand why, it is first important to note that for this optimization problem it was hardest to satisfy the stress constraint in the outer regions of the wing, towards the wingtip. Stresses in this region are dominated by torsional stresses as the bending stresses tend to zero at the wingtip. By stiffening the wing towards the root, the deflections and loads are decreased so that the stress constraint can be satisfied in the outer regions of the wing. However, because regions near

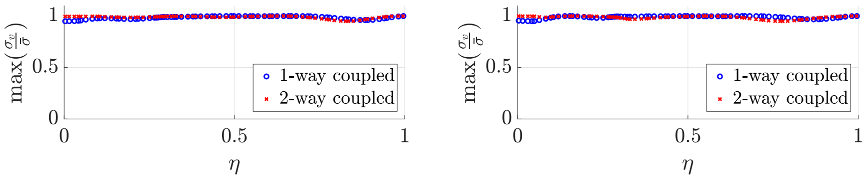

(a) $\beta = 1$, straight wall spars (b) $\beta = 1$, curved wall spars

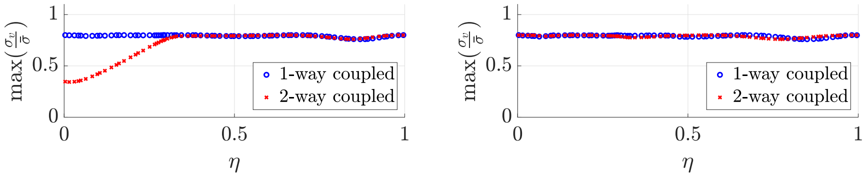

(c) $\beta = 0.8$, straight wall spars (d) $\beta = 0.8$, curved wall spars

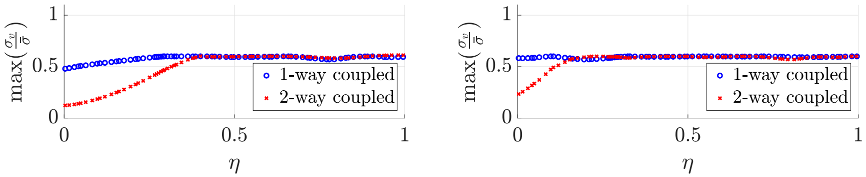

(e) $\beta = 0.6$, straight wall spars (f) $\beta = 0.6$, curved wall spars

Figure 4.5: Ratio of maximum stress to upper bound at spanwise sections of designs optimized with 1- and 2-way coupling. Figure retrieved from [P2].

the root have an increased stiffness, the stress constraint becomes inactive at the root. This is observed for larger β-values in straight wall spar designs because the additional torsional stiffness provided by curved wall spars reduces the torsional stresses at the wingtip.

Table 4.1 presents the relative change in mass between 1- and 2-way coupled designs, i.e. $\Delta_m = \frac{m_2 - m_1}{m_1}$. Increasing the stiffness has a direct relation to an increase in mass, where 2-way coupled designs have consistently larger mass. These results have shown that calculating loads in the deformed configuration can have a large impact on the optimization problem and the converged design. This highlights the importance of solving the 2-way coupled aeroelastic problem.

Table 4.1: Relative difference in mass between designs optimized with 1- and 2-way coupling for straight and curved wall spars.

β	Straight Δ_m [%]	Curved Δ_m [%]
1	21.8	21.7
0.8	148.7	40.4
0.6	130.0	79.8

4.3.2 Optimization of Deformable Flying Wing Configurations

The wingbox parameterization introduced in previous studies can also be combined with the airfoil parameterization (introduced in Section 3.3.1), i.e. $\mathbf{d} = \{\boldsymbol{c}, \boldsymbol{t}, \boldsymbol{p}, \boldsymbol{\alpha}, \boldsymbol{w}, \boldsymbol{h}, \boldsymbol{s}, \boldsymbol{a}, \boldsymbol{e}\}$. This parameterization then allows for simultaneous optimization of the external wing geometry and internal structure. Consider the optimization problem below with an objective to minimize drag subject to constraints on lift-weight equilibrium, stress and pitching moments.

$$
\begin{aligned}
\min_{\mathbf{d} \,\in\, \mathbb{R}^{N_d}} \quad & : D(\mathbf{d}, \boldsymbol{\mu}, \mathbf{u}) & & \\
\text{subject to} \quad & : L(\mathbf{d}, \boldsymbol{\mu}, \mathbf{u}) = W(\mathbf{d}) & & \\
& \quad \hat{\sigma}_i(\mathbf{d}, \mathbf{u}) - \bar{\sigma} \leq 0 & \text{for} \quad & i = 1, ..., N_\sigma \\
& \quad M_p(\mathbf{d}, \boldsymbol{\mu}, \mathbf{u}) = 0 & & \\
& \quad \underline{d} \leq d_i \leq \bar{d} & \text{for} \quad & i = 1, ..., N_d
\end{aligned}
\tag{4.8}
$$

The weight is defined as the sum of weights from the beam, 5% of the wing volume, and a payload. The total weight must be equal to the lift in cruise i.e. $\alpha_\infty = 0°$. The pitching moment should also be zero in cruise conditions, where M_p is calculated about an axis that is parallel to the y axis and intersects the midpoint of the quarter chord curve. The stress constraint is enforced in a high load case representing take off, where $\alpha_\infty = 10°$.

The optimization problem is solved for three sweep angles, $\Lambda = \{0°, 15°, 30°\}$, with a NACA 5-digit airfoil parameterization, and where the physics models are 2-way coupled. Planforms and deformations of optimized designs are shown in Figure 4.6. Each design converges with a large aspect and taper ratio which is expected as this will reduce the induced drag and deformations (and in turn the stresses). Torsional loads increase with the sweep, leading to larger planform areas for swept wings because a stiffer structure is required to balance the

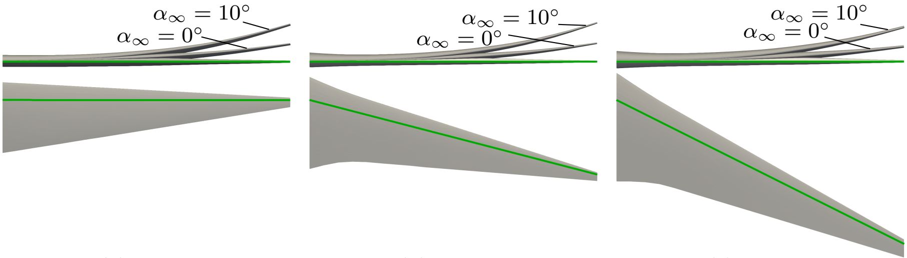

(a) $\Lambda = 0°$ (b) $\Lambda = 15°$ (c) $\Lambda = 30°$

Figure 4.6: Planform and elevation views with deflections for designs optimized with different sweep angles, Λ. Beam axis is shown in green. Figure adapted from [P2].

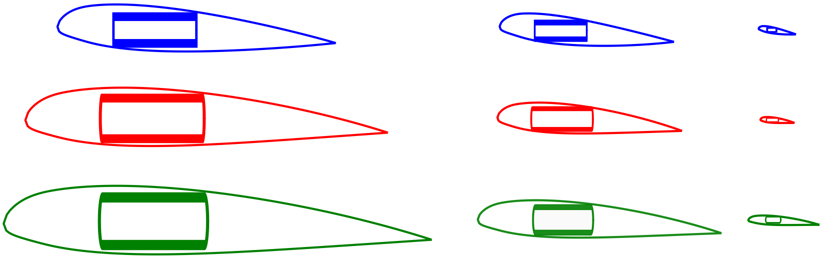

Figure 4.7: Airfoil and beam cross sections at root, mid-span, and wingtip (left to right) for optimized designs with $\Lambda = 0°$ (top), $\Lambda = 15°$ (middle), $\Lambda = 30°$ (bottom). Figure retrieved from [P2].

larger loads. The change in chord length when sweep is increased can also be seen from the airfoil sections shown in Figure 4.7.

Figure 4.7 also shows the cross sections of the beam where spar walls remain straight for the unswept wing. This is not surprising because the beam axis is in-line with the pitching axis about which the total moment is specified to be zero in the optimization problem. It then follows that the torsional loads are low in this case and as such it is not beneficial to create curved wall spars. When the sweep increases so does the torsional loads, and curved wall spars become more pronounced. The position of the pitching axis in unswept wings also leads to differences in airfoil shape compared to the swept wings. The airfoil parameterization allows a reflex camber line to form in order to aid the optimizer in satisfying the pitching moment constraint. However, reflex camber is only needed for the unswept wing, where the pitching axis is in line with the airfoils which makes it difficult to balance moments along the wing. When wings are swept, the airfoils at the root are forward of the pitching axis and the wingtip is aft. This gives the optimizer more control over balancing the moments from lift created forward and aft of the pitching axis.

Figure 4.8 shows the maximum stress ratio per section plotted against the normalized span. The constraint is active for most of the span in each case, but for the unswept wing, the stresses tend to zero at the wingtip. Bending stresses tend to zero at the wingtip but torsional stresses do not. The fact that the unswept design has no stresses towards the wingtip demonstrates that the torsional loads have been removed from the design through creating a reflex camber line.

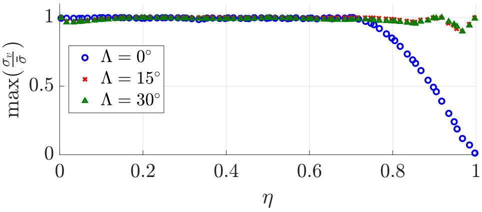

Figure 4.8: Ratio of maximum stress to upper bound at spanwise sections of optimized designs with different sweep angles. Figure retrieved from [P2].

4.4 Shape Optimization of Solid Foam Core Wings

This section will adopt a beam parameterization that is introduced in [P4], where a solid isotropic cross section is assumed. This parameterization is applicable to solid foam core wings used for aerospace applications such as drones or model aircraft. The parameterization is shown in Figure 4.9, and is based on the definition of NACA 4-digit airfoils profiles. The cross sectional properties can be then calculated from the airfoil definitions, given in Appendix D, equations (D1)-(D3).

Three centers are labeled in Figure 4.9: the elastic, shear, and beam centers. Elastic and shear centers are needed to calculate the constitutive stiffness matrix defined in (2.30). For isotropic materials, the elastic center, (e_x, e_z), is coincident to the geometric center of the airfoil, and is derived analytically using the NACA 4-digit definitions, whereas the location of the shear center can be approximated as $(s_x, s_z) = (0.89e_x, 1.45e_z)$, as described in [P4]. The beam center corresponds to the location of the finite element. Theoretically, the beam center can be defined anywhere, but certain advantages can be achieved by choosing an appropriate location. For example, if it is coincident to the elastic or shear center, the expression for $\mathbf{K}_{cs}$ in (2.30) could be simplified as the elastic or shear center terms can be eliminated. For 2-way coupled aeroelastic problems, it is advantageous to specify the beam center at the quarter chord point, as shown in Figure 4.9. This is be-

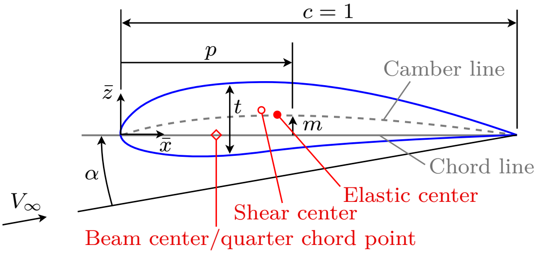

Figure 4.9: NACA 4-digit airfoil parameterization with structural centers labeled. Figure retrieved from [P4].

cause the quarter chord point is an approximate of the location of the aerodynamic center, which by definition, is the point where the pitching moment does not change with angle of attack. This means that torsional loads are roughly constant as the beam deforms, making the coupled problem easier to converge because large changes in twist will only induce a small change to the load. Refer to the discussion in Appendix C on convergence behavior for large deformations.

The following subsections include studies based on the parameterization above. The first will investigate the effects of including a non-linear deformation model in the aeroelastic optimization of induced drag minimization problems. The second subsections presents studies on aeroelastic optimization of non-planar wings and compares the performance of flexible raised and drooped wing designs.

4.4.1 Linear vs. Non-Linear Structural Analysis

This study will compare designs achieved with linear and non-linear deformation models. Consider the optimization problem defined below, where the objective is to minimize induced drag subject to constraints on lift-weight equilibrium, and tip displacement, u_t.

$$
\begin{array}{lll}
\underset{\mathbf{d}\,\in\,\mathbb{R}^{N_d}}{\min} & : D(\mathbf{d},\mathbf{u},\boldsymbol{\mu}) & \\
\text{subject to} & : L(\mathbf{d},\mathbf{u},\boldsymbol{\mu}) = W(\mathbf{d}) & \\
 & \quad u_t(\mathbf{u}) \leq \bar{u}_t & \\
 & \quad \underline{d} \leq d_i \leq \bar{d} & \text{for} \quad i = 1, ..., N_d
\end{array}
\tag{4.9}
$$

The problem is solved using both linear and non-linear beam finite element models introduced in Section 2.3, with different upper bounds on tip displacement. In light of the findings presented in Section 4.3, only 2-way coupled analysis is considered for these problems. Converged designs are shown in Figure 4.10 in undeformed and deformed configurations.

Each design converges to a tapered high aspect ratio wing, which is expected as the taper stiffens the wing towards the root to reduce deflections, and a high aspect ratio reduces weight and induced drag. The tip displacement constraint is active in each case where a linear FE model was used, but when a non-linear FE model is used the constraint is only active for low $\bar{u}_t$ values. To understand why, it is important to revisit the differences in the FE models. Degrees of freedom are defined to give transverse deflections in two directions, an axial displacement, and rotations of the cross section about 3 axes. When a linear FE model is used, the axial displacement is related purely to axial loads, and for a beam in pure bending the displacement will only be in the transverse direction. When the non-linear FE model is used, the constitutive relations are satisfied within a locally for each element which are rotated as the beam deforms. This means in pure bending, the non-linear FE model also captures rotations of

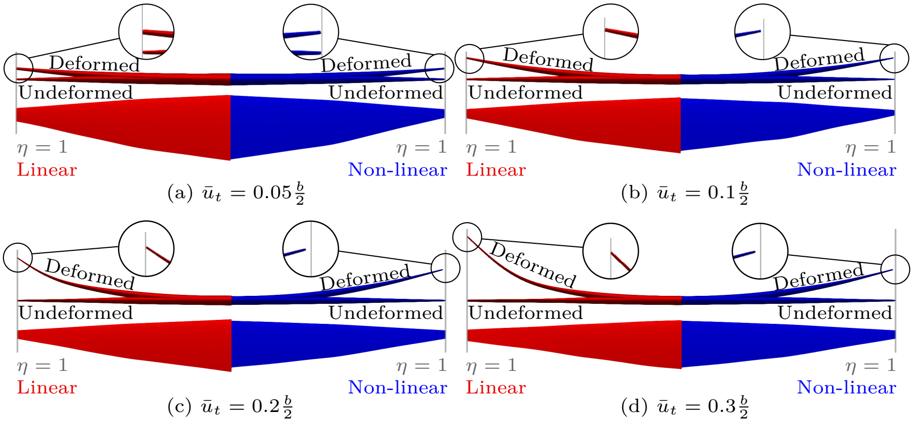

(a) $\bar{u}_t = 0.05\frac{b}{2}$ (b) $\bar{u}_t = 0.1\frac{b}{2}$

(c) $\bar{u}_t = 0.2\frac{b}{2}$ (d) $\bar{u}_t = 0.3\frac{b}{2}$

Figure 4.10: Converged designs using linear (left) and non-linear (right) beam finite element models for different upper bounds on tip displacement, $\bar{u}_t$. Details show the deformations at the wingtip. Figure retrieved from [P4].

the beam, corresponding to an axial displacement at the wingtip, as shown in details in Figure 4.10. This offset of the wingtip corresponds to a shortening of the wingspan, which was shown in Section 3.3.2 to have a significant impact on the achievable minimum induced drag.

Because the wingspan shortening effect cannot be captured by a linear FE model, unphysical deformations are predicted where the curved length of the wing has increased (refer to Figure 4.10d) and a good aerodynamic performance is maintained for large deformations. However, the performance would be degraded for large deformations with a non-linear FE model and as such the tip constraint is inactive. For example, the wing achieved with a linear FE model in Figure 4.10d has an inviscid lift-to-drag ratio of 70.4 compared to 64.4 for the non-linear design. This study demonstrates the importance of capturing non-linear deformations for induced drag minimization problems, where it is crucial to capture the change in effective wingspan when the wing deforms.

4.4.2 Aeroelastic Optimization of Non-Planar Wings

Studies presented here will solve a similar optimization problem to that defined (4.9), only now an additional constraint is added on the root bending moment, and non-planar geometry is allowed to form. The problem is defined as

$$\begin{array}{lll} \underset{\mathbf{d}\,\in\,\mathbb{R}^{N_d}}{\min} & : D(\mathbf{d},\mathbf{u},\boldsymbol{\mu}) & \\ \text{subject to} & : L(\mathbf{d},\mathbf{u},\boldsymbol{\mu}) = W(\mathbf{d}) & \\ & \;\; u_t(\mathbf{u}) \leq \bar{u}_t & \\ & \;\; M_r(\mathbf{d},\mathbf{u},\boldsymbol{\mu}) \leq \bar{M}_r & \\ & \;\; \underline{d} \leq d_i \leq \bar{d} & \text{for} \quad i = 1, \ldots, N_d \end{array} \tag{4.10}$$

The optimization problem is solved for unswept wings with symmetric airfoils where $\mathbf{d} = \{\delta \boldsymbol{c}, \boldsymbol{t}, \boldsymbol{\alpha}, \delta \hat{\boldsymbol{z}}\}$. Optimized designs are shown in Figure 4.11 for different upper bounds on M_r where $\bar{M}_r$ is defined in terms of a scalar M_0 which is equal to the bending moment produced by wings in Figure 4.10d.

Both raised and drooped wings form when there is a relaxed constraint on M_r, but the wings are planar for $\bar{M}_r = 0.85 M_0$, where converged designs are very similar for both cases. These wings have a larger taper ratio than the planar wing in Figure 4.10d, allowing more lift to be created near the root rather than near the wingtip, which reduces the bending moment. For other values of $\bar{M}$, drooped designs have consistently achieved larger lift-to-drag ratios than raised wings. For example, with $\bar{M}_r = M_0$ the drooped wing has a lift-to-drag ratio of 71.0 versus 68.9 for the raised wing. These differences in performance are directly related to the deformed geometry. Similar to the non-linear wings in Figure 4.10, the effective wingspan is reduced when a raised wing deforms. However, the effective wingspan is increased when a drooped wing deforms, refer to details in Figure 4.11. Because increasing the wingspan leads to large reductions in induced drag (refer to Section 3.3.2), these differences in the effective wingspan in the deformed configuration allows drooped wings to out perform raised wings.

In [P3] is was found that drooped wings were not beneficial when viscous effects were included. However, this finding was based on rigid undeformable wings. It is not yet known whether the reductions in induced drag that occur from increasing the effective wingspan in the deformed configuration is enough to offset the larger viscous drag that occurs when wings are drooped.

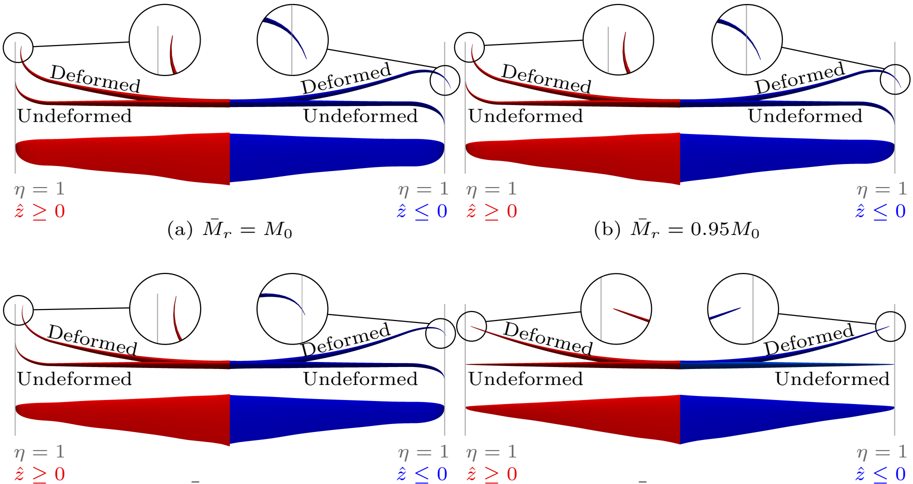

(a) $\bar{M}_r = M_0$

(b) $\bar{M}_r = 0.95 M_0$

(c) $\bar{M}_r = 0.9 M_0$

(d) $\bar{M}_r = 0.85 M_0$

Figure 4.11: Converged designs with raised (left) and drooped (right) wings for different upper bounds on bending moment, $\bar{M}_r$. Details show the deformations at the wingtip. Figure retrieved from [P4].

5 Conclusions

5.1 Summary of Outcomes and Contributions

A framework has been developed to solve aerodynamic and aeroelastic shape optimization problems. Physics models are based on low- to mid-fidelity methods in order to keep computational cost low. Geometry is parameterized based on local definitions to allow large geometric changes throughout the optimization routine, where spanwise filtering is used to ensure smoothness and avoid numerical artifacts. The methodology was applied to a number of studies whose findings are summarized below:

1. Boundary Conditions
   It is well documented that for panel methods, a Dirichlet boundary condition (BC) reduces computational cost compared to a Neumann BC [2, 75]. Section 3.2.1 has compared BCs with respect to optimization problems, and has found that resulting designs are insensitive to choice of BC, but there is a factor of 2 difference in the computational cost of gradients (in favor of a Dirichlet BC) which accounts for 80-90% of the total cost.

2. Induced Drag Calculations
   Section 3.2.2 compares designs achieved with different drag calculations methods where numerical errors in surface pressure integration allowed the optimizer to produce unphysical results that reduce the objective function. These results were achieved with a constant-strength source-doublet panel method, where Trefftz plane integration was found to be necessary to ensure physical results throughout the optimization routine.

3. Regularization for Inviscid Problems
   Free-form parameterizations, such as those described by B-splines, can create geometries that exploit the assumption of inviscid flow. This requires a large amount of regularization to ensure features such as a blunt leading edge, sharp trailing edge etc. It is then recommended to define a parameterization that implicitly satisfies these requirements such as the NACA parameterization presented in Section 3.3.1.

4. Wing vs. Airfoil Parameterization
   Parameterizing the wing geometry, such as the wingspan, sweep and non-planar geometry, can achieve a much larger reduction in induced drag compared to only parameterizing airfoil sections of planar wings. The wingspan has proven particularly important for reducing the induced drag, where the optimizer was not able to improve the performance of planar wings with a reduced wingpan.

5. Panel-Beam Coupling
   A 3D panel-beam method was introduced for aeroelastic optimization problems, and is demonstrated with linear and non-linear co-rotating beam models. To the author's knowledge, this is the first example of these coupled methods being used for gradient-based optimization. A generalized load-displacement transfer scheme is introduced which is applicable to any choice of panel or beam finite element regardless of order, nodes per element etc.

6. Curved Wall Spars
   The high resolution of topology optimization results presented in [80] allowed the formation of curved wall spars, which the authors argue has created trade-offs between torsional and bending stiffness. Section 4.3 investigated this theory and curved wall spars were shown to improve performance for both compliance minimization and stress constrained problems due to the ability to create these trade-offs.

7. 2-way Coupling for Panel-Beam Problems
   Including 2-way coupling for aeroelastic problems, i.e. calculating loads in the deformed configuration, has been shown to have a large effect on optimized designs as there can be a large change in aerodynamic loading when the wing deforms. This highlights the importance of solving the coupled panel-beam physics in optimization problems, a fact that has been previously demonstrated for other physics models, e.g. [60, 82, 83].

8. Non-linear Deformations
   For pure bending, a linear finite element model will only capture transverse deformations without the element rotations due to bending. These rotations will correspond to a shortening of the wingspan which has a large effect on the induced drag (refer to point 4). It is then important to use non-linear deformation models when solving induced drag minimization problems in order to capture the effect of a shortening wingspan.

5.2 Future Work

There are a number of ongoing projects that extend upon the methods presented in this thesis, of which brief descriptions are outlined below:

1. Deformable drooped wings with viscous effects
   Section 4.4.2 demonstrated that deformable drooped wings can achieve large inviscid lift-to-drag ratios due an increase in effective wingspan in the deformed configuration. However, [P3] found that rigid drooped wings were not beneficial when viscous effects were included. Future work will investigate the performance of deformable drooped wings with viscous approximations.

2. Coupled Shape and Topology Optimization
   A goal of this thesis was to develop methods that could interface with different structural models. Appendix A presents a topology optimization study with 1-way coupling and a fixed outer wing geometry. This work will be extended to include simultaneous shape and topology optimization of the wing surface and internal structure, as well as 2-way coupling.

3. High-Order Panels
   Point 2 of Section 5.1 concludes that far-field calculations are needed to avoid numerical errors in C_P distributions. This conclusion is based on a constant-strength source-doublet panel method. However, it is known that errors in C_P distributions can be reduced by implementing higher-order methods. Future work will investigate whether high-order methods reduce discretization error to such an extent that C_P distributions can be used to create viable optimized designs. A more detailed description on this is provided in Appendix F.

4. Rotor Design
   This thesis has focused on the application of methods to the design of aircraft wings. Ongoing work will extend methods to other engineering applications, such as wind turbine blades.

The methods presented in this thesis can also be extended to many other applications that are currently not under consideration by the author and co-workers, but may be of interest to the reader. These include:

5. Advanced Wake Models
   Iterative wake models have been discussed in Section 2.2.5, but were deemed too expensive for the current work where a fixed freestream wake model was used instead. The current wake model is able to predict similar results when designs are regularized as shown in [P1], but there are limitations to the model such as assuming steady-state flow where a more advanced wake model would be required for unsteady problems.

6. Advanced Cross Sectional Analysis
   Throughout this thesis, cross sectional stiffness properties for beam models were calculated either through analytic expressions or approximations. Extending methods to use cross sectional analysis tools such as BECAS [84] or VABS [85, 86] will allow the user to calculate properties of arbitrary cross sections consisting of anisotropic materials.

7. Boundary Layer Coupling
   Point 3 of Section 5.1 concludes that the B-spline parameterization offers too much design freedom for inviscid problems which then requires more regularization to stop the optimizer taking advantage of the inviscid flow. By coupling boundary layer analysis, viscous effects can be accounted for directly in the model and it is expected that additional design freedom could be provided in the parameterization.

Bibliography

[1] J. Nocedal and S.J. Wright. *Numerical Optimization.* Springer New York, 2006.

[2] J. Katz and A. Plotkin. *Low-Speed Aerodynamics.* Cambridge Aerospace Series. Cambridge University Press, 2001.

[3] K.J. Bathe. *Finite element procedures.* Prentice Hall, 1996.

[4] M.A. Crisfield. *Non-linear finite element analysis of solids and structures; Vol. 1: Essentials.* Wiley, 1991.

[5] G. Cayley. "On Aerial Navigation Parts 1-3". In: *Nicholson's Journal of Natural Philosophy* (1809-1810).

[6] Wikimedia Commons. *1905 Wright Flyer III.* User: MLWatts. 1905. URL: `https://commons.wikimedia.org/wiki/File:1905_Wright_Flyer_III_(flight_46).jpg`.

[7] Wikimedia Commons. *Spitfire Planform.* User: Arpingstone. 2006. URL: `https://commons.wikimedia.org/wiki/File:Spitfire.planform.arp.jpg`.

[8] Creative Commons. *WAL Boeing 707- 720B with Indian head Logo - 1962.* User: slap757. 1962. URL: `https://search.creativecommons.org/photos/006b3bba-4067-4a6a-b062-1f8533807702`.

[9] Creative Commons. *Boeing 777X.* User: LunchWithaLens. 2020. URL: `https://search.creativecommons.org/photos/f446e381-5954-4c84-966f-3f41eaa58c57`.

[10] J.D. Anderson. *Fundamentals of aerodynamics.* McGraw-Hill Education, 2011.

[11] M.M. Munk. *The Minimum Induced Drag of Aerofoils.* NACA Technical Report no. 121. National Aeronautics and Space Administration, 1923.

[12] P.M. Peeters, J. Middel, and A. Hoolhorst. *Fuel efficiency of commercial aircraft: An overview of historical and future trends.* NLR Contractor Report CR-2005-669. Netherlands National Aerospace Laboratory, 2005.

[13] *Boeing 777X Technical Specifications.* Accessed: Spt. 2020. URL: `https://www.boeing.com/commercial/777x/`.

[14] F.T. Johnson, E.N. Tinoco, and N.J. Yu. "Thirty years of development and application of CFD at Boeing Commercial Airplanes, Seattle". In: *Computers and Fluids* 34.10 (2005), pp. 1115–1151. DOI: `https://doi.org/10.1016/j.compfluid.2004.06.005`.

[15] R.T. Whitcomb. "A design approach and selected wind tunnel results at high subsonic speeds for wing-tip mounted winglets". In: NASA Technical Note TN D-8260 (1976).

[16] M. Potsdam, M. Page, R. Liebeck, M. Potsdam, M. Page, and R. Liebeck. "Blended Wing Body analysis and design". In: *15th Applied Aerodynamics Conference*. 1997. DOI: `https://doi.org/10.2514/6.1997-2317`.

[17] R.H. Liebeck. "Design of the Blended Wing Body Subsonic Transport". In: *Journal of Aircraft* 41.1 (2004), pp. 10–25. DOI: `https://doi.org/10.2514/1.9084`.

[18] Z. Lyu and J.R.R.A. Martins. "Aerodynamic design optimization studies of a blended-wing-body aircraft". In: *Journal of Aircraft* 51.5 (2014), pp. 1604–1617. DOI: `https://doi.org/10.2514/1.C032491`.

[19] J. Katz, S. Byrne, and R. Hahl. "Stall resistance features of lifting-body airplane configurations". In: *Journal of Aircraft* 36.2 (1999), pp. 471–474. DOI: `https://doi.org/10.2514/2.2456`.

[20] M. Drela. "Development of the D8 transport configuration". In: *29th AIAA Applied Aerodynamics Conference 2011* (2011). DOI: `https://doi.org/10.2514/6.2011-3970`.

[21] T.A. Reist and D.W. Zingg. "High-fidelity aerodynamic shape optimization of a lifting-fuselage concept for regional aircraft". In: *Journal of Aircraft* 54.3 (2017), pp. 1085–1097. DOI: `https://doi.org/10.2514/1.C033798`.

[22] B.S. Lazos and K.D. Visser. "Aerodynamic comparison of Hyper-Elliptic Cambered Span (HECS) wings with conventional configurations". In: *Collection of Technical Papers - AIAA Applied Aerodynamics Conference* 3 (2006), pp. 1608–1625. DOI: `https://doi.org/110.2514/6.2006-3469`.

[23] S. Khosravi and D.W. Zingg. "Aerostructural optimization of drooped wings". In: *Journal of Aircraft* 55.3 (2018), pp. 1261–1268. DOI: `https://doi.org/10.2514/1.C034605`.

[24] A.R. Rodriguez. "Morphing aircraft technology survey". In: *Collection of Technical Papers - 45th AIAA Aerospace Sciences Meeting* 21 (2007), pp. 15064–15079.

[25] S. Barbarino, O. Bilgen, R.M. Ajaj, M.I. Friswell, and D.J. Inman. "A review of morphing aircraft". In: *Journal of Intelligent Material Systems and Structures* 22.9 (2011), pp. 823–877. DOI: `https://doi.org/10.1177/1045389X11414084`.

[26] X. Lachenal, S. Daynes, and P.M. Weaver. "Review of morphing concepts and materials for wind turbine blade applications". In: *Wind Energy* 16.2 (2013), pp. 283–307. DOI: `https://doi.org/10.1002/we.531`.

[27] ICAO. *Global Environmental Trends - Present and Future Aircraft Noise and Emissions*. International Civil Aviation Organization. 2019.

[28] The World Bank group. *World Development Indicators: Passenger Air Transport*. Accessed: Oct. 2020. URL: `https://databank.worldbank.org/source/world-development-indicators`.

[29] IATA. *20 Year Passenger Forecast.* International Air Transport Association. 2020.

[30] I. Kroo. “VKI lecture series on Innovative Configurations and Advanced Concepts for Future Civil Aircraft”. In: (2005).

[31] I. Kroo. “Drag due to lift: Concepts for prediction and reduction”. eng. In: *Annual Review of Fluid Mechanics* 33.1 (2001), pp. 587–617. DOI: `https://doi.org/10.1146/annurev.fluid.33.1.587`.

[32] W.S. Dorn, R.E. Gomory, and H.J. Greenberg. “Automatic design of optimal structures”. In: *Journal De Mecanique* 3.1 (1964), pp. 25–52.

[33] T. Sokół. “A 99 line code for discretized Michell truss optimization written in Mathematica”. In: *Structural and Multidisciplinary Optimization* 43.2 (2011), pp. 181–190. DOI: `https://doi.org/10.1007/s00158-010-0557-z`.

[34] T. Zegard and G.H. Paulino. “GRAND — Ground structure based topology optimization for arbitrary 2D domains using MATLAB”. In: *Structural and Multidisciplinary Optimization* 50.5 (2014), pp. 861–882. DOI: `https://doi.org/10.1007/s00158-014-1085-z`.

[35] T. Zegard and G.H. Paulino. “GRAND3 — Ground structure based topology optimization for arbitrary 3D domains using MATLAB”. In: *Structural and Multidisciplinary Optimization* 52.6 (2015), pp. 1161–1184. DOI: `https://doi.org/10.1007/s00158-015-1284-2`.

[36] M.P. Bendsøe and N. Kikuchi. “Generating optimal topologies in structural design using a homogenization method”. In: *Computer Methods in Applied Mechanics and Engineering* 71.2 (1988), pp. 197–224. DOI: `https://doi.org/10.1016/0045-7825(88)90086-2`.

[37] O. Sigmund. “A 99 line topology optimization code written in matlab”. In: *Structural and Multidisciplinary Optimization* 21.2 (2001), pp. 120–127. DOI: `https://doi.org/10.1007/s001580050176`.

[38] M.P. Bendsœ and O. Sigmund. *Topology Optimization - Theory, Methods, and Applications.* Springer Verlag, 2003.

[39] T.E. Bruns and D.A. Tortorelli. “Topology optimization of non-linear elastic structures and compliant mechanisms”. In: *Computer Methods in Applied Mechanics and Engineering* 190.26-27 (Mar. 2001), pp. 3443–3459. DOI: `https://doi.org/10.1016/s0045-7825(00)00278-4`.

[40] T. Borrvall and J. Petersson. “Topology optimization of fluids in Stokes flow”. In: *International Journal for Numerical Methods in Fluids* 41.1 (2003), pp. 77–107. DOI: `https://doi.org/10.1002/fld.426,10.1002/fld.426`.

[41] C.S. Andreasen, A.R. Gersborg, and O. Sigmund. “Topology optimization of microfluidic mixers”. In: *International Journal for Numerical Methods in Fluids* 61.5 (2009), pp. 498–513. DOI: `https://doi.org/10.1002/fld.1964`.

[42] C.B. Dilgen, S.B. Dilgen, D.R. Fuhrman, O. Sigmund, and B.S. Lazarov. "Topology optimization of turbulent flows". In: *Computer Methods in Applied Mechanics and Engineering* 331 (2018), pp. 363–393. DOI: `https://doi.org/10.1016/j.cma.2017.11.029`.

[43] G.H. Yoon, J.S. Jensen, and O. Sigmund. "Topology optimization of acoustic-structure interaction problems using a mixed finite element formulation". In: *International Journal for Numerical Methods in Engineering* 70.9 (2007), pp. 1049–1075. DOI: `https://doi.org/10.1002/nme.1900`.

[44] G.H. Yoon. "Topology optimization for stationary fluid-structure interaction problems using a new monolithic formulation". In: *International Journal for Numerical Methods in Engineering* 82.5 (2010), pp. 591–616. DOI: `https://doi.org/10.1002/nme.2777`.

[45] C. Lundgaard, J. Alexandersen, M. Zhou, C.S. Andreasen, and O. Sigmund. "Revisiting density-based topology optimization for fluid-structure-interaction problems". In: *Structural and Multidisciplinary Optimization* 58.3 (2018), pp. 969–995. DOI: `https://doi.org/10.1007/s00158-018-1940-4`.

[46] J.R.R.A. Martins and J.T. Hwang. "Review and unification of methods for computing derivatives of multidisciplinary computational models". In: *AIAA Journal* 51.11 (2013), pp. 2582–2599. DOI: `https://doi.org/10.2514/1.J052184`.

[47] N.R. Secco and J.R.R.A. Martins. "RANS-based aerodynamic shape optimization of a strut-braced wing with overset meshes". In: *AIAA/ASCE/AHS/ASC Structures, Structural Dynamics, and Materials Conference, 2018* (2018), 21 pp., 21 pp. DOI: `https://doi.org/10.2514/6.2018-0413`.

[48] D. Koo and D.W. Zingg. "Investigation into aerodynamic shape optimization of planar and nonplanar wings". In: *AIAA Journal* 56.1 (2018), pp. 250–263. DOI: `https://doi.org/10.2514/1.J055978`.

[49] M.H.A. Madsen, F. Zahle, N.N. Sørensen, and J.R.R.A. Martins. "Multipoint high-fidelity CFD-based aerodynamic shape optimization of a 10 MW wind turbine". In: *Wind Energy Science* 4.2 (2019), pp. 163–192. DOI: `https://doi.org/10.5194/wes-4-163-2019`.

[50] J. Elliott and J. Peraire. "Practical 3D aerodynamic design and optimization using unstructured meshes". In: *6th Symposium on Multidisciplinary Analysis and Optimization* (1996), pp. 1819–1828. DOI: `https://doi.org/10.2514/6.1996-4170`.

[51] G.K.W. Kenway and J.R.R.A. Martins. "Multipoint high-fidelity aerostructural optimization of a transport aircraft configuration". In: *Journal of Aircraft* 51.1 (2014), pp. 144–160. DOI: `https://doi.org/10.2514/1.C032150`.

[52] G.K.W. Kenway, G.J. Kennedy, and J.R.R.A. Martins. “Scalable parallel approach for high-fidelity steady-state aeroelastic analysis and adjoint derivative computations”. In: *AIAA Journal* 52.5 (2014), pp. 935–951. DOI: `https://doi.org/10.2514/1.J052255`.

[53] H. Gagnon and D.W. Zingg. “Euler-equation-based drag minimization of unconventional aircraft configurations”. In: *Journal of Aircraft* 53.5 (2016), pp. 1361–1371. DOI: `https://doi.org/10.2514/1.C033591`.

[54] R.M. Hicks and P.A. Henne. “Wing design by numerical optimization”. In: *Journal of Aircraft* 15.7 (1978), pp. 407–412. DOI: `https://doi.org/10.2514/3.58379`.

[55] J. Reuther, A. Jameson, J. Farmer, L. Marlinelli, and D. Saunders. “Aerodynamic shape optimization of complex aircraft configurations via an adjoint formulation”. In: *34th Aerospace Sciences Meeting and Exhibit* (1996). DOI: `https://doi.org/10.2514/6.1996-94`.

[56] G.J. Kennedy and J.R.R.A. Martins. “Parallel Solution Methods for Aerostructural Analysis and Design Optimization”. In: *13th AIAA/ISSMO Multidisciplinary Analysis and Optimization Conference*. American Institute of Aeronautics and Astronautics Inc., 2010. DOI: `https://doi.org/10.2514/6.2010-9308`.

[57] G.J. Kennedy and J.R.R.A. Martins. “A Parallel Aerostructural Optimization Framework for Aircraft Design Studies”. In: *Structural and Multidisciplinary Optimization* 50.6 (2014), pp. 1079–1101. DOI: `https://doi.org/10.1007/s00158-014-1108-9`.

[58] T. Goetzendorf-Grabowski and J. Mieloszyk. “Common Computational Model for Coupling Panel Method with Finite Element Method”. In: *Aircraft Engineering and Aerospace Technology* 89.5 (2017), pp. 654–662. DOI: `https://doi.org/10.1108/AEAT-01-2017-0044`.

[59] P.W. Jansen, R.E. Perez, and J.R.R.A. Martins. “Aerostructural optimization of nonplanar lifting surfaces”. In: *Journal of Aircraft* 47.5 (2010), pp. 1490–1503. DOI: `https://doi.org/10.2514/1.44727`.

[60] P.D. Dunning, B.K. Stanford, and H.A. Kim. “Coupled aerostructural topology optimization using a level set method for 3D aircraft wings”. In: *Structural and Multidisciplinary Optimization* 51.5 (2015), pp. 1113–1132. DOI: `https://doi.org/10.1007/s00158-014-1200-1`.

[61] J.P. Jasa, J.T. Hwang, and J.R.R.A. Martins. “Open-source coupled aerostructural optimization using Python”. In: *Structural and Multidisciplinary Optimization* 57.4 (2018), pp. 1815–1827. DOI: `https://doi.org/10.1007/s00158-018-1912-8`.

[62] R.T. Haftka. “Optimization of flexible wing structures subject to strength and induced drag constraints”. In: *AIAA Journal* 15.8 (1977), pp. 1101–1106. DOI: `https://doi.org/10.2514/3.7400`.

[63] M. Sessarego, J. Feng, N. Ramos García, and S. Horcas. “Design optimization of a curved wind turbine blade using neural networks and an aero-elastic vortex method under turbulent inflow”. In: *Renewable Energy* 146 (2020), pp. 1524–1535. DOI: `https://doi.org/10.1016/j.renene.2019.07.046`.

[64] N. Ramos García, J.N. Sørensen, and W.Z. Shen. “Three-Dimensional Viscous-Inviscid Coupling Method for Wind Turbine Computations”. In: *Wind Energy* 19.1 (2016), pp. 67–93. DOI: `https://doi.org/10.1002/we.1821`.

[65] D.R. Bristow and G.G. Grose. *Modification of the Douglas Neumann Program to Improve the Efficiency of Predicting Component Interference and High Lift Characteristics.* NASA Contractor Report CR-3020. National Aeronautics and Space Administration, 1978.

[66] B. Maskew. “Prediction of Subsonic Aerodynamic Characteristics: A Case for Low-Order Panel Methods”. In: *Journal of Aircraft* 19.2 (1982), pp. 157–163. DOI: `https://doi.org/10.2514/3.57369`.

[67] H. Lamb. *Hydrodynamics.* 6th. Courier Corporation, 1945.

[68] B. Maskew. *Program VSAERO Theory Document : A Computer Program for Calculating Nonlinear Aerodynamic Characteristics of Arbitrary Configurations.* NASA contractor report CR-4023. National Aeronautics and Space Administration, 1987.

[69] J. Katz and B. Maskew. “Unsteady Low-Speed Aerodynamic Model for Complete Aircraft Configurations”. In: *Journal of Aircraft* 25.4 (1988), pp. 302–310. DOI: `https://doi.org/10.2514/3.45564`.

[70] L.D. Ashley, M.D. Dudley, S.K. Iguchi, L. Browne, and J. Katz. *Potential Flow Theory and Operation Guide for the Panel Code PMARC.* Technical memorandum 102851. National Aeronautics and Space Administration, 1991.

[71] S.C. Smith. *A Computational and Experimental Study of Nonlinear Aspects of Induced Drag.* Technical Paper 3598. National Aeronautics and Space Administration, 1996.

[72] M. Drela. *Flight Vehicle Aerodynamics.* The MIT Press, 2014.

[73] R. Parnes. *Solid mechanics in engineering.* Wiley, 2001.

[74] J.B. Kosmatka. *The use of cross-section warping functions in composite rotor blade analysis.* Report no. SSRP-92/11. National Aeronautics and Space Administration, 1992.

[75] L.L. Erickson. *Panel Methods - An Introduction.* NASA Technical Paper 2995. National Aeronautics and Space Administration, 1990.

[76] J. Lee. “A Potential Based Panel Method for the Analysis of Marine Propellers in Steady Flow”. PhD thesis. Massachusetts Institute of Technology, 1987.

[77] C.P. Van Dam. “Efficiency characteristics of crescent-shaped wings and caudal fins”. In: *Nature* 325.6103 (1987), pp. 435–437. DOI: `https://doi.org/10.1038/325435a0`.

[78] B.S. Lazos. “Biologically inspired fixed-wing configuration studies”. In: *Journal of Aircraft* 42.5 (2005), pp. 1089–1098. DOI: `https://doi.org/10.2514/1.10496`.

[79] J.R.R.A. Martins, J.J. Alonso, and J.J. Reuther. “A coupled-adjoint sensitivity analysis method for high-fidelity aero-structural design”. In: *Optimization and Engineering* 6.1 (2005), pp. 33–62. DOI: `https://doi.org/10.1023/B:OPTE.0000048536.47956.62`.

[80] N. Aage, E. Andreassen, B.S. Lazarov, and O. Sigmund. “Giga-voxel computational morphogenesis for structural design”. In: *Nature* 550.7674 (2017), pp. 84–86. DOI: `https://doi.org/10.1038/nature23911`.

[81] J.C. Vassberg, M.A. DeHaan, S.M. Rivers, and R.A. Wahls. “Development of a common research model for applied CFD validation studies”. In: *Collection of Technical Papers - AIAA Applied Aerodynamics Conference* (2008). DOI: `https://doi.org/10.2514/6.2008-6919`.

[82] K. Maute and M. Allen. “Conceptual design of aeroelastic structures by topology optimization”. In: *Structural and Multidisciplinary Optimization* 27.1-2 (2004), pp. 27–42. DOI: `https://doi.org/10.1007/s00158-003-0362-z`.

[83] B.K. Stanford and P.D. Dunning. “Optimal topology of aircraft rib and spar structures under aeroelastic loads”. In: *Journal of Aircraft* 52.4 (2015), pp. 1298–1311. DOI: `https://doi.org/10.2514/1.C032913`.

[84] J.P.A.A. Blasques. *User’s Manual for BECAS: A cross section analysis tool for anisotropic and inhomogeneous beam sections of arbitrary geometry.* Risø DTU - National Laboratory for Sustainable Energy, 2012.

[85] W. Yu, V.V. Volovoi, D.H. Hodges, and X. Hong. “Validation of the variational asymptotic beam sectional analysis”. In: *AIAA Journal* 40.10 (2002), pp. 2105–2112. DOI: `https://doi.org/10.2514/2.1545`.

[86] W. Yu, D.H. Hodges, and J.C. Ho. “Variational asymptotic beam sectional analysis - An updated version”. In: *International Journal of Engineering Science* 59 (2012), pp. 40–64. DOI: `https://doi.org/10.1016/j.ijengsci.2012.03.006`.

[87] Y. Luo, Q. Li, and S. Liu. “Topology optimization of shell–infill structures using an erosion-based interface identification method”. In: *Computer Methods in Applied Mechanics and Engineering* 355 (2019), pp. 94–112. DOI: `https://doi.org/10.1016/j.cma.2019.05.017`.

[88] A.M. Kuethe and J.D. Schetzer. *Foundations of Aerodynamics.* Wiley, 1950.

[89] B. Göthert. *Plane and Three-Dimensional Flow at High Subsonic Speeds. (Extension of the Prandtl Rule).* Technical memorandum 1105. National Advisory Commitee for Aeronautics, 1946.

[90] U. Kuettler and W.A. Wall. "Fixed-point fluid-structure interaction solvers with dynamic relaxation". In: *Computational Mechanics* 43.1 (2008), pp. 61–72. DOI: `https://doi.org/10.1007/s00466-008-0255-5`.

[91] I.H. Abbott and A.E. von Doenhoff. *Theory of Wing Sections.* Dover Publications, 1959.

[92] P.W. Christensen and A. Klarbring. *An Introduction to Structural Optimization.* Vol. 153. Solid Mechanics and Its Applications, 2008. DOI: `https://doi.org/10.1007/978-1-4020-8666-3`.

[93] D.R. Bristow. *Development of Panel Methods for Subsonic Analysis and Design.* NASA Contractor Report CR-3234. National Aeronautics and Space Administration, 1980.

[94] R.L. Carmichael and L.L. Erickson. "PANAIR - A Higher Order Panel Method for Predicting Subsonic or Supersonic Linear Potential Flows about Arbitrary Configurations". In: *14th Fluid and Plasma Dynamics Conference.* American Institute of Aeronautics and Astronautics Inc., 1981. DOI: `https://doi.org/10.2514/6.1981-1255`.

[95] J.L. Hess. *An Improved Higher Order Panel Method for Three-Dimensional Lifting Potential Flow.* Technical Report NADC-79277-60. Naval Air Development Center, 1981.

Appendices

A Topology Optimization of Aircraft Wings

A method is presented here for solving topology optimization problems with a 1-way coupled panel and 3D continuum finite element method. The panel geometry is embedded within a 3D finite element mesh as shown in Figure A1a. Loads are transferred from the panel to nodes of the elements cut by the panel geometry. The load transfer scheme is shown in Figure A1b, where panels are triangulated by joining diagonal nodes. A polygon, $\mathcal{P}_i$, is defined by the intersection of the triangulated panels and the element, where multiple polygons may be defined for a single element. The load transfer, given in (A1), is a function of the surface area of $\mathcal{P}_i$, the panel's C_P value, and the normal vector of $\mathcal{P}_i$. The load is assumed to act at the center of $\mathcal{P}_i$ and is distributed to the finite element nodes using the interpolation functions.

$$\mathbf{f}_e = \mathbf{N}(\mathcal{P}_i)^{\mathrm{T}} q_\infty S_i C_{P,i} \boldsymbol{n}_i \tag{A1}$$

The topology optimization problem is parameterized using a *Solid Isotropic Material with Penalization* (SIMP) method. The SIMP method is an interpolation scheme used for topology optimization of elasticity problems where the Young's modulus of element e, is given by

$$E_e = \underline{E} + (\bar{E} - \underline{E})\rho_e^p \tag{A2}$$

where ρ_e is a the *density* of element e with bounds between 0 and 1, $\bar{E}$ is the Young's modulus of a solid element ($\rho_e = 1$), $\underline{E}$ is the Young's modulus of the void element ($\rho_e = 0$), and p is a penalization parameter used to penalize intermediate ρ-values.

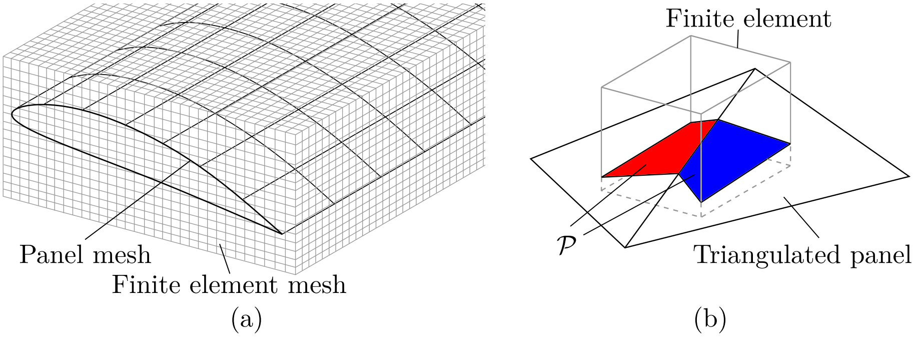

(a)

(b)

Figure A1: (a) discretization for the panel-continuum finite element problem, and (b) load transfer scheme.

The intersection of the panel and element can be use to determine which elements are inside and outside the wing. Design variables are defined such that external elements are void and internal elements are defined by ρ_e. The skin is defined to be solid using the method presented in [87], where a wall thickness is prescribed such that it is between 2 and 3 elements at any point on the airfoil.

The optimization problem is defined in (A3), where the objective is to minimize the sum of compliance over a range of angles of attack and the design is subject to a volume constraint of 12%. This is the same problem formulation used in Section 4.3 with the beam model and in topology optimization studies in [80].

$$\begin{aligned} \min_{\mathbf{d}\,\in\,\mathbb{R}^{N_d}} \quad & : f = \sum_{\alpha_\infty} C_{\alpha_\infty}(\mathbf{d}, \mathbf{u}) \\ \text{subject to} \quad & : V(\mathbf{d}) - \bar{V} \leq 0 \\ & \quad \underline{d} \leq d_e \leq \bar{d} \qquad\qquad \text{for} \quad e = 1, ..., N_d \end{aligned} \tag{A3}$$

Results are shown in Figure A2 for a rectangular wing of aspect ratio 7 that is meshed with over 7 million finite elements inside the wing and solved with angles of attack, $\alpha_\infty = \{0°, 3°, 5°\}$. The design has multiple spar-like structures spreading out from the quarter chord point near the root. There is also a thickened skin towards the root, and multiple smaller truss-like structures towards the tip. Comparing to topology optimized designs in [80], both designs consist of large plate-like structures and smaller truss-like structures. A typical wingbox has not been created in the current design, and the curved wall spars presented in [80] have not formed. This is likely due to the differences in discretization and wing geometry, where the current rectangular wing is bending-dominated with low torsional loads because there is no sweep or camber. However, the current results do demonstrate that optimized designs are quite far from the rib-spar structures commonly used in aircraft today. The current results act as a proof of concept and will be further explored in future work.

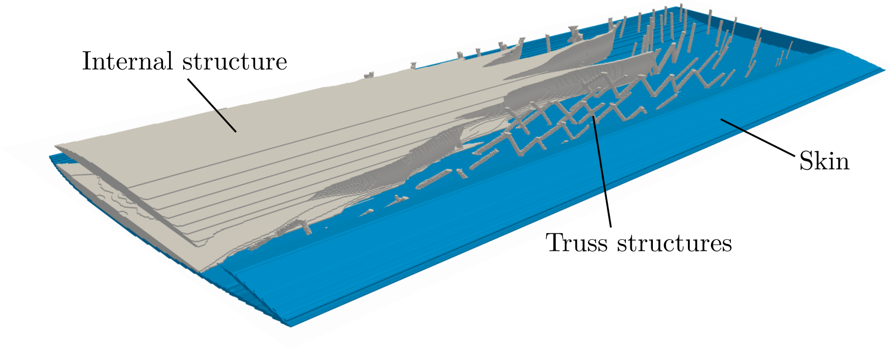
Internal structure
Skin
Truss structures

(a)

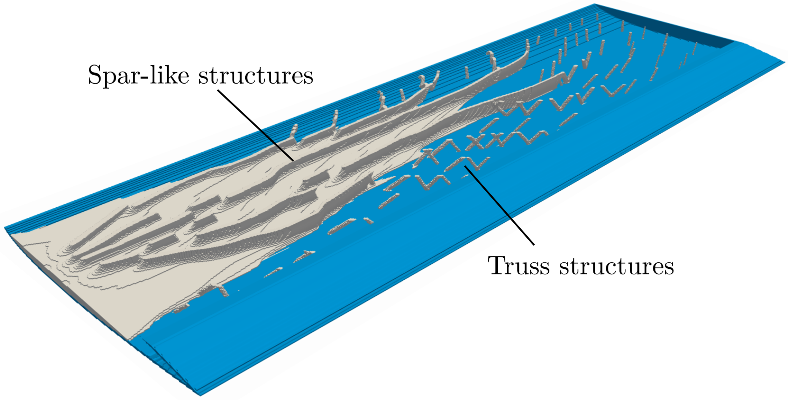
Spar-like structures
Truss structures

(b)

Figure A2: Topology optimization results for a rectangular wing: (a) top skin cut away, (b) top skin and upper flange structures cut away. Skin is colored in blue, and topology optimized structure in grey.

B Compressibility Correction

With minor edits, the panel method presented in 2.2 can be modified to account for compressibility effects, provided the flow is fully subsonic or supersonic. This is done through solving the Prandtl-Glauert equation [88, 72] defined as

$$\beta^2 \frac{\partial^2 \phi}{\partial x^2} + \frac{\partial^2 \phi}{\partial y^2} + \frac{\partial^2 \phi}{\partial z^2} = 0 \tag{B1}$$

assuming the freestream is in the x-direction. The scalar, β, is known as the Prandtl-Glauert factor and is defined as $\beta = \sqrt{|1 - M_\infty^2|}$ where M_∞ is the Mach number of the freestream. Note that if $M_\infty = 0$, then $\beta = 1$, and (B1) reduces to the Laplace equation given in (2.6). Göthert's extension [89, 72], takes advantage of this through a simple transformation, $\phi(x, y, z, M_\infty) \rightarrow \phi_0(x_0, y_0, z_0, 0)$, which corresponds to

$$\{\boldsymbol{x}_0, \boldsymbol{y}_0, \boldsymbol{z}_0\} = \{\boldsymbol{x}, \beta\boldsymbol{y}, \beta\boldsymbol{z}\} \quad , \quad \phi_0 = \beta^2 \phi \tag{B2}$$

The transformed coordinates are then used to solve the incompressible flow problem where ϕ_0 satisfies the Laplace equation in (2.6). The solution to (B1), ϕ, and physical properties in equations (2.19)-(2.23) are first calculated using transformed coordinates, yielding quantities denoted below with the subscript 0, and are then corrected using the following reverse transformations which are derived from (B2).

$$\begin{gathered} C_P = \frac{1}{\beta^2} C_{P,0} \quad , \quad L = \frac{1}{\beta^3} L_0 \quad , \quad D = \frac{1}{\beta^4} D_0 \\ C_L = \frac{1}{\beta^2} C_{L_0} \quad , \quad C_D = \frac{1}{\beta^3} C_{D_0} \end{gathered} \tag{B3}$$

C A Comparison of Coupling Methods

Solution methods for both fixed-point iterations and Newton methods are outlined in Algorithms 1 and 2, respectively. Both methods are initialized by zeroing the solution on the first design iteration, and by using the solution to the previous design iteration on each subsequent design step. Assuming that the change in design is small between iterations, initializing in this manner ensures $\mathbf{s}_0$ is close to the converged solution. The fixed-point iteration method involves solving both systems in sequence, where loads calculated in the panel method are applied to the FE problem. The panel method is then solved again with geometry deformed by the displacements calculated in the FE problem. The process continues back and forth until the norm of the change in state variables, $\mid \Delta \mathbf{s} \mid$, is below a given tolerance, ϵ. In the Newton method neither subproblem is solved, only the residual and Jacobian matrix (derivative of the residual with respect to state variables) are calculated. The Jacobian matrix is then used to calculate an update step in the state variables. Convergence is usually determined when the residual is less than the tolerance, ϵ, however for comparison purposes, here it is determined using the change state variables.

Figure C1 compares Newton and fixed-point iterations with respect to wall-clock time, for the same external wing geometry but with different wingbox geometries, where the cross sectional shape of the beam is scaled to vary the mass. As discussed in Section 2.4 the Newton method has a slower convergence with respect to wall-clock time because of the large expense associated with calculating the Jacobian matrix. For light-weight beams the compliance increases and the wing experiences large deformations. For these wings a small change in loading can create a large change in the deformations (and vice-versa). This makes the coupled problem difficult to converge and increases the wall-clock time. For very compliant wings (low mass) the coupled problem may diverge.

Algorithm 1: Fixed-Point

```
Result: $\mathbf{s}$
Initialize $\mathbf{s}_0$
$i = 0$
while $\mid \Delta s \mid > \epsilon$ do
    $i \leftarrow i + 1$
    $\boldsymbol{\mu} \leftarrow$ SolvePanel($\mathbf{d}$,$\mathbf{u}$)
    $\mathbf{u} \leftarrow$ SolveFE($\mathbf{d}$,$\boldsymbol{\mu}$)
    $\mathbf{s}_i \leftarrow \{\boldsymbol{\mu}, \mathbf{u}\}^{\mathrm{T}}$
    $\Delta \mathbf{s} \leftarrow \mathbf{s}_i - \mathbf{s}_{i-1}$
end
```

Algorithm 2: Newton

```
Result: $\mathbf{s}$
Initialize $\mathbf{s}_0$
$i \leftarrow i + 1$
while $\mid \Delta s \mid > \epsilon$ do
    $i \leftarrow i + 1$
    $\mathbf{R} \leftarrow$ CalcResidual($\mathbf{d}$,$\mathbf{s}$)
    $\frac{\partial \mathbf{R}}{\partial \mathbf{s}} \leftarrow$ CalcJacobian($\mathbf{d}$,$\mathbf{s}$)
    $\Delta \mathbf{s} \leftarrow \frac{\partial \mathbf{R}}{\partial \mathbf{s}}^{-1} \mathbf{R}$
    $\mathbf{s}_i \leftarrow \mathbf{s}_{i-1} + \Delta \mathbf{s}$
end
```

Algorithm C: Methods for solving 2-way coupled problems based on (1) fixed-point iterations and (2) Newton method.

When reducing weight, the onset of divergence happens sooner for fixed-point iterations as they are less stable. Damping or relaxation methods can be implemented to stabilize the coupled problem and improve convergence time of the fixed-point iterations [90]. However, as convergence time is reduced for stiff wings, relaxation may not be necessary when implemented with stress or tip deflection constraints.

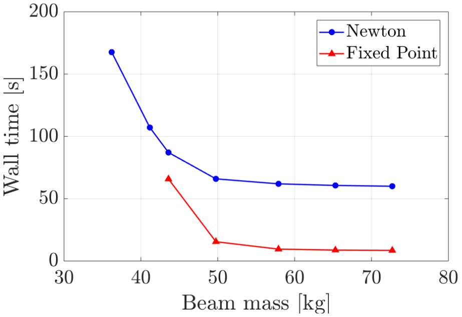

Figure C1: Coupled solution methods with wings of different stiffness.

D NACA Airfoil Parameterizations

There are several different NACA airfoil families of which most are described in detail in [91]. Parameterization methods in this thesis are based on NACA 4- and 5-digit airfoils which are summarized here. The parameterization is shown in Figure D1 and is defined using the following parameters: chord length, c, maximum thickness, t, maximum camber m, and position of maximum camber, p. NACA airfoil families consist of a set of airfoils formed from discrete values of the airfoil parameters. In our parameterization, the design space is smoothed such that the optimizer can select any value for these parameters from a continuous design space.

The airfoils are defined by the sum of a thickness and camber distribution. For NACA 4-digit profiles these distributions are defined (for a sharp TE) in the local coordinate system $(\bar{x}, \bar{z})$ as

$$\bar{z}_t = 5tc\left(0.2969\sqrt{\frac{\bar{x}}{c}} - 0.1260\frac{\bar{x}}{c} - 0.3516\left(\frac{\bar{x}}{c}\right)^2 + 0.2843\left(\frac{\bar{x}}{c}\right)^3 - 0.1036\left(\frac{\bar{x}}{c}\right)^4\right) \tag{D1}$$

$$\bar{z}_m = \begin{cases} \frac{mc}{p^2}\left(2p\frac{\bar{x}}{c} - \left(\frac{\bar{x}}{c}\right)^2\right), & \text{if } 0 \leq \frac{\bar{x}}{c} \leq p \\ \frac{mc}{(1-p)^2}\left(1 - 2p + 2p\frac{\bar{x}}{c} - \left(\frac{\bar{x}}{c}\right)^2\right), & \text{if } p \leq \frac{\bar{x}}{c} \leq 1 \end{cases} \tag{D2}$$

$$\begin{aligned} \bar{x}_{af} &= \bar{x} \mp \bar{z}_t \sin\theta \\ \bar{z}_{af} &= \bar{z}_m \pm \bar{z}_t \cos\theta \end{aligned} \tag{D3}$$

Thickness is traditionally defined perpendicular to the camber line where θ is the angle between the chord line and a tangent to the camber line at $\bar{x}$, i.e. $\theta = \tan^{-1}({}^{d\bar{z}_m}/_{d\bar{x}})$. However, using this definition, the derivatives ${}^{d\theta}/_{dp}$ and ${}^{d\theta}/_{dc}$ are discontinuous at the point $\frac{\bar{x}}{c} = p$ which may cause issues in the optimization. To avoid this we take the thickness to be perpendicular to the chord line ($\theta = 0°$, see Figure D1).

NACA 5-digit airfoils use the same thickness distribution in (D1), but with a different camber distribution that is defined to give either a non-reflexed or a

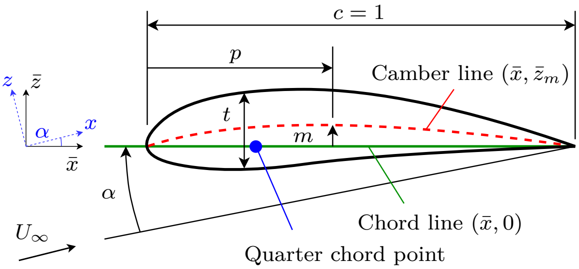

Figure D1: NACA airfoil definition with labeled parameters. Figure adapted from [P1].

reflexed airfoil. This thesis considers only the reflexed camber line defined as

$$\bar{z}_m = \begin{cases} \frac{k_1 c}{6}\left(\left(\frac{\bar{x}}{c} - r\right)^3 - \frac{k_2}{k_1}(1-r)^3 \frac{\bar{x}}{c} - r^3 \frac{\bar{x}}{c} + r^3\right), & \text{if } 0 \leq \frac{\bar{x}}{c} \leq r \\ \frac{k_1 c}{6}\left(\frac{k_2}{k_1}\left(\frac{\bar{x}}{c} - r\right)^3 - \frac{k_2}{k_1}(1-r)^3 \frac{\bar{x}}{c} - r^3 \frac{\bar{x}}{c} + r^3\right), & \text{if } r \leq \frac{\bar{x}}{c} \leq 1 \end{cases} \tag{D4}$$

where camber line coefficients depend on a specified theoretical optimal lift coefficient, which is taken as 0.3 throughout. This gives the camber line properties in Table D1, where either p or m needs to be prescribed.

Table D1: Camber line coefficients for reflexed NACA 5-digit profiles with a theoretical optimal lift coefficient of 0.3.

p	m	r	k_1	$\frac{k_2}{k_1}$
0.10	0.0164	0.130	51.990	0.000764
0.15	0.0208	0.217	15.793	0.00677
0.20	0.0240	0.318	6.520	0.0303
0.25	0.0273	0.441	3.191	0.1355

E B-Spline Airfoil Parameterization

The B-spline parameterization (shown in Figure E1) represents the airfoil coordinates, $\boldsymbol{X}$, using a B-spline of polynomial degree d and $n+1$ control points, $\mathbf{P}_i$, via

$$\boldsymbol{X}(k) = \sum_{i=0}^{n} N_{i,d}(k)\mathbf{P}_i \tag{E1}$$

where the degree of the curve must satisfy $1 \leq d \leq n$, and $N_{i,d}(k)$ are the basis functions which are defined recursively and in a non-decreasing sequence of scalars (known as knots), k_i, for $i = 0, 1, ..., n+d+1$ [92]. The Cox-de Boor recursion formula defines the basis functions.

$$N_{i,0}(k) = \begin{cases} 1 & \text{if } k_i \leq k < k_{i+1} \\ 0 & \text{otherwise} \end{cases} \qquad \text{where } 0 \leq i \leq n+d \tag{E2}$$

$$N_{i,j}(k) = \frac{k - k_i}{k_{i+j} - k_i} N_{i,j-1}(k) + \frac{k_{i+j+1} - k}{k_{i+j+1} - k_{i+1}} N_{i+1,j-1}(k) \qquad \text{where } 1 \leq j \leq d\ ;\ 0 \leq i \leq n+d-j \tag{E3}$$

In order to specify contact at the beginning of the spline (corresponding to the trailing edge) the first $d+1$ knots are equal to 0. Likewise, in order to specify contact at the end point (also corresponding to the trailing edge) the last $d+1$ knots are equal to 1. Note that this means the denominator of some terms in (E3) may become zero, in which case those terms are set to zero. All other knots are equally spaced.

If a specific airfoil is desired for the initial design, control points must be specified that correctly map to the desired airfoil of coordinates. These control points are found by solving a least squares problem defined as

$$\min_{\mathbf{P}} \sum_{j=1}^{2} \left\| \left[\sum_{i=0}^{n} N_{i,d}(k)\mathbf{P}_{ij} \right] - \boldsymbol{X}_j \right\|^2 \tag{E4}$$

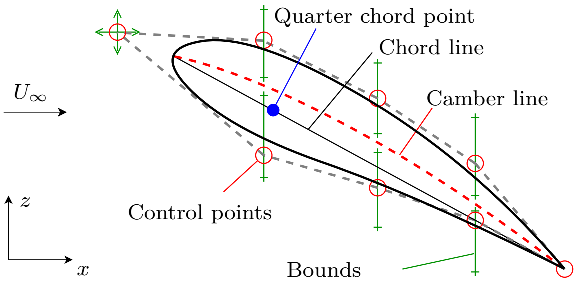

Figure E1: B-spline airfoil parameterization. Figure adapted from [P1].

where the parameterization constraints in Figure 3.6b are satisfied.

For optimization problems, geometry constraints are enforced on parameters such as the curvature. The curvature at any point on the B-spline can be calculated as

$$\kappa = \frac{x'z'' - z'x''}{\left[(x')^2 + (z')^2\right]^{\frac{3}{2}}} \tag{E5}$$

where x and z are the airfoil coordinates, i.e. $\boldsymbol{X} = \{\boldsymbol{x}, \boldsymbol{z}\}$, and the primes represent first and second derivatives of the coordinates. The derivative of a B-spline can also be represented as a B-spline with one less control point and a reduced order, i.e. the first derivative, $\mathbf{Q}_i$ has an order $d-1$ and n control points, and the second derivative, $\mathbf{R}_i$, has an order $d-2$ and $n-1$ control points.

$$\begin{aligned} \boldsymbol{X}' &= \sum_{i=0}^{n-1} N_{i,d-1}(k)\mathbf{Q}_i \\ \boldsymbol{X}'' &= \sum_{i=0}^{n-2} N_{i,d-2}(k)\mathbf{R}_i \end{aligned} \tag{E6}$$

where

$$\begin{aligned} \mathbf{Q}_i &= \frac{d}{k_{i+d+1} - k_{i+1}}\left(\mathbf{P}_{i+1} - \mathbf{P}_i\right) \\ \mathbf{R}_i &= \frac{d-1}{k_{i+d} - k_{i+1}}\left(\mathbf{Q}_{i+1} - \mathbf{Q}_i\right) \end{aligned} \tag{E7}$$

F Higher Order Panel Methods

Section 3.2.2 has demonstrated that optimization algorithms can take advantage of numerical errors in pressure distributions to reduce the objective function but create designs with a non-physical performance. This was overcome by calculating induced drag through far-field calculations within a Trefftz plane. However, there are a number of limitations in using Trefftz plane calculations, such as the assumption of steady-state flow. By introducing high order panels the accuracy of pressure distributions is increased through reducing the numerical error [2]. An example of this is shown in Figure F1 where a 2D panel method is used to achieve the C_P distribution around a NACA 1412 airfoil (shown in Figure F1a) using both constant-strength and linearly-varying strength panels. There are noticeable differences in the C_P distribution at every x location. These differences reduce for most x locations as the panel discretization increases, however some errors remain, mainly at the leading and trailing edge. Here, the problem was solved with a coarse mesh of 50 panels so that the error is clearly visible from the plot alone. The detail in Figure F1b shows the trailing edge of the C_P distribution, where for constant-strength panels the the upper and lower surfaces intersect and do not fully converge at $\frac{x}{c} = 1$. This is due to numerical errors in the solution and is not present in the linear-strength panels which have a smooth distribution at the trailing edge.

High order panel methods have been implemented in the past [93, 94, 95, 70], but have not been applied to gradient-based optimization problems. The important point here is whether implementing high order panel methods can reduce numerical errors to such an extent where gradients from pressure distributions can be used to create viable optimized designs. If so, the applicability of panel methods to optimization problems will be extended as they are not limited to the assumptions of the Trefftz plane calculations.

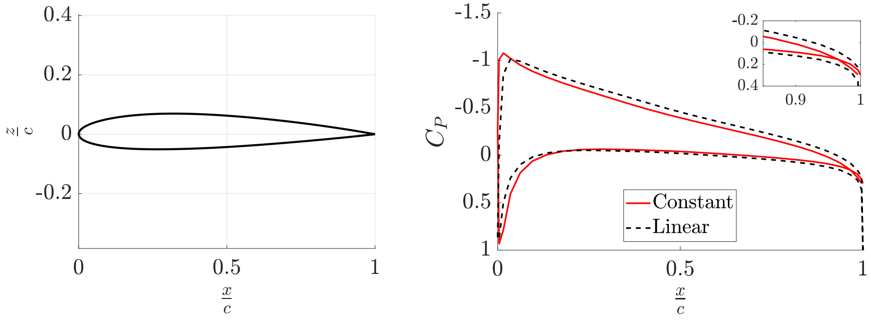

(a) (b)

Figure F1: Comparison of pressure distributions for constant- and linearly-varying strength panels: (a) NACA 1412 airfoil, and (b) C_P distributions.

Part 2. Publications

Publication [P1]

Cian Conlan-Smith, Néstor Ramos-García, Ole Sigmund, and Casper Schousboe Andreasen. “Aerodynamic Shape Optimization of Aircraft Wings Using Panel Methods”. In: *AIAA Journal* 58.9 (2020), pp. 3765–3776. DOI: `https://doi.org/10.2514/1.J058979`

P1

On Aerodynamic Shape Optimization of Aircraft Wings using Panel Methods

Cian Conlan-Smith [*], Néstor Ramos-García [†], Ole Sigmund [‡] and Casper Schousboe Andreasen [§]
Technical University of Denmark, DK-2800 Lyngby, Denmark.

Panel methods are frequently applied to aerodynamic shape optimization problems due to their fast turnaround time and ability to model arbitrary geometries. Despite being advantageous for design optimization, we have found that panel methods can predict non-physical results for unconventional geometries. This work presents robust methods to solve optimization problems using panel methods that are not susceptible to numerical errors. Important factors are highlighted with regard to choice in boundary conditions, induced drag calculation, wake modeling, and regularization. Two parameterization methods are introduced where wing geometry is defined locally by airfoils at discrete span-wise positions and regularized by filtering along the span. Such methods of defining the geometry locally, enlarge the design space and allow the optimizer to converge to reliable designs. Results also suggest that: enforcing a Dirichlet boundary condition rather than a Neumann formulation provides significant cost savings in gradient calculations; far-field force calculations should be adopted for optimization problems as numerical errors in surface pressure integration have a strong influence on the gradients; and the additional design freedom of a B-spline parameterization can be disadvantageous as the low-fidelity of the inviscid model cannot correctly capture aerodynamic properties of irregular airfoil geometries.

Nomenclature

$\boldsymbol{A}$ = doublet aerodynamic influence coefficient
$\boldsymbol{B}$ = source aerodynamic influence coefficient
b = wingspan
c = chordlength
D = total drag
$\boldsymbol{F}$ = total force

---

[*] PhD student, Department of Mechanical Engineering, Section of Solid Mechanics, cicosm@mek.dtu.dk. Member AIAA.
[†] Senior Researcher, Department of Wind Energy, Section of Fluid Mechanics.
[‡] Professor, Department of Mechanical Engineering, Section of Solid Mechanics.
[§] Associate Professor, Department of Mechanical Engineering, Section of Solid Mechanics.

f = generic function

L = total Lift

M_∞ = free-stream Mach number

M_r = root bending moment

M_p = pitching moment

m = maximum relative camber

$\boldsymbol{n}$ = normal vector

$\boldsymbol{P}$ = coordinates of control points

p = relative position of maximum camber

R = filter radius

S = wing planform area

t = maximum relative thickness

U = total velocity

$\boldsymbol{X}$ = coordinates

α = twist

β = $\sqrt{1 - M_\infty^2}$, transformation factor

$\boldsymbol{\delta}$ = design variables

η = $\frac{2y}{b}$, normalized span location

κ = curvature

λ = Lagrange multiplier

μ = doublet strength

ϕ = potential function

ρ = density

σ = source strength

Æ = $\frac{b^2}{S}$, aspect ratio

C_P = pressure coefficient

$\mathcal{F}$ = generic function in Lagrangian form

$\boldsymbol{\mathcal{W}}$ = filter matrix

Subscripts

D = associated with Dirichlet boundary condition

N = associated with Neumann boundary condition

ref = associated with reference case

TP = calculated via Trefftz plane integration

C_P = calculated via C_P integration

∞ = associated with free-stream

I. Introduction

Panel methods were developed in the 1960s and 70s within the aviation industry for evaluating the performance of preliminary aircraft designs [1–3]. Based on potential flow theory these methods provide the velocity field and pressure distribution around arbitrary geometries. As boundary element methods, panel methods only require a surface mesh of the geometry, leading to a fast computational time when compared to computational fluid dynamics (CFD) based on finite volume and finite element methods, which require a volume mesh of the entire fluid domain. This makes panel methods attractive for aerodynamic optimization where a solution to the physics problem is required for each design iteration. Additionally, as only a surface mesh is used, it is easier to avoid mesh distortion or remeshing, which is common in shape optimization with CFD.

In the 1970s researchers began to investigate the design of airfoils through numerical optimization. In a series of works by Hicks et al. [4–6] airfoils were parametrized using high order polynomials or Joukowski transformations. Venkataraman [7] introduced the idea of using splines to parametrize the airfoil where two Bézier curves were used to define upper and lower surfaces, and have since been used to define thickness and camber distributions [8, 9]. Basis splines (B-splines) were later adopted for similar parameterization methods [10–12] as they are less susceptible to bumps or fluctuations because the order of the curve is not defined by the number of points. Consequently, B-splines have shown to achieve better off-design performance when compared to Bézier curves [13–15]. B-spline representations have since become the most popular parametrization method for airfoil optimization [16–18]. However in recent times, parameterizing using free-form deformation (FFD) techniques has also gained much popularity [19, 20].

The first automated design processes for 3D wings using panel methods involved solving inverse problems [21, 22] where the wing geometry is achieved such that it produces a user specified pressure distribution. However, it can be difficult to specify a target pressure distribution that creates the desired or optimal performance. By the end of the 1990s CFD methods had already started to be applied to more general 3D aerodynamic [23, 24] and multidisciplinary optimization (MDO) problems [25]. The growing interest in optimization studies saw the need for fast calculations of aerodynamic loads, where panel methods are effective. Choi et al. [26, 27] created a framework for multi-fidelity optimization with the ability to solve the Euler equations and linearized potential flow problems via a panel method (PanAir [28]). Similar gradient-free studies also implementing PanAir were conducted by Alonso et al. [29], and Rahnarayan et al. [30] who implemented PanAir as the high-fidelity method and an area rule method as a low-fidelity method. Kennedy and Martins demonstrated a parallel framework for aero-elastic MDO using a panel method (TriPan) and finite element (FE) solver [31, 32]. TriPan has been applied to a number of subsequent aero-structural optimization problems such as the design of composite wings [33], wing-box topology optimization [34, 35], matrix-free optimization [36], and unsteady problems [37, 38]. Goetzendorf-Grabowski and Mieloszyk [39, 40] present another coupled panel-FE framework for MDO based on the open-source PANUKL code.

The aim of this work is to firstly highlight the main considerations and challenges in using panels methods in optimization problems, and secondly to introduce novel parametrization methods for aerodynamic optimization problems that allow large changes in geometry. Despite there being interest in panel methods for optimization problems the literature lacks detailed comparisons and discussions of their application. Approached from an optimization perspective, external Neumann and internal Dirichlet boundary conditions are compared in their performance with respect to computational time, ability to predict solutions, and applicability to optimization problems. Challenges have been found in applying these methods to optimization problems with regard to choice of wake model and force calculation, especially when the parameterization methods allow large changes in the geometry. Traditionally, wing optimization problems have been parameterized using global variables such as a taper ratio and predefined airfoils. Using such global variables to define the geometry restricts the design space which can lead to sub-optimal designs. We introduce free-form parameterization approaches where airfoil sections are defined locally and design variables are filtered along the span for regularization and avoidance of numerical artifacts.

The current work uses a subsonic constant source-doublet panel method based on MIRAS [41]. An introduction to the panel method is detailed in Section II covering the problem formulation, wake modeling and aerodynamic force calculations. Section III describes the mesh discretization and two parameterization methods which are later compared. The optimization approach is detailed in Section IV, including the formulation of the optimization problem, regularization, and sensitivity analysis. The results section (Section V) discusses the choice of boundary condition, wake model, and force calculation method with respect to their performance and applicability to optimization problems. Optimization results are also presented for two parameterization methods and compared for their performance and ability to predict realistic designs. Finally, the findings are concluded in Section VI. Additionally, the appendix includes verification studies with comparisons to lifting-line theory, VSAERO panel code, and SU2 finite volume method.

II. Panel Method

In this work we implement a combined source and doublet panel method with a Prantl-Glauert compressibility correction [42, 43]. We shortly repeat the basic theory here to provide a basis for later discussions and comparisons. A typical panel method discretization is shown in Fig. 1 with collation points defined at the center of each panel. Both Neumann and Dirichlet boundary conditions are considered and are based on a zero internal perturbation formulation

[44, 45]. The governing equations are defined as

$$\mathbf{A}_N\boldsymbol{\mu} + (\mathbf{B}_N + \mathbf{I})\boldsymbol{\sigma} = \mathbf{0} \tag{1a}$$

$$\mathbf{A}_D\boldsymbol{\mu} + \mathbf{B}_D\boldsymbol{\sigma} = \mathbf{0} \tag{1b}$$

where **A** and **B** are aerodynamic influence coefficients (AIC) for doublet and source distributions respectively. Subscripts N and D represent AIC for Neumann and Dirichlet boundary conditions, i.e. the influence on the velocity or potential function at a collocation point. Influence coefficients are derived using the methods outlined in [46], Section 10.4. It is important to note that each panel will influence every other point in the domain, meaning that **A** and **B** are dense matrices. For a zero internal perturbation formulation the source strengths, $\boldsymbol{\sigma}$, are calculated using via

$$\sigma_i = \boldsymbol{U}_\infty \cdot \boldsymbol{n}_i \tag{2}$$

and equation (1) is used to solve for doublet strengths, $\boldsymbol{\mu}$.

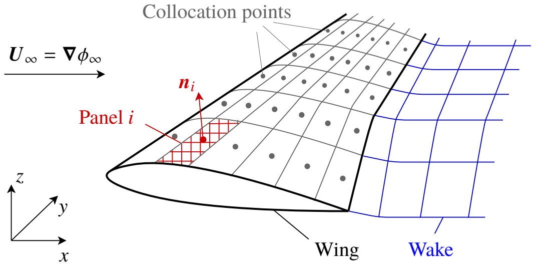

Fig. 1 Schematic of a wing and its wake discretized into quadrilateral panels.

As shown in Fig. 1 the wing's wake is also meshed which is required to satisfy the Kutta condition and calculate the induced drag. Two wake models are compared in this work, the first is a fixed wake consisting of a vortex sheet projected in the free-stream direction. This model is computationally efficient because of a low number of panels and governing equations are only solved once. However, the method may become inaccurate for wing geometries that create a large variance in the structure of the wake. An alternative is a force-free wake model [41, 47, 48] which is an iterative procedure that is able to capture complicated wake geometries, but requires (1) to be solved on each iteration leading to a large computational expense.

Once the singularity distribution is known, the velocity at each panel's collocation point can be calculated as the gradient of the potential function in local coordinates (l,m,n).

$$\boldsymbol{U}_i = (U_l, U_m, U_n)_i^T = \left(\frac{\partial \phi}{\partial l}, \frac{\partial \phi}{\partial m}, \frac{\partial \phi}{\partial n} \right)_i^T \tag{3}$$

The pressure coefficient, C_P, is calculated via the Bernoulli equation (4), and can be integrated over the body surface to find the total force, $\boldsymbol{F}$, pitching moment, M_p, and root bending moment, M_r.

$$C_{P,i} = 1 - \frac{\|\boldsymbol{U}_i\|^2}{\|\boldsymbol{U}_\infty\|^2} \tag{4}$$

$$\boldsymbol{F} = \frac{1}{2}\rho_\infty {U_\infty}^2 \int_S C_P \boldsymbol{n} dS \simeq \frac{1}{2}\rho_\infty {U_\infty}^2 \sum_{i=1}^{N_S} C_{P,i} S_i \boldsymbol{n}_i \tag{5}$$

$$M_p = \frac{1}{2}\rho_\infty {U_\infty}^2 \int_S C_P \left\{ \begin{smallmatrix} z \\ x \end{smallmatrix} \right\}^{\mathrm{T}} \left\{ \begin{smallmatrix} n_x \\ n_z \end{smallmatrix} \right\} dS \simeq \frac{1}{2}\rho_\infty {U_\infty}^2 \sum_{i=1}^{N_S} C_{P,i} S_i \left\{ \begin{smallmatrix} z \\ x \end{smallmatrix} \right\}_i^{\mathrm{T}} \left\{ \begin{smallmatrix} n_x \\ n_z \end{smallmatrix} \right\}_i \tag{6}$$

$$M_r = \frac{1}{2}\rho_\infty {U_\infty}^2 \left\| \int_S C_P y \left\{ \begin{smallmatrix} n_x \\ n_z \end{smallmatrix} \right\} dS \right\| \simeq \frac{1}{2}\rho_\infty {U_\infty}^2 \left\| \sum_{i=1}^{N_S} C_{P,i} S_i y_i \left\{ \begin{smallmatrix} n_x \\ n_z \end{smallmatrix} \right\}_i \right\| \tag{7}$$

where x_i, y_i, and z_i are coordinates of panel i's collocation point (with the origin at the root). Lift and induced drag are defined by projecting $\boldsymbol{F}$ perpendicular and parallel to the free-stream direction, which in our case is always in the x-direction

$$L_{C_P} = \boldsymbol{F} \cdot \mathbf{z} \tag{8}$$

$$D_{C_P} = \boldsymbol{F} \cdot \mathbf{x} \tag{9}$$

where D_{C_P} and L_{C_P} are the forces calculated via C_P-integration. Alternatively, the forces can be calculated through far-field calculations using a Trefftz plane integration method, L_{TP} and D_{TP} [43, 49]. This reduces lift and drag calculations to a 2D integral over the intersection of the wake and the Trefftz plane, s_w (refer to Fig. 2).

$$L_{TP} = \rho_\infty V_\infty \int_{s_w} \Delta\phi dy \simeq \rho_\infty V_\infty \sum_{i=1}^{N_w} \mu_i s_i \cos(\theta_i) \tag{10}$$

$$D_{TP} = -\frac{1}{2}\rho_\infty \int_{s_w} \Delta\phi \frac{\partial \phi}{\partial n} ds_w \simeq -\frac{1}{2}\rho_\infty \sum_{i=1}^{N_w} \mu_i s_i \boldsymbol{u}_i . \boldsymbol{n}_i \tag{11}$$

where $\Delta\phi$ is the potential jump over s_w, θ_i is the inclination of wake panel i in the Trefftz plane, $\boldsymbol{n}$ is normal to s_w in the Trefftz plane.

Induced drag is the only type of drag considered in this work. Aerodynamic loads can be normalized to find

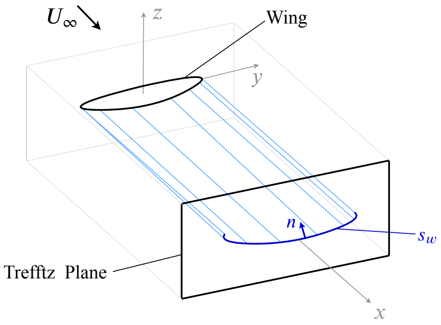

Fig. 2 Schematic of the Trefftz plane integration method.

coefficients of lift and drag.

$$C_L = \frac{L}{{}^1\!/\!_2 \rho_\infty {U_\infty}^2 S} \tag{12}$$

$$C_D = \frac{D}{{}^1\!/\!_2 \rho_\infty {U_\infty}^2 S} \tag{13}$$

If the Prandtl-Glauert correction is used, the quantities in equations (4)-(13) are first calculated using coordinates from Göthert's transformation [43, 50], yielding quantities denoted with the subscript $_0$ below, and are then corrected using the Prandtl-Glauert factor, $\beta = \sqrt{1 - {M_\infty}^2}$.

$$C_P = \frac{1}{\beta^2} C_{P,0} \quad , \quad L = \frac{1}{\beta^3} L_0 \quad , \quad D = \frac{1}{\beta^4} D_0 \quad , \quad C_L = \frac{1}{\beta^2} C_{L_0} \quad , \quad C_D = \frac{1}{\beta^3} C_{D_0} \tag{14}$$

III. Discretization and Parametrization

The wing geometry is discretized into quadrilateral panels where nodal points are typically defined to be equally-spaced in the span-wise direction, and in a cosine distribution in the chord-wise direction creating a bias towards leading and trailing edges. This bias allows more detail in the C_P distributions making the C_p-integration less prone to numerical error. The location of nodes in the x- and z-directions are given by airfoil geometries defined at N_s span-wise locations each with N_{af} nodes. Airfoil sections are defined in one of two ways – using the definition of NACA airfoils, and B-spline representations. Half the span is modeled, without a fuselage, and symmetry is enforced by modifying influence coefficients to include an influence from the wing's mirror image about the root. Unless otherwise stated a mesh of 6000 (40 span-wise, 150 chord-wise) panels was used for a single wing.

When using quadrilateral panels it is not guaranteed that the four nodes will lie in the same plane, as it takes only three points to define a plane. The panel is instead defined using an average plane as described in [51]. The end sections of the wing are also meshed creating an enclosed geometry. When implementing a panel method the problem is ill-defined for an enclosed mesh that separates internal and external domains with doublet panels [52]. There are multiple ways around this such as defining an additional source panel with some known potential in the internal domain, or only specifying source panels (i.e. non-lifting panels) in certain locations. We have adopted the latter where the wing's end-caps consist of source only panels.

A. NACA parameterization

This parameterization is based on the polynomial equations for defining NACA 4- and 5-digit airfoils [53], where 4 parameters are used (refer to Fig. 3): chord length c, maximum thickness t, maximum camber m, and position of maximum camber p. However, note that NACA 5-digit airfoils do not require both m and p to be defined, and the ideal lift coefficient (first coefficient) is specified. The NACA 4- and 5-digit airfoil family consists of a set of airfoils formed from discrete values of these parameters. Our parameterization differs in that the design space is smoothed such that the optimizer can select any value for these parameters from a continuous design space. Additionally, thickness is traditionally defined perpendicular to the camber line, however, using this definition, the derivatives are discontinuous at the point of maximum camber which may cause issues in the optimization. To avoid this we take the thickness to be perpendicular to the chord line (see Fig. 3). The twist, α, is included as an additional variable, giving the NACA parameterization a possible 5 design variables per airfoil section. The wing coordinates, $\boldsymbol{X}$, are achieved by rotating airfoil coordinates, $(\bar{x}, \bar{z})$, through α and assembling airfoil sections with their quarter chord point on the y-axis.

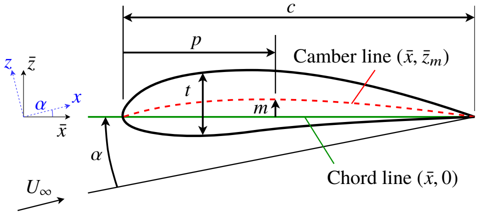

Fig. 3 Design variables used in the NACA parameterization: c = chord length, t = maximum thickness, m = maximum camber, p = position of maximum camber, and α = twist.

B. B-spline parameterization

Here the wing coordinates, $\boldsymbol{X}$, are given by a series of airfoils represented as B-spline curves with control points $\mathbf{P}$ (definitions of B-splines are presented in [54]). In our B-spline parameterization, represented in Fig. 4, the relative spacings between control points in the x-direction are kept constant, where all control points scale in the x-direction about the trailing edge, which is controlled by a single design variable per section. Control points are then free to move vertically independent of one another as controlled by one design variable per control point. The spline is clamped so that it starts and ends at the first and last control point which are coincident. The wing is assembled from each airfoil section with a common axis at the quarter chord point. Bounds are imposed on each degree of freedom in the z-direction such that the spline does not self-intersect. If a control point approaches one of these bounds and the other control point at the same x-coordinate is not nearby (i.e. the airfoil is not collapsing), then the bound is updated to enlarge the range. When the bounds are defined or updated they are specified at a small distance from the camber line of the design on the current iteration.

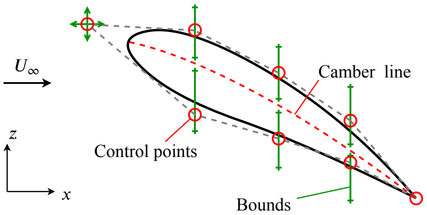

Fig. 4 B-spline airfoil parametrization with control points (red circles), their degrees of freedom/bounds (green), and camber line (dashed red) shown.

IV. Optimization approach

A. Physical considerations when optimizing lifting surfaces

Typically optimization problems will be posed using absolute quantities, such as L and D, rather than non-dimensional quantities, such as C_L and C_D, as they are generally more stable for the optimization problem. For example, consider a minimum constraint on C_L. The value of C_L can be continually increased by shrinking the planform area (refer to (12)) where a minimum bound on S is required to prevent the problem being ill-posed. Oppositely, for a minimum constraint on L there should exist an optimum design where the constraint is active and the area of the wing has not reduced to a non-physical size. The most important constraint is the minimum bound on L, as induced drag is dependent on lift, there will be no induced drag for $L = 0$ which is a trivial optimal solution.

B. Span-wise regularization

Regularization is necessary to prevent clustering of nodes and drastic variations in geometry which may be non-physical, non-manufacturable, or cause numerical issues [55, 56]. Design variables are applied at a discrete set of airfoil sections with a single panel between sections. A large variation in geometry between sections cannot be accurately represented by a single panel and leads to non-physical results which the optimizer is able to exploit. Filtering is used to control the variation between sections where the filter size can act as a feature control parameter.

Design variables are filtered based on the span-wise positions of neighboring sections. A filter radius, R, is defined such that a neighboring section, j, will have a weight proportional to its span-wise distance if the distance between sections is less than R, and carry no weight if the distance is greater than R. This is similar to a density filter commonly adopted in topology optimization [57]. Weights are stored within the filter matrix, $\boldsymbol{\mathcal{W}}$, the independent design variables are contained within $\boldsymbol{\delta}$, and the filtered or physical design variables, $\tilde{\boldsymbol{\delta}}$, are defined as

$$\tilde{\boldsymbol{\delta}} = \boldsymbol{\mathcal{W}}\boldsymbol{\delta} \tag{15}$$

where

$$\mathcal{W}_{ij} = \frac{1}{\sum\limits_{k=1}^{N_s} w_{ik}} w_{ij} \quad \text{where} \quad w_{ij} = \max[0, R - d_{ij}] \tag{16}$$

For the NACA parameterization design variables are defined as $\boldsymbol{\delta} = \{\boldsymbol{c}, \boldsymbol{t}, \boldsymbol{m}, \boldsymbol{p}, \boldsymbol{\alpha}\}$ where each airfoil parameter is filtered along the span. For the B-spline parameterization the design variables are the coordinates of the B-spline control points, $\boldsymbol{\delta} = \mathbf{P}$. The coordinates of control points i (where $i = 1, ..., n+1$ for each airfoil section, j) are filtered along the span using the same method as the NACA parameterizations.

C. Airfoil regularization

As the flow is inviscid the method is unable to predict flow separation. The optimizer is able to exploit this deficiency through creating sharp edges or bumped surfaces which reduce the objective function but lead to unrealistic pressure distributions. To prevent this, a constraint on the maximum curvature is used. For the NACA parameterization the maximum curvature is always at the leading edge of the airfoil. Curvature is related to radius by $\kappa = {}^1\!/_r$, where the leading edge radius for any NACA airfoil is approximated as

$$r_{\text{LE}} = 1.1019 t^2 c \tag{17}$$

We wish to constrain the normalized maximum curvature, $\hat{\kappa}$, that is the maximum curvature of the airfoil whose coordinates are scaled between 0 and 1 in the x-direction, yielding

$$\hat{\kappa}_j = \frac{1}{1.1019 {t_j}^2} \tag{18}$$

For the B-spline parameterization curvature is first calculated at each node, i, on the spline.

$$\kappa_i = \frac{x_i' z_i'' - z_i' x_i''}{\left[(x_i')^2 + (z_i')^2\right]^{\frac{3}{2}}} \tag{19}$$

The maximum curvature is then approximated by aggregating $\boldsymbol{\kappa}$ using a p-norm function and similar to the NACA parameterizations is normalized by c_j to give $\hat{\kappa}_j$ for airfoil section j

$$\hat{\kappa}_j = c_j \left[\sum_{i=1}^{N_{af}} \kappa_i{}^{\zeta} \right]^{\frac{1}{\zeta}} \tag{20}$$

where ζ is taken to be equal to 10 throughout.

D. Sensitivity Analysis

The method of moving asymptotes (MMA) [58] is used as the optimizer which requires sensitivities to determine how design variables should change between iterations of the optimization procedure. Here, an adjoint method is used for calculating sensitivities. The objective or constraint function of interest, f, can be expressed in augmented Lagrangian form as

$$\mathcal{F} = f + \boldsymbol{\lambda}^T \mathbf{R} \tag{21}$$

where $\boldsymbol{\lambda}$ is the Lagrange multiplier, and $\mathbf{R}$ is the residual to the state equation given in (1a) and (1b) for Neumann and Dirichlet BCs respectively. Note that $\boldsymbol{\lambda}$ is arbitrary as $\mathbf{R} = \mathbf{0}$, thus $\mathcal{F} = f$ for any $\boldsymbol{\lambda}$. To conduct shape optimization we require the sensitivities of $\mathcal{F}$ with respect to the nodal coordinates, $\boldsymbol{X}$. Differentiating (21) with respect to nodal coordinates and expanding using the chain rule yields

$$\frac{d\mathcal{F}}{d\boldsymbol{X}} = \frac{\partial f}{\partial \boldsymbol{X}} + \frac{\partial f}{\partial \boldsymbol{\mu}} \frac{d\boldsymbol{\mu}}{d\boldsymbol{X}} + \boldsymbol{\lambda}^T \left[\frac{\partial \mathbf{R}}{\partial \boldsymbol{X}} + \frac{\partial \mathbf{R}}{\partial \boldsymbol{\mu}} \frac{d\boldsymbol{\mu}}{d\boldsymbol{X}} \right] \tag{22}$$

Note the difference between partial, $^{\partial}/_{\partial x}$ and total, $^{d}/_{dx}$ derivative operators, where partial derivatives capture only the explicit dependence without resolving the state equation, whereas total derivatives capture implicit dependencies also. Implicit dependencies are difficult to calculate and as such we seek a value of $\boldsymbol{\lambda}$ which causes all total derivatives to vanish. Equation (22) can be re-expressed as

$$\frac{d\mathcal{F}}{d\boldsymbol{X}} = \frac{\partial f}{\partial \boldsymbol{X}} + \boldsymbol{\lambda}^T \frac{\partial \mathbf{R}}{\partial \boldsymbol{X}} + \left[\frac{\partial f}{\partial \boldsymbol{\mu}} + \boldsymbol{\lambda}^T \frac{\partial \mathbf{R}}{\partial \boldsymbol{\mu}} \right] \frac{d\boldsymbol{\mu}}{d\boldsymbol{X}} \tag{23}$$

By setting terms in the square brackets in (23) equal to zero and solving for $\boldsymbol{\lambda}$ the implicit derivatives are eliminated. This corresponds to solving the adjoint problem.

$$\boldsymbol{\lambda}^T = -\frac{\partial f}{\partial \boldsymbol{\mu}} \left[\frac{\partial \mathbf{R}}{\partial \boldsymbol{\mu}} \right]^{-1} = -\frac{\partial f}{\partial \boldsymbol{\mu}} \mathbf{A}^{-1} \tag{24}$$

and thus it follows that

$$\frac{d\mathcal{F}}{d\boldsymbol{X}} = \frac{\partial f}{\partial \boldsymbol{X}} + \boldsymbol{\lambda}^T \frac{\partial \mathbf{R}}{\partial \boldsymbol{X}} \tag{25}$$

Differentiating the state equation in (1a) or (1b) with respect to the nodal coordinates yields the residual derivatives

$$\frac{\partial \mathbf{R}}{\partial \boldsymbol{X}} = \frac{\partial \mathbf{A}_N}{\partial \boldsymbol{X}}\boldsymbol{\mu} + \frac{\partial \mathbf{B}_N}{\partial \boldsymbol{X}}\boldsymbol{\sigma} + \mathbf{B}_N \frac{\partial \boldsymbol{\sigma}}{\partial \boldsymbol{X}} + \frac{\partial \boldsymbol{\sigma}}{\partial \boldsymbol{X}} \tag{26a}$$

$$\frac{\partial \mathbf{R}}{\partial \boldsymbol{X}} = \frac{\partial \mathbf{A}_D}{\partial \boldsymbol{X}}\boldsymbol{\mu} + \frac{\partial \mathbf{B}_D}{\partial \boldsymbol{X}}\boldsymbol{\sigma} + \mathbf{B}_D \frac{\partial \boldsymbol{\sigma}}{\partial \boldsymbol{X}} \tag{26b}$$

where suffixes (a) and (b) are for Neumann and Dirichlet BCs respectively. Up to now sensitivities are calculated with respect to Göthert's transformed coordinates, $\boldsymbol{X}_0$. Using the chain rule sensitivities are transformed back to the real coordinates, then subsequently to physical design variables, $\tilde{\boldsymbol{\delta}}$, and finally independent design variables, $\boldsymbol{\delta}$, as defined by the parametrization method in Section III.

$$\frac{d\mathcal{F}}{d\boldsymbol{\delta}} = \frac{d\mathcal{F}}{d\boldsymbol{X}_0}\frac{d\boldsymbol{X}_0}{d\boldsymbol{X}}\frac{d\boldsymbol{X}}{d\tilde{\boldsymbol{\delta}}}\frac{d\tilde{\boldsymbol{\delta}}}{d\boldsymbol{\delta}} = \frac{d\mathcal{F}}{d\boldsymbol{X}_0}\begin{bmatrix} \mathbf{I} & \mathbf{0} & \mathbf{0} \\ \mathbf{0} & \frac{1}{\beta}\mathbf{I} & \mathbf{0} \\ \mathbf{0} & \mathbf{0} & \frac{1}{\beta}\mathbf{I} \end{bmatrix}\frac{d\boldsymbol{X}}{d\tilde{\boldsymbol{\delta}}}\boldsymbol{\mathcal{W}} \tag{27}$$

where $\frac{d\mathcal{F}}{d\boldsymbol{X}_0}$ is calculated using (25), $\frac{d\boldsymbol{X}}{d\tilde{\boldsymbol{\delta}}}$ is the derivative of parameterization method defined in Section III, and $\boldsymbol{\mathcal{W}}$ is the filter matrix defined in (16).

V. Results

For the following optimization studies we define a reference wing with a rectangular planform, aspect ratio, Æ = 6 (b = 6 m and c = 1 m) and constant NACA0012 airfoils throughout the span. The performance characteristics of this wing are shown in Fig. 5. Optimized designs are compared to this wing's performance at Mach 0.4 with an angle of attack of 6°, induced drag, $D_{\text{ref}} = 915.6$ N and total lift, $L_{\text{ref}} = 34525.4$ N. The properties of this wing also give the bounds for constraint functions in all optimization problems.

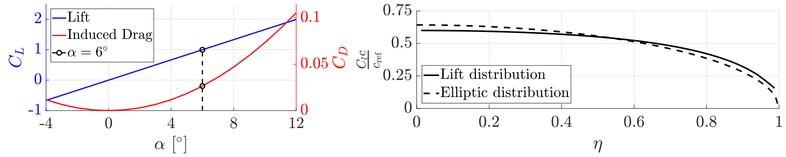

(a) **(b)**

Fig. 5 Performance characteristics of the reference wing: (a) lift and induced drag coefficients for varying angles of attack, α, and (b) normalized sectional lift area distribution along the half span for $\alpha = 6°$.

All optimization problems are defined as to minimize the induced drag. Another important concept for these problems is the elliptic lift distribution. From lifting line theory it is known that for planar wings the least induced drag is produced when there is an elliptic lift distribution along the span [43, 46]. Hence the optimal solution should have an elliptic lift distribution which helps validate our optimized results. From Fig. 5b we see that the reference wing's lift distribution has large differences to the elliptic distribution which indicate non-optimality.

A. Choice of methods

1. Boundary conditions

For the same mesh size the Dirichlet BC is approximately twice as computationally efficient as the Neumann BC [46]. This is apparent in the formulation of the influence coefficients, $\mathbf{A}_N$, $\mathbf{B}_N$ and $\mathbf{A}_D$, $\mathbf{B}_D$, where the Neumann BC requires the calculation of a vector (velocity in each direction) and the Dirichlet BC only requires a scalar (potential). As these are dense systems of equations, assembling the influence coefficient matrices is the most expensive part of the panel method accounting for roughly 80% of the computational effort. When adjoint sensitivities are calculated (through methods discussed in section IV.D) 90% of the computational effort is spent on calculating sensitivities. Solutions are dependent on each point in the domain meaning that every panel in the mesh is dependent on the nodal coordinates of every other panel. Assuming quadrilateral panels, each entry of the dense matrices $\mathbf{A}$ and $\mathbf{B}$, will depend on 8 nodal points, 4 per panel (trailing edge panels have more dependencies due to the Kutta condition). This is why the sensitivity analysis dominates the computational time. Gradients are also calculated in half the time when using a Dirichlet BC compared to the Neumann BC due to the nature of their formulation. This leads to a substantial reduction in the computational effort required for the Dirichlet problem compared to the Neumann. Note that the influence between any two panels and their corresponding dependence on nodal points is independent of any other influence between any two panels. This means that assembly of the influence coefficients and their derivatives is easily implemented in parallel.

We also demonstrate the effect that the choice of boundary condition has on optimized designs. Consider a fixed span wing with constant NACA0012 airfoils throughout the span. The objective is to minimize the induced drag (calculated via Trefftz plane integration) subject to a lift constraint where each airfoil section has a twist variable. The problem is defined in (28) and results are shown in Fig. 6.

$$
\begin{aligned}
\min_{\boldsymbol{\alpha}\,\in\,\mathbb{R}^{N_s}} \quad & : D_{TP}(\boldsymbol{\alpha}) \\
\text{subject to} \quad & : L_{\text{ref}} - L_{TP}(\boldsymbol{\alpha}) \leq 0 \\
& \quad \underline{\alpha} \leq \alpha_i \leq \bar{\alpha} \quad \text{for } \; i = 1, \ldots, N_S
\end{aligned}
\tag{28}
$$

As shown in Fig. 6, Neumann and Dirichlet boundary conditions produce the same designs with a reduction in induced drag of 1.4%. The design responses are a close match to the elliptic lift distribution shown in Fig. 6b. The results of this study show that both formulations create similar optimized designs, irrespective of the choice of boundary condition. Due to the computational benefits a Dirichlet BC is used for all subsequent studies. However, it is important to note that Dirichlet BC is formulated from an internal and external domain and thus requires the geometry to have a finite thickness. This means that only the Neumann BC is applicable in cases where the geometry is thin or represented

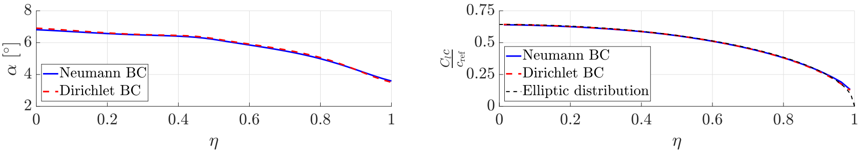

(a) **(b)**

Fig. 6 Twist Optimization results: (a) twist and (b) lift distributions along the half-span of optimized designs.

by a sheet, e.g. sails, kites, etc.

2. Force calculations

Section II introduced two ways of calculating forces on the wing – C_P and Trefftz plane integration. Both methods are appropriate for calculating the induced drag of standard or well defined wing geometries, however, results generated from C_P-integration have shown to be sensitive to the number of panels and the complexity of the wing geometry [49, 59]. The discrepancy in C_P-integration is due to cancellation errors which are of a similar magnitude to the induced drag [43]. This makes C_P-integration unreliable but it is still commonly adopted with an appropriate mesh to produce accurate results. We have found that larger differences in these methods can occur when applied to optimization problems. As an example consider the optimization problem to minimize induced drag at a fixed angle of attack of 6°, subject to a lift constraint where each section is defined by NACA0012 airfoils and has a chord length design variable. Optimized designs are shown in Fig. 7 where forces are calculated using C_P and Trefftz plane integration.

$$\begin{aligned} \min_{\boldsymbol{c}\,\in\,\mathbb{R}^{N_S}} \quad & : D(\boldsymbol{c}) \\ \text{subject to} \quad & : L_{\text{ref}} - L(\boldsymbol{c}) \leq 0 \\ & \quad \underline{c} \leq c_i \leq \bar{c} \quad \text{for } i = 1, \dots, N_S \end{aligned} \tag{29}$$

Design	D_{C_P}/D_{ref}	D_{TP}/D_{ref}
Reference	1.004	1.000
min D_{C_P}	0.980	1.005
min D_{TP}	0.998	0.986

Table 1 Drag for wings shown in Fig. 7 calculated via C_P and Trefftz plane integration, and normalized by the drag of the reference case (calculate via Trefftz plane integration).

When using C_P-integration the design is pushed towards an unconventional geometry with a large chord at the tips. Conversely, when using Trefftz plane integration the design converges to a near elliptic wing which is known to be

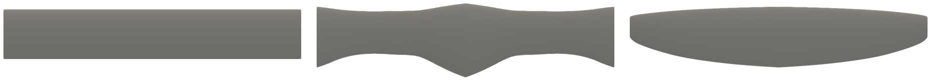

(a) Initial design/reference **(b)** min D_{C_P} **(c)** min D_{TP}

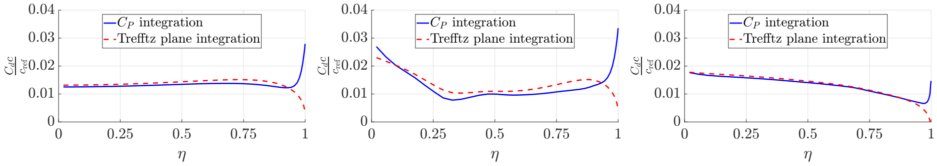

(d) Initial design/reference **(e)** min D_{C_P} **(f)** min D_{TP}

Fig. 7 Wing planforms and normalized sectional drag area distributions for initial and optimized designs with drag calculated from C_P and Trefftz plane integration.

the optimal design for this problem. Results from C_p-integration tend to have numerical errors at the tip where the loads increase drastically, whereas the loads from Trefftz plane integration tend to zero towards the tip (refer to Figs. 7d-7f). These unrealistic results can have large sensitivities that drive the optimizer to create unconventional designs that exploit the numerical error in order to decrease the objective function (refer to Table 1). Lift calculations are not as susceptible to these numerical errors as the magnitude of the error is generally much smaller than the lift. However, a dependence on the inviscid pressure distribution can still produce undesirable results for optimization problems. As the flow is inviscid, phenomena such as separation can not be predicted by the model, which can lead to non-physical C_P distributions and an over prediction of the surface pressure. The above study suggests that C_P-integration is not suitable for optimization where large variations in geometry is permitted. In using a Trefftz plane method there is less numerical error and the optimization problem is more robust.

3. Wake model

Let us consider the optimization problem where the angle of attack is fixed at 6° and the only variables are the chord length at each section. We seek to maximize the Oswald span efficiency factor, e (minimize negative e) subject to a minimum bound on lift. According to lifting line theory, an optimal wing for this problem will have an efficiency factor of 1 which is the upper bound for planar wings. Planforms of optimized wings for various filter radii are shown in Fig. 8.

$$\begin{aligned} \min_{\boldsymbol{c}\,\in\,\mathbb{R}^{N_S}} \quad & : -e = -\frac{C_L(\boldsymbol{c})^2}{\pi C_D(\boldsymbol{c}) AR(\boldsymbol{c})} \\ \text{subject to} \quad & : L_{\text{ref}} - L(\boldsymbol{c}) \leq 0 \\ & \quad \underline{c} \leq c_i \leq \bar{c} \quad \text{for} \ \ i = 1, \ldots, N_S \end{aligned} \tag{30}$$

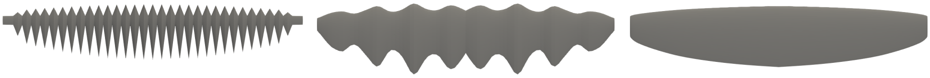

(a) $R = 0$ (b) $R = \frac{b}{12}$ (c) $R = \frac{b}{6}$

Fig. 8 Planform of optimization results for the problem defined in (30) **with various filter radii.**

With a small filter radius more detailed features (numerical artifacts) can be created in the optimized designs. This allows the optimizer to create a fluctuating chord distribution along the span yielding wavy planform geometries (Fig. 8a and 8b). As a free-stream wake is used, the wake takes the same shape as the trailing edge of the wing projected parallel to the free-stream. The wavy structure of the wake can then create a localized upwash, reducing the drag at certain locations along the wing. The optimized designs (calculated using a free-stream wake model) in Fig. 8b and 8c have span efficiency factors of 1.03 and 1.00 respectively. Post-analyzing the same designs using a force-free wake model (introduced in Section II, method presented in [41]) the span efficiencies are 0.83 and 0.98 respectively i.e. there is a large error of 24% for the wavy design (Fig. 8b) and 2% error for the elliptic design (Fig. 8c). The higher-fidelity force-free wake model captures the actual geometry of the wavy design's wake which levels out in the middle of the wake, removing the wavy-structure and subsequent upwash (see Fig. 9a and 9c). For the optimized design in Fig. 8a the force-free wake model does not converge as the wake self intersects and the calculations blow up. This study shows that realistic designs can be created using the lower-fidelity free-stream wake model provided sufficient regularization is used. The study also predicts that less regularization would be required with a force-free wake model but span-wise filtering is still needed to ensure robustness. As mentioned previously, the force-free wake model comes with a larger computational cost, therefore, only the free-stream wake model is used for optimization problems.

Filter radius, R	e, Free-Stream Wake	e, Force-Free Wake
0	1.18	-
$\frac{b}{12}$	1.03	0.83
$\frac{b}{6}$	1.00	0.98

Table 2 Span efficiency factors for wings optimized with different filter radii. Wings are optimized with a free-stream wake model and post-analyzed designs with a force-free wake model.

B. Optimization of fixed-span wings

We will optimize the design for reducing drag under cruise conditions, where a desirable property is to have zero pitching moment, and as such we have enforced a constraint that $M_p = 0$. From the previous discussions, we have seen that chord and twist can be used to achieve optimized designs with a similar performance. The previous designs have adopted large twist angles in order to satisfy the lift constraint. In practice large twist is generally avoided as it can lead to stall at higher angles of attack. Instead, camber is used to produce the desired lift with small values of twist.

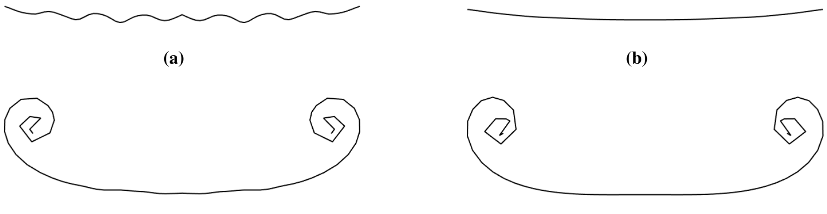

(a)

(b)

(c)

(d)

Fig. 9 Wake geometry in the Trefftz plane with (a) free-stream wake models for designs in (a) Fig. 8b and (b) Fig. 8c; and force-free wake models for designs in (c) Fig. 8b, and (d) Fig. 8c.

The following studies include maximum bounds on twist angles but allow cambered airfoils. The design is solved with parametrization methods based on NACA 5 and B-splines airfoils. The NACA 5 parameterization is used rather than a NACA 4 because it is capable of creating a reflex camber line. This allows the airfoil sections to produce both positive and negative pitching moments without creating negative twist. The NACA 4 parameterization can only produce negative pitching moments with a negative twist and thus cannot satisfy both lift and pitching moment constraints. The design problem is defined in (31) which includes the aforementioned constraints and those discussed in Section IV.

$$
\begin{array}{lll}
\underset{\boldsymbol{\delta}\,\in\,\mathbb{R}^{N_\delta}}{\min} & : \; D_{TP}(\boldsymbol{\delta}) & \\
\text{subject to} & : \; L_{\text{ref}} - L_{TP}(\boldsymbol{\delta}) \leq 0 & \\
 & \quad M_p(\boldsymbol{\delta}) = 0 & \\
 & \quad \boldsymbol{\alpha} - \alpha_{\max} \leq 0 & \text{for } \; i = 1, \ldots, N_S \\
 & \quad \hat{\boldsymbol{\kappa}} - \hat{\kappa}_{\max} = 0 & \text{for } \; i = 1, \ldots, N_S \\
 & \quad \underline{\delta} \leq \delta_i \leq \bar{\delta} & \text{for } \; i = 1, \ldots, N_\delta
\end{array}
\tag{31}
$$

Note that for the NACA 5 parametrization the constraint on twist, $\boldsymbol{\alpha}$ is instead satisfied implicitly by the upper bound on the design variables (last constraint in (31)).

We set the upper bound on twist to be equal to the angle of attack of the reference case. Results for NACA 5 and B-spline parameterizations are shown in Fig. 10 including half-span planforms with lower and upper surface C_P, sectional lift area distributions, C_P distributions at various η locations, and airfoil stacks. The NACA 5 design converges to a wing of aspect ratio 9.4 and taper ratio of 0.59. The high aspect ratio is expected, as the most effective way to reduce the induced drag is to increase Æ. The B-spline parameterization has converged to a wing of aspect ratio 7.6 and taper ratio of 0.54. The two designs have converged to similar planform geometries with an optimal elliptic lift distribution, and both produce a 1.48% reduction in total induced drag compared to the reference wing. A reflex camberline has been used in both cases to satisfy the pitching moment constraint and the designs produce similar C_P distributions. The B-spline design tends to have thicker airfoils, especially towards the tip. As the flow is inviscid the airfoil thickness has minimal effect on lift or drag but we suspect that thick airfoils would be avoided if viscous effects were considered.

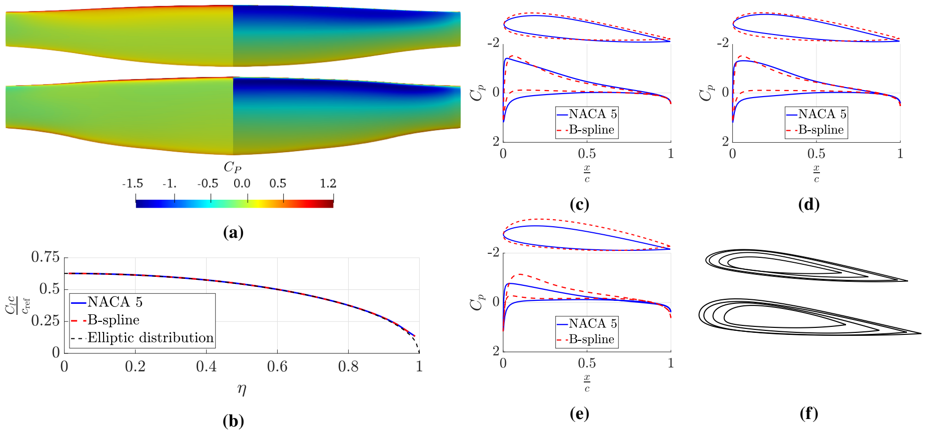

(a)

(b)

(c)

(d)

(e)

(f)

Fig. 10 (a) planforms with lower and upper surface C_P, for NACA 5 (top) and B-spline (below), (b) lift distributions, C_P distributions and airfoils at (c) η = 0.05, (d) η = 0.50, (e) η = 0.95, and (f) airfoil stacks with NACA-5 (top) and B-spline (below).

By taking a closer look at the individual airfoil sections we gain greater insight into the differences between the different parameterizations. Figure 11 shows the airfoil camber distributions for the NACA 5 and B-spline designs near the root, mid-section, and tip. There is a larger camber in the NACA 5 profiles and a reflex camberline is present throughout the wing. Less camber is used in B-spline profiles as there is greater freedom in the parameterization allowing the optimizer to create a reflex camberline without increasing the maximum camber. These lower cambered airfoils produce less lift. The reduction in lift (compared the the NACA 5 design) is compensated for by increasing the chord length which in-turn yields a lower aspect ratio wing. Both designs also reduce the camber from root to tip which helps achieve their elliptic lift distribution. The tip profiles of the B-spline design do not have a reflex camberline. Such airfoil sections are not possible in the NACA 5 parameterization which demonstrates the greater freedom of the B-spline parameterization.

The B-spline results presented here have shown to work well for this case. However, it took a large effort in order to get this parameterization to work efficiently. Ultimately, the B-spline parameterization has a lot more freedom to create unpredictable geometries, which can take advantage of the inviscid nature of the problem. This is because the design space is enlarged to include many possible airfoil sections that can produce the optimal span loading, thus the optimization problem is non-unique. Although it is not needed for the results presented here, we have found that these

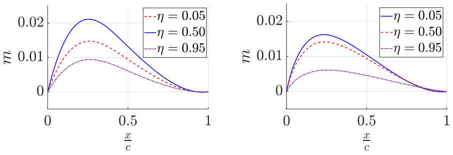

(a) **(b)**

Fig. 11 Camber distributions for airfoil sections at various η locations in the (a) NACA 5 and (b) B-spline designs

issues can be overcome by imposing additional curvature constraints or more restrictive variable bounds. However, as the motivation behind the B-spline parametrization was to enlarge the design space, it is somewhat counterproductive for it to be restricted through additional geometry constraints.

The extra freedom allowed by the B-spline parameterization method has not offered any advantage in performance over the NACA-5 parametrization. Additionally, the B-spline parameterization updates design variable bounds (as described in section III) throughout the optimization procedure in order to create a large design space whilst ensuring the spline does not self-intersect. Updating design variable bounds in this manner leads to slow convergence. Self-intersection cannot occur in the NACA parameterization methods which allows for a large design space without the need for bound updates and yields a faster convergence. Considering the increase in complexity of the problem and minimal gains in the wing's performance, the B-spline parameterization seems inappropriate for inviscid optimization problems as there is too much design freedom for the modeled physics. Accounting for viscous effects through a coupled viscous solver or finite volume methods may alleviate some of these issues experienced with the B-spline parameterization. However, this is outside the scope of this work.

C. Optimization of variable-span wings

Up to now we have considered wings with fixed wingspans. When it comes to induced drag minimization, the optimizer will always converge to the largest possible wingspan as this is the most effective way to reduce induced drag. Table 3 shows optimization results for the same problem defined in (31) with a NACA-5 parametrization and small perturbations to the span. The converged designs for each problem have negligible differences in their geometry, however the small changes to the wingspan has a significant effect on their induced drag. Altering the cross sections in the previous example made it possible to achieve a reduction in drag of 1.5% but as shown here if the span was 0.1 m shorter, the optimized design will create a drag force 1.9% higher than the reference wing. It is obvious from these results that the span has a large impact on the induced drag. This makes it difficult to improve or match the performance of the reference case with a wing of smaller span.

Wings with large wingspans are not always possible as an increased span leads to larger moments and stresses. A

Design	$^{D}/_{D_{\text{ref}}}$
Reference	1.000
$\min D$, $b = 6$ m	0.985
$\min D$, $b = 6.1$ m	0.953
$\min D$, $b = 5.9$ m	1.019

Table 3 Drag of optimized designs with perturbed wingspans, each are normalized with the drag of reference case.

structural model is not considered in this work but an important physical consideration is to impose an upper bound on the wing's root bending moment defined in (7). The optimization problem for the NACA-5 parametererization is defined as

$$\begin{aligned}
\min_{\boldsymbol{\delta} \in \mathbb{R}^{N_\delta}} \quad &: \; D_{TP}(\boldsymbol{\delta}) \\
\text{subject to} \quad &: \; L_{\text{ref}} - L(\boldsymbol{\delta}) \leq 0 \\
&\quad M_p(\boldsymbol{\delta}) = 0 \\
&\quad M_R(\boldsymbol{\delta}) - M_{R,\max} \leq 0 \\
&\quad \boldsymbol{\alpha} - \alpha_{\max} \leq 0 \qquad \text{for } \; i = 1, \ldots, N_S \\
&\quad \hat{\boldsymbol{\kappa}} - \hat{\kappa}_{\max} = 0 \qquad \text{for } \; i = 1, \ldots, N_S \\
&\quad \underline{\delta} \leq \delta_i \leq \bar{\delta} \qquad \text{for } \; i = 1, \ldots, N_\delta
\end{aligned} \tag{32}$$

where $\boldsymbol{\delta}$ contains an additional variable, b, controlling the wingspan. The maximum bound on root bending moment, $M_{R,\max}$, is defined as the root bending moment for the reference case. Results are shown in Fig. 12 for maximum bounds on span of 6 m, 7 m, and 8 m.

As expected, all designs have converged to the largest possible span. The design with $b_{\max} = 6$ m converges close to what we have seen previously without the bending moment constraint (Fig. 10). Designs with larger values of $b_{\max}$ have a similar planform near the root but the chord is reduced significantly towards the tip, such that the portion of the wing for $y > 3$ m has a minimal contribution to the root bending moment. The bending moment constraint is active for each of the three designs but the constraint has a greater impact on the design for larger a span. This is also demonstrated by studying the airfoil sections and corresponding C_P distributions where the $b_{\max} = 6$ m design is similar to the original design and large differences arise when a larger wingspan is permitted. The small airfoil sections towards the tip will in-turn lead to increased stresses and larger deformations towards the tip. This demonstrates the difficulty in producing structurally practical designs without structural coupling. When the root bending moment constraint is applied, the optimized design for a planar wing has a non-elliptic bell-shaped lifting distribution, as can be seen from Fig. 12b. These lift distributions are similar to the optimal bending moment constrained designs presented in [43], Chapter 5.10. The optimizer used a combination of increasing the outer taper and reducing twist towards the tip in order to create

P1

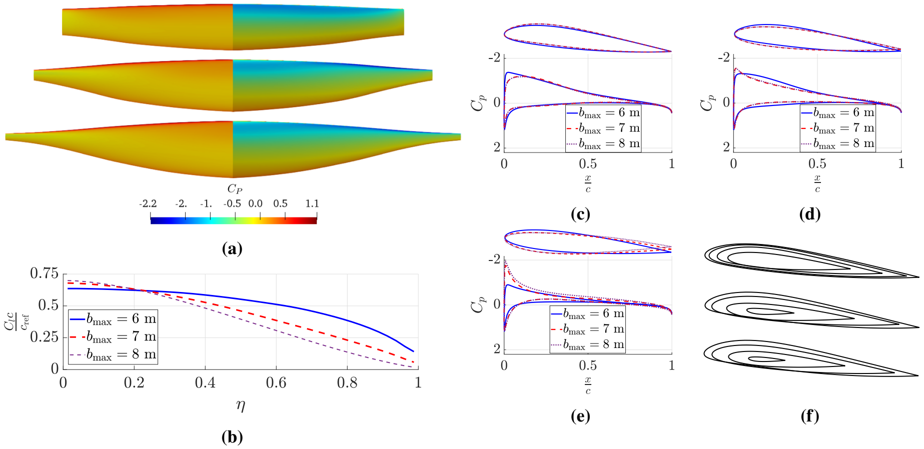

(a) (b) (c) (d) (e) (f)

Fig. 12 (a) lower and upper surface C_P planforms with $b_{\max} = 6$ m (above), $b_{\max} = 7$ m (center) and $b_{\max} = 8$ m (below), (b) lift distributions, C_P distributions and airfoils at (c) $\eta = 0.05$, (d) $\eta = 0.50$, (e) $\eta = 0.95$, and (f) airfoil stacks with $b_{\max} = 6$ m (above), $b_{\max} = 7$ m (center) and $b_{\max} = 8$ m (below).

these bell-shaped lift distributions.

Table 4 shows the total induced drag for designs optimized with and without the bending moment constraint. The converged designs are heavily effected by enforcing the constraint on M_R as the drag increases drastically. However, the constrained designs are still able to provide better solutions by increasing the span. This shows the importance of structural considerations in the shape optimization of the wing.

Design	$^{D}/_{D_{\text{ref}}}$ no M_R constraint	$^{D}/_{D_{\text{ref}}}$ M_R constrained
Reference	1.000	1.000
$b_{\max} = 6$ m	0.985	0.985
$b_{\max} = 7$ m	0.724	0.793
$b_{\max} = 8$ m	0.555	0.783

Table 4 Induced drag normalized by the drag of the reference case for designs with different maximum bounds on wingspan, with and without a constraint on root bending moment, M_R.

VI. Conclusion

Approaches to aerodynamic shape optimization of aircraft wings using panel methods have been introduced and compared by their ability to produce optimized designs. This work has found some important issues in the use of panel methods for solving optimization problems. For example, an internal Dirichlet boundary condition (BC) has been shown to be beneficial over an external Neumann BC as it leads to substantial cost savings for sensitivity analysis which dominates the computational effort. We have also found that calculating forces from C_p-integration is susceptible to large numerical errors that the optimizer is able to exploit in order to decrease the objective function through non-physical results. This finding suggests that C_p-integration is not suitable for induced drag calculations in optimization problems when the parameterization can allow large changes in geometry. Additionally, two methods of local parameterization are introduced, one based on the definitions of NACA 4- and 5-digit profiles, and the other using a B-spline representation, where design variables are filtered along the span to regularize the geometry. We have shown that span-wise regularization is required to prevent the optimizer from exploiting numerical weaknesses in the panel method. Both parametrization methods have proven to work well and produce similar values of the objective function, however a B-spline approach offers more design freedom than necessary for the available physics and hence requires more regularization to ensure robustness. Based on our findings we also conclude that the major challenge in using panel methods for aerodynamic optimization is to ensure that results remain physical and the optimizer is not taking advantage of the inviscid nature of the model. On this note it is expected that less regularization would be required with a model that can capture viscous effects. Finally we have demonstrated the difficulty in achieving structurally practical designs through structural considerations in the aerodynamic shape optimization problem. Future work will seek to extend the methods presented here to include a coupled structural model.

Appendix

A. Verification Studies

1. Lifting-line theory comparison

From lifting-line theory one can derive the following expression for the coefficient of induced drag for an elliptic wing [42, 46]

$$C_D = \frac{C_L^2}{\pi Æ} \tag{33}$$

where Æ is the wing's aspect ratio. Additionally, the coefficient of lift can be approximated as

$$C_L = C_{l_\alpha}\left(\frac{Æ}{Æ+2}\right)\alpha \tag{34}$$

where C_{l_α} is the slope of the 2D lift coefficient curve from thin airfoil theory, and is approximately equal to 2π [46]. Using these expressions we compare the results of our panel method to lifting line theory for an elliptic wing with $Æ = 5$ and comprising of symmetric airfoils.

Results from all analysis methods have a strong correlation with the lifting line theory for predicting lift at a given angle of attack. When integrating the pressure distribution with a Dirichlet boundary condition (BC) or using a Trefftz

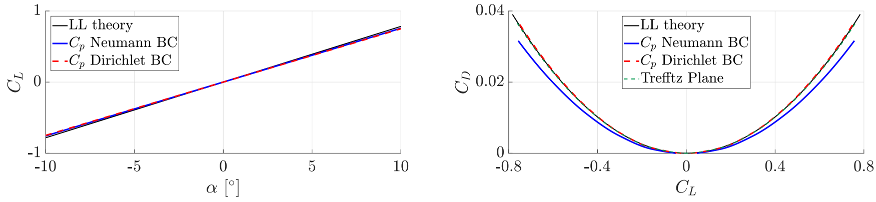

(a) **(b)**

Fig. 13 Comparison between lifting-line (LL) theory and results of the panel method for an elliptic wing. Results are compared for Neumann and Dirichlet boundary conditions with C_P integration and a Trefftz plane integration method.

plane method there is also a strong correlation in predicting the induced drag. However integrating the pressure distribution with a Neumann BC the results begin to deviate from lifting line theory for high lift. Note that the Trefftz plane integration method can be used with either BC with negligible differences between the two.

2. VSAERO comparison

We also compare our results with those achieved using VSAERO for three wing planforms. VSAERO calculates subsonic aerodynamic characteristics via a low-order constant source-doublet panel method [51], similar to the method implemented here. VSAERO results are achieved with a Dirichlet boundary condition and internal stagnation formulation. The first case is an unswept rectangular wing with an aspect ratio, Æ = 5.9. The second case is a swept wing with Æ = 5.6, no taper, and a sweep of 20°. Cases 1 and 2 comprise of NACA0012 airfoils. The third case has a sweep of 45°, taper ratio of 0.5, aspect ratio of 3, and NACA64A010 airfoils. Experimental and VSAERO results are taken from [60]. Figure 14 compares these results to Neumann and Dirichlet boundary conditions.

Fig. 14a and 14b shows the local C_l distribution with normalized semi-span, $\eta = {}^{2y}/_{b}$ where b is the wingspan. We see negligible differences in C_l between VSAERO, Neumann and Dirichlet results, and some minor deviations compared to experimental results at the root and tip. The current work uses more panels than those presented in [60] (VSAERO) allowing our results to capture more detail around the wing tip ($\eta = 1$). In Fig. 14c the current work also matches VSAERO solutions but all numerical results diverge from the experimental as the viscous effects are excluded. There are however only small differences in the local C_P distributions as demonstrated in Fig. 14d.

3. SU2 comparison

Finally we compare the panel method to results generated using SU2 [61] which is used to solve the inviscid Euler equations via a finite volume method. For this study we look at the ONERA M6 wing, which was designed in 1972 as a test case for complex flow phenomena such as transonic shocks and separated flow. Fig. 15 shows C_P distributions for an angle of attack of 5° and Mach numbers of 0.4 and 0.8.

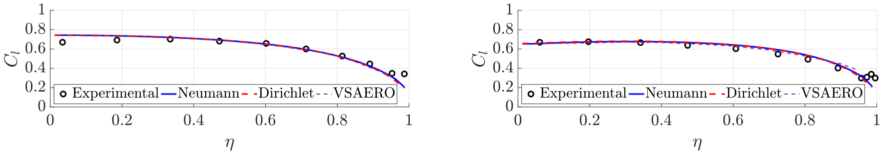

(a) Half-span lift distribution for case 1 at $\alpha = 8°$

(b) Half-span lift distribution for case 2 at $\alpha = 8°$

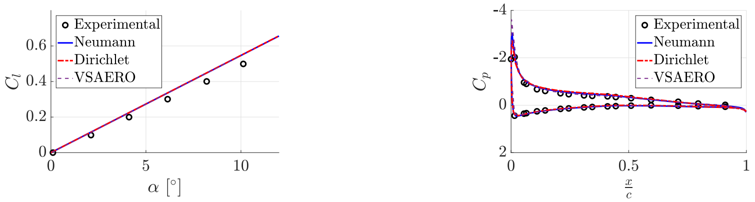

(c) Lift vs. angle of attack for case 3

(d) C_P distribution at $y/b = 0.55$ for case 3 at $\alpha = 8.23°$

Fig. 14 Comparison between experimental, VSAERO, Neumann and Dirichlet BC results for various wing cases.

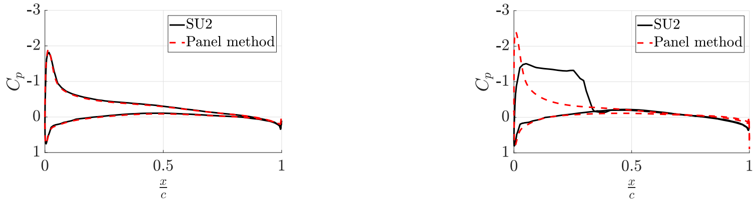

(a)

(b)

Fig. 15 Comparison between C_P distributions at $\eta = 0.5$ achieved from SU2 and panel method (current work) for the ONERA M6 wing at (a) Mach 0.4 and (b) Mach 0.8 with an angle of attack of 5°.

From Fig. 15 we see a good agreement between results when the flow is subsonic and a large deviation in results for transonic flows. This deviation is due to a shockwave which forms on the upper surface that the panel method is unable to predict. The inability to model shocks is one of the limitations of panel methods, however it is not an issue in this work as we are only concerned with cases where the flow is fully subsonic.

The main advantage of panel methods is their fast computational time. Table 5 compares computational times for our panel method and SU2 with single and multi-gird (3 levels) solvers using a single core. In each case the ONERA M6 wing is meshed with typical mesh sizes of 6,000 panels and roughly 500,000 finite volume elements. For the SU2 simulations the flow was converged five orders of magnitude in the density residual. The superiority of panel methods with respect to computational time can be clearly seen from these results.

	Panel (current)	SU2	SU2 multi-grid (3 levels)
Iterations	1	265	112
Time (s)	28.6	1255.4	1037.1

Table 5 Timing comparison for current panel method and SU2.

Funding Sources

The authors would like to thank the Villum Foundation for their financial support as part of the InnoTop VILLUM investigator project.

References

[1] Hess, J. L., and Smith, A. M. O., "Calculation of Potential Flow about Arbitrary Bodies," *Progress in Aerospace Sciences*, Vol. 8, 1967, pp. 1–138. doi:https://doi.org/10.1016/0376-0421(67)90003-6.

[2] Woodward, F. A., "Analysis and Design of Wing-Body Combinations at Subsonic and Supersonic Speeds," *Journal of Aircraft*, Vol. 5, No. 6, 1968, pp. 528–534. doi:https://doi.org/10.2514/3.43979.

[3] Hess, J. L., *Calculation of Potential Flow about Arbitrary Three-Dimensional Lifting Bodies*, Technical Report MDC J5679/01, Department of the Navy, 1972.

[4] Hicks, R. M., Murman, E. M., and Vanderplaats, G. N., *An Assessment of Airfoil Design by Numerical Optimization*, Technical memorandum X-3092, National Aeronautics and Space Administration, 1974.

[5] Hicks, R. M., and Vanderplaats, G. N., "Application of Numerical Optimization to the Design of Supercritical Airfoils without Drag-Creep," *SAE Technical Paper 770440*, 1977. doi:https://doi.org/10.4271/770440.

[6] Hicks, R. M., and Szelazel, C. A., *Airfoil Design by Numerical Optimization using a Minicomputer*, Technical memorandum 78502, National Aeronautics and Space Administration, 1978.

[7] Venkataraman, P., "A new procedure for airfoil definition," *Proc. 13th Applied Aerodynamics Conference*, American Institute of Aeronautics and Astronautics Inc., 1995. doi:https://doi.org/10.2514/6.1995-1875.

[8] Rogalsky, T., Derksen, R. W., and Kocabiyik, S., "Differential Evolution in Aerodynamic Optimization," *Canadian Aeronautics and Space Journal*, Vol. 46, No. 4, 2000, pp. 183–190. doi:https://doi.org/10.1.1.35.6925.

[9] Derksen, R. W., and Rogalsky, T., "Bezier-PARSEC: An Optimized Aerofoil Parameterization for Design," *Advances in Engineering Software*, Vol. 41, No. 7-8, 2010, pp. 923–930. doi:https://doi.org/10.1016/j.advengsoft.2010.05.002.

[10] Kyle Anderson, W., and Bonhaus, D. L., *Aerodynamic Design on Unstructured Grids for Turbulent Flows*, Technical memorandum 112867, National Aeronautics and Space Administration, 1997. doi:https://doi.org/10.1.1.30.2143.

[11] Kyle Anderson, W., and Venkatakrishnan, V., “Aerodynamic Design Optimization on Unstructured Grids with a Continuous Adjoint Formulation,” *Computers and Fluids*, Vol. 28, No. 4, 1999, pp. 443 – 480. doi:https://doi.org/10.1.1.77.7165.

[12] Nielsen, E. J., and Kyle Anderson, W., “Aerodynamic Design Optimization on Unstructured Meshes using the Navier-Stokes Equations,” *AIAA Journal*, Vol. 37, No. 11, 1999, pp. 1411–1419. doi:https://doi.org/10.2514/3.14337.

[13] Padula, S. L., and Li, W., “Options for Robust Airfoil Optimization under Uncertainty,” *9th AIAA/ISSMO Symposium on Multidisciplinary Analysis and Optimization*, 2002. doi:https://doi.org/10.1.1.77.9271.

[14] Li, W., Huyse, L., and Padula, S., “Robust Airfoil Optimization to Achieve Drag Reduction over a Range of Mach Numbers,” *Structural and Multidisciplinary Optimization*, Vol. 24, No. 1, 2002, pp. 38–50. doi:https://doi.org/10.1007/s00158-002-0212-4.

[15] Nemec, M., Zingg, D. W., and Pulliam, T. H., “Multipoint and Multi-Objective Aerodynamic Shape Optimization,” *AIAA Journal*, Vol. 42, No. 6, 2004, pp. 1057–1065. doi:https://doi.org/10.2514/1.10415.

[16] Lepine, J., Trepanier, J.-Y., and Pepin, F., “Wing aerodynamic design using an optimized NURBS geometrical representation,” *38th Aerospace Sciences Meeting and Exhibit*, American Institute of Aeronautics and Astronautics Inc., 2000. doi:https://doi.org/10.2514/6.2000-669.

[17] Painchaud-Ouellet, S., Tribes, C., Trépanier, J. Y., and Pelletier, D., “Airfoil Shape Optimization using a Nonuniform Rational B-splines Parameterization under Thickness Constraint,” *AIAA Journal*, Vol. 44, No. 10, 2006, pp. 2170–2178. doi:https://doi.org/10.2514/1.15117.

[18] Martín, M. J., Andrés, E., Widhalm, M., Bitrián, P., and Lozano, C., “Non-Uniform Rational B-Splines-Based Aerodynamic Shape Design Optimization with the DLR TAU Code,” *Proceedings of the Institution of Mechanical Engineers, Part G: Journal of Aerospace Engineering*, Vol. 226, No. 10, 2012, pp. 1225–1242. doi:https://doi.org/10.1177/0954410011421704.

[19] Samareh, J. A., “Aerodynamic Shape Optimization Based on Free-Form Deformation,” *Proc. 10th Multidisciplinary Analysis and Optimization Conference*, 2004. doi:https://doi.org/10.2514/6.2004-4630.

[20] Kenway, G. K. W., Kennedy, G. J., and Martins, J. R. R. A., “A CAD-Free Approach to High-Fidelity Aerostructural Optimization,” *Proc. 13th Multidisciplinary Analysis and Optimization Conference*, 2010. doi:https://doi.org/10.2514/6.2010-9231.

[21] Fornasier, L., “Wing Design Process by Inverse Potential Flow Computer Programs,” *AGARD Conference Proceedings No.280. the Use of Computers As a Design Tool*, 1980.

[22] Hawk, J., and Bristow, D. R., “Development of MCAERO Wing Design Panel Method with Interactive Graphics Modules,” *NASA Contractor Report CR-3775*, 1984.

[23] Chang, I. C., Van Dam, C. P., and Torres, F. J., “Wing Design Code using Three-Dimensional Euler Equations and Optimization,” *Aircraft Design and Operations Meeting*, American Institute of Aeronautics and Astronautics Inc., 1991. doi:https://doi.org/10.2514/6.1991-3190.

[24] Jameson, A., Pierce, N. A., and Martinelli, L., "Optimum Aerodynamic Design using the Navier-Stokes Equations," *35th Aerospace Sciences Meeting and Exhibit*, American Institute of Aeronautics and Astronautics Inc., 1997. doi:https://doi.org/10.1.1.420.356.

[25] Reuther, J. J., Alonso, J. J., Martins, J. R. R. A., and Smith, S. C., "A Coupled Aero-Structural Optimization Method for Complete Aircraft Configurations," *37th Aerospace Sciences Meeting and Exhibit*, American Institute of Aeronautics and Astronautics Inc., 1999. doi:https://doi.org/10.1.1.23.3192.

[26] Choi, S., Alonso, J. J., Kim, S., Kroo, I. M., and Wintzer, M., "Two-Level Multi-Fidelity Design Optimization Studies for Supersonic Jets," *43rd AIAA Aerospace Sciences Meeting and Exhibit*, American Institute of Aeronautics and Astronautics Inc., 2005. doi:https://doi.org/10.2514/1.34362.

[27] Choi, S., Alonso, J. J., Kroo, U. M., and Wintzer, M., "Multifidelity Design Optimization of Low-Boom Supersonic Jets," *Journal of Aircraft*, Vol. 45, No. 1, 2008, pp. 106–118. doi:https://doi.org/10.2514/1.28948.

[28] Carmichael, R. L., and Erickson, L. L., "PANAIR - A Higher Order Panel Method for Predicting Subsonic or Supersonic Linear Potential Flows about Arbitrary Configurations," *14th Fluid and Plasma Dynamics Conference*, American Institute of Aeronautics and Astronautics Inc., 1981. doi:https://doi.org/10.2514/6.1981-1255.

[29] Alonso, J. J., LeGresley, P., and Pereyra, V., "Aircraft Design Optimization," *Mathematics and Computers in Simulation*, Vol. 79, No. 6, 2009, pp. 1948–1958. doi:https://doi.org/10.1016/j.matcom.2007.07.001.

[30] Rajnarayan, D., Haas, A., and Kroo, I., "A Multifidelity Gradient-Free Optimization Method and Application to Aerodynamic Design," *12th AIAA/ISSMO Multidisciplinary Analysis and Optimization Conference*, American Institute of Aeronautics and Astronautics Inc., 2008, pp. 2008–6020. doi:https://doi.org/10.2514/6.2008-6020.

[31] Kennedy, G. J., and Martins, J. R. R. A., "Parallel Solution Methods for Aerostructural Analysis and Design Optimization," *13th AIAA/ISSMO Multidisciplinary Analysis and Optimization Conference*, American Institute of Aeronautics and Astronautics Inc., 2010. doi:https://doi.org/10.2514/6.2010-9308.

[32] Kennedy, G. J., and Martins, J. R. R. A., "A Parallel Aerostructural Optimization Framework for Aircraft Design Studies," *Structural and Multidisciplinary Optimization*, Vol. 50, No. 6, 2014, pp. 1079–1101. doi:https://doi.org/10.1007/s00158-014-1108-9.

[33] Kennedy, G. J., and Martins, J. R. R. A., "A Comparison of Metallic and Composite Aircraft Wings using Aerostructural Design Optimization," *12th AIAA Aviation Technology, Integration and Operations (ATIO) Conference and 14th AIAA/ISSMO Multidisciplinary Analysis and Optimization Conference*, American Institute of Aeronautics and Astronautics Inc., 2012. doi:https://doi.org/10.2514/6.2012-5475.

[34] James, K. A., Kennedy, G. J., and Martins, J. R. R. A., "Concurrent Aerostructural Topology Optimization of a Wing Box," *Computers and Structures*, Vol. 134, 2014, pp. 1–17. doi:https://doi.org/10.1016/j.compstruc.2013.12.007.

[35] Chin, T. W., and Kennedy, G. J., "Large-Scale Compliance-Minimization and Buckling Topology Optimization of the Undeformed Common Research Model Wing," *57th AIAA/ASCE/AHS/ASC Structures, Structural Dynamics, and Materials Conference*, American Institute of Aeronautics and Astronautics Inc., 2016. doi:https://doi.org/10.2514/6.2016-0939.

[36] Lambe, A. B., and Martins, J. R. R. A., "Matrix-Free Aerostructural Optimization of Aircraft Wings," *Structural and Multidisciplinary Optimization*, Vol. 53, No. 3, 2016, pp. 589–603. doi:https://doi.org/10.1007/s00158-015-1349-2.

[37] Kennedy, G. J., and Martins, J. R. R. A., "An Adjoint-Based Derivative Evaluation Method for Time-Dependent Aeroelastic Optimization of Flexible Aircraft," *AIAA/ASME/ASCE/AHS/ASC Structures, Structural Dynamics and Materials Conference*, 2013, pp. AIAA 2013–1530. doi:https://doi.org/10.2514/6.2013-1530.

[38] Kennedy, G. J., Kenway, G. K., and Martins, J. R., "Towards Gradient-Based Design Optimization of Flexible Transport Aircraft with Flutter Constraints," *15th AIAA/ISSMO Multidisciplinary Analysis and Optimization Conference*, American Institute of Aeronautics and Astronautics Inc., 2014, pp. 601–14, 601–614. doi:https://doi.org/10.2514/6.2014-2726.

[39] Goetzendorf-Grabowski, T., and Mieloszyk, J., "Common Computational Model for Coupling Panel Method with Finite Element Method," *Aircraft Engineering and Aerospace Technology*, Vol. 89, No. 5, 2017, pp. 654–662. doi:https://doi.org/10.1108/AEAT-01-2017-0044.

[40] Mieloszyk, J., and Goetzendorf-Grabowski, T., "Introduction of Full Flight Dynamic Stability Constraints in Aircraft Multidisciplinary Optimization," *Aerospace Science and Technology*, Vol. 68, 2017, pp. 252–260. doi:https://doi.org/10.1016/j.ast.2017.05.024.

[41] Ramos García, N., Sørensen, J., and Shen, W., "Three-Dimensional Viscous-Inviscid Coupling Method for Wind Turbine Computations," *Wind Energy*, Vol. 19, No. 1, 2016, p. 67–93. doi:https://doi.org/10.1002/we.1821.

[42] Kuethe, A., and Schetzer, J., *Foundations of Aerodynamics*, Wiley, 1950.

[43] Drela, M., *Flight Vehicle Aerodynamics*, The MIT Press, 2014.

[44] Bristow, D., and Grose, G., *Modification of the Douglas Neumann Program to Improve the Efficiency of Predicting Component Interference and High Lift Characteristics*, NASA Contractor Report CR-3020, National Aeronautics and Space Administration, 1978.

[45] Maskew, B., "Prediction of Subsonic Aerodynamic Characteristics: A Case for Low-Order Panel Methods," *Journal of Aircraft*, Vol. 19, No. 2, 1982, pp. 157–163. doi:https://doi.org/10.2514/3.57369.

[46] Katz, J., and Plotkin, A., *Low-Speed Aerodynamics*, Cambridge Aerospace Series, Cambridge University Press, 2001.

[47] Katz, J., and Maskew, B., "Unsteady Low-Speed Aerodynamic Model for Complete Aircraft Configurations," *Journal of Aircraft*, Vol. 25, No. 4, 1988, pp. 302–310. doi:https://doi.org/10.2514/3.45564.

[48] Ashley, L. D., Dudley, M. D., Iguchi, S. K., Browne, L., and Katz, J., *Potential Flow Theory and Operation Guide for the Panel Code PMARC*, Technical memorandum 102851, National Aeronautics and Space Administration, 1991.

[49] Smith, S. C., *A Computational and Experimental Study of Nonlinear Aspects of Induced Drag*, Technical Paper 3598, National Aeronautics and Space Administration, 1996.

[50] Göthert, B., *Plane and Three-Dimensional Flow at High Subsonic Speeds. (Extension of the Prandtl Rule)*, Technical memorandum 1105, National Advisory Commitee for Aeronautics, 1946.

[51] Maskew, B., *Program VSAERO Theory Document : A Computer Program for Calculating Nonlinear Aerodynamic Characteristics of Arbitrary Configurations*, NASA contractor report CR-4023, National Aeronautics and Space Administration, 1987.

[52] Erickson, L., *Panel Methods - An Introduction*, NASA Technical Paper 2995, National Aeronautics and Space Administration, 1990.

[53] Abbott, I. H., and von Doenhoff, A. E., *Theory of Wing Sections*, Dover Publications, 1959.

[54] Christensen, P. W., and Klarbring, A., "An Introduction to Structural Optimization," *Solid Mechanics and Its Applications*, Vol. 153, 2008, pp. 1–220. doi:https://doi.org/10.1007/978-1-4020-8666-3.

[55] Petersson, J., and Sigmund, O., "Slope constrained Topology Optimization," *International Journal for Numerical Methods in Engineering*, Vol. 41, No. 8, 1998, pp. 1417–1434. doi:https://doi.org/10.1002/(sici)1097-0207(19980430)41:8<1417::aid-nme344>3.0.co;2-n.

[56] Firl, M., Wüchner, R., and Bletzinger, K.-U., "Regularization of Shape Optimization Problems Using FE-based Parametrization," *Struct. Multidiscip. Optim.*, Vol. 47, No. 4, 2013, pp. 507–521. doi:https://doi.org/10.1007/s00158-012-0843-z.

[57] Bruns, T., and Tortorelli, D., "Topology optimization of non-linear elastic structures and compliant mechanisms," *Computer Methods in Applied Mechanics and Engineering*, Vol. 190, No. 26-27, 2001, pp. 3443–3459. doi:https://doi.org/10.1016/s0045-7825(00)00278-4.

[58] Svanberg, K., "The Method of Moving Asymptotes - a New Method for Structural Optimization," *International Journal for Numerical Methods in Engineering*, Vol. 24, No. 2, 1987, pp. 359–373. doi:https://doi.org/10.1002/nme.1620240207.

[59] Lee, J., "A Potential Based Panel Method for the Analysis of Marine Propellers in Steady Flow," Ph.D. thesis, Massachusetts Institute of Technology, 1987.

[60] Margason, R. J., Kjelgaard, S. O., Sellers, W. L., Morris, C. E. K., Walkley, K. B., and Shields, E. W., "Subsonic Panel Methods - A Comparison of Several Production Codes," *23rd Aerospace Sciences Meeting*, American Institute of Aeronautics and Astronautics Inc., 1985. doi:https://doi.org/10.2514/6.1985-280.

[61] Economon, T. D., Palacios, F., Copeland, S. R., Lukaczyk, T. W., and Alonso, J. J., "SU2: An Open-Source Suite for Multiphysics Simulation and Design," *AIAA Journal*, Vol. 54, No. 3, 2016, pp. 828–846. doi:https://doi.org/10.2514/1.J053813.

Publication [P2]

Cian Conlan-Smith and Casper Schousboe Andreasen. “A coupled 3D panel-beam model for aeroelastic optimization of aircraft wings”. In: *AIAA Journal* (2020). Accepted/In press.

P2

A coupled 3D panel-beam model for aeroelastic optimization of aircraft wings

Cian Conlan-Smith [*] and Casper Schousboe Andreasen [†]
Technical University of Denmark, DK-2800 Lyngby, Denmark.

This work introduces an aeroelastic optimization framework with a coupled 3D panel method and Timoshenko beam finite element model. The method allows for optimization of both the exterior surface of the wing and interior structural properties. We investigate the effects of curved wall spars on the aeroelastic performance of converged designs, which have been shown to provide an improved performance due to the ability to create trade-offs between bending and torsional stiffness. Studies also highlight the importance of calculating aerodynamic loads in the deformed configuration and solving the coupled aeroelastic problem to convergence.

Nomenclature

A = cross sectional area

$\mathbf{A}$ = doublet aerodynamic influence coefficient

a = flange thickness

$\mathbf{B}$ = source aerodynamic influence coefficient

b = wingspan

C_f = $\frac{f}{\frac{1}{2}\rho_\infty V_\infty^2 c}$, normal load coefficient

C_m = $\frac{m}{\frac{1}{2}\rho_\infty V_\infty^2 c^2}$, moment coefficient

C_P = pressure coefficient

c = chord length

$\bar{c}$ = $\frac{\int_0^{\frac{b}{2}} c^2 dy}{\int_0^{\frac{b}{2}} c dy}$, mean aerodynamic chord

D = drag

$\mathbf{d}$ = design variables

E = Young's modulus

e = spar center offset

G = shear modulus

---

[*] PhD student, Department of Mechanical Engineering, Section of Solid Mechanics, cicosm@mek.dtu.dk. Member AIAA.

[†] Associate Professor, Department of Mechanical Engineering, Section of Solid Mechanics.

h = wingbox height
I_x = second moment of area about local x-axis
I_z = second moment of area about local z-axis
$\mathbf{K}$ = stiffness matrix
K_T = torsional stiffness
L = lift
M_p = pitching moment
m = maximum relative camber
$\boldsymbol{n}$ = normal vector
$\mathbf{P}$ = applied load vector
p = relative position of maximum camber
S = wing planform area
s = spar thickness
$\mathbf{s}$ = state variables
t = maximum relative thickness
$\mathbf{U}$ = displacement vector
V = velocity
w = wingbox width
α = twist
η = $\frac{2y}{b}$, normalized span location
Λ = sweep angle
μ = doublet strength
Φ = potential function
ψ = objective function
ρ = density
σ = source strength
σ_v = von Mises stress
θ = pitch angle
Æ = $\frac{b^2}{S}$, aspect ratio

Subscripts

a = associated with aerodynamic model
b = associated with beam model

∞ = associated with freestream

I. Introduction

The application of multidisciplinary optimization (MDO) to the design of aircraft wings was first conducted in 1977 [1]. This study used gradient based optimization to demonstrate that such methods can be used to achieve designs with optimized trade-offs between weight and drag. Since then there has been a huge growth in the development of aeroelastic optimization methods and their application to a wide range of physics models with varying fidelity, from coupled lifting line-beam models [2] to large scale finite volume and finite element models [3–6]. Increasing fidelity of the models results in a large increase of computational expense which is of particular importance when applied to optimization problems as the physics model needs to be solved for each iteration of the optimization routine. To allow fast calculations of aerodynamic loads and structural deformations our focus is on low- to mid-range fidelity methods such as those based on potential flow theory.

Following their earlier work, Haftka et al [7, 8] later coupled a beam finite element model and vortex lattice method (VLM) with a profile drag correction obtained from experimental data. More recently, Jasa et al developed OpenAeroStruct, an open source aeroelastic framework that also uses a VLM-beam model based on Euler beams of tubular cross section [9]. The method was later adopted to model more practical wingbox configurations [10]. Dunning et al [11] applied a similar doublet lattice method with a 3D continuum mesh to the topology optimization of NASA's common research model (CRM) wing [12]. A higher fidelity option for the aerodynamics model is a 3D panel method, which has been used for MDO studies in the past. One such method was developed by Kennedy et al [13] which has been applied to a number of different studies with structural coupling to both shell [14, 15] and 3D continuum elements [16, 17]. Goetzendorf-Grabowski and Mieloszyk [18, 19] also implemented a coupled panel-shell framework for MDO.

The focus here is on MDO of aircraft wings, but it is important to note that the developed methods are also applicable to the design of other aeroelastic structures such as wind turbine blades. However, MDO studies of wind turbines in the literature commonly adopt models based on blade element momentum theory [20–23], usually coupled with beam models. Some exceptions include: Sessarego et al [24] who coupled a lifting line with a force-free wake and multi-body beam finite element method; and McWilliam et al [25, 26] who applied Lagrangian vortex dynamics to aero-structural MDO.

In structural optimization (SO), Aage et al [27] presented studies on topology optimization of the CRM wing under different loading conditions. The ultra-high resolution (1 billion finite elements) of this study allowed structural features to emerge that were unable to develop in previous lower resolutions studies due to a restricted design space. One such feature is curved wall spars which achieve an increased torsional stiffness at the cost of only slightly decreasing bending stiffness.

The objective of the current work is to develop a coupled framework for solving aeroelastic optimization problems based on 3D panel methods and beam finite elements. These coupled models allow fast calculations of the physics of deformable wings with medium fidelity, and to our knowledge, have not been applied to MDO studies in the past. The coupled model expands upon a framework previously developed by the authors to conduct aerodynamic shape optimization of aircraft wings using 3D panel methods [28]. A newly derived generalized load-displacement transfer scheme is presented for coupled panel-beam methods. Design variables are used to control both the exterior shape of the wing and structural design of the interior. In this way, the optimizer has complete control over the external surface and internal domain of the wing, thus expanding the design space. A simple beam cross section parametrization is introduced in order to explore the effect of curved wall spars on the performance of optimized designs. Although the current parametrization is a simplification of the wing box structure we note that the method can be applied to a more advanced parametrization using cross sectional analysis tools such as VABS [29, 30] or BECAS [31].

The next section of this article introduces the reader to the panel-beam discretization and how the design is parametrized. Section III outlines the physics modeling, which include: the 3D panel method; beam finite element model; the derivation of a generalized load-displacement transfer for coupled panel-beam models; and solution methods for the coupled system. The results section presents studies that explore the effect of introducing curved wall spars in the wingbox design with respect to SO for compliance minimization, SO and MDO for mass minimization with stress constraints, and MDO for drag minimization with stress constraints. Additionally, these studies will highlight the importance of calculating aerodynamic loads in the deformed configuration and the effect of sweep on optimized designs. Finally the findings are concluded in Section V. Readers are referred to the appendices for a background discussion on the cross sectional stiffness of curved wall spars, details on stress calculations, and a derivation of sensitivity analysis.

II. Discretization and parametrization

A. Discretization

Fig. 1 shows the discretization of the problem using panels and beam finite elements. The surface of the wing is defined by a discrete set of airfoil sections which are assembled on a common axis corresponding to their quarter chord point. This quarter-chord axis is defined by the sweep angle Λ from the y-z plane, and lies in the x-y plane (i.e. no dihedral) for cases where the wing geometry is optimized. Airfoil sections are defined parallel to the x-z plane with a uniform spacing in the span-wise direction (y-direction), refer to Fig. 1a. The wing surface is discretized by quadrilateral panels which span the distance between airfoil sections. The root of the wing is at $y = 0$ in the global coordinate system. Inside the wing, a single beam finite element also extends between any two neighboring airfoil sections. Beam nodes are located on the camber line of each airfoil section at the same fraction, κ, of the chord length, c (refer to Fig. 1b). A beam element joins the nodes on consecutive airfoil sections and the orientation of the element is defined by a local coordinate system (x_b, y_b, z_b). In the aerodynamic model symmetry is enforced by accounting for the influence from the mirror image of the wing about the x-z plane, and the freestream flow is defined by the pitch angle, θ, measured from the z-y plane. For certain optimization problems a pitching moment constraint will be enforced about the center of gravity, cg. Typically the location of cg is dependent on the entire aircraft and payload. In our examples cg will be defined at the root airfoil midway downstream of the quarter chord axis, i.e. with the quarter chord axis starting at the origin and ending at the tip airfoil at a point $(x_t, y_t, 0)$, cg is defined to be at $(\frac{x_t}{2}, 0, 0)$. This will correspond to modeling a flying wing configuration with an appropriately distributed payload.

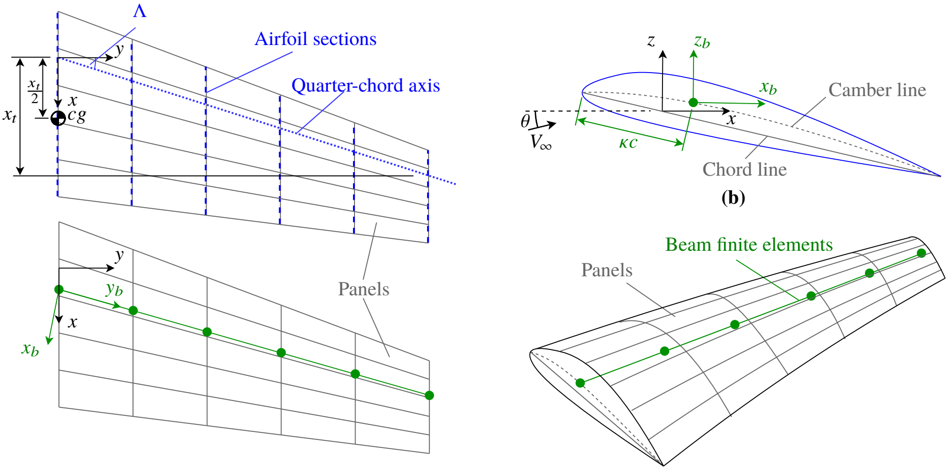

(a) (b) (c)

Fig. 1 Model discretization with airfoil parametrization shown in blue and beam finite elements shown in green: (a) planforms highlighting wing geometry and beam finite elements, (b) root airfoil section, and (c) 3D view.

B. Airfoil parametrization

For cases where the airfoil geometry is optimized we adopt the design variable description and airfoil parametrization introduced in [28]. Here, airfoils are defined based on a modified definition of the NACA 4 or NACA 5-digit airfoils. This parametrization uses up to five design variables per section to define an airfoil, namely, chord length c, maximum thickness t, maximum camber m, position of maximum camber p, and twist α (each labeled in Fig. 2). Airfoil design variables are filtered in the span-wise direction (as described in [28]) in order to avoid numerical artifacts.

C. Beam parametrization

In the structural model we assume that the load is carried only by the wing box which is defined by 5 design variables per section, as shown in Fig. 3. The wing box of height, h, and width, w, comprises of forward and aft spars of equal

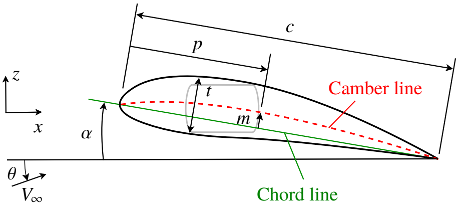

Fig. 2 Parametrization for airfoil sections based on NACA airfoil definitions, with maximum of 5 design variables: chord length c, maximum thickness t, maximum camber m, twist α.

thickness, s, and upper and lower flanges of equal thickness, a. We include a fifth variable, e, which defines the center offset of the spar walls whose curved geometry is elliptic. The advantage of using ellipses (defined by major and minor axes) rather than circular arcs (defined by a radius and angle) is that the curves are less susceptible to roundoff errors when they approach a right-angled wingbox where the radius of a circular arc will grow to infinity and the angle tend to zero. The dimension, w, is between the centroids of the elliptic sections which means the internal area of the wingbox is kept roughly constant as the spar walls become increasingly more curved. This creates a fairer basis to compare straight and curved wall spars. The quantities w, h, and e define the outer dimensions of the wingbox where thicknesses a and s are inset from the external wingbox geometry. Beam cross sections are parametrized in this manner at each airfoil section. The parametrization method is capable of tending from one extreme where spar walls are straight to the other extreme where the spar walls are semi-circular.

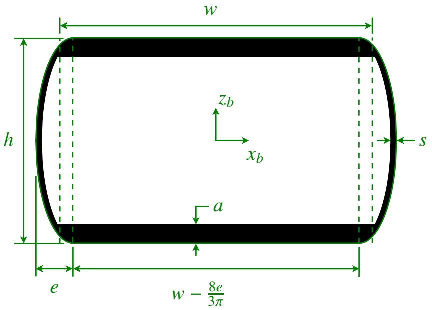

Fig. 3 Parametrization for a beam cross section based on 5 design variables: width w, height h, flange thickness a, spar thickness s, and spar center offset, e.

Upper bounds are placed on the design variables to ensure that the beam geometry is contained within the airfoil geometry. As the airfoil geometry is also defined by design variables these upper bounds are defined as fractions of the airfoil chord length and maximum thickness, e.g. $w = \bar{w}c$, where $\bar{w}$ is the design variable with bounds defined by

$0.01 \leq \bar{w} \leq 0.4$. If the beam design variable is at the upper bound, the airfoil section geometry must be enlarged in order to increase the size of the beam. By defining the wingbox geometry in this manner the optimizer will know, for example, that c must increase in order to increase w, as there will be a gradient with respect to c. By defining w directly and setting the upper bound on w, no sensitivity information about the external geometry with respect to the internal geometry will be available to the optimizer.

The beam parameterization does not account for connections between the wingbox and the outer skin. At first this may seem somewhat unrealistic, however, the parameterization is robust enough to allow a large variance in stiffness properties whilst maintaining physical values. It should then be possible to reproduce the resulting stiffness properties using more conventional rib-spar structures.

III. Physics modeling

This section presents physics model of the coupled 3D panel and beam finite element methods. Two coupling methods are considered where aerodynamic loads can be calculated in either undeformed or deformed configurations. For the undeformed case the loads are calculated via the panel method and applied to the beam, where both models are solved only once. We will refer to this method as 1-way coupled. The second coupling method will be referred to as 2-way coupled, where displacements from the finite element model are used to perturb the panel geometry in the aerodynamic solver and the coupled problem is solved to convergence.

A. Aerodynamic model

The aerodynamic pressure loads are captured using constant source-doublet panels with a Prandtl-Glauert compressibility correction as introduced in [28]. We implement a Dirichlet boundary condition with a zero internal perturbation formulation defined by the governing equation

$$\mathbf{R}_a(\boldsymbol{\mu}, \mathbf{U}, \mathbf{d}) = \mathbf{A}(\mathbf{U}, \mathbf{d})\boldsymbol{\mu} + \mathbf{B}(\mathbf{U}, \mathbf{d})\boldsymbol{\sigma}(\mathbf{U}, \mathbf{d}) = \mathbf{0} \tag{1}$$

where $\mathbf{A}$ and $\mathbf{B}$ are the aerodynamic influence coefficients which depend on the design variables, $\mathbf{d}$, and (for 2-way coupling) the solution to the finite element problem, $\mathbf{U}$. Equation (1) is used to solve for the doublet strengths, $\boldsymbol{\mu}$, with the source strengths are defined as

$$\sigma_i = \boldsymbol{V}_\infty \cdot \boldsymbol{n}_i \tag{2}$$

where $\boldsymbol{V}_\infty$ is the freestream velocity and $\boldsymbol{n}_i$ is the outward pointing normal of panel i. Once the doublet strengths are known the local velocity across a panel i, can be calculated as the gradient of the potential function, Φ, which simplifies to

$$\boldsymbol{V}_i = \boldsymbol{\nabla}\Phi_i = \left(\frac{d\mu}{d\bar{x}}, \frac{d\mu}{d\bar{y}}, 0\right)_i^T + \left(\boldsymbol{V}_\infty \cdot \bar{\boldsymbol{x}}, \boldsymbol{V}_\infty \cdot \bar{\boldsymbol{y}}, 0\right)_i^T \tag{3}$$

where $\bar{x}$ and $\bar{y}$ are local panel coordinates whose axes are define by unit vectors $\bar{\boldsymbol{x}}$ and $\bar{\boldsymbol{y}}$ in the global reference frame. Local velocity is then used to calculate the pressure coefficient via the Bernoulli equation

$$C_{P,i} = 1 - \frac{|| \boldsymbol{V}_i ||^2}{|| \boldsymbol{V}_\infty ||^2} \tag{4}$$

The total induced drag and lift are calculated using a far-field approximation via a Trefftz-plane integration as it has been found to be more numerically stable for optimization problems compared with C_P-integration [28]. Trefftz-plane integration is calculated as [32]

$$D = -\frac{1}{2}\rho_\infty \sum_{i=1}^{N_w} \mu_i l_i \boldsymbol{v}_i . \boldsymbol{n}_i \tag{5}$$

$$L = \rho_\infty V_\infty \sum_{i=1}^{N_w} \mu_i \cos(\phi_i) l_i \tag{6}$$

where N_w is the number of wake panels, l_i and ϕ_i are the length and orientation of wake panel i in the Trefftz-plane. Because panel methods assume inviscid and incompressible flow, the induced drag is the only type of drag captured by this model. It is possible to couple these methods to viscous solvers [33] but this will require prior knowledge of the boundary layer shape which is difficult to predict when airfoils are free to change during the optimization procedure. As a result, only the induced drag is considered in this work. A fixed wake model is used whose shape is achieved by projecting the trailing edge downstream in the free-stream direction.

B. Structural model

The internal structure of the wing is modeled using one-dimensional cubic beam finite elements. Element degrees of freedom (DOF) and local loads are shown in Fig. 4.

Aerodynamic loads calculated in the panel method are transferred to beam nodes in form of a load vector, **P**, which consists of local forces, $\boldsymbol{F}$, and moments, $\boldsymbol{M}$. These loads are dependent on both the design variables, **d**, and the solution to the panel method, $\boldsymbol{\mu}$. Only aerodynamic loads are applied, where self-weight is not considered. We note that by neglecting self-weight the loading will be slightly higher as the wing's weight would impose a force counteracting the lifting loads, thus potentially reducing the stresses. The global vector of nodal displacements and rotations, **U**, is determined via the governing equation for the beam,

$$\mathbf{R}_b(\boldsymbol{\mu}, \mathbf{U}, \mathbf{d}) = \mathbf{K}(\mathbf{d})\mathbf{U} - \mathbf{P}(\boldsymbol{\mu}, \mathbf{U}, \mathbf{d}) = \mathbf{0} \tag{7}$$

It is noted that for 2-way coupling, **P** is also dependent on **U** as the aerodynamic loads are calculated in the deformed configuration. The global stiffness matrix, **K**, is a function of **d**, and formed from assembling element stiffness matrices,

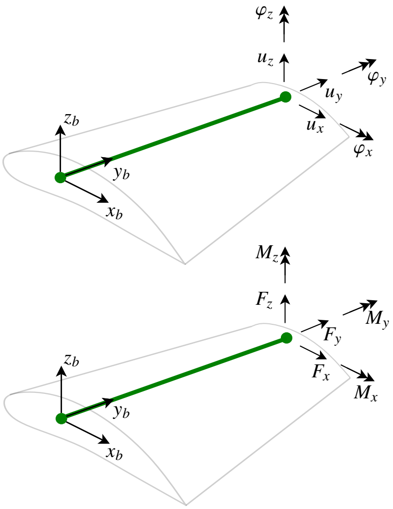

Fig. 4 A beam finite element with local coordinate system, degrees of freedom and applied loads: displacements, $\{u_x, u_y, u_z\}$; rotations, $\{\phi_x, \phi_y, \phi_z\}$; conjugate forces, $\{F_x, F_y, F_z\}$; and applied moments, $\{M_x, M_y, M_z\}$.

$\mathbf{K}_e$ via

$$\mathbf{K}_e(\mathbf{d}) = \int_0^{l_e} \mathbf{T}(\mathbf{d})^{\mathrm{T}}\mathbf{B}^{\mathrm{T}}\mathbf{K}_{cs}(\mathbf{d})\mathbf{B}\mathbf{T}(\mathbf{d})dl \tag{8}$$

where $\mathbf{T}$ is a rotation matrix accounting for the orientation of the beam in the global coordinate system (refer to Fig. 1). By evaluating the integral in (8) using gauss quadrature, one can account for a varying cross section along the element. The constitutive model for a cross section of the beam is based on an axial model, thin-walled torsional model, and Timoshenko model in bending. Only doubly symmetric cross sections and isotropic materials are considered in this work and as such the constitutive stiffness matrix, $\mathbf{K}_{cs}$, is a diagonal matrix with the following non-zero entries

$$K_{cs,11} = GA \ , \ K_{cs,22} = EA \ , \ K_{cs,33} = GA \ , \ K_{cs,44} = EI_x \ , \ K_{cs,55} = GK_T \ , \ K_{cs,66} = EI_z \tag{9}$$

From the dimensions shown in Fig. 3 analytical expressions for area and second moments of area can be derived using the principles of superposition and the parallel axis theorem. These are standard methods which are well documented [34] and as final expressions are long they are not presented here. Note that the shear correction factors in (9) have been neglected as they are not readily available for all curved wall spar geometries. However, as these values are typically higher for curved cross sections, we suspect that including shear factors would increase the incentive for the optimizer to create curved wall spars. If the reader is interested in achieving shear correction factors for a given wingbox with curved wall spars we recommend using VABS [29, 30] or BECAS [31] cross-sectional analysis tools.

The matrix **B** in (8) is the strain displacement matrix defined such that the strains and curvatures can be achieved by

$$\begin{Bmatrix}\boldsymbol{\varepsilon}\\ \boldsymbol{\kappa}\end{Bmatrix} = \mathbf{B}\mathbf{U}_e = [\mathbf{N}' + \boldsymbol{S}\mathbf{N}]\mathbf{U}_e \tag{10}$$

where **N** are the shape functions, whose derivatives are denoted by the prime, and $\boldsymbol{S}$ is used to account for rotations of the cross section in calculating the strains due to bending [35], i.e. $\varepsilon_x = \frac{du_x}{dl} + \varphi_z$ and $\varepsilon_z = \frac{du_z}{dl} - \varphi_x$ (refer to DOF in Fig. 4).

C. Load-displacement transfer

The beam finite element model assumes sections remain planar and undergo rigid body displacements and rotations. Since nodes of an airfoil section on the panel mesh lie in-plane with a single node on the beam mesh, the perturbations of a single aerodynamic node, $\delta\boldsymbol{X}_a$, is described using displacements and rotations of the beam node at the same span-wise location. Assuming small rotations the displacement transfer can be defined as

$$\delta\boldsymbol{X}_a = \delta\boldsymbol{u}_b - \boldsymbol{r}\times\delta\boldsymbol{\varphi}_b = \delta\boldsymbol{u}_b + \delta\boldsymbol{\varphi}_b\times\boldsymbol{r} \tag{11}$$

where $\delta\boldsymbol{u}_b$ and $\delta\boldsymbol{\varphi}_b$ are displacements and rotations at the beam node, and $\boldsymbol{r}$ is a spatial vector from the beam node to the aerodynamic node.

Aerodynamic forces are transferred to the beam in form of distributed loads **f** and **m**. The total load acting on an element is achieved integrating distributed loads from along the element and summing the contribution from each of the N panels at the same span-wise section.

$$\boldsymbol{P}_e = \begin{Bmatrix}\boldsymbol{F}\\ \boldsymbol{M}\end{Bmatrix} = \sum_{i=1}^{N}\int_0^{l_e}\begin{Bmatrix}\mathbf{f}\\ \mathbf{m}\end{Bmatrix}dl \tag{12}$$

To ensure consistency it is required that the total force calculated in the aerodynamic model matches the applied load in the beam model. To ensure conservativeness the virtual work performed by the structural load undergoing virtual displacements and rotations must be equal to the virtual work of the panel method [36]. Using this requirement we can derive a consistent and conservative load-displacement transfer method. The virtual work of a beam element loaded by a single panel (as shown in Fig. 5) is defined as

$$\delta W_b = \int_0^{l_e}\begin{Bmatrix}\mathbf{f}\\ \mathbf{m}\end{Bmatrix}^{\mathrm{T}}\begin{Bmatrix}\delta\boldsymbol{u}\\ \delta\boldsymbol{\varphi}\end{Bmatrix}dl = \int_0^{l_e}\left(\mathbf{f}^{\mathrm{T}}\delta\boldsymbol{u} + (\boldsymbol{r}\times\mathbf{f})^{\mathrm{T}}\delta\boldsymbol{\varphi}\right)dl \tag{13}$$

where the applied moments arise from translating the force from the panel to the beam element meaning that $\mathbf{m} = \boldsymbol{r}\times\mathbf{f}$, with $\boldsymbol{r}$ being a spatial vector from the beam element to the panel. Manipulating the second term in the integrand by

$(\boldsymbol{r} \times \mathbf{f})^{\mathrm{T}} \delta\boldsymbol{\varphi} = \delta\boldsymbol{\varphi}^{\mathrm{T}}(\boldsymbol{r} \times \mathbf{f}) = (\delta\boldsymbol{\varphi} \times \boldsymbol{r})^{\mathrm{T}}\mathbf{f} = \mathbf{f}^{\mathrm{T}}(\delta\boldsymbol{\varphi} \times \boldsymbol{r})$, yields

$$\delta W_b = \int_0^{l_e} \mathbf{f}^{\mathrm{T}}(\delta\boldsymbol{u} + \delta\boldsymbol{\varphi} \times \boldsymbol{r})dl \tag{14}$$

The virtual work of the aerodynamic model by a single panel is

$$\delta W_a = \int_S q_\infty C_P \boldsymbol{n}^{\mathrm{T}} \delta\boldsymbol{X}_a dS \tag{15}$$

The panel method assumes that C_P is constant over the panel and each panel is flat meaning that $\boldsymbol{n}$ is also constant over the panel. Additionally, we assume perturbations in the chord-wise direction of the panel are constant. Using equation (11) and representing dS as wdl we find that

$$\delta W_a = q_\infty C_P J_l \boldsymbol{n}^{\mathrm{T}} \int_0^{l_e} w(\delta\boldsymbol{u} + \delta\boldsymbol{\varphi} \times \boldsymbol{r})dl \tag{16}$$

where J_l is a linear mapping introduced to account for cases where the length of the panel is not equal to the element length, l_e (refer to Fig. 5). By equating equations (14) and (16), the distributed load, $\mathbf{f}$ from a single panel can be defined as

$$\mathbf{f} = q_\infty C_P J_l w \boldsymbol{n} \tag{17}$$

The applied load can now be calculated by inserting (17) and $\mathbf{m} = \boldsymbol{r} \times \mathbf{f}$ into (12).

D. 2-way coupled solution method

The coupled problem can be solved using fixed point iterations in which the panel method is solved in the undeformed configuration and calculated loads are used to solve the beam problem. The displacements from the beam problem are then passed back to the panel method and loads are calculated in the deformed configuration. This process continues until the change in state variables, $\mathbf{s} = \{\boldsymbol{\mu}\ \mathbf{U}\}^{\mathrm{T}}$, between iterations is less than the tolerance ϵ.

Alternatively a Newton method is used where the residual $\mathbf{R} = \{\mathbf{R}_a\ \mathbf{R}_b\}^{\mathrm{T}}$ is calculated on each iteration and a solution step, $\delta\mathbf{s}$, is calculated using the Jacobian $\frac{\partial \mathbf{R}}{\partial \mathbf{s}}$, as

$$\delta\mathbf{s} = \frac{\partial \mathbf{R}}{\partial \mathbf{s}}^{-1} \mathbf{R} \tag{18}$$

where

$$\frac{\partial \mathbf{R}}{\partial \mathbf{s}} = \begin{bmatrix} \frac{\partial \mathbf{R}_a}{\partial \boldsymbol{\mu}} & \frac{\partial \mathbf{R}_a}{\partial \mathbf{U}} \\ \frac{\partial \mathbf{R}_b}{\partial \boldsymbol{\mu}} & \frac{\partial \mathbf{R}_b}{\partial \mathbf{U}} \end{bmatrix} = \begin{bmatrix} \mathbf{A} & \left[\frac{\partial \mathbf{A}}{\partial \mathbf{U}}\boldsymbol{\mu} + \frac{\partial \mathbf{B}}{\partial \mathbf{U}}\boldsymbol{\sigma} + \mathbf{B}\frac{\partial \sigma}{\partial \mathbf{U}}\right] \\ -\frac{\partial \mathbf{P}}{\partial \boldsymbol{\mu}} & \left[\mathbf{K} - \frac{\partial \mathbf{P}}{\partial \mathbf{U}}\right] \end{bmatrix} \tag{19}$$

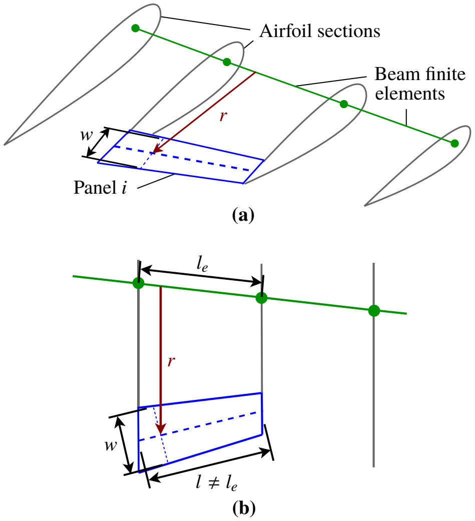

Fig. 5 Schematic of load displacement transfer scheme from a single panel in (a) 3D and (b) planform views.

The solution is terminated once the residual norm is less than the tolerance ϵ.

Fixed point iterations generally take more iterations to converge as it is a first order convergence scheme and the Newton method is second order. However, a fixed point iteration method does not require the user to calculate the Jacobian matrix, which for the panel method can take up to 8 times the computational cost of the forward problem [28]. This means fixed point iterations generally converge to a solution faster than the Newton method with respect to wall-clock time. However, the Newton method is more robust for compliant wings where deformations are large [9]. Generally, we use fixed point iterations due to the reduced computational cost, and a value of $\epsilon = 10^{-3}$ was used for optimization problems as it was found to be a good trade-off between accuracy and computational time.

IV. Results

The results section is divided into two subsections. The first subsection, (A), contains studies where the internal structure of the CRM wing is optimized for compliance minimization and stress-constrained mass minimization. The goal of these studies is to provide the reader with insight into the beam parametrization, coupling procedure, and problem formulation. Subsection (B) details multidisciplinary shape optimization studies where both the external wing geometry and the internal beam structure is parameterized by design variables. Each problem is solved for a freestream velocity of Mach 0.4 using 4000 panels and 40 beam finite elements. All optimization problems are solved using the method of moving asymptotes [37] where gradients are calculated using adjoint sensitivity analyses. Readers are referred to appendix C for derivations of gradients.

A. Structural optimization of the CRM wing

As a first study we investigate a fixed skin CRM wing optimization with design variables, $\mathbf{d} = \{\boldsymbol{w}, \boldsymbol{h}, \boldsymbol{a}, \boldsymbol{s}, \boldsymbol{e}\}$. The objective is to minimize compliance subject to a volume constraint, as defined in (20), where compliance is summed for multi-load cases with each case weighted equally, and the volume fraction is defined as the volume of the beam divided by the total volume of the wing. This is a similar formulation to the topology optimization study presented in [27] where curved wall spars appeared. Here, the problem is solved using only 1-way coupling (i.e. in the undeformed configuration). Studies are presented with pitch angles, $\theta = \{0°, 5°, 10°\}$. The beam nodes are positioned at the 40% of the chord length in each section, as shown in Fig. 6a. The primary loading of the beam in each case is given in Figs. 6b and 6c, where coefficients are calculated using the mean aerodynamic chord.

$$\begin{aligned} \min_{\mathbf{d} \in \mathbb{R}^{N_\mathrm{d}}} \quad &: \ \psi = \sum_{\theta} C_\theta(\mathbf{U}, \mathbf{d}) \\ \text{subject to} \quad &: \ V(\mathbf{d}) - \bar{V} \leq 0 \\ & \quad \underline{d} \leq d_i \leq \bar{d} \qquad \text{for } \ i = 1, \ldots, N_\mathrm{d} \end{aligned} \tag{20}$$

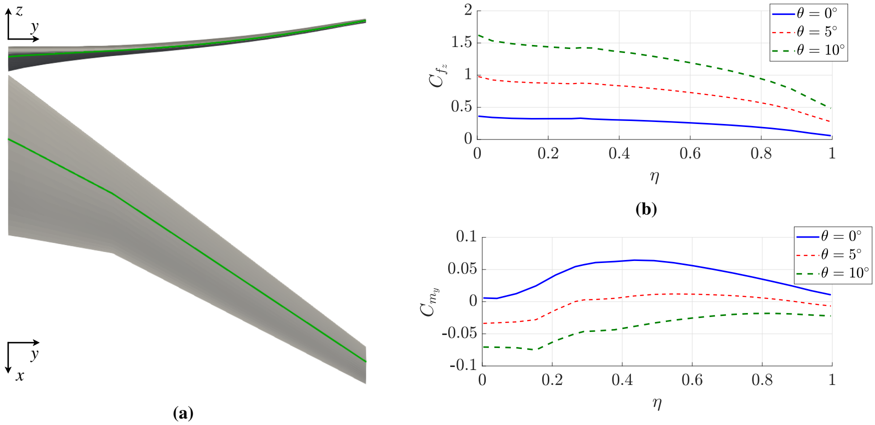

(a)

(b)

(c)

Fig. 6 Undeformed CRM wing geometry and primary beam loading at different pitch angles: (a) plan and elevation of the CRM wing with beam axis shown in green, (b) normal load coefficient, (c) torsional load coefficient.

The optimization problem is solved where the spar walls are straight, i.e. $\boldsymbol{e} = \mathbf{0}$ in Fig. 3, and where curved wall spars are allowed to form, i.e. $\boldsymbol{e}$ is a design variable, in order to investigate possible gains. The relative difference in the objective function between optimized designs with fixed straight wall spars and when curved wall spars are allowed to form is shown in Fig. 7, where $\Delta_C = \frac{\psi_{e=0} - \psi_e}{\psi_{e=0}}$, . The results show a reduction in compliance with the curved wall

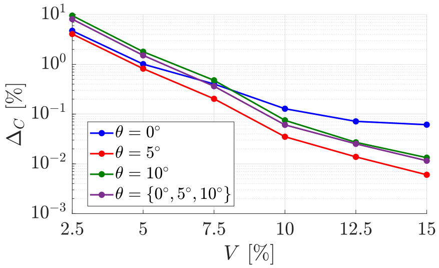

Fig. 7 Reduction in compliance when curved wall spars are allowed for different volume fractions.

spars for a range of volume fractions, $\bar{V}$. The reduction in compliance is due to an increased torsional stiffness of the curved wall spars. However, this increase in torsional stiffness corresponds to a reduction in bending stiffness (refer to appendix A for an example study). As the volume fraction of the structure increases the optimizer is less likely to use curved wall spars and the performance of the two designs are similar. This is because the thicker-walled box sections already provide adequate torsional stiffness, as can be seen in the definition of K_T (appendix A, equation (26)). On the other hand when tight restrictions are placed on the available material the use of curved wall spars become more advantageous, with reductions in compliance of up to 10%.

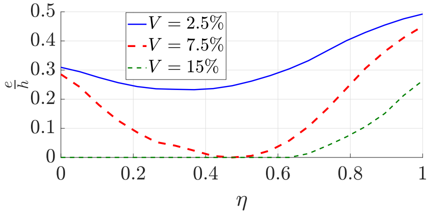

Fig. 8 Span-wise variation in curvature of the spar walls for the $\theta = \{0°, 5°, 10°\}$ case with different volume fractions. Spar walls are straight for $\frac{e}{h} = 0$ and semi-circular for $\frac{e}{h} = 0.5$.

Fig. 8 plots the ratio of e to h along the span of the wing for different volume fractions in the multi-load case. The ratio of e to h describes how curved the spar walls are, where $\frac{e}{h} = 0$ corresponds to straight wall spars and $\frac{e}{h} = 0.5$ to semi-circular spar walls. Curved wall spars form mainly around the tip and root of the wing, and are less likely to appear for higher volume fractions as previously discussed. Cross sections of wing and beam at the root, mid-section, and tip for a selection of volume fractions are shown in Fig. 9. From these sections it is clear to see the straight and curved wall spar designs tend to converge for higher volume fractions. For low volume fractions the beam is wider in the mid-sections of the wing than the root or tip. This increases the torsional stiffness away from the root where is it not possible to increase the height due to the restrictions of the airfoil section. In this case the torsional stiffness peaks around the Yehudi break, whereas for larger volume fractions the largest torsional stiffness is at the root, corresponding to the largest airfoil section. Differences in the performance of these structures may not be intuitively obvious from the cross sections alone. A more informative way to compare the differences in design is to look at the distribution along the wing of the sectional stiffness properties as shown in Fig. 10. Here the sectional stiffness is normalized with wing's planform area S, span b, and mean aerodynamic chord $\bar{c}$. These distributions show that by introducing curved wall spars the optimizer can sacrifice bending stiffness for an increase in torsional stiffness. This is most evident for low volume fractions as designs converge for when the volume fraction increases.

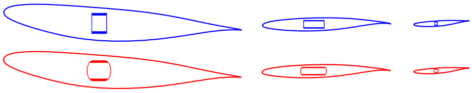

(a) $V = 2.5\%$

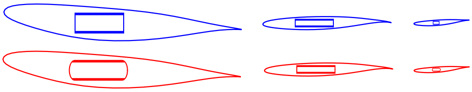

(b) $V = 7.5\%$

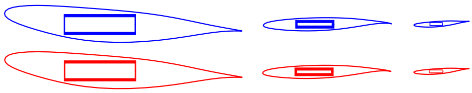

(c) $V = 15\%$

Fig. 9 Airfoil and beam sections for $\theta = \{0°, 5°, 10°\}$ case with different volume fractions. Root, mid, and tip sections from left to right with straight wall spar designs are shown on top, curved wall spars designs are shown below.

Comparing to the topology optimized designs presented in [27], the spars have a higher curvature in our case. However, it is important to note that the airfoil skin thickness is included in topology optimized designs which will increase the torsional stiffness. As discussed earlier, one may argue the current beam parametrization is non-physical as the connection between the wingbox and airfoil skin is not considered. However, the simplified model is adequate for demonstrating the differences in performance of curved wall spar structures. Additionally, the parametrization allows stiffness distributions to be optimized in a manner that is robust and produces physical values. It can then be possible to realize these stiffness distributions using more traditional rib-spar structures post-optimization.

When dimensions of the wingbox are free to change, as in the previous example, it can be difficult to demonstrate the trade-offs between straight and curved wall spars as the wingbox dimensions have a large impact on the stiffness properties of the beam (refer to appendix A). It is more clearly demonstrated by fixing the wingbox dimensions and solving (20) again with only one design variable per section to control the shape of the spars, i.e. $\mathbf{d} = \boldsymbol{e}$. All other wingbox dimensions are defined by the optimized design with straight wall spars in the previous problem. Fig. 11 shows the difference in sectional bending and torsional stiffness along the wing for the multi-load case, $\theta = \{0°, 5°, 10°\}$.

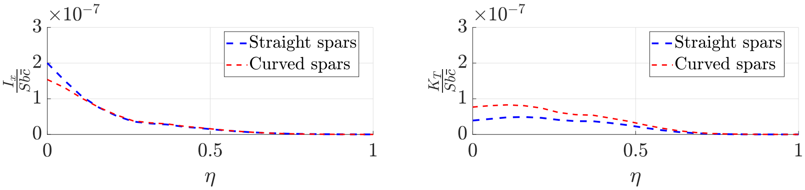

(a) $\bar{V}$ = 2.5%, **bending stiffness**

(b) $\bar{V}$ = 2.5%, **torsional stiffness**

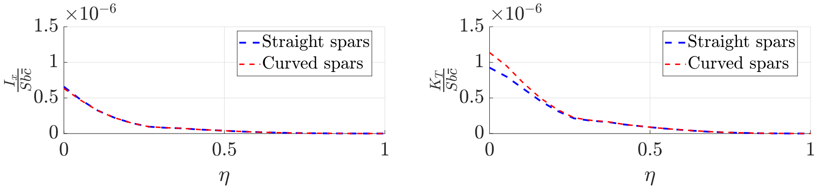

(c) $\bar{V}$ = 7.5%, **bending stiffness**

(d) $\bar{V}$ = 7.5%, **torsional stiffness**

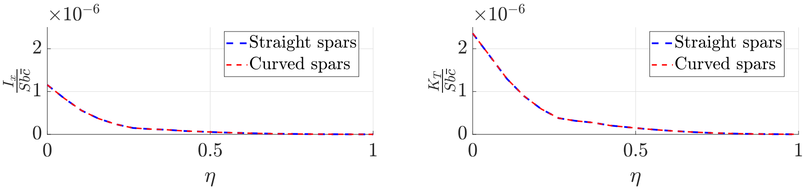

(e) $\bar{V}$ = 15%, **bending stiffness**

(f) $\bar{V}$ = 15%, **torsional stiffness**

Fig. 10 Stiffness properties of converged designs for primary loading in multi-load case, $\theta = \{0°, 5°, 10°\}$**. Solved for different volume fractions,** $\bar{V}$**, with both straight and curved wall spars.**

For these designs the optimizer can curve the spar walls leading to increases in torsional stiffness at the cost of reducing bending stiffness. This clearly shows the freedom of the parametrization to create optimized trade-offs between torsional and bending stiffness. As the spars become thicker, creating curved wall spars becomes less advantageous, and for a volume fraction, $V \geq 15\%$, the spar walls remain straight. Curved wall spars mainly form towards the tip of the wing and in some cases at the root. This makes sense as at the tip of the wing the bending strain tends to zero but the torsional strain does not. For low volume fractions allowing curved wall spars can lead to an increase in torsional stiffness of over 10%.

Compliance minimization is the standard problem formulation for structural optimization problems. However, it is not uncommon that aircraft wings are designed to experience large deformations, and by minimizing compliance the deflections are minimized. A more natural formulation for structural optimization of an aircraft wing would be to

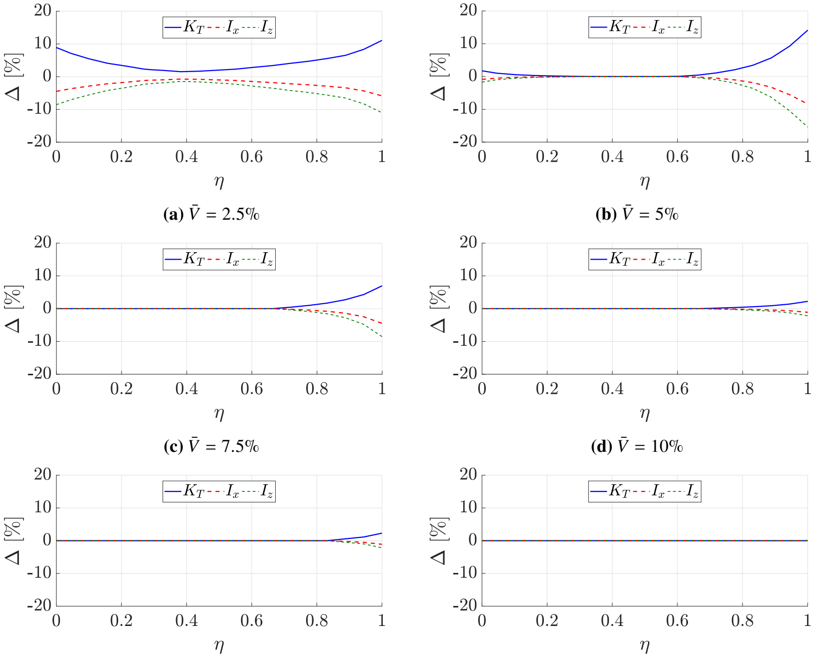

(a) $\bar{V}$ = 2.5% **(b)** $\bar{V}$ = 5%

(c) $\bar{V}$ = 7.5% **(d)** $\bar{V}$ = 10%

(e) $\bar{V}$ = 12.5% **(f)** $\bar{V}$ = 15%

Fig. 11 Difference in sectional stiffness between curved and straight wall spars for different bounds on volume fraction, $\bar{V}$, and only one design variable, e.

minimize mass subject to stress constraints, defined as

$$\begin{aligned} \min_{\mathbf{d}\,\in\,\mathbb{R}^{N_\mathrm{d}}} \quad &: \; m(\mathbf{d}) \\ \text{subject to} \quad &: \; \frac{\hat{\sigma}_i(\mathbf{U},\mathbf{d})}{\bar{\sigma}} - \beta \le 0 \qquad \text{for } \; i = 1, \ldots, N_r \\ & \quad \underline{d} \le d_i \le \bar{d} \qquad\qquad\; \text{for } \; i = 1, \ldots, N_\mathrm{d} \end{aligned} \tag{21}$$

where $\hat{\sigma}_i$ is the maximum stress in region i, $\bar{\sigma}$ is the yield/ultimate stress, and β is a fixed scalar which introduces a safety factor. A p-norm function is used to approximate the maximum stress and aggregate the stresses into N_r regional constraints by

$$\max(\sigma_v) \simeq \hat{\sigma} = c_I \sigma_{pn} = c_I \left(\sum_i \sigma_{v,i}^p \right)^{\frac{1}{p}} \tag{22}$$

where c_I is a scaling parameter used to ensure the p-norm correctly approximates the maximum von Mises stress and is defined as [38]

$$c_I = \zeta \frac{\max(\sigma_v)_{I-1}}{\sigma_{pn,I-1}} + (1-\zeta)c_{I-1} \tag{23}$$

where I is the design iteration number and ζ is taken to be 0.5 throughout. The von Mises stress, σ_v is calculated at the gauss points, at 16 locations on the cross section as described in appendix B. Stress constraints are enforced on N_r regions, to improve the performance of the p-norm approximation. These regions are defined based on span-wise location where the beam is divided into N_r equal segments. Typically, $N_r = 20$ was used with 40 finite elements and 4 gauss points along the element, leading to a total of 128 stress calculations per region.

Here, the problem is solved using both 1- and 2-way coupling methods. The CRM wing is again taken as the fixed outer geometry. For $\beta = 1$, curved wall spars achieve a reduction in mass of 13-14% for both 1- and 2-way coupled problems. The reasoning for this is the same as previously discussed for the compliance minimization problem: the curved wall spar parametrization is better able to create optimized trade-offs between torsional stiffness and bending stiffness. The maximum stress ratio in each section along the wing is shown in Fig. 12 for different values of β. The changes in mass when going from 1-way coupling to 2-way coupling ($\Delta_m = \frac{m_2 - m_1}{m_1}$) is shown in Table 1 and the stiffness distributions for straight wall spar designs are shown in Fig. 13.

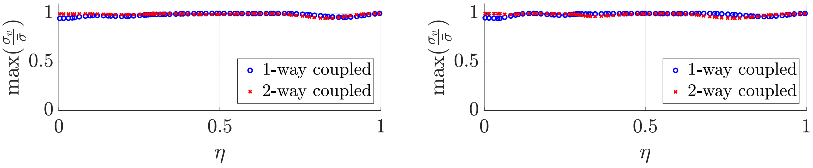

(a) $\beta = 1$, straight wall spars **(b) $\beta = 1$, curved wall spars**

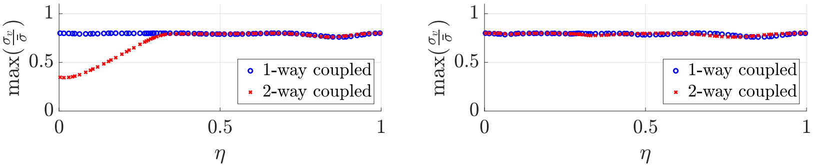

(c) $\beta = 0.8$, straight wall spars **(d) $\beta = 0.8$, curved wall spars**

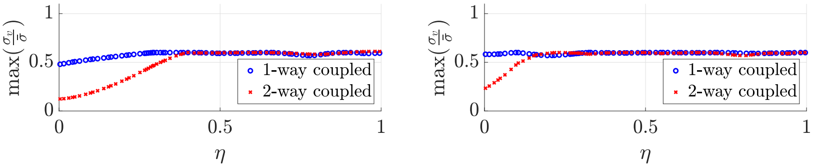

(e) $\beta = 0.6$, straight wall spars **(f) $\beta = 0.6$, curved wall spars**

Fig. 12 Maximum stress ratio at sections along the beam for optimized designs with 1- and 2-way coupling.

spar walls	β	Δ_m [%]
straight	1	21.8
straight	0.8	148.7
straight	0.6	130.0
curved	1	21.7
curved	0.8	40.4
curved	0.6	79.8

Table 1 Difference in mass, Δ_m between 1-way coupled to 2-way coupled designs, for both straight and curved wall spars.

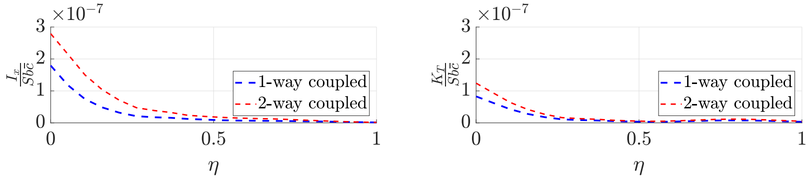

(a) $\beta = 1$**, bending stiffness** **(b)** $\beta = 1$**, torsional stiffness**

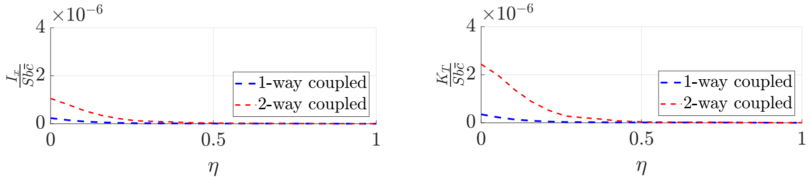

(c) $\beta = 0.8$**, bending stiffness** **(d)** $\beta = 0.8$**, torsional stiffness**

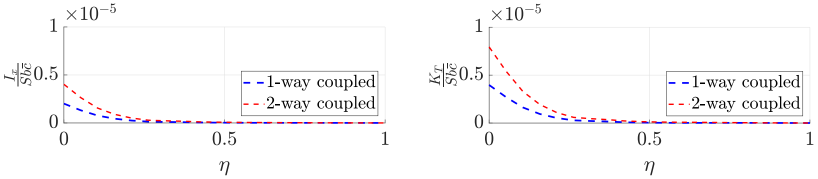

(e) $\beta = 0.6$**, bending stiffness** **(f)** $\beta = 0.6$**, torsional stiffness**

Fig. 13 Stiffness properties for straight wall spar designs in primary loading with different β values.

For $\beta = 1$ the maximum stress distribution is constant along the length of the wing regardless of coupling method or spar definition. When a stricter constraint is enforced on the stresses the 1-way coupled designs appear to have similar stress distributions along the wing. However, for 2-way coupled designs the stresses are reduced towards the root due to an increased stiffness in that region (refer to Fig. 13). By increasing the stiffness at the root, the deflections along the wing are reduced. The increased stiffness means that the stress constraint is not active at the root, but by reducing the deflections, the loading is reduced and the stress constraint can be satisfied in the outer regions of wing. The onset of this occurs for higher β values with straight wall spars, as the curved wall spars allow a larger torsional stiffness which can be used to reduce stresses in the outer portions of the wing. This allows the design to satisfy the stress constraint without as much material placed at the root to restrict deformations. The additional stiffness does however result in more mass to be added at the root of the wing leading to large differences in the objective function between 1- and 2-way coupled designs, as shown in Table 1. When stress constraints are relaxed, i.e. $\beta = 1$, there is still a difference of 21% in the objective function between 1- and 2-way coupled designs. This study demonstrates the importance of solving these problems in the deformed configuration, i.e. using a 2-way coupled method. This finding aligns with previous studies in the literature, where different physics models were used [11, 39, 40].

B. Multidisciplinary shape optimization

Finally, we consider the case where the external geometry is defined by design variables using the NACA 5-digit airfoil parametrization, and the beam sections are also allowed to vary, i.e. $\mathbf{d} = \{\boldsymbol{c}, \boldsymbol{t}, \boldsymbol{p}, \boldsymbol{\alpha}, \boldsymbol{w}, \boldsymbol{h}, \boldsymbol{a}, \boldsymbol{s}, \boldsymbol{e}\}$. Consider the optimization problem defined in (24) with the objective of minimizing drag in cruise conditions ($\theta = 0°$).

$$\begin{aligned}
\min_{\mathbf{d} \in \mathbb{R}^{N_\mathrm{d}}} \quad &: \ D(\boldsymbol{\mu}, \mathbf{U}, \mathbf{d}) \\
\text{subject to} \quad &: \ L(\boldsymbol{\mu}, \mathbf{U}, \mathbf{d}) = W_T(\mathbf{d}) \\
& \quad \hat{\sigma}_i(\boldsymbol{\mu}, \mathbf{U}, \mathbf{d}) - \bar{\sigma} \leq 0 \quad \text{for } i = 1, \ldots, N_r \\
& \quad M_p(\boldsymbol{\mu}, \mathbf{U}, \mathbf{d}) = 0 \\
& \quad \underline{d} \leq d_i \leq \bar{d} \qquad\qquad\quad \text{for } i = 1, \ldots, N_\mathrm{d}
\end{aligned} \tag{24}$$

In order to satisfy equilibrium in cruise, the total lift must be equal to the aircraft weight. This is enforced by a constraint, where the weight is defined as the sum of the wingbox structure, W_b, a payload, W_p, and 5% of the wing volume to account for skin thickness, ribs and additional stiffeners, W_v.

$$W_T(\mathbf{d}) = W_b(\mathbf{d}) + W_v(\mathbf{d}) + W_p \tag{25}$$

The optimization problem is also subject to stress constraints at an additional load case with a pitch angle, $\theta = 10°$, simulating a high lift condition. As only the lift-induced drag is considered, the optimizer will seek to reduce lift in order to reduce the drag. This in-turn will require the weight to be reduced due to the first constraint on lift-weight equilibrium. The weight is bounded by the stress constraint because if the weight continues to reduce, the beam will experience large strains leading to large stresses. The final constraint is on the pitching moment in cruise which must be equal to zero. The pitching moment is calculated about a point mid-way downstream of quarter chord axis (refer to Fig. 1). We note that the pitching moment constraint can be neglected and the problem will still converge to reasonable designs. However, the pitching moment is directly related to the airfoil camber and without this additional consideration the optimizer could use twist, camber or any combination of two to produce the desired lift for a minimum drag. This creates many possible solutions to the optimization problem, thus the pitching moment constraint offers a means to include an additional practical consideration whilst making the optimization problem better posed.

Sweep is used in aircraft wings to delay the formation of shock waves in transonic flow, a phenomena which cannot be predicted by the panel method. It is also used to ensure stability which is of particular importance in flying wing configurations. Here, optimization problems are solved for fixed sweep angles $\Lambda = \{0°, 15°, 30°\}$ where converged designs are shown in Fig. 14. The loading for converged designs are shown in Fig. 15, with geometry and performance details tabulated in Table 2.

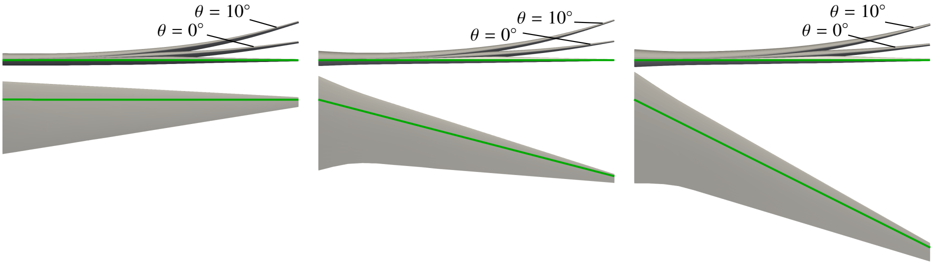

(a) $\Lambda = 0°$ **(b)** $\Lambda = 15°$ **(c)** $\Lambda = 30°$

Fig. 14 Planform and deflections for converged designs with different sweep angles, Λ. Beam axis shown in green.

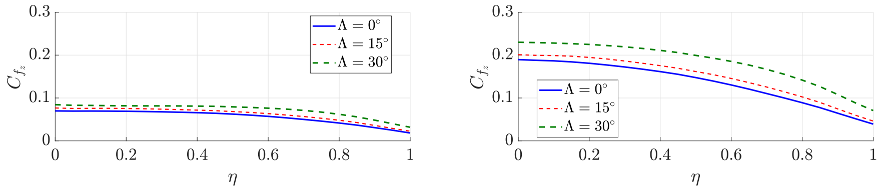

(a) $\theta = 0°$ **(b)** $\theta = 10°$

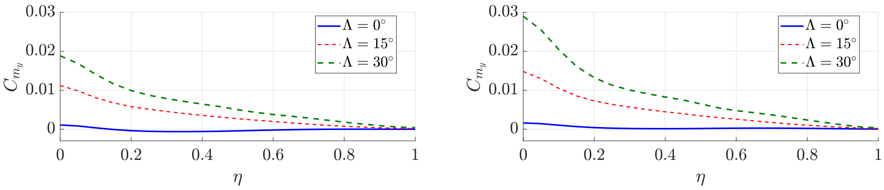

(c) $\theta = 0°$ **(d)** $\theta = 10°$

Fig. 15 Primary beam loading for converged designs in cruise and high load cases: (a)-(b) normal load coefficient, (c)-(d) torsional load coefficient.

All designs produce high lift to drag ratios between 55 and 60 which is expected as induced drag is the only type of

Λ	Æ	$\frac{U_t}{b}$ [%]	$\frac{L}{D}$
0°	14.5	6.72	59.1
15°	12.1	6.45	57.6
30°	9.9	5.96	55.8

Table 2 Aspect ratio, tip deflection and lift to drag ratio for converged designs with different sweep angles, Λ.

drag considered. The lift to drag ratio steadily decreases with increasing sweep. Each design converges to large aspect ratio wings which is expected as the most effective way to minimize induced drag is to increase aspect ratio. Designs also have large taper ratios which is motivated by the structural model in order to reduce deformations. This also leads to a large chord length at the root, particularly in swept wings where the loading is high. The stiffer structures that arise in larger swept wings create reductions in the tip displacement, U_t. The airfoil sections at the root, mid-section, and tip for each design are shown in Fig. 16.

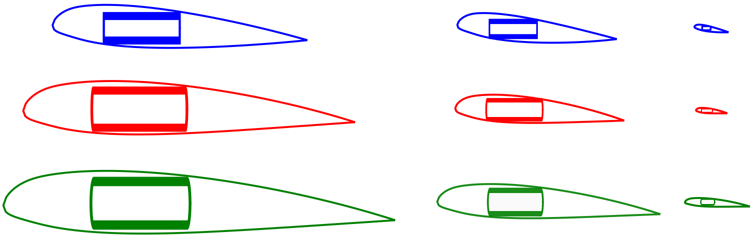

Fig. 16 Cross sections at root, mid-span, and tip (left to right) for $\Lambda = 0°$ (top), $\Lambda = 15°$ (middle), $\Lambda = 30°$ (bottom).

The airfoil parametrization allows a reflex camber line to form in order to aid the fulfillment of the pitching moment constraint. However, only the unswept wing used a reflex camber-line. The swept wings experience higher torsional loads leading to larger twist deformations and the pitching moment constraint to be satisfied in the deformed configuration.

The maximum stress ratio per section is plotted in Fig. 17 for each of the optimized designs. When there is no sweep, the point where the pitching moment is calculated is near-coincident to the beam axis, meaning the pitching moment constraint pushes the torsional loads to near zero (refer to 15). Without torsional loads the optimized design does not converge with curved wall spars as to do so will reduce bending stiffness (Fig. 16). Also, the bending stresses tend to zero towards the tip of the wing, so with low torsional stresses the maximum von Mises stress will also tend to zero towards at the tip as seen in Fig. 17. Stress distributions for the swept wing cases are similar, as are their cross sections (Fig. 16) and loading (Fig. 15). However the loading increases with increasing sweep which requires more stiffness and a larger wingbox. As stated previously, the stiffness distributions give more of an insight into the properties of the beam, these are shown in Fig. 18. Compared to the CRM wing results in Section IV.A, the curved wall spars of these design are more moderate because torsional loads are lower. There is also a larger difference between the flange and spar thicknesses of these designs because bending loads are more dominant. But this difference in wall thickness also means torsional stiffness can be reduced for large-curved spar walls (refer to appendix A).

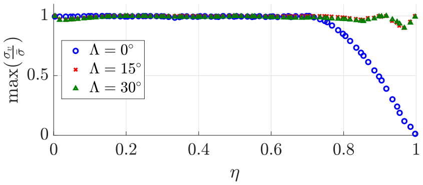

Fig. 17 Maximum stress-ratio in the beam cross-section plotted along the wing for different sweep angles.

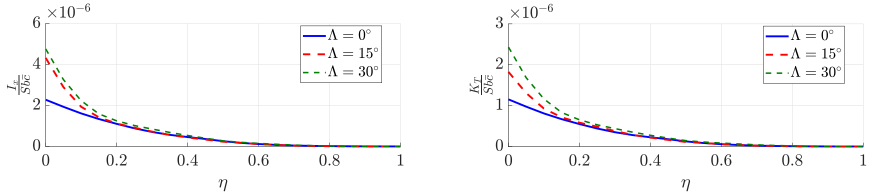

(a) **(b)**

Fig. 18 Bending and torsional stiffness distributions for optimized designs with different sweep angles.

As a comparison we consider the case where $\Lambda = 15°$ and the problem is solved using 1-way coupling. Planform and airfoil sections for the optimized design is shown in Fig. 19. When 1-way coupling is used the design has similar planform to that of 2-way coupled design. However, there are more differences in the cross sections. The twist is reduced towards the tip in order to satisfy the pitching moment constraint in the undeformed configuration. Due to reductions in twist and the 1-way coupling, the torsional loads are lower in this case leading to less-curved spar walls and a shorter width in the wing box (w in Fig. 3). This also provides a reduction in mass, which leads to a lower lift through the equilibrium constraints, and a lower lift-induced drag. From lifting line theory, we know the induced drag is proportional to the square of lift, so the drag will reduce at a faster rate than the lift. This allows the 1-way coupled design to increase the lift to drag ratio to 61.3.

V. Conclusion

The current work introduces a framework for solving aeroelastic optimization problems based on coupled 3D panel and beam finite element methods, with a generalized load-displacement transfer scheme. The framework has proven to work effectively in producing optimized designs with mid-fidelity physics models. Straight and curved wall spars are

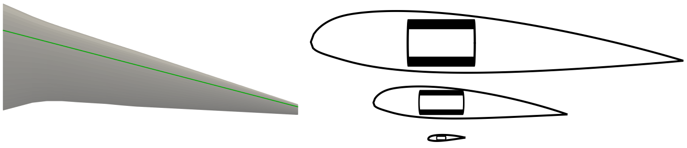

(a) (b)

Fig. 19 Optimized design for 1-way coupling with $\Lambda = 15^\circ$: (a) Planform with beam axis shown in green, (b) cross sections at root (top), mid-span (middle), and tip (bottom).

compared based on their performance in compliance minimization and stress-constrained problems. In both cases, the curved wall spars have proven to achieve better designs as they offer more design freedom to create trade-offs between torsional and bending stiffness. This confirms the predictions presented in [27] where curved wall spars first appeared. Comparisons are presented between 1- and 2-way coupling methods where it is shown that the change in loading for deformed configurations can have a significant effect on the optimized design and its performance. This highlights the importance of calculating loads in the deformed configuration and solving the aeroelastic problem to convergence. The current beam parametrization method represents a simplified wingbox that is used to demonstrate the capabilities of the MDO framework and arrive at the conclusions previously stated. However, the methods presented here can easily be extended to a more advanced cross-sectional parametrization and analysis for sectional stiffness properties. Alternatively, the current parametrization method is robust enough to allow a large variance in stiffness properties along the wing whilst remaining physical. These span-wise stiffness distributions can be realized post-optimization using more common aerospace structures such as spar and rib configurations.

Appendices

A. Effect of curved spar walls

Consider a single beam cross section parameterized as described in Section II.C. Fig. 20 plots the relative difference in stiffness properties, Δ, when spar walls become increasingly more curved. The spar walls are straight for $^e/_h = 0$ and semi-circular for $^e/_h = 0.5$. The torsional stiffness for thin walled sections is defined as

$$K_T = \frac{4A_s^2}{\oint \frac{ds}{t(x_b, z_b)}} \tag{26}$$

where s is the perimeter of the wingbox defined by the wall's centerline, A_s is the area enclose by s, and t is the wall thickness.

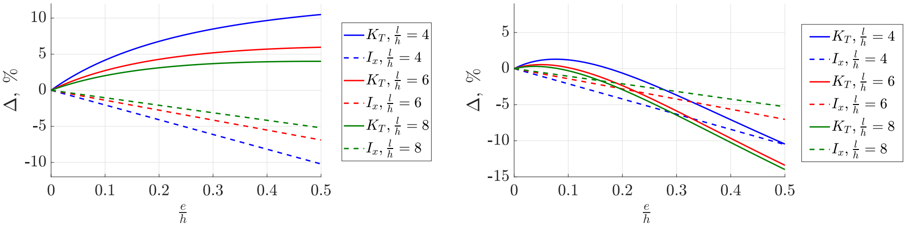

(a) $\frac{a}{s} = 1$ **(b)** $\frac{a}{s} = 10$

Fig. 20 Effect on torsional and bending stiffness by curving the spar walls for two different spar-flange thickness ratios.

Increasing the curvature of the spar walls can lead to increased torsional stiffness but reductions in bending stiffness. For a constant wall thickness the torsional stiffness is proportional to the square of the cross-sectional area over the perimeter. This is why cylinders represents the optimal design for purely torsional loads, and why we see an increase in torsional stiffness for curved wall spars. However, these relationships can also vary with the differences in thickness between spars and flanges, where it is less advantageous for common thick-flange, thin-webbed beam structures. This is due to the beam parametrization method as when the spar walls curve some material is also removed from the flanges. If the flanges are thicker than the spars, then by equation (26), the thickness of the flange can have a larger contribution to the torsional stiffness. In this way, large-curved spar walls will remove more material from the flange leading to reductions in torsional stiffness.

B. Stress analysis

Four stress states exist the beam: longitudinal stress; torsional stress; and shear stress in the two transverse directions. These stresses are defined for a thin-walled Timoshenko beam as follows

$$\sigma_L = E(\varepsilon_y + \kappa_z x_b - \kappa_x z_b) \tag{27}$$

$$\tau_T = \frac{G K_T}{2 A t(x_b, z_b)} \kappa_y \tag{28}$$

$$\tau_{F_x} = \frac{G A Q_z(x_b, z_b)}{I_z t(x_b, z_b)} \varepsilon_x \tag{29}$$

$$\tau_{F_z} = \frac{G A Q_x(x_b, z_b)}{I_x t(x_b, z_b)} \varepsilon_z \tag{30}$$

where x_b and z_b are local coordinates on the cross section at the point of stress evaluation, t is the local thickness, and Q is the first moment of area.

In the assumptions of thin-walled cross sections the shear direction is defined by the shear flow, and the total shear, τ_x and τ_z, is the sum of the individual contributions, τ_T, τ_{F_x}, and τ_{F_z} [34]. The shear flow diagrams for our cross section are shown in Figs. 21a-21c. The maximum von Mises stress can occur at a possible 16 locations in a given cross section (shown in Fig. 21d). The exact location will depend on the loading conditions of the beam. Von Mises stress is calculated at each of these 16 locations in the cross sections via

$$\sigma_v = \sqrt{{\sigma_y}^2 + 3({\tau_x}^2 + {\tau_z}^2)} \tag{31}$$

C. Sensitivity analysis

All sensitivities are calculated via a discrete adjoint method. Consider the objective/constraint function f expressed in augmented Lagrangian form as

$$\mathcal{F} = f(\boldsymbol{\mu}, \mathbf{U}, \mathbf{d}) + \boldsymbol{\lambda}_a^{\mathrm{T}} \mathbf{R}_a(\boldsymbol{\mu}, \mathbf{U}, \mathbf{d}) + \boldsymbol{\lambda}_b^{\mathrm{T}} \mathbf{R}_b(\boldsymbol{\mu}, \mathbf{U}, \mathbf{d}) \tag{32}$$

where $\boldsymbol{\lambda}_a$ and $\boldsymbol{\lambda}_b$ are Lagrangian multipliers for aerodynamic and beam models respectively. The total derivative of $\mathcal{F}$ with respect to $\mathbf{d}$ is derived to be

$$\frac{d\mathcal{F}}{d\mathbf{d}} = \frac{\partial f}{\partial \mathbf{d}} + \boldsymbol{\lambda}_a^{\mathrm{T}} \left[\frac{\partial \mathbf{A}}{\partial \mathbf{d}} \boldsymbol{\mu} + \frac{\partial \mathbf{B}}{\partial \mathbf{d}} \boldsymbol{\sigma} + \mathbf{B} \frac{\partial \boldsymbol{\sigma}}{\partial \mathbf{d}} \right] + \boldsymbol{\lambda}_b^{\mathrm{T}} \left[\frac{\partial \mathbf{K}}{\partial \mathbf{d}} \mathbf{U} - \frac{\partial \mathbf{P}}{\partial \mathbf{d}} \right] \tag{33}$$

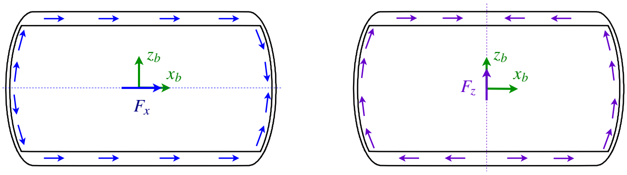

(a) **Shear flow for shear force, F_x** (b) **Shear flow for shear force, F_z**

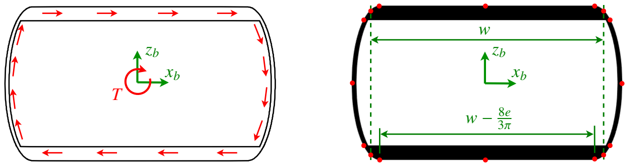

(c) **Shear flow for torsion, T** (d) **Stress evaluation points**

Fig. 21 Methods for stress evaluation.

where the operator $\frac{\partial}{\partial \mathbf{d}}$ captures only explicit dependence on **d**, and $\boldsymbol{\lambda}_a$ and $\boldsymbol{\lambda}_b$ are calculated through solving the following adjoint equations

$$\begin{aligned} \boldsymbol{\lambda}_a^{\mathrm{T}}\mathbf{A} - \boldsymbol{\lambda}_b^{\mathrm{T}}\frac{\partial \mathbf{P}}{\partial \boldsymbol{\mu}} &= -\frac{\partial f}{\partial \boldsymbol{\mu}} \\ \boldsymbol{\lambda}_a^{\mathrm{T}}\left[\frac{\partial \mathbf{A}}{\partial \mathbf{U}}\boldsymbol{\mu} + \frac{\partial \mathbf{B}}{\partial \mathbf{U}}\boldsymbol{\sigma} + \mathbf{B}\frac{\partial \boldsymbol{\sigma}}{\partial \mathbf{U}}\right] + \boldsymbol{\lambda}_b^{\mathrm{T}}\left[\mathbf{K} - \frac{\partial \mathbf{P}}{\partial \mathbf{U}}\right] &= -\frac{\partial f}{\partial \mathbf{U}} \end{aligned} \tag{34}$$

or

$$\frac{\partial \mathbf{R}}{\partial \mathbf{s}}^{\mathrm{T}}\boldsymbol{\lambda} = -\frac{\partial f}{\partial \mathbf{s}} \tag{35}$$

with $\boldsymbol{\lambda} = \{\boldsymbol{\lambda}_a \ \boldsymbol{\lambda}_b\}^{\mathrm{T}}$.

Funding Sources

This work is funded by the Villum Foundation under the InnoTop VILLUM investigator project.

References

[1] Haftka, R. T., "Optimization of flexible wing structures subject to strength and induced drag constraints," *AIAA Journal*, Vol. 15, No. 8, 1977, pp. 1101–1106. doi:https://doi.org/10.2514/3.7400.

[2] Grossman, B., Strauch, G. J., Eppard, W. M., Gurdal, Z., and Haftka, R. T., "Integrated aerodynamic/structural design of a sailplane wing," *Journal of Aircraft*, Vol. 25, No. 9, 1988, pp. 855–860. doi:https://doi.org/10.2514/3.45670.

[3] Martins, J. R., Alonso, J. J., and Reuther, J. J., "High-fidelity aerostructural design optimization of a supersonic business jet," *Journal of Aircraft*, Vol. 41, No. 3, 2004, pp. 523–530. doi:https://doi.org/10.2514/1.11478.

[4] Barcelos, M., and Maute, K., "Aeroelastic design optimization for laminar and turbulent flows," *Computer Methods in Applied Mechanics and Engineering*, Vol. 197, No. 19-20, 2008, pp. 1813–1832. doi:https://doi.org/10.1016/j.cma.2007.03.009.

[5] Kenway, G. K., Kennedy, G. J., and Martins, J. R., "Scalable parallel approach for high-fidelity steady-state aeroelastic analysis and adjoint derivative computations," *AIAA Journal*, Vol. 52, No. 5, 2014, pp. 935–951. doi:https://doi.org/10.2514/1.j052255.

[6] Brooks, T. R., Kenway, G. K., and Martins, J. R., "Benchmark aerostructural models for the study of transonic aircraft wings," *AIAA Journal*, Vol. 56, No. 7, 2018, pp. 2840–2855. doi:https://doi.org/10.2514/1.j056603.

[7] Unger, E. R., Haftka, R. T., Grossman, B., and Mason, W. H., "Efficient optimization of integrated aerodynamic-structural design," *International Journal for Numerical Methods in Engineering*, Vol. 28, No. 3, 1989, pp. 593–607. doi:https://doi.org/doi:10.1002/nme.1620280308.

[8] Grossman, B., Polen, D. M., Sobieszczanski-Sobieski, J., Haftka, R. T., Kao, P.-J., and Rais-Rohani, M., "Integrated aerodynamic-structural design of a transport wing," *Journal of Aircraft*, Vol. 27, No. 12, 1990, pp. 1050–1056. doi:https://doi.org/10.2514/3.45980.

[9] Jasa, J. P., Hwang, J. T., and Martins, J. R., "Open-source coupled aerostructural optimization using Python," *Structural and Multidisciplinary Optimization*, Vol. 57, No. 4, 2018, pp. 1815–1827. doi:https://doi.org/10.1007/s00158-018-1912-8.

[10] Chauhan, S., Shamsheer, and Martins, R. R. A., Joaquim, "Low-fidelity aerostructural optimization of aircraft wings with a simplified wingbox model using OpenAeroStruct," *Engopt 2018 Proceedings of the 6th International Conference on Engineering Optimization*, 2018, pp. 418–431. doi:https://doi.org/10.1007/978-3-319-97773-7_38.

[11] Dunning, P. D., Stanford, B. K., and Kim, H. A., "Coupled aerostructural topology optimization using a level set method for 3D aircraft wings," *Structural and Multidisciplinary Optimization*, Vol. 51, No. 5, 2015, pp. 1113–1132. doi:https://doi.org/10.1007/s00158-014-1200-1.

[12] Vassberg, J. C., DeHaan, M. A., Rivers, S. M., and Wahls, R. A., "Development of a common research model for applied CFD validation studies," *Collection of Technical Papers - AIAA Applied Aerodynamics Conference*, 2008. doi:https://doi.org/10.2514/6.2008-6919.

[13] Kennedy, G. J., and Martins, J. R. R. A., "A parallel aerostructural optimization framework for aircraft design studies," *Structural and Multidisciplinary Optimization*, Vol. 50, No. 6, 2014, pp. 1079–1101. doi:https://doi.org/10.1007/s00158-014-1108-9.

[14] Kennedy, G. J., and Martins, J. R. R. A., "Parallel solution methods for aerostructural analysis and design optimization," *13th AIAA/ISSMO Multidisciplinary Analysis and Optimization Conference*, American Institute of Aeronautics and Astronautics Inc., 2010. doi:https://doi.org/10.2514/6.2010-9308.

[15] Kennedy, G. J., and Martins, J. R. R. A., "A comparison of metallic and composite aircraft wings using aerostructural design optimization," *12th AIAA Aviation Technology, Integration and Operations (ATIO) Conference and 14th AIAA/ISSMO Multidisciplinary Analysis and Optimization Conference*, American Institute of Aeronautics and Astronautics Inc., 2012. doi:https://doi.org/10.2514/6.2012-5475.

[16] James, K. A., Kennedy, G. J., and Martins, J. R. R. A., “Concurrent aerostructural topology optimization of a wing box,” *Computers and Structures*, Vol. 134, 2014, pp. 1–17. doi:https://doi.org/10.1016/j.compstruc.2013.12.007.

[17] Chin, T. W., and Kennedy, G. J., “Large-scale compliance-minimization and buckling topology optimization of the undeformed common research model wing,” *57th AIAA/ASCE/AHS/ASC Structures, Structural Dynamics, and Materials Conference*, American Institute of Aeronautics and Astronautics Inc., 2016. doi:https://doi.org/10.2514/6.2016-0939.

[18] Goetzendorf-Grabowski, T., and Mieloszyk, J., “Common computational model for coupling panel method with finite element method,” *Aircraft Engineering and Aerospace Technology*, Vol. 89, No. 5, 2017, pp. 654–662. doi:https://doi.org/10.1108/AEAT-01-2017-0044.

[19] Mieloszyk, J., and Goetzendorf-Grabowski, T., “Introduction of full flight dynamic stability constraints in aircraft multidisciplinary optimization,” *Aerospace Science and Technology*, Vol. 68, 2017, pp. 252–260. doi:https://doi.org/10.1016/j.ast.2017.05.024.

[20] Kenway, G., and Martins, J. R., “Aerostructural shape optimization of wind turbine blades considering site-specific winds,” *12th AIAA/ISSMO Multidisciplinary Analysis and Optimization Conference, MAO*, 2008, pp. 2008–6025. doi:https://doi.org/10.2514/6.2008-6025.

[21] Ashuri, T., Zaaijer, M., Martins, J., van Bussel, G., and van Kuik, G., “Multidisciplinary design optimization of offshore wind turbines for minimum levelized cost of energy,” *Renewable Energy*, Vol. 68, 2014, pp. 893 – 905. doi:https://doi.org/10.1016/j.renene.2014.02.045.

[22] Zahle, F., Tibaldi, C., Pavese, C., McWilliam, M., Blasques, J. P. A. A., and Hansen, M. H., “Design of an aeroelastically tailored 10 MW wind turbine rotor,” *Journal of Physics: Conference Series (online)*, Vol. 753, No. 6, 2016, p. 062008. doi:10.1088/1742-6596/753/6/062008.

[23] Wang, Z., Suiker, A. S., Hofmeyer, H., van Hooff, T., and Blocken, B., “Coupled aerostructural shape and topology optimization of horizontal-axis wind turbine rotor blades,” *Energy Conversion and Management*, Vol. 212, 2020, p. 112621. doi:https://doi.org/10.1016/j.enconman.2020.112621.

[24] Sessarego, M., Feng, J., Ramos García, N., and Horcas, S. G., “Design optimization of a curved wind turbine blade using neural networks and an aero-elastic vortex method under turbulent inflow,” *Renewable Energy*, Vol. 146, 2020, pp. 1524–1535. doi:https://doi.org/10.1016/j.renene.2019.07.046.

[25] McWilliam, M., Lawton, S., and Crawford, C., “Towards a framework for aero-elastic multidisciplinary design optimization of horizontal axis wind turbines,” *51st AIAA Aerospace Sciences Meeting including the New Horizons Forum and Aerospace Exposition*, ???? doi:https://doi.org/10.2514/6.2013-200.

[26] McWilliam, M. K., “Towards multidisciplinary design optimization capability of horizontal axis wind turbines,” Ph.D. thesis, University of Victoria, 2015.

[27] Aage, N., Andreassen, E., Lazarov, B. S., and Sigmund, O., "Giga-voxel computational morphogenesis for structural design," *Nature*, Vol. 550, No. 7674, 2017, pp. 84–86. doi:https://doi.org/10.1038/nature23911.

[28] Conlan-Smith, C., Ramos-García, N., Sigmund, O., and Schousboe Andreasen, C., "Aerodynamic shape optimization of aircraft wings using panel methods," *AIAA Journal*, Published online May 2020. doi:https://doi.org/10.2514/1.J058979.

[29] Yu, W., Volovoi, V. V., Hodges, D. H., and Hong, X., "Validation of the variational asymptotic beam sectional analysis," *AIAA Journal*, Vol. 40, No. 10, 2002, pp. 2105–2112. doi:10.2514/2.1545.

[30] Yu, W., Hodges, D. H., and Ho, J. C., "Variational asymptotic beam sectional analysis - An updated version," *International Journal of Engineering Science*, Vol. 59, 2012, pp. 40–64. doi:10.1016/j.ijengsci.2012.03.006.

[31] Blasques, J. P. A. A., *User's Manual for BECAS: A cross section analysis tool for anisotropic and inhomogeneous beam sections of arbitrary geometry*, Risø DTU - National Laboratory for Sustainable Energy, 2012.

[32] Drela, M., *Flight vehicle aerodynamics*, MIT Press, 2014.

[33] Ramos García, N., Sørensen, J., and Shen, W., "Three-dimensional viscous-inviscid coupling method for wind turbine computations," *Wind Energy*, Vol. 19, No. 1, 2016, p. 67–93. doi:https://doi.org/10.1002/we.1821.

[34] Parnes, R., *Solid mechanics in engineering*, Wiley,, 2001.

[35] Giavotto, V., Borri, M., Mantegazza, P., and Ghiringhelli, G., "Anisotropic beam theory and applications," *Computers and Structures*, Vol. 16, No. 1-4, 1983, pp. 403–413. doi:https://doi.org/10.1016/0045-7949(83)90179-7.

[36] Martins, J. R., Alonso, J. J., and Reuther, J. J., "A coupled-adjoint sensitivity analysis method for high-fidelity aero-structural design," *Optimization and Engineering*, Vol. 6, No. 1, 2005, pp. 33–62. doi:https://doi.org/10.1023/B:OPTE.0000048536.47956.62.

[37] Svanberg, K., "The method of moving asymptotes - a new method for structural optimization," *International Journal for Numerical Methods in Engineering*, Vol. 24, No. 2, 1987, pp. 359–373. doi:https://doi.org/10.1002/nme.1620240207.

[38] Le, C., Norato, J., Bruns, T., Ha, C., and Tortorelli, D., "Stress-based topology optimization for continua," *Structural and Multidisciplinary Optimization*, Vol. 41, No. 4, 2010, pp. 605–620. doi:https://doi.org/10.1007/s00158-009-0440-y.

[39] Maute, K., and Allen, M., "Conceptual design of aeroelastic structures by topology optimization," *Structural and Multidisciplinary Optimization*, Vol. 27, No. 1-2, 2004, pp. 27–42. doi:https://doi.org/10.1007/s00158-003-0362-z.

[40] Stanford, B. K., and Dunning, P. D., "Optimal topology of aircraft rib and spar structures under aeroelastic loads," *Journal of Aircraft*, Vol. 52, No. 4, 2015, pp. 1298–1311. doi:https://doi.org/10.2514/1.C032913.

Publication [P3]

Cian Conlan-Smith, Néstor Ramos-García, and Casper Schousboe Andreasen. “Aerodynamic shape optimization of non-planar wings”. In: *Journal of Aircraft* (2020). Submitted/under review.

Aerodynamic shape optimization of non-planar wings

Cian Conlan-Smith [*], Néstor Ramos-García [†] and Casper Schousboe Andreasen [‡]
Technical University of Denmark, DK-2800 Lyngby, Denmark.

Aircraft wings are commonly designed with non-planar geometry, such as winglets, in order to improve aerodynamic efficiency. This work presents a method for generating non-planar wing designs through gradient-based optimization, which is then used to investigate the performance characteristics of non-planar wings. The non-planar parameterization is defined to give a large design space that allows the formation of highly non-planar features and permits large changes to the geometry. Aerodynamic characteristics are captured using an inviscid 3D panel method with approximations for viscous drag. The methodology is demonstrated by optimizing reference wings from literature and comparing aerodynamic performance. Investigations are also performed on the differences between raised and drooped wings, and how these designs can improve on the performance of planar wings. Results suggest that the converged designs and their performance is highly dependent on how the geometry is restricted. If a large design space is provided, both raised and drooped wings are able to produce designs with similar performance when only inviscid analysis is considered. When accounting for viscous effects, results suggest that drooped wings are not beneficial for drag reduction.

Nomenclature

$\mathbf{A}$ = doublet aerodynamic influence coefficient matrix

a = x-coordinate of quarter chord curve

$\mathbf{B}$ = source aerodynamic influence coefficient matrix

b = wingspan

C_d = $\frac{d}{\frac{1}{2}\rho_\infty V_\infty^2 c}$, sectional drag coefficient

C_D = $\frac{D}{\frac{1}{2}\rho_\infty V_\infty^2 S}$, drag coefficient

C_{D_i} = $\frac{D_i}{\frac{1}{2}\rho_\infty V_\infty^2 S}$, induced drag coefficient

C_l = $\frac{l}{\frac{1}{2}\rho_\infty V_\infty^2 c}$, sectional lift coefficient

C_L = $\frac{L}{\frac{1}{2}\rho_\infty V_\infty^2 S}$, lift coefficient

---

[*] PhD student, Department of Mechanical Engineering, Section of Solid Mechanics, cicosm@mek.dtu.dk. Member AIAA.

[†] Senior Researcher, Department of Wind Energy, Section of Aero and Fluid Dynamics.

[‡] Associate Professor, Department of Mechanical Engineering, Section of Solid Mechanics.

C_P = pressure coefficient

c = chord length

d = sectional drag

D = drag

D_i = induced/inviscid drag

D_v = viscous drag

e = efficiency factor

L = lift

$\boldsymbol{n}$ = normal vector

q = z-coordinate of quarter chord curve

S = wing planform area

V = velocity

$\mathbf{x}$ = design variables

α = angle of attack

α_i = induced angle of attack

η = $\frac{2y}{b}$, normalized span location

μ = doublet strength

ρ = density

σ = source strength

Æ = $\frac{b^2}{S}$, aspect ratio

Subscripts

t = associated with wingtip

∞ = associated with freestream

I. Introduction

Studies on optimal designs for aircraft wings date back to at least the 1920s where Munk [1] derived that an elliptically loaded planar wing is required to achieve a minimum induced drag. This has since become common knowledge where an elliptic planform wing is the optimal design for planar, untwisted, unswept wings. When considering non-planar and swept wings there is no definitive optimal design, however certain non-planar wings have been shown to improve efficiencies beyond that of the elliptic wing. The most notable early study in this area comes from Cone [2] who derived a mathematical basis for achieving an optimal span loading for non-planar wings in order to minimize induced drag.

Recent years have seen a growing interest in bio-inspired wing design, in order to achieve designs that are believed to be close to optimal. The motivation is that birds have naturally evolved over the course of millions years to develop highly efficient wings. Van Dam [3], inspired by the caudal fins of fish, studied the performance of crescent shaped wings and found that the aerodynamic efficiency of an elliptic wing can be improved by introducing a backward curved sweep. Lazos [4] compared different bio-inspired wing configurations to the elliptic wing to demonstrate the possible gains in efficiency. The most noteworthy configuration is a hyper elliptic cambered span (HECS) drooped wing, which was inspired by the shape of seagull wings in high-speed gliding flight, and produced a large lift-to-drag ratio over a wide range of C_L values. The concept of a drooped wing is represented in Fig. 1, where spanwise camber of the wing is downward (or drooped) compared to more traditional wings which may be raised to create features such as a winglet. Lazos and Visser [5] later compared different HECS wing designs with conventional wing configurations (such as a tapered wing with winglet) which also demonstrated large gains in lift-to-drag ratios.

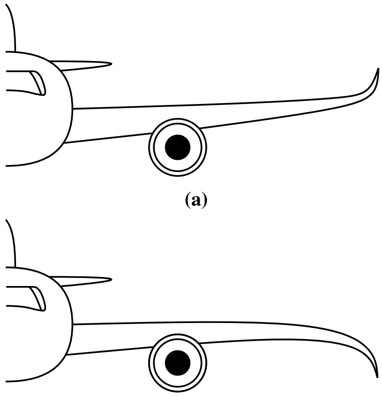
(a)

(b)

Fig. 1 Concept for (a) raised and (b) drooped wings.

Nguyen et al. [6] conducted parameter studies on the aeroelastic performance of aircraft wing concepts, where the authors present large reductions in drag when drooped wings are utilized. The drooped wing designs here are again motivated by seagull wings in gliding flight. Khosravi and Zingg [7] conducted aeroelastic optimization studies of drooped wings which produce efficiency gains of up to 5% compared to optimized planar wings.

There are also some conflicting studies that did not predict increased performance for drooped wings. Ranjan et al. [8] performed drag minimization studies on both raised and drooped HECS wings with tapered unswept planforms. The optimization procedure was based on Cone's method of optimal span loading which predicted the same performance for raised and drooped HECS wings. Solving the RANS equations post-optimization showed that raised wings outperformed drooped, but both improved on the elliptic wing. Liersh et al [9], and Pomeroy and Visser [10] both present studies on spanwise cambered elliptic wings and found that reductions in drag was achieved with raised wings, but not with drooped wings. However, the wings were drooped to a much lesser extent than those in previously mentioned studies, with inclinations of up to 15 degs and 30 degs respectively, versus almost 90 degs.

The literature has mixed conclusions on whether drooped wings offer a more efficient alternative to more conventional raised winglet designs. However, there are few examples in literature where these comparisons are based on designs achieved through numerical optimization procedures. Of those examples that have treated this as an optimization problem, most have done so with a relatively restricted design space.

The current work applies gradient-based optimization routines to design non-planar wings whose geometry is defined on a spanwise sectional basis, thus creating a large design space. Subsequently the method is used to investigate the potential gains for optimizing non-planar wings compared to planar and non-planar designs presented in literature, the differences in performance of raised and drooped wings, and explanations behind these differences. The authors have previously developed a framework for aerodynamic and aeroelastic shape optimization based on panel methods [11, 12], which has been extended to include non-planar wing parameterizations and viscous drag approximations in the current work. The following section will discuss the non-planar parametrization and discretization of the model. Panel methods are summarized in Section III, including lift and drag calculation methods. The results section is subdivided into 3 subsections detailing a comparison of optimized designs to those in the literature, an investigation on raised vs. drooped wings, and a study accounting for viscous effects. Finally, the findings are concluded in Section V.

II. Discretization & parameterization

The design parameterization and panel discretization of the wing is shown in Fig. 2. A series of airfoil sections are assembled on a discrete quarter chord curve that is defined by control points on the curve with x-coordinates, $\boldsymbol{a}$, and z-coordinates, $\boldsymbol{q}$. The airfoil sections are defined within a plane that is normal to the quarter chord curve from the perspective of the x-axis. Within this plane, airfoils have a twist angle, θ, measured from the x-axis. The control points on the quarter chord curve are defined with a half cosine distribution in the y-direction, quadrilateral panels are defined between each set of neighboring airfoil sections, and all problems are solved with a mesh size of 40x100, i.e. 41 airfoil sections are defined.

The sectional parameters $\boldsymbol{c}$, $\boldsymbol{a}$, $\boldsymbol{q}$ and $\boldsymbol{\theta}$, shown in Fig. 2, can be controlled using design variables, $\mathbf{x}$. Design variables are used to define $\boldsymbol{\theta}$ explicitly at each section, but all other design variables define the change in the parameter, e.g. $\delta\boldsymbol{q}$, where $q_{j+1} = q_j + \delta q_{j+1}$. By defining the design variables in this manner it is easy to enforce that parameters are monotonically increasing/decreasing along the span, avoiding fluctuating geometries and requiring less regularization.

To ensure smooth designs and avoid numerical artefacts the design variables are filtered with neighboring sections in the spanwise direction as described in [11]. Previous work has demonstrated that when an inviscid model is used only small improvements can be gained by optimizing airfoil sections along the wing [11]. In the current work, the focus is on investigating the potential gains of non-planar geometry, and as such all examples will use constant NACA0012 airfoil

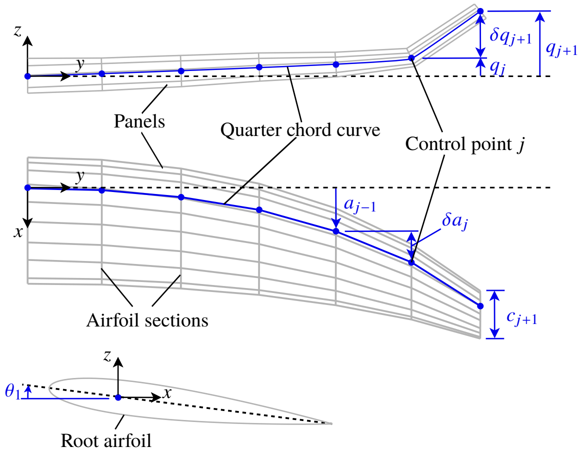

Fig. 2 Parametrization of the wing geometry with elevation (top), planform (middle), and root airfoil (below). A quarter-chord curve is defined by parameters a and q, where airfoils are assembled normal to the curve from the perspective of the x-axis.

profiles throughout the span. However, all methods can easily be extended to allow varying cross sections [11, 12].

III. Panel Methods

The aerodynamic characteristics are captured using a 3D panel method introduced in previous works [11–13]. A Dirichlet boundary condition is implemented using constant source-doublet panels for the wing, and constant doublet panels in the wake. The governing equation for the panel method is defined as

$$\mathbf{A}(\mathbf{x}, \boldsymbol{\mu})\boldsymbol{\mu} + \mathbf{B}(\mathbf{x})\boldsymbol{\sigma}(\mathbf{x}) = \mathbf{0} \tag{1}$$

where $\boldsymbol{\mu}$ and $\boldsymbol{\sigma}$ are doublet and source strengths, and $\mathbf{A}$ and $\mathbf{B}$ are aerodynamic influence coefficients (AIC) for doublet and source distributions respectively. Derivations of AIC's are provided in [14], and using a zero-internal perturbation formulation yields $\sigma_k = \boldsymbol{V}_\infty \cdot \mathbf{n}_k$, where $\mathbf{n}_k$ is the normal vector of panel k. The doublet strength $\boldsymbol{\mu}$, can then be solved for using (1).

Once the doublet distribution is known, $\boldsymbol{\mu}$ can be differentiated numerically over the surface of the wing to yield the velocity, $\boldsymbol{V}_k$, at panel k's center. Given the surface velocities, the coefficient of pressure can be calculated via the Bernoulli equation.

$$C_{P,k} = 1 - \frac{\| \boldsymbol{V}_k \|^2}{V_\infty^2} \tag{2}$$

Lift and drag could be calculated from C_P distributions, however, surface pressure integration is prone to numerical errors which can create non-physical results for unconventional wing designs. As the optimizer is likely to exploit these numerical weaknesses, a Trefftz integration method is used which has proven to be less susceptible to numerical errors [11, 15]. Using Trefftz plane integration, the lift and induced drag can be calculated as

$$D_i = -\frac{1}{2}\rho_\infty \sum_{j=1}^{N_s} \mu_j s_j \boldsymbol{v}_j . \boldsymbol{n}_j \tag{3}$$

$$L = \rho_\infty V_\infty \sum_{j=1}^{N_s} \mu_i \cos(\beta_j) s_j \tag{4}$$

where s_j, β_j, and $\boldsymbol{n}_j$ are the length, orientation, and normal vector of the wake panel in the Trefftz plane at section j, and N_s is the number of panels in the spanwise direction. The wake geometry is described by projecting the trailing edge downstream in the freestream direction, and extends 30 semispans downstream. Velocities in the Trefftz plane, $\boldsymbol{v}_j$, are calculated using the circulation around the wake panel edge, Γ_k as defined in [16]

$$\boldsymbol{v}_j = \frac{1}{2\pi} \sum_{k=1}^{N_s} K_k \Gamma_k \frac{\hat{\boldsymbol{x}} \times \mathbf{r}_{jk}}{||\mathbf{r}_{jk}||^2} \tag{5}$$

where $\hat{\boldsymbol{x}}$ is the normal vector of the Trefftz plane, $\mathbf{r}_{jk}$ is a spatial vector between the wake panel edge and the calculation point j, and K_k is a kernel which desingularizes the vortex core and is defined using the definition in [17] as

$$K = \frac{||\mathbf{r}_{jk}||^2}{\left(r_c^{2\zeta} + ||\mathbf{r}_{jk}||^{2\zeta}\right)^{\frac{1}{\zeta}}} \tag{6}$$

where r_c is the viscous core radius which we define as 20% of the chord length, and ζ is taken to be 2 which represents a Lamb–Oseen vortex model.

The total drag is then computed as the sum of induced and viscous drag, i.e. $D = D_i + D_v$, where viscous drag can be calculated as

$$D_v = \frac{1}{2}\rho_\infty V_\infty^2 \sum_{j=1}^{N_s} c_j s_j C_{d,j} \tag{7}$$

where s_j is the length of the wing section j, and $C_{d,j}$ the local drag coefficient. C_d is calculated from 2D airfoil data (generated via XFoil [18]) by interpolating with respect to the local effective angle of attack, α_{ef}, and Reynolds number. It is important to note that as C_d is calculated using 2D airfoil data, spanwise flow is not considered in the viscous drag calculation.

Airfoils are defined in the center of each wing section within in a plane normal to the quarter chord line as shown in Fig. 3a. The Reynolds number is calculated using the freestream velocity within the airfoil plane and the chord length at each wing section. A method is introduced for calculating the effective angle of attack for non-planar wings. Other than

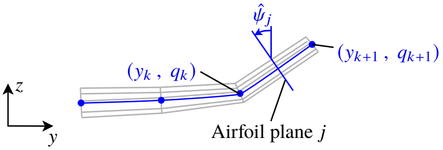

(a) *y*-*z* plane

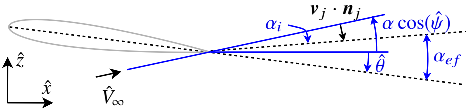

(b) Airfoil plane *j*

Fig. 3 Schematic indicating angles for effective angle of attack calculation: (a) definition of airfoil plane, and (b) airfoil section with relevant angles.

non-planar geometry, the method also accounts for twist, freestream angle of attack, and induced angle of attack.

The effective angle of attack is measured within the airfoil plane shown in Fig. 3, where a reference system, $(\hat{x}, \hat{z})$, is defined within the plane such that $\hat{x}$ is parallel with the global x-axis. The freestream velocity within the plane is then

$$\hat{\boldsymbol{V}}_\infty = \{V_{\infty,x}\ ,\ V_{\infty,z}\cos(\hat{\psi}) - V_{\infty,y}\sin(\hat{\psi})\}^{\mathrm{T}} \tag{8}$$

where $\hat{\psi}$ is the inclination of the wing section as represented in Fig. 3a. sin and cos terms can be calculated from the control points on the quarter chord curve as

$$\sin(\hat{\psi}_j) = \frac{q_{k+1} - q_k}{\sqrt{((y_{k+1} - y_k)^2 + (q_{k+1} - q_k)^2)}} \quad , \quad \cos(\hat{\psi}_j) = \frac{y_{k+1} - y_k}{\sqrt{((y_{k+1} - y_k)^2 + (q_{k+1} - q_k)^2)}} \tag{9}$$

The effective angle of attack can be calculated as the sum of angles shown in Fig. 3b

$$\alpha_{ef} = \hat{\alpha} + \hat{\theta} - \alpha_i \tag{10}$$

where $\hat{\alpha}$ is angle of attack within the plane which can be calculated from $\hat{\boldsymbol{V}}$, $\hat{\theta}$ is the twist of the wing section, and α_i is the induced angle of attack. The induced angle of attack is calculated using the downwash velocity in the Trefftz plane, $\boldsymbol{v}_j$

$$\{\alpha_i\}_j = \tan^{-1}\left(\frac{\boldsymbol{v}_j.\boldsymbol{n}_j}{||\hat{\boldsymbol{V}}_\infty||}\right) \simeq \frac{\boldsymbol{v}_j.\boldsymbol{n}_j}{||\hat{\boldsymbol{V}}_\infty||} \tag{11}$$

where α_i is in-plane with the airfoil section. Note that $\hat{\theta}$ is associated with the wing section, as opposed to θ, in Fig. 2, which represent values at the control points.

IV. Results

In this section, optimization procedures will be used to maximize the aerodynamic performance of the wing. One important parameter for comparing the performance of aircraft wings is the span efficiency factor defined as

$$e = \frac{C_L^2}{\pi A\!\!\!R C_{D_i}} \tag{12}$$

where $A\!\!\!R$ is the wing's aspect ratio, and only the induced drag is considered. The parameter, e, compares the efficiency of a wing to that of an elliptic wing which has a value $e = 1$. The efficiency is constant for a given wing irrespective of angle of attack or freestream velocity (for incompressible inviscid flow). An alternative parameter for characterizing performance is the lift-to-drag ratio, ${}^{L}/_{D}$, where typically the viscous drag is also included. Unlike e, ${}^{L}/_{D}$ varies with angle of attack and freestream velocity. When viscous drag is not included, ${}^{L}/_{D}$ is unrealistically high for low angles of attack and singular for zero lift as there will be no induced drag. If viscous drag is included, ${}^{L}/_{D}$ will be small for low and high angles of attack, and have an optimum α where ${}^{L}/_{D}$ is at a maximum.

Optimization studies are solved using the gradient-based method of moving asymptotes [19], where the initial design is a rectangular untwisted planar wing with all constraints satisfied. All sensitivity analysis is conducted using a discrete adjoint approach where gradient derivations can be found in [11].

A. A Comparison with Reference Designs

Consider the optimization problem defined in (13), where the objective is to maximize the efficiency factor, e, with a fixed aspect ratio, $A\!\!\!R$, and constraints on a and q values at the wingtip (notated by subscript t).

$$\begin{aligned}
\min_{\mathbf{x}\,\in\,\mathbb{R}^{N_\mathrm{x}}} \quad &: \; -e(\mathbf{x}, \boldsymbol{\mu}) \\
\text{subject to} \quad &: \; A\!\!\!R(\mathbf{x}) = A\!\!\!R_0 \\
&\quad |a_t(\mathbf{x})| \le \bar{a}_t \\
&\quad |q_t(\mathbf{x})| \le \bar{q}_t \\
&\quad \underline{\mathrm{x}} \le \mathrm{x}_j \le \bar{\mathrm{x}} \quad \text{for } j = 1, \ldots, N_\mathrm{x}
\end{aligned} \tag{13}$$

Optimized designs are compared to three reference cases from the literature where each wing has the same aspect ratio, $A\!\!\!R_0 = 7$. The three reference wings are shown in Fig. 4a-c. The first case is has a standard elliptic planform which is the known optimal design for planar, unswept, untwisted wings. The second is a planar crescent wing introduced in [3], which was motivated by caudal fins of fish and has an elliptic chord and sweep distribution. The final reference case is a non-planar wing with a hyper-elliptic cambered span (HECS). The HECS wing was introduced in [4] and was motivated by the shape of seagull wings in gliding flight. By allowing specific design variables we can create appropriate comparisons to these reference wings. An elliptic wing will correspond to solving (13) with only chord length defined by design variables, i.e. $\mathbf{x} = \delta\mathbf{c}$. Likewise the crescent and HECS wings can be compared to designs achieved with $\mathbf{x} = \{\delta\mathbf{c}, \delta\boldsymbol{a}\}$ and $\mathbf{x} = \{\delta\mathbf{c}, \delta\boldsymbol{a}, \delta\boldsymbol{q}\}$, respectively. Optimized designs are shown in Fig. 4d-f, and the efficiency of reference and optimized designs are shown in Table 1.

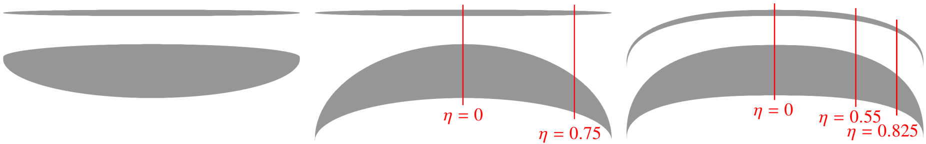

(a) Elliptic **(b)** Crescent **(c)** HECS

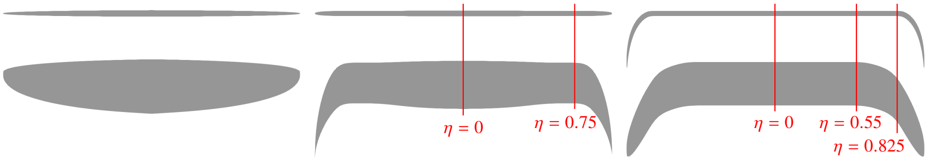

(d) $\mathbf{x} = \delta\mathbf{c}$ **(e)** $\mathbf{x} = \{\delta\mathbf{c}, \delta\boldsymbol{a}\}$ **(f)** $\mathbf{x} = \{\delta\mathbf{c}, \delta\boldsymbol{a}, \delta\boldsymbol{q}\}$

Fig. 4 Elevation and planform views for reference designs, (a)-(c), and optimized designs, (d)-(f). Markers are included at η locations when wings begin to sweep and droop ($\eta = 0$ for reference wings).

Reference	e_{ref}	Optimized	e_{opt}
Elliptic	1.004	$\mathbf{x} = \delta\mathbf{c}$	1.004
Crescent	1.019	$\mathbf{x} = \{\delta\mathbf{c}, \delta\boldsymbol{a}\}$	1.027
HECS	1.178	$\mathbf{x} = \{\delta\mathbf{c}, \delta\boldsymbol{a}, \delta\boldsymbol{q}\}$	1.291

Table 1 Comparison of efficiency factors for reference wings and optimized designs defined by design variables, x. All designs have an aspect ratio of 7.

An elliptic wing is known that to have an efficiency, $e = 1$, which is closely predicted by the model with only a 0.4% error. The optimized design for $\mathbf{x} = \delta\mathbf{c}$ converges to the same elliptic wing and hence the same performance is achieved. As this is the known optimal design, this case helps to validate the optimization procedure.

The crescent wing predicts an increase in efficiency of 1.5% over the elliptic wing. When the crescent wing was first introduced in [3] an increase in efficiency of 8% was predicted. The difference in e is likely due to differences in discretization or drag calculation methods. For example e-factors in Table 1 are achieved with Trefftz plane method, but calculating lift and drag directly from pressure integration yields values of $e = 1.085$, giving a 8.5% increase. Van Dam later conducted experimental investigations into crescent wings and found increases in efficiency of between 2 and 4% [20]. As previously stated, the Trefftz method is used because it less susceptible to numerical error such as discretization errors. Smith [15] demonstrates that e-factors from C_P integration are very the dependent on the mesh, whereas Trefftz plane calculations are not. When setting $\mathbf{x} = \{\delta\mathbf{c}, \delta\boldsymbol{a}\}$, the optimizer converges to a very different planform than that of the crescent wing, and with increase in e of 2.3%. Rather than gradually sweeping the wing, the optimized design is straight until $\eta \simeq 0.75$ before drastically sweeping to create raked wing tips.

The HECS wing produces an increase of 17.4% in efficiency compared to the elliptic wing, whereas the optimized design for $\mathbf{x} = \{\delta\mathbf{c}, \delta\boldsymbol{a}, \delta\boldsymbol{q}\}$ produces 28.7% increase. The optimized design is similar to the HECS wing in that it has produced swept drooped wings. However, the location in which the wings start to sweep and droop are further outboard than the HECS wing, which has a gradual change in sweep and droop from $\eta = 0$. The optimized wing starts to sweep around $\eta \simeq 0.55$, maintains a constant chord until this point, and droops around $\eta \simeq 0.825$. Both constraints on a_t and q_t are active for this case, which indicates that larger e-factors can be achieved if the constraints were relaxed.

We further investigate the location of sweep and droop by taking a closer look at the different HECS wing designs. The geometry of HECS wings are defined by the equation for a hyper ellipse. Using the wing parametrization in Fig. 2, equivalent HECS wing geometries can be achieved through defining hyper elliptic distributions of c, a, and q as

$$\left(\frac{c}{c_{max}}\right)^p + \left(\frac{y}{0.5b}\right)^p = 1 \tag{14a}$$

$$\left(\frac{a_t - a}{a_t}\right)^p + \left(\frac{y}{0.5b}\right)^p = 1 \tag{14b}$$

$$\left(\frac{q_t - q}{q_t}\right)^p + \left(\frac{y}{0.5b}\right)^p = 1 \tag{14c}$$

where for a hyper elliptic distribution $p > 2$, and $p = 2$ corresponds to an elliptic distribution. The reference HECS wing used $p = 2.5$, but with a slightly different definition where leading and trailing edges were defined rather than c and a distributions, refer to [4] for definition. Each equation is defined with the same p-value where q_t and a_t values are defined to be equal to that of the HECS reference wing, and q_t is negative for drooped wings. The aspect ratio is kept constant which corresponds to the following definition for maximum chord length (at the root)

$$c_{max} = \frac{b}{\mathit{AR}} \frac{\mathcal{F}\left(\frac{p+2}{p}\right)}{\mathcal{F}\left(\frac{p+1}{p}\right)^2} \tag{15}$$

where the operator $\mathcal{F}(\square)$ represents the gamma function, which is defined for positive real numbers as

$$\mathcal{F}(u) = \int_0^\infty \exp(-t)t^{u-1}dt \quad \text{where } u \in \mathbb{R}\,,\ u > 0 \tag{16}$$

Fig. 5 shows the change in e-factors for HECS wings produced with different values for p, where the reference HECS is equivalent to the definition in (14) with $p = 2.5$.

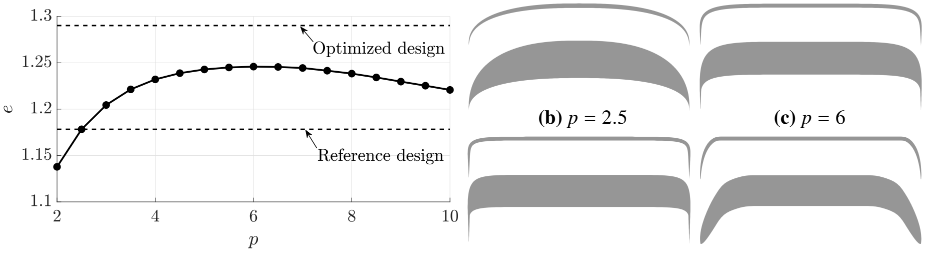

(a)

(b) p = 2.5

(c) p = 6

(d) p = 10

(e) Optimized Design

Fig. 5 (a) Variation in efficiency, e, with respect to the exponent, p, used in the HECS wing definition given in (14)**. e-factors also shown for reference and optimized designs shown in Figs 4c and 4f respectively. (b-d) Wing geometries for different values of p, and (e) Optimized wing geometry**

By increasing the value of p the wing remains approximately planar for a larger portion of the inboard span and the spanwise location where the wing begins to droop is pushed further outboard creating a larger curvature in the cambered span. From Fig. 5a, this HECS parameterization has an optimum p-value where e is maximum at approximately $p = 6$. Referring to Figs. 5c and 5e, the design with $p = 6$ has a similar spanwise camber to that of the optimized design. However, the optimized design has predicted a greater efficiency due to the freedom to deviate from a hyper elliptic distribution, and create different sweep and chord distributions.

B. Raised vs. Drooped Wings

The optimized results shown in Fig. 4 demonstrate that large increases in efficiency can be seen achieved when q-values are allowed to change. But the previous study only permitted drooped wings to form in order to create a comparison with the reference HECS wing. The following studies aim to address the question of whether negative q-values (drooped wings) can achieve a higher efficiency than positive q-values (raised wings), and how the resulting designs achieve gains in efficiency compared to planar wings.

Consider the optimization problem in (17), with the objective to maximize e, and an upper constraint on the wingtip value of q. Here, only one design variable per section is included, $\mathbf{x} = \delta \boldsymbol{q}$, where $\boldsymbol{a} = \mathbf{0}$, and $\boldsymbol{c} = b/\text{Æ}_0$ to give a rectangular planform with an aspect ratio equal to that of previous studies.

$$\begin{aligned} \min_{\mathbf{x} \in \mathbb{R}^{N_\mathrm{x}}} \quad & : \; -e(\mathbf{x}, \boldsymbol{\mu}) \\ \text{subject to} \quad & : \; |q_t(\mathbf{x})| \leq \bar{q}_t \\ & \quad \underline{\mathrm{x}} \leq \mathrm{x}_j \leq \bar{\mathrm{x}} \qquad \text{for} \;\; j = 1, \ldots, N_\mathrm{x} \end{aligned} \tag{17}$$

Optimization results are shown in Fig. 6 for $q > 0$ and $q < 0$, and are compared to a planar wing of equal planform. Spanwise lift and drag distributions, as well as C_p distributions at specific cross sections are shown in Fig. 7 for an angle of attack of 3.5 deg, and efficiency factors for each design are given in Table 2.

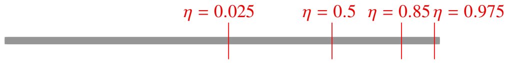

(a) Planar, $q = 0$

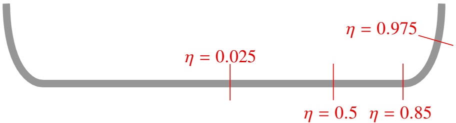

(b) Rasied, $q > 0$

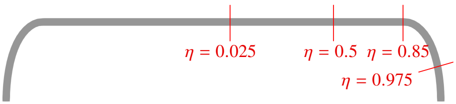

(c) Drooped, $q < 0$

Fig. 6 Front views for (a) planar rectangular wing, (b) optimized design for $q > 0$, and (c) optimized design for $q < 0$. Specific sections are labeled in each case, which corresponds to the loading shown in Fig. 7.

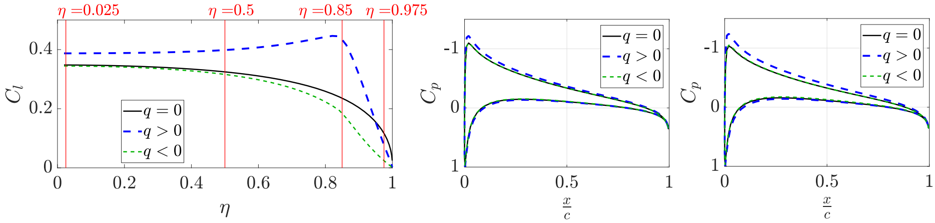

(a) Lift distribution **(c)** C_p at $\eta = 0.025$ **(d)** C_p at $\eta = 0.5$

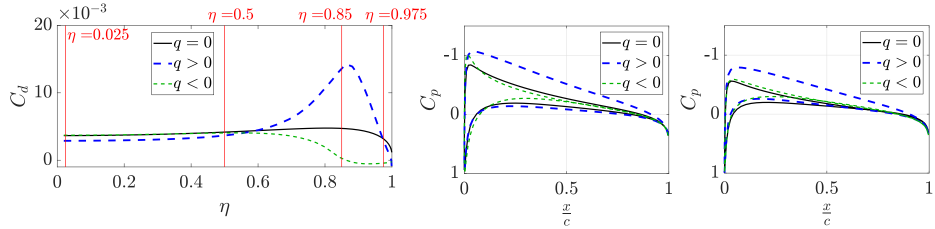

(b) Drag distribution **(e)** C_p at $\eta = 0.85$ **(f)** C_p at $\eta = 0.975$

Fig. 7 Loading of wings shown in Fig. 6. (a) and (b) show spanwise lift and drag distributions respectively, where cross sectional C_p distributions at the labeled η locations is shown in (c)-(f).

Both raised and drooped wings converge to the maximum wingtip bound on q. They also have a similar q-distribution where one is roughly the negative of the other. Both wings remain planar until $\eta \simeq 0.85$. However, there is a large difference in the efficiency factors, where compared to the rectangular planar wing, the drooped wing achieves a 24% increase, and the raised wing only a 16% increase.

Wing	e
Planar, $q = 0$	0.980
Raised, $q > 0$	1.138
Drooped, $q < 0$	1.219

Table 2 Efficiency factors for the rectangular planform wings shown in Fig. 6

The spanwise lift and drag distributions in Fig. 7a-b provide a greater insight into these differences in efficiency between the three wing designs. When the wings are raised there is an induced lift along the span of the wing, but also an increase in drag towards the tip. This increase in lift improves the efficiency but is hindered by the increase in drag. The opposite occurs for the drooped wings where the lift is reduced, and there is a large reduction in drag towards the tip. A similar trend to the lift distributions can be seen in the accompanying C_P distributions in Fig. 7c-f where the pressure difference has increased throughout the span for raised wings, and reduced towards the tip for drooped wings. The gains in efficiency from raised and drooped wings are due to achieving an increased lift and reduced drag respectively, but based on Fig. 7 alone it is not clear why this behavior is seen.

Using Cone's method of optimal spanwise loading [2] there should be no difference in efficiency between optimal raised and drooped wings for this optimization problem. The gain in performance of drooped wings is usually described as a result shifting the wingtip vortex core further outboard away from the wing [5]. However, this phenomena cannot be predicted by the current wake model, nor can it be predicted by the potential flow based models used in many of the studies presented in the literature that experienced an improved performance for drooped wings, e.g. [6, 8, 9, 21]. Liersch et al [9] offer an alternative explanation where the difference is due to effects of induced velocities parallel to the freestream, which can be demonstrated with the current model.

From the C_p distributions shown Fig. 7c-f it is clear that the velocity across the upper surface has increased for raised wings, and at some sections, reduced for drooped wing. There is also a clear pressure difference between upper and lower surfaces in each case along the entire span of wing. Therefore, we know there is a circulation in the sections towards the wingtips which will induce a velocity. By raising or drooping the wing these induced velocities will behave differently. To demonstrate this, we define a scalar $\bar{V}$ as the velocity normalized by the freestream and projected in the freestream direction i.e.

$$\bar{V} = \frac{\boldsymbol{V}}{\|\boldsymbol{V}_\infty\|} \cdot \frac{\boldsymbol{V}_\infty}{\|\boldsymbol{V}_\infty\|} = \frac{1}{\|\boldsymbol{V}_\infty\|^2}\boldsymbol{V} \cdot \boldsymbol{V}_\infty \tag{18}$$

Fig. 8 shows $\bar{V}$ within a cut plane at the quarter point, $\frac{x}{c} = 0.25$, for planar, raised and drooped wings. The raised wing has significantly increased the velocity in the freestream direction along the entire upper surface. This corresponds with an increase in lift seen in Fig. 7a which peaks when the wing begins to cant upwards, also corresponding to the largest velocity in Fig. 8. For the drooped wing, the inboard velocities are very similar to the planar wing. Towards the tip the induced velocities are reduced (compared to the planar wing) on the upper surface and are larger on the lower surface. As the difference between upper and lower surfaces reduces so too does the pressure difference, and both lift and drag is significantly reduced.

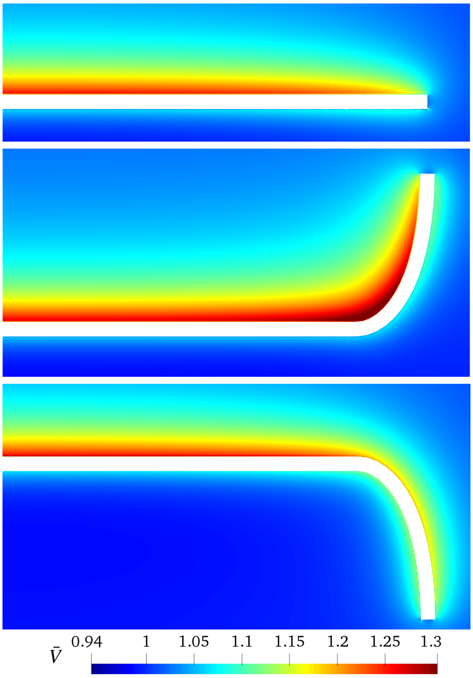

Fig. 8 Normalized velocity projected in the freestream direction, $\bar{V} = \frac{1}{\|\boldsymbol{V}_\infty\|^2}\boldsymbol{V} \cdot \boldsymbol{V}_\infty$, for planar (top), raised (middle), and drooped (bottom) rectangular wings. Cut plane defined at quarter chord point.

The induced drag is directly related to the induced downwash in the wake. Off-stream velocity vectors in the Trefftz plane are shown in Fig. 9 for the planar, raised, and drooped wings. As expected the planar wing has a distinct circulation around the tip of the wake. When the wing is raised, the flow above the wake in region $0.5 < \eta < 1$ has a larger vertical component than is seen for the planar wing. This corresponds to a larger downwash which gives the increase in drag in Fig. 7b. For both the planar and raised wings, there is a downwash everywhere in the flow for $\eta < 1$, i.e. the vertical component of velocity is negative. When the wing is drooped, there is a positive vertical component to the velocity above the wake in the region $0.85 < \eta < 1$. In the same region, the velocity below the wake is negative, meaning the potential jump (or downwash) over the wake should be close to 0, thus producing very little drag. This is also clearly seen in this region in Fig. 7b. Note that the vectors in Fig. 9 indicate the velocity direction only, and the vector magnitudes do not represent the magnitude of velocity.

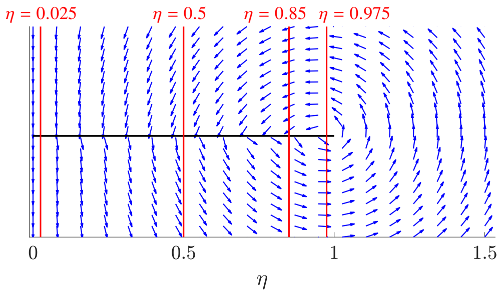

(a) Planar, $q = 0$

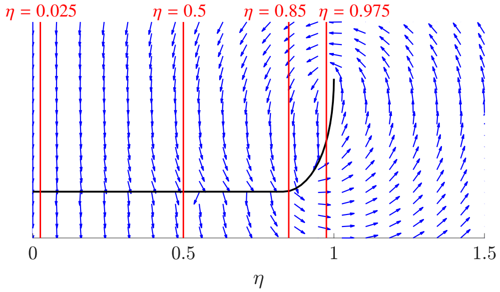

(b) Raised, $q > 0$

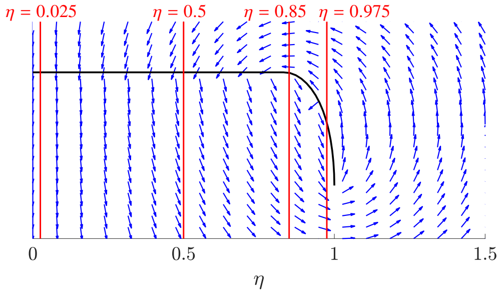

(c) Drooped, $q < 0$

Fig. 9 Velocity vectors in the Trefftz plane for (a) planar, (b) raised, and (c) drooped wings. Vectors are used to indicate direction only, where vector magnitudes are not representative of velocity magnitudes.

From Table 2 one would assume that drooped wings are superior to raised wings as they can create a larger gain in efficiency. However, the optimization study in (17) has a restricted design space as only q was allowed to change and the chord distribution was fixed. In most practical designs the wing will taper towards the tip, which in the case for raised wings would alleviate some the increased drag experienced towards the tip in Fig. 7b. The optimization problem in (13) is solved again for both raised and drooped wings with $\mathbf{x} = \{\delta \boldsymbol{c}, \delta \boldsymbol{a}, \delta \boldsymbol{q}\}$ and different values of $\bar{q}_t$, where q_0 is the original value of $\bar{q}_t$ from previous studies. Optimized designs are shown in Fig. 10 with lift and drag distributions shown in Fig. 11 and efficiency factors are given in Table 3.

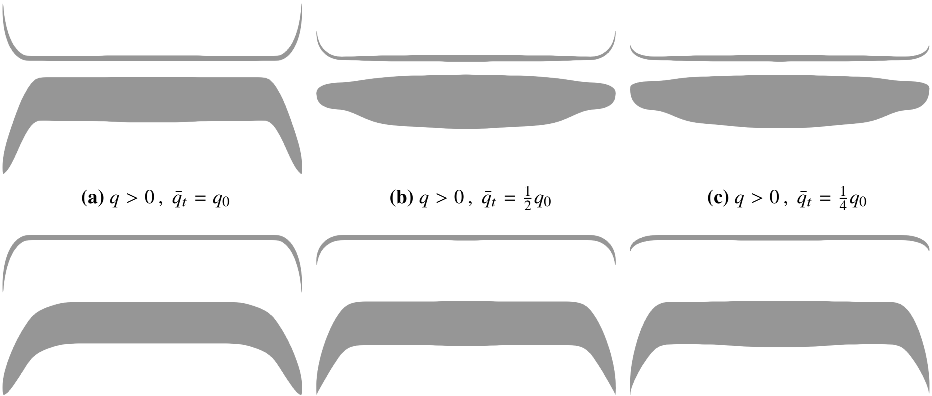

(a) $q > 0\,,\ \bar{q}_t = q_0$ (b) $q > 0\,,\ \bar{q}_t = \frac{1}{2}q_0$ (c) $q > 0\,,\ \bar{q}_t = \frac{1}{4}q_0$

(d) $q < 0\,,\ \bar{q}_t = q_0$ (e) $q < 0\,,\ \bar{q}_t = \frac{1}{2}q_0$ (f) $q < 0\,,\ \bar{q}_t = \frac{1}{4}q_0$

Fig. 10 Elevation and plan views of optimized designs for raised ($q > 0$) and drooped ($q < 0$) wings with different bounds on q_t.

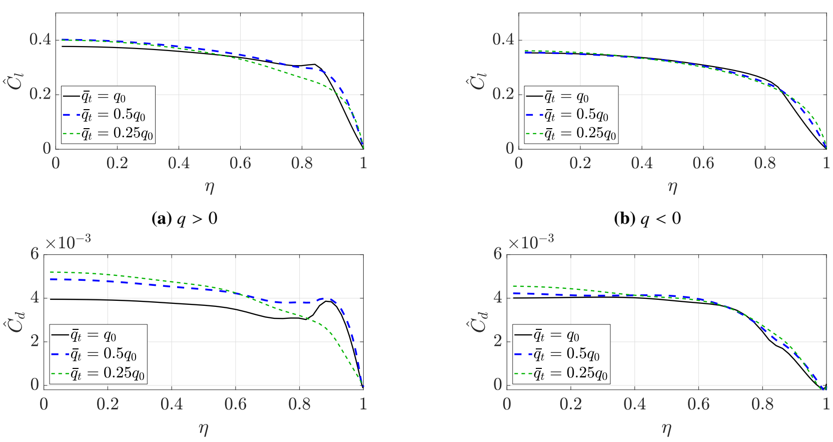

(a) $q > 0$ (b) $q < 0$

(c) $q > 0$ (d) $q < 0$

Fig. 11 Lift and drag distributions for designs shown in Fig. 10, where lift and drag coefficients represented with a circumflex are calculated using the mean aerodynamic chord.

As shown in Table 3, drooped and raised wings achieve efficiency factors with negligible differences for a given bound on q_t. This study has increased the design space such that the maximum efficiency can be achieved irrespective of whether the wings are raised or drooped. The raised wings in this case are able to match the performance of the drooped wings by reducing the peak in drag towards the tip by tapering the wing, compare Figs 11c and 7b. Drooped

$\bar{q}_t$	$q > 0$	$q < 0$
q_0	1.290	1.291
$\frac{1}{2}q_0$	1.152	1.157
$\frac{1}{4}q_0$	1.074	1.078

Table 3 Efficiency factors for the designs shown in Fig. 10.

designs have created sweep which has the effect of increasing lift towards the tip [22] (Fig. 11a), but this also eliminates the low drag region seen in Fig. 7b. The optimizer has then created a trade-off between increasing lift and decreasing drag in order to maximize e.

Each drooped wing in Fig. 10 has a similar planform, but with small differences in c and a distributions where lower bounds on q_t have a shorter chord length at the tip, and larger bounds on q_t have a more gradual change in a. When the wings are raised with a large bound on q_t the design converges to a similar planform to that of the drooped wings but with a larger sweep towards the tip. As the constraint on q_t is restricted one would expect the converged designs to tend towards the equivalent design for a planar wing, shown in Fig. 4e. The drooped wing in Fig. 10f does have a similar planform, but the raised wing designs tend towards the elliptic wing. This suggests that large sweep can have negative effects for raised wingtips. To demonstrate this, analysis was conducted on the designs in Fig. 10 where they are solved upside-down, and efficiency factors are presented in Table 4.

$\bar{q}_t$	Opt. $q > 0$	Opt. $q < 0$
q_0	1.267	1.267
$\frac{1}{2}q_0$	1.118	1.109
$\frac{1}{4}q_0$	1.051	1.039

Table 4 Efficiency factors for the designs shown in Fig. 10, when upside-down.

All wings see a reduction in e when solved upside-down. As stated previously, e should be constant irrespective of angle of attack, but they have changed when the sign on α has changed. This is due to differences in induced velocities when the wing is raised or drooped as discussed previously. For large values of q_t there is no difference in e between designs optimized for raised or drooped wings. For low q_t the designs with large-raked wingtips perform worse when the wing is raised relative to the freestream (i.e. design optimized for drooped wings). To further demonstrate the effect of sweep on optimized designs, the problem in (17) is solved with no sweep, i.e. $\mathbf{x} = \{\boldsymbol{c}, \boldsymbol{q}\}$, where $\bar{q}_t = \frac{1}{4}q_0$, and result are shown in Fig. 12. Both raised and drooped wings satisfy the maximum bound of q_t, and produce efficiency factors of 1.074 and 1.055 respectively. Compared to the designs where sweep was included (Fig. 10) the raised wing converges to the same design, with the same efficiency, but the efficiency of the drooped wing has decreased significantly.

In the introduction it was discussed how the literature has contradicting results on whether raised or drooped wings

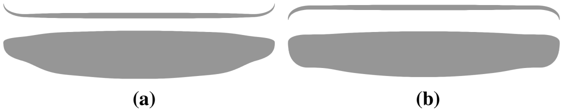

Fig. 12 Elevation and plan views of unswept optimized designs for (a) raised and (b) drooped wings.

can outperform one another. Tables 2–4 give similar contradictions which arise based on how the design space is restricted. Allowing a large design space achieves designs with negligible differences in e between raised or drooped wings with the same geometry restrictions. Results also presented here suggest not only that including sweep is crucial for improving performance in drooped but it can also reduce performance in raised wings. However, up to now the design space has also been somewhat restricted as twist has not yet been considered as a design variable, which grants more freedom to vary the span loading.

The literature also contains an important point of discussion on how the aspect ratio is defined when comparing the efficiency of planar and non-planar wings. In the previous examples $\mathcal{R}$ is defined using the projected wingspan and planform area, as this is the standard definition. However, in using this definition it is not surprising that a non-planar wing can produce a large improvement in efficiency since the lifting surface has been increased without cost to the optimization problem. An alternative approach is to define these parameters using the unfolded wing geometry based on the curved length of the wing. When comparing planar and non-planar wings this difference in the geometry definition produces very different results and has been discussed in detail in [9, 23]. When solving the optimization problem with the aspect ratio defined from the unfolded wing geometry the designs converge to the same planar wings in Fig. 4d or 4e depending on whether a is included as a design variable. In general, we note that if the curved geometry is constrained, the design will always converge to a planar wing with the maximum allowable wingspan. However, in aircraft design there is usually a constraint on the wingspan due to structural or practical reasons. With this constraint satisfied, the wing's performance can be improved by creating non-planar geometry.

C. Optimization with Inviscid & Viscous Drag

Creating non-planar geometry may increase e, but the surface area will also increase which will increase the viscous drag. Referring back to the designs presented in Section IV.A, their performance can also be compared with respect to drag coefficients and lift-to-drag ratio, as shown in Fig. 13, where the optimized design refers to the case with $\mathbf{x} = \{\delta \boldsymbol{c}, \delta \boldsymbol{a}, \delta \boldsymbol{q}\}$, shown in Fig. 4f, and all problems are solved with a freestream velocity of Mach 0.4. Fig. 13a plots both inviscid and viscous drag, where the design is optimized with respect to only inviscid drag. The optimized design produces the least inviscid drag for all values of C_L, but produces more viscous drag at low C_L values where the viscous drag is dominant. This is evident also in Fig. 13b where the lift-to-drag ratio is lower for low C_L values, where the optimized wing produced a C_L value of ~ 0.3. However, each wing produces a similar maximum L/D with the optimized design at 32.84 compared to 32.48 and 32.55 with HECS wings $p = 2.5$ and $p = 6$ respectively.

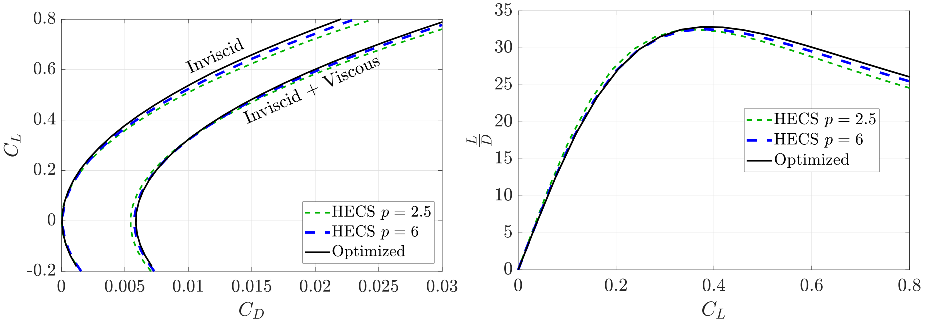

(a) **(b)**

Fig. 13 Comparison between different wings: (a) drag coefficient for a range of lift coefficients for inviscid drag alone and inviscid plus viscous drag, (b) lift-to-drag ratio for viscous solutions.

Consider the optimization problem given in (19), to maximize L/D at a specified C_L, fixed aspect ratio, the same geometry constraint on a_t, and $\bar{q}_t = \frac{1}{2}q_0$. The problem is solved for both raised and drooped wings, with multiple specified values of C_L. In each case, the problem is also solved where only induced drag is consider and where induced and viscous drag is considered. Each problem includes all design variables, i.e. $\mathbf{x} = \{\delta\boldsymbol{c}, \delta\boldsymbol{a}, \delta\boldsymbol{q}, \boldsymbol{\theta}\}$. Note also that by specifying the C_L and Æ the lift is also specified and maximizing L/D is equivalent to minimizing D. Results are shown in Figs 14 and 15 for drooped and raised wings respectively with L/D values shown in Table 5.

$$\begin{array}{lll} \underset{\mathbf{x}\,\in\,\mathbb{R}^{N_\mathrm{x}}}{\min} & : & -\dfrac{L}{D}(\mathbf{x}, \boldsymbol{\mu}) \\ \text{subject to} & : & \text{Æ}(\mathbf{x}) = \text{Æ}_0 \\ & & C_L(\mathbf{x}, \boldsymbol{\mu}) = C_{L_0} \\ & & |a_t(\mathbf{x})| \leq \bar{a}_t \\ & & |q_t(\mathbf{x})| \leq \bar{q}_t \\ & & \underline{\mathrm{x}} \leq \mathrm{x}_j \leq \bar{\mathrm{x}} \qquad \text{for} \;\; j = 1, \ldots, N_\mathrm{x} \end{array} \tag{19}$$

For purely inviscid analysis, each of the raised and drooped wings converged to similar raked wingtip designs where constraints on a_t and q_t are active. In previous problems, the raised wing designs with the same bound on q_t converged to wings which were almost elliptic (refer to 10b). This difference is likely due to the inclusion of twist as a design variable which offers more design freedom to tailor the spanwise load distribution.

Considering cases with only inviscid analysis, there are negligible differences in converged designs with different C_L-values – for both raised and drooped wings. When viscous drag is considered and $C_{L_0} = 0.2$, the constraint on q is

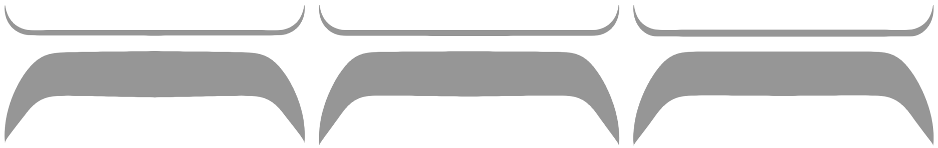

(a) $D = D_i\ ,\ C_{L_0} = 0.2$ **(b)** $D = D_i\ ,\ C_{L_0} = 0.4$ **(c)** $D = D_i\ ,\ C_{L_0} = 0.6$

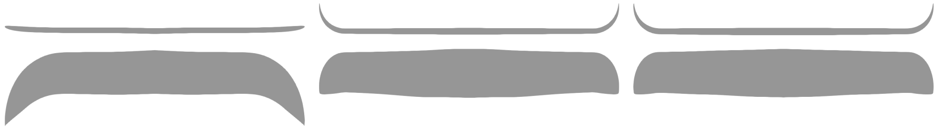

(d) $D = D_i + D_v\ ,\ C_{L_0} = 0.2$ **(e)** $D = D_i + D_v\ ,\ C_{L_0} = 0.4$ **(f)** $D = D_i + D_v\ ,\ C_{L_0} = 0.6$

Fig. 14 Elevation and planform views for converged raised wing designs with (a)-(c) inviscid analysis and (d)-(f) viscous analysis, for different specified values of C_L.

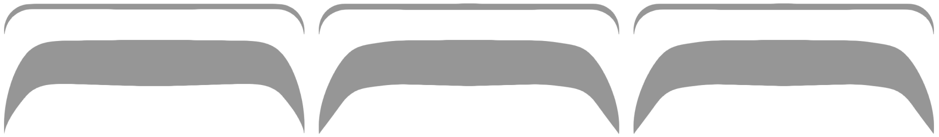

(a) $D = D_i\ ,\ C_{L_0} = 0.2$ **(b)** $D = D_i\ ,\ C_{L_0} = 0.4$ **(c)** $D = D_i\ ,\ C_{L_0} = 0.6$

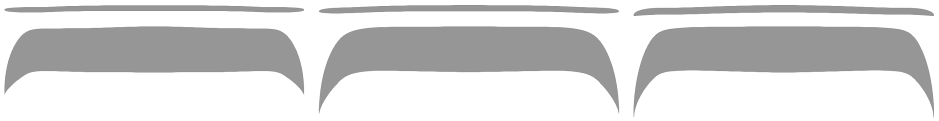

(d) $D = D_i + D_v\ ,\ C_{L_0} = 0.2$ **(e)** $D = D_i + D_v\ ,\ C_{L_0} = 0.4$ **(f)** $D = D_i + D_v\ ,\ C_{L_0} = 0.6$

Fig. 15 Elevation and planform views for converged drooped wing designs with (a)-(c) inviscid analysis and (d)-(f) viscous analysis, for different specified values of C_L.

D	C_{L_0}	$^L/_D$ $q > 0$	$^L/_D$ $q < 0$	$\frac{D_i}{D_i+D_v}$ $q > 0$	$\frac{D_i}{D_i+D_v}$ $q < 0$
D_i	0.2	124.1	123.6	1.0	1.0
D_i	0.4	62.9	62.1	1.0	1.0
D_i	0.6	42.5	42.1	1.0	1.0
$D_i + D_v$	0.2	29.7	29.6	0.256	0.257
$D_i + D_v$	0.4	35.1	33.7	0.521	0.555
$D_i + D_v$	0.6	31.5	29.6	0.685	0.648

Table 5 Lift-to-drag ratios for wings optimized at different C_L values with and without viscous effects, and ratio of induced drag to total drag.

not active in either case. The low C_L value means that the induced drag is low as it will tend to 0 for $C_L = 0$. Because the viscous drag does not tend to zero, it is dominant in these designs where C_L is low, refer to Table 5 columns 5 and 6. Because the viscous drag is dominant, it is not beneficial to increase q as to do so will increase D_v.

When C_{L_0} is increased the induced drag increases much faster than the viscous drag. This makes it beneficial for raised wing designs to create large winglets as to do so will increase the lift. Designs for $q < 0$ do not create drooped wings when viscosity is considered for any value of C_{L_0}. When a larger C_L is specified, there is a large change in a towards the wingtip where designs converge to wings similar to the optimized swept planar wing in Fig. 4e. Increasing a in this manner improves the inviscid efficiency, as demonstrated previously. The fact that drooped wings did not form suggests that the reduction in induced drag as a results of drooping the wing is less than the increase in viscous drag that will also be created.

For each inviscid case, raised and drooped wings produced similar lift-to-drag ratios. This is in keeping with results presented in the previous section where the same e-factors could be achieved regardless of whether wings are raised or drooped. When viscous effects are considered, similar designs are produced for $C_{L_0} = 0.2$, with similar lift-to-drag ratios. When C_{L_0} is increased, the raised wings outperform designs with $q < 0$.

Fig. 16 shows the lift and drag relationships for designs optimized with viscous effects for $C_{L_0} = \{0.2, 0.6\}$. Optimizing with larger C_L values has produced designs with a larger maximum lift-to-drag ratio. The lift-to-drag ratio is highest for raised wing designs with $C_{L_0} = 0.6$, at 34.9, compared to 33.7 with $q < 0$ and 33.1 for both designs with $C_{L_0} = 0.2$.

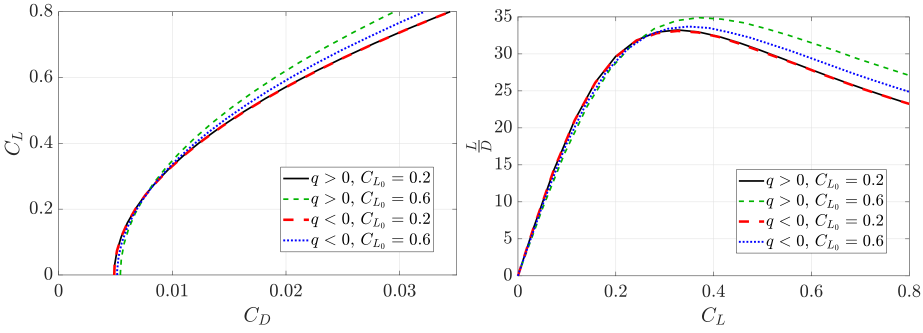

(a) **(b)**

Fig. 16 Lift and drag properties for converged designs with viscous calculations in Figs 14 and 15: (a) drag coefficient and (b) lift-to-drag ratio, for a range of lift coefficients.

It is also important to note that when minimizing the sum of induced and viscous drag, the optimizer may choose to minimize one over the other. This can cause the optimizer to converge to local minima with irregular geometry and equal or worse performance. In order to avoid this bias, it is important to start with a reasonable initial design. As stated previously, each optimization problem presented in this work starts with an initial design of a rectangular wing with no twist and all constraints satisfied. However, similar results have also been achieved with other common planar wing designs such as tapered or elliptic wings. Multiple solutions and local minima for these types of optimization problems with a large design space have also been discussed in the past [24].

V. Conclusions

An optimization procedure is introduced for non-planar wings where design variables are defined locally in order to enlarge the design space. By increasing the design space, the optimizer is able to create large changes to the geometry in order to achieve optimized designs. This is the main advantage of the method which has been able to create designs that predict improved performance over reference wings from literature. The aerodynamic improvements of drooped wings is commonly explained by the effect of shifting the wingtip vortex core further outboard. Results presented here have shown that the benefits of drooped wings can be captured with fixed wake models. It has been demonstrated that the predicted improvements in aerodynamic performance for both raised and drooped wings was due to the effects of induced velocities parallel to freestream, which behave differently depending on whether the wing is raised or drooped. This work also applies the optimization framework to explore the question of which is more efficient, raised or drooped wings? Some studies presented in the literature show raised wings outperforming drooped wings, and other studies present the opposite. It has been shown that optimization studies can also yield conflicting results depending on how the optimization problem is posed. Ultimately, with a large enough design space, raised and drooped wings should be able to converge to designs with equal performance when only inviscid analysis is considered. When viscous approximations were included, drooped wings have not shown to be beneficial.

Acknowledgments

The authors would like to acknowledge and thank the Villum Foundation for the financial support provided through the InnoTop Villum Investigator project.

References

[1] Munk, M. M., *The Minimum Induced Drag of Aerofoils*, NASA Technical Report TR-121, National Aeronautics and Space Administration, 1923.

[2] Cone, C. D. J., *The Theory of Induced Lift and Minimum Induced Drag of Nonplanar Lifting Systems*, NASA Technical Report TR-139, National Aeronautics and Space Administration, 1962.

[3] Van Dam, C., “Efficiency characteristics of crescent-shaped wings and caudal fins,” *Nature*, Vol. 325, No. 6103, 1987, pp. 435–437. doi:https://doi.org/10.1038/325435a0.

[4] Lazos, B. S., “Biologically inspired fixed-wing configuration studies,” *Journal of Aircraft*, Vol. 42, No. 5, 2005, pp. 1089–1098. doi:https://doi.org/10.2514/1.10496.

[5] Lazos, B. S., Visser, K. D., Lazos, B. S., Lazos, B. S., Visser, K. D., and Visser, K. D., “Aerodynamic comparison of Hyper-Elliptic Cambered Span (HECS) wings with conventional configurations,” *Collection of Technical Papers - AIAA Applied Aerodynamics Conference*, Vol. 3, 2006, pp. 1608–1625. doi:https://doi.org/110.2514/6.2006-3469.

[6] Nguyen, N., Trinh, K., Reynolds, K., Kless, J., Aftosmis, M., Urnes, J., and Ippolito, C., “Elastically shaped wing optimization and aircraft concept for improved cruise efficiency,” *51st AIAA Aerospace Sciences Meeting Including the New Horizons Forum and Aerospace Exposition*, 2013.

[7] Khosravi, S., and Zingg, D. W., “Aerostructural optimization of drooped wings,” *Journal of Aircraft*, Vol. 55, No. 3, 2018, pp. 1261–1268. doi:https://10.2514/1.C034605.

[8] Ranjan, P., Ansell, P. J., and James, K. A., “Optimal hyperelliptic cambered span configurations for minimum drag,” *Journal of Aircraft*, Vol. 56, No. 1, 2019, pp. 356–368. doi:https://doi.org/110.2514/1.C034992.

[9] Liersch, C. M., Streit, T., and Visser, K. D., “Numerical implications of spanwise camber on minimum induced drag configurations,” *47th AIAA Aerospace Sciences Meeting Including the New Horizons Forum and Aerospace Exposition*, 2009.

[10] Pomeroy, B. W., and Visser, K. D., “A computational study of induced drag behavior for spanwise cambered wings,” *28th AIAA Applied Aerodynamics Conference*, Vol. 1, 2010. doi:https://doi.org/10.2514/6.2010-4227.

[11] Conlan-Smith, C., Ramos-García, N., Sigmund, O., and Andreasen, C. S., “Aerodynamic Shape Optimization of Aircraft Wings Using Panel Methods,” *AIAA Journal*, Vol. 58, No. 9, 2020, pp. 3765–3776. doi:https://doi.org/10.2514/1.J058979.

[12] Conlan-Smith, C., and Andreasen, C. S., “A coupled 3D panel-beam model for aeroelastic optimization of aircraft wings,” *AIAA Journal*, 2020. Accepted/In press.

[13] Ramos García, N., Sørensen, J., and Shen, W., “Three-Dimensional Viscous-Inviscid Coupling Method for Wind Turbine Computations,” *Wind Energy*, Vol. 19, No. 1, 2016, p. 67–93. doi:https://doi.org/10.1002/we.1821.

[14] Katz, J., and Plotkin, A., *Low-Speed Aerodynamics*, Cambridge Aerospace Series, Cambridge University Press, 2001.

[15] Smith, S. C., *A Computational and Experimental Study of Nonlinear Aspects of Induced Drag*, Technical Paper 3598, National Aeronautics and Space Administration, 1996.

[16] Drela, M., *Flight Vehicle Aerodynamics*, The MIT Press, 2014.

[17] Leishman, J. G., Bhagwat, M. J., and Bagai, A., “Free-Vortex Filament Methods for the Analysis of Helicopter Rotor Wakes,” *Journal of Aircraft*, Vol. 39, No. 5, 2002, pp. 759–775. doi:https://doi.org/10.2514/2.3022.

[18] Drela, M., “XFOIL: An Analysis and Design System for Low Reynolds Number Airfoils,” *Low Reynolds Number Aerodynamics*, edited by T. J. Mueller, Springer Berlin Heidelberg, Berlin, Heidelberg, 1989, pp. 1–12.

[19] Svanberg, K., “The Method of Moving Asymptotes - a New Method for Structural Optimization,” *International Journal for Numerical Methods in Engineering*, Vol. 24, No. 2, 1987, pp. 359–373. doi:https://doi.org/10.1002/nme.1620240207.

[20] Van Dam, C., Vijgen, P., and Holmes, B., “Experimental Investigation on the effect of crescent planform on lift and drag,” *Journal of Aircraft*, Vol. 28, No. 11, 1991, pp. 713–720. doi:https://doi.org/10.2514/3.46087.

[21] Andrews, S. A., Perez, R. E., and Allan, W. D., “Aerodynamic implications of gull’s drooped wing-tips,” *Bioinspiration and Biomimetics*, Vol. 8, No. 4, 2013. doi:https://doi.org/110.1088/1748-3182/8/4/046003.

[22] Nickel, K., and Wohlfahrt, M., *Tailless Aircraft in Theory and Practice*, AIAA education series, American Institute of Aeronautics and Astronautics, 1994.

[23] Streit, T., Visser, K., and Liersch, C., “Minimal induced drag for non-planar lifting surfaces with moderate and small aspect ratio,” *Notes on Numerical Fluid Mechanics and Multidisciplinary Design*, Vol. 112, 2010, pp. 545–553. doi: https://doi.org/110.1007/978-3-642-14243-7_67.

[24] Bons, N. P., He, X., Mader, C. A., and Martins, J. R., “Multimodality in aerodynamic wing design optimization,” *AIAA Journal*, Vol. 57, No. 3, 2019, pp. 1004–1018. doi:https://doi.org/10.2514/1.J057294.

P3

Publication [P4]

Cian Conlan-Smith and Casper Schousboe Andreasen. “Aeroelastic optimization of solid foam core wings subject to large deformations”. In: *AIAA Journal* (2020). To be submitted.

Aeroelastic shape optimization of solid foam core wings subject to large deformations

Cian Conlan-Smith [*], and Casper Schousboe Andreasen [†]
Technical University of Denmark, DK-2800 Lyngby, Denmark.

This work presents studies on aeroelastic shape optimization of aircraft wings subject to large deformations with the objective of minimizing induced drag. The physics are captured using a coupled 3D panel method and a nonlinear co-rotating beam finite element model. The wing is defined by a series of airfoils that are parameterized based on the definition of NACA 4-digit airfoils. The method assumes a solid cross section of isotropic material which is representative of foam core wings. Analytic expressions are derived for most of the cross sectional stiffness properties, while approximations are introduced for the location of the shear center and the torsional stiffness. Optimized designs achieved using linear and nonlinear deformation models are compared and features discussed. Results highlight the importance of capturing nonlinear beam models to accurately capture changes in wingspan due to large deformations, as even small differences in the wingspan can have a large effect on the induced drag. Non-planar wings with raised and drooped wingtips are also optimized, where drooped wings have achieved larger lift-to-drag ratios due to the increase in effective wingspan in the deformed configuration.

Nomenclature

$\mathbf{A}$ = aerodynamic influence coefficient matrix
$\mathbf{B}$ = strain displacement matrix
b = wingspan
C_P = pressure coefficient
c = chord length
$\mathbf{d}$ = design variables
D = drag
$\mathbf{f}$ = applied load
$\mathbf{K}$ = global (tangent) stiffness matrix

---

[*] PhD student, Department of Mechanical Engineering, Section of Solid Mechanics, cicosm@mek.dtu.dk. Member AIAA.

[†] Associate Professor, Department of Mechanical Engineering, Section of Solid Mechanics.

$\mathbf{K}_{cs}$ = constitutive stiffness matrix
L = lift
$\mathbf{m}$ = conjugate moments
m = maximum camber
$\mathbf{n}$ = conjugate forces
$\mathbf{N}$ = shape functions
$\hat{\boldsymbol{n}}$ = normal vector
p = position of maximum camber
q_∞ = $\frac{1}{2}\rho_\infty V_\infty^2$, dynamic pressure
$\mathbf{R}$ = residual vector
$\mathbf{S}$ = skew matrix operator
t = maximum thickness
$\mathbf{T}$ = rotation matrix
V = velocity
W = weight
$\mathbf{x}$ = finite element nodal coordinates
α = twist
η = $\frac{2y}{b}$, normalized span location
μ = doublet strength
ρ = density
σ = source strength
$\boldsymbol{\theta}$ = finite element nodal rotations
Æ = $\frac{b^2}{S}$, aspect ratio

Subscripts

e = associated with finite element
t = associated with wingtip
0 = associated with undeformed configuration
∞ = associated with freestream

I. Introduction

Lift induced drag accounts for roughly 40% of aircraft drag during cruise and up to 90% during climb and takeoff [1]. The most effective way to reduce in the induced drag is to increase the wingspan, but this can have the adverse effect of increasing bending moments and stresses which impose limits on the wingspan. Non-planar wing configurations have shown to improve the efficiency of aircraft wings without increasing the wingspan and subsequent bending moments. Some examples of non-planar wing geometries may include winglets, C-wings, or more unconventional designs such as spanwise cambered or drooped wings. Many challenges are associated with non-conventional wing designs such as drooped wings, such as complicated manufacturing techniques and complex loading conditions which can lead to large deformations. When wings experience large deformations there can also be large change in aerodynamic loading which can lead to a degraded performance.

There are multiple models for capturing large deformations via nonlinear beam finite element methods. One such method is a co-rotating formulation [2, 3] where deflection is defined as a combination of rigid body rotations and deformations with respect to a local reference frame, in which the normal linear constitutive models are satisfied. An alternative method is a multi-body formulation, where the structure is divided into a number of bodies whose local deformations are usually captured via a linear model. This method is adopted in the HAWC2 code [4] which is frequently used for the analysis of wind turbine blades. Hodges [5] developed a mixed formulation method that was used to demonstrate the importance of capturing nonlinear large deformations in predicting dynamic aeroelastic behavior of aircrafts [6].

Beam models are commonly been used for aeroelastic optimization studies. Jasa et al [7] developed an open source aeroelastic framework based on a coupled vortex lattice method (VLM) and Euler beam models. Jansen et al [8] previously applied a similar model to optimize non-planar lifting surfaces where reductions in drag of up to 26% were achieved with optimized designs containing winglets, C-wings, or raked wingtips depending on the problem formulation. Xie et al [9] also used a VLM coupled with a geometrically nonlinear beam finite element model, to conduct aeroelastic optimization studies subject to large deformations and flutter constraints.

3D panel methods have also been used in the past for aeroelastic optimization studies. In these cases, the panel method is usually coupled with shell finite element models. For example, Kennedy et al [10] applied these methods to the design composite wings, Burdette et al [11] to morphing wings that adapt to changing operating conditions throughout a specified mission, and Mieloszyk et al [12] to dynamic stability constrained problems. Another noteworthy contribution comes from James et al [13] who presents a topology optimization study with a coupled panel method and 3D continuum elements.

Higher fidelity aerodynamic models have also been used for aeroelastic optimization studies. Usually the Euler equations are solved, and are coupled to shell finite element models. These include the following notable examples. Khosravi and Zingg [14] who conducted aeroelastic optimization studies of drooped wings and found optimized designs with non-planar geometry could increase aircraft range by 2.6% compared to optimized planar designs. Kenway et al [15, 16] conducted aeroelastic shape optimization studies of the CRM wing [17], where a full aircraft configuration was included in the model. Maute et al [18] conducted topology optimization studies on predefined rib and spar structures.

At this point it is worth noting that apart from [9] each of the aforementioned aeroelastic optimization studies used linear deformation models. However, there are some examples where panel methods have been coupled with nonlinear finite element models without optimization. For example, Gori et al [19] used a co-rotating shell finite element model with an unsteady panel method to model the flapping wings of a micro air vehicle.

The authors have previously developed frameworks for aerodynamic and aeroelastic shape optimization of aircraft wings using a coupled panel method and linear beam finite element model [20–22]. The current work expands on this framework to solve coupled aeroelastic problems subject to large deformations. The finite element model is based on a nonlinear co-rotating beam formulation where elements are locally subject to a generalized Timoshenko constitutive model. Cross sectional stiffness properties are calculated using analytical expressions where possible, which have been derived for the current work, and approximations for properties that cannot be derived analytically. The optimization procedure is applied to the design of both planar and non-planar wings with solid foam cores. The remaining sections of this article are structured as follows. The next section outlines a parameterization for non-planar aircraft wings and the panel-beam discretization. Physics models are discussed in Section III, which includes: the panel method with load calculations, co-rotating beam formulation, beam constitutive model, and the panel-beam coupling procedure. The results section includes comparisons between designs achieved with linear and nonlinear deformation models, and aeroelastic optimization studies for non-planar wings. Finally, the article is concluded in Section V. Three appendices are also included which give information on achieving 3D rotation matrices for the finite element problem, derivations and calculations for cross sectional properties, and equations used to calculate sensitivities.

II. Parameterization Methods

The panel-beam parameterization is shown in Fig. 1, where the external surface of the wing is meshed with quadrilateral panels, and beam finite elements are defined inside in the wing. The first beam node (at the root) lies at the origin, and every other node is defined at a point $(0, \hat{y}, \hat{z})$. Airfoil sections are defined at each node with their quarter chord point coincident to the node. Each airfoil lies within a plane that bisects the angle between finite elements from the perspective of the x-axis.

The airfoil sections are parameterized using the method shown in Fig. 2, which was first introduced in [20]. The parameterization uses the definition of NACA 4-digit profiles [23] which are based on 4 parameters: chord c, maximum thickness t, maximum camber m, and position of maximum camber p. The twist, α, is included as a fifth parameter and is defined from the x-axis, within the same plane as the airfoil.

The structure of the wing is modeled as a solid isotropic cross section which represents a solid foam-core. Cross sectional stiffness properties and centers (labeled in Fig. 2) are achieved using the definitions of NACA 4-digit profiles, as will be discussed in Section III.C.

Design variables, $\mathbf{d}$, are used control the parameters shown in Figs 1 and 2, i.e. $c, t, m, p, \alpha, \hat{z}$. For the parameters,

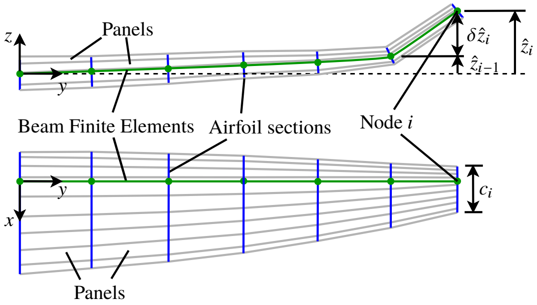
Panels
z
y
$\delta\hat{z}_i$
$\hat{z}_i$
$\hat{z}_{i-1}$
Beam Finite Elements
Airfoil sections
Node i
y
x
c_i
Panels

Fig. 1 Elevation (top) and planform (below) views of the panel-beam discretization and parameterization with important parameters are labeled.

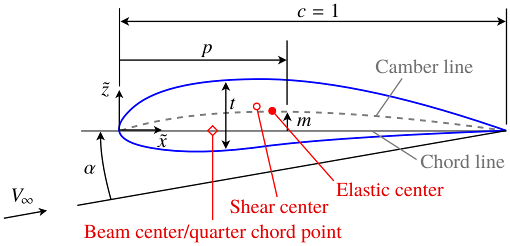
$c = 1$
p
Camber line
$\tilde{z}$
t
m
$\tilde{x}$
Chord line
α
V_∞
Elastic center
Shear center
Beam center/quarter chord point

Fig. 2 Airfoil parameterization with variables and structural centers labeled. The airfoil is defined in a local coordinate system $(\tilde{x}, \tilde{z})$ with its origin at the leading edge, and the $\tilde{x}$-axis co-linear with the chord line.

c and $\hat{z}$, the design variables control the change in these parameters rather than the explicit value, i.e. $\delta\hat{z}$ rather than $\hat{z}$, where $\hat{z}_i = \hat{z}_{i-1} + \delta\hat{z}_i$. This acts as a form of regularization where the parameters are defined such that they are monotonically increasing/decreasing along the span of the wing, thus avoiding fluctuating geometry. Design variables control the values of all other parameters explicitly, and all variables are filtered along the span in order to ensure a smooth variance between cross sections and avoid numerical artifacts [20].

III. Physics Models

This section describes the physics models used in this work and has been divided into four subsections. The first subsection gives a brief introduction to the panel method and includes references to previous work for further details. Subsection III.B describes the finite element implementation for a co-rotating beam model, which can also be reduced to a linear form. Details on the constitutive model are given in Subsection III.C, including descriptions of methods for calculating cross sectional properties. Finally, the load-displacement transfer and solution method for solving the coupled problem are described in Subsection III.D.

A. Panel Method

The aerodynamic performance of the wing is captured using a constant-strength source-doublet panel method as described in [20, 24]. The governing equation for the panel method is defined as

$$\mathbf{A}_{\mu}(\mathbf{u},\mathbf{d})\boldsymbol{\mu} + \mathbf{A}_{\sigma}(\mathbf{u},\mathbf{d})\boldsymbol{\sigma}(\mathbf{u},\mathbf{d}) = \mathbf{0} \tag{1}$$

where $\boldsymbol{\mu}$ is a vector of doublet strengths, $\boldsymbol{\sigma}$ is a vector of source strengths, and $\mathbf{A}_{\mu}$ and $\mathbf{A}_{\sigma}$ are doublet and source aerodynamic influence coefficients (AIC) respectively. Source strengths are defined as $\sigma_i = \boldsymbol{V}_{\infty} \cdot \hat{\boldsymbol{n}}_i$, were $\hat{\boldsymbol{n}}_i$ is the normal vector of panel i, and the doublet strengths are calculated by solving (1). Note that AICs and source strengths are dependent on the design variables, $\mathbf{d}$, and the structural deformations, $\mathbf{u}$.

Once $\boldsymbol{\mu}$ is known, the potential function is numerically differentiated over the panel surfaces to find the surface velocities. Given the surface velocities, the coefficient of pressure is calculated via the Bernoulli equation.

$$C_{P,i} = 1 - \frac{||\ \boldsymbol{V}_i\ ||^2}{||\ \boldsymbol{V}_{\infty}\ ||^2} \tag{2}$$

A Trefftz plane integration method is used to calculate aerodynamic forces as it has proven to be less susceptible discretization errors, compared with surface pressure integration [20, 25]. Using Trefftz plane integration, the lift, drag, and root bending moment are calculated using the following definitions given in [26]

$$D = -\frac{1}{2}\rho_{\infty} \sum_{i=1}^{N_w} \mu_i l_i \boldsymbol{v}_i . \hat{\boldsymbol{n}}_i \tag{3}$$

$$L = \rho_{\infty} V_{\infty} \sum_{i=1}^{N_w} \mu_i \cos(\theta_i) l_i \tag{4}$$

$$M_r = \rho_{\infty} V_{\infty} \sum_{i=1}^{N_w} \mu_i s_i |y_i \cos(\theta_i) + z_i \sin(\theta_i)| \tag{5}$$

where l_i, θ_i, $\hat{\boldsymbol{n}}_i$, and (y_i, z_i) are the length, orientation, normal vector, and center point of the wake panel i in the Trefftz plane. It is important to note that the induced drag is the only type of drag considered in this work.

B. Co-Rotating Beam Formulation

The structural deformations of the wing are captured using a co-rotating formulation with one dimensional beam finite elements. The co-rotating beam theory used in this work is described in detail in [2, 27, 28] and the finite element implementation is only summarized here. Fig. 3 shows a beam element in undeformed and deformed configurations. The local orientation at a distance ζ along a beam element of length l_e is described in 3D space by the rotation matrix, $\mathbf{T} = \{\boldsymbol{t}_1^{\zeta}, \boldsymbol{t}_2^{\zeta}, \boldsymbol{t}_3^{\zeta}\}$.

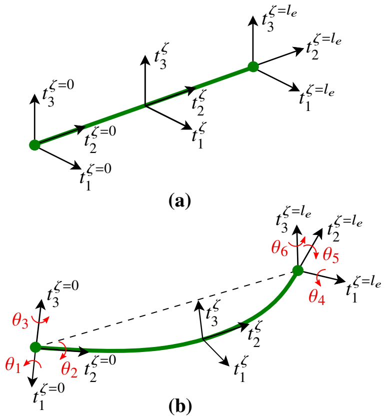

Fig. 3 Local element description with rotational degrees of freedom shown in red. (a) undeformed element, (b) deformed element.

The local orientation, $\mathbf{T}$, is calculated via the procedure outlined in Appendix A using the local rotations, $\boldsymbol{\theta}_\zeta$, which is found by interpolating $\boldsymbol{\theta} = \{\theta_1, \theta_2, \theta_3, \theta_4, \theta_5, \theta_6\}^{\mathrm{T}}$ i.e. $\boldsymbol{\theta}_\zeta = \mathbf{N}(\zeta)\boldsymbol{\theta}$, where $\mathbf{N}$ contains the interpolation functions. Local generalized strains, $\boldsymbol{\varepsilon}$, and curvatures, $\boldsymbol{\kappa}$, are calculated as

$$\boldsymbol{\varepsilon} = \mathbf{T}^{\mathrm{T}}\mathbf{B}\mathbf{x} - \mathbf{T}_0^{\mathrm{T}}\mathbf{B}\mathbf{x}_0 \tag{6a}$$

$$\boldsymbol{\kappa} = \mathbf{T}^{\mathrm{T}}\mathbf{B}\boldsymbol{\theta} \tag{6b}$$

where the subscript 0 describes the undeformed configuration, $\mathbf{B}$ contains the derivative of the interpolation functions, and $\mathbf{x}$ is the coordinates of the finite element nodes in the deformed configuration, i.e. $\mathbf{x} = \mathbf{x}_0 + \Delta\mathbf{x}$. Note also that $\Delta\mathbf{x}$ and $\boldsymbol{\theta}$ can be combined to form the displacement vector, $\mathbf{u} = [\Delta\mathbf{x}, \boldsymbol{\theta}]$. The internal force vector is calculated as

$$\mathbf{p}_e(\mathbf{d}, \mathbf{u}) = \int_0^{l_e} \bar{\mathbf{B}}^{\mathrm{T}}\bar{\mathbf{T}}^{\mathrm{T}}\mathbf{K}_{cs}(\mathbf{d})\bar{\boldsymbol{\varepsilon}}\,dl \tag{7}$$

where $\bar{\boldsymbol{\varepsilon}}$ contains the local strains and curvatures calculated from (6), and $\mathbf{K}_{cs}$ is the constitutive stiffness matrix, which will be discussed in Section III.C. The matrices $\bar{\mathbf{B}}$ and $\bar{\mathbf{T}}$ in (7) are defined as

$$\bar{\mathbf{B}} = \mathbf{B} + \begin{bmatrix} \mathbf{0} & N_1\mathbf{S}(\mathbf{B}\mathbf{x}) & \mathbf{0} & N_2\mathbf{S}(\mathbf{B}\mathbf{x}) & \cdots \\ \mathbf{0} & \mathbf{0} & \mathbf{0} & \mathbf{0} & \cdots \end{bmatrix}^{\mathrm{T}} \tag{8}$$

$$\bar{\mathbf{T}} = \begin{bmatrix} \mathbf{T} & \mathbf{0} \\ \mathbf{0} & \mathbf{T} \end{bmatrix} \tag{9}$$

where the operation $\mathbf{S}(\boldsymbol{a})$ produces a skew matrix defined as

$$\mathbf{S}(\boldsymbol{a}) = \begin{pmatrix} 0 & -a_3 & a_2 \\ a_3 & 0 & -a_1 \\ -a_2 & a_1 & 0 \end{pmatrix} \tag{10}$$

It also important to note that although it is not indicated in the above, $\mathbf{x}$ and $\mathbf{T}$ are dependent on both the design variables and the displacements. It then follows that $\bar{\mathbf{B}}$ and $\bar{\mathbf{T}}$ also hold a dependance on $\mathbf{d}$ and $\mathbf{u}$.

Finally, the element tangent stiffness matrix, $\mathbf{K}_e$, is calculated as

$$\mathbf{K}_e(\mathbf{d}, \mathbf{u}) = \int_0^{l_e} \bar{\mathbf{B}}^{\mathrm{T}} \bar{\mathbf{T}}^{\mathrm{T}} \mathbf{K}_{cs}(\mathbf{d}) \bar{\mathbf{T}} \bar{\mathbf{B}} dl + \mathbf{K}_g(\mathbf{d}, \mathbf{u}) \tag{11}$$

where $\mathbf{K}_g$ is the element geometric stiffness matrix defined as

$$\mathbf{K}_g = \int_0^{l_e} \begin{bmatrix} \mathbf{0} & -\mathbf{S}(\mathbf{n}) B_1 N_1 & \mathbf{0} & -\mathbf{S}(\mathbf{n}) B_1 N_2 & \cdots \\ \mathbf{0} & -\mathbf{S}(\mathbf{m}) B_1 N_1 & \mathbf{0} & -\mathbf{S}(\mathbf{m}) B_1 N_2 & \cdots \\ \mathbf{0} & -\mathbf{S}(\mathbf{n}) B_2 N_1 & \mathbf{0} & -\mathbf{S}(\mathbf{n}) B_2 N_2 & \cdots \\ \vdots & \vdots & \vdots & \vdots & \end{bmatrix} + \begin{bmatrix} \mathbf{0} & \mathbf{0} & \mathbf{0} & \cdots \\ \mathbf{S}(\mathbf{n}) B_1 N_1 & \mathbf{S}(\mathbf{Bx}) \mathbf{S}(\mathbf{n}) N_1 N_1 & \mathbf{S}(\mathbf{n}) B_2 N_1 & \cdots \\ \mathbf{0} & \mathbf{0} & \mathbf{0} & \cdots \\ \mathbf{S}(\mathbf{n}) B_1 N_2 & \mathbf{S}(\mathbf{Bx}) \mathbf{S}(\mathbf{n}) N_1 N_2 & \mathbf{S}(\mathbf{n}) B_2 N_2 & \cdots \\ \vdots & \vdots & \vdots & \end{bmatrix} dl \tag{12}$$

and $\mathbf{n}$ and $\mathbf{m}$ are calculated by solving the constitutive relation $\begin{Bmatrix} \mathbf{n} \\ \mathbf{m} \end{Bmatrix} = \bar{\mathbf{T}} \mathbf{K}_{cs} \bar{\boldsymbol{\varepsilon}}$. It is important to note that this definition of $\mathbf{K}_g$ gives a consistent tangent stiffness matrix. Some methods may make assumptions when deriving the geometric stiffness matrix, such as small strain or neglecting the geometric dependence of $\mathbf{T}$, which will make $\mathbf{K}_g$ inconsistent and can lead to large errors in the sensitivity analysis.

The residual form of the nonlinear beam problem is expressed as

$$\mathbf{R}(\mathbf{d}, \mathbf{u}, \mu) = \mathbf{p}(\mathbf{d}, \mathbf{u}) - \mathbf{f}(\mathbf{d}, \mathbf{u}, \mu) = \mathbf{0} \tag{13}$$

where $\mathbf{f}$ is the external applied load, and $\mathbf{p}$ is the global internal force vector formed from the assembling $\mathbf{p}_e$ vectors calculated via (7). A Newton scheme is used to solve the nonlinear problem, via an incremental load method where the degrees of freedom are updated via

$$\Delta \mathbf{u} = \mathbf{K}^{-1} \mathbf{R} \tag{14}$$

where $\mathbf{K}$ is the global tangent stiffness matrix formed by assembling element stiffness matrices calculated via (11).

In certain cases, a conventional linear beam finite element model will be used for comparison purposes. When a linear model is used, the element descriptions remain the same, but the geometric terms in (11) are neglected and the system is solved by

$$\mathbf{K}(\mathbf{d})\mathbf{u} = \mathbf{f}(\mathbf{d}, \mathbf{u}, \mu) \tag{15}$$

where **K** now has no dependence on **u**. Because the linear model neglects geometric terms it is usually applicable in cases where deformations are small.

C. Constitutive Stiffness Matrix

The constitutive stiffness matrix is defined below, based on a generalized Timoshenko model [29] where isotropic materials are assumed.

$$\mathbf{K}_{cs} = \begin{bmatrix} \mathbf{K}_{11} & \mathbf{K}_{12} \\ \mathbf{K}_{12}^{\mathrm{T}} & \mathbf{K}_{22} \end{bmatrix} \tag{16a}$$

$$\mathbf{K}_{11} = \begin{bmatrix} GA & 0 & 0 \\ 0 & EA & 0 \\ 0 & 0 & GA \end{bmatrix} \tag{16b}$$

$$\mathbf{K}_{12} = \begin{bmatrix} 0 & -GAs_z & 0 \\ EAe_z & 0 & -EAe_x \\ 0 & GAs_x & 0 \end{bmatrix} \tag{16c}$$

$$\mathbf{K}_{22} = \begin{bmatrix} E(I_{xx} + Ae_z^2) & 0 & -E(I_{xz} + Ae_xe_z) \\ 0 & G(J + As_z^2 + As_x^2) & 0 \\ -E(I_{xz} + Ae_xe_z) & 0 & E(I_{zz} + Ae_x^2) \end{bmatrix} \tag{16d}$$

where (e_x, e_z) and (s_x, s_z) describe the locations of the elastic and shear centers relative to the beam center.

Cross sectional properties can be calculated through integrating over cross section numerically (e.g. using tools such as VABS [30] or BECAS [31]), or analytical expressions can be derived by integrating over the cross section. To avoid the need to discretize the cross sections and additional computational cost in numerical integration, we opt for using an analytical approach where cross sectional properties are derived in Appendix B. However, analytical expressions for the torsional stiffness of airfoils and the location of the shear center are not readily available. It is known that the torsional stiffness of NACA 4-digit profiles are nearly independent of airfoil thickness or camber, and are approximated as [32]

$$J = k_t t^3 c^4 \tag{17}$$

where k_t is a torsion coefficient that is assumed to be constant for all airfoils. Using the cross sectional analysis tool, BECAS [31], it was found that $k_t \simeq 0.15$, which is in agreement with results presented in [32].

A similar method is introduced for approximating the location of the shear center labeled in Fig. 2. The shear center's chordwise location is approximated as $\tilde{s}_x \simeq 0.89\tilde{e}_x$ and $\tilde{s}_z \simeq 1.45\tilde{e}_z$, where $(\tilde{e}_x, \tilde{e}_z)$ are calculated from analytical expressions and tildes represent that terms are defined in the local coordinate system with the origin at the leading edge (refer to Fig. 2). This approximation for the shear center of the airfoils has shown to be accurate to within a distance of 2% of the chord length in the $\tilde{x}$ direction and 0.7% of the chord length in the $\tilde{z}$ direction (refer to Table 3 in Appendix B).

In this work the beam center has been defined at the quarter chord point as shown in Fig. 2. Theoretically it could be defined anywhere in the cross section and it may be tempting to place the beam center coincident to the elastic or shear center such that (e_x, e_z) or (s_x, s_z) is equal to $(0, 0)$, and (16) can simplified. However, the quarter chord point is approximately equal to the aerodynamic center which by definition is the point where the pithing moment is constant with changes in angle of attack. This means that as the beam deforms, there is little change in the torsional loads making it easier to converge the coupled problem.

D. Solution Procedure and Load-Displacement Transfer

Beam and panel methods are coupled using fixed-point iterations where loads calculated in the panel method are applied to the beam model, then deformations calculated in the beam model are used to deform the panel geometry, and loads are recalculated in the deformed configuration. This process continues until the change in solutions between update steps is less than a tolerance, ϵ, which is set as $\epsilon = 10^{-3}$ when solving optimization problems. An Aitken relaxation scheme is implemented based on methods outlined in [33]. This coupling scheme has proven to reduce the computational cost compared to Newton methods for these types of aeroelastic problems due of cost associated with calculating the Jacobian matrix [7, 21]. For more details on solution procedures for aeroelastic problems readers are referred to [34].

The authors adopt the generalized load-displacement transfer scheme derived in [21] for coupled panel-beam problems. The airfoil sections are defined in the t_1-t_3 plane at the beam nodes (refer to Fig. 3) and undergo rigid body translations and rotations due to the deflection of the beam, i.e.

$$\mathbf{X}_{ij} = \Delta\mathbf{x}_i + \mathbf{r}_{ij} \times \boldsymbol{\theta}_i \tag{18}$$

where $\mathbf{X}_{ij}$ is the panel-mesh nodal coordinates for panel node j at airfoil section i, $\Delta\mathbf{x}_i$ and $\boldsymbol{\theta}_i$ the beam displacements and rotations at beam node/airfoil section i, and $\mathbf{r}_{ij}$ is a spatial vector from beam node i to panel node j. The total force applied on a beam element is the sum of the contributions from pressure loads on the panels at the same spanwise location,

$$\mathbf{f}_e = \sum_{k=1}^{N} \int_0^{l_e} \begin{Bmatrix} \mathbf{n} \\ \mathbf{m} \end{Bmatrix} dl \tag{19}$$

where $\mathbf{n}$ are the conjugate forces acting on the panel, and $\mathbf{m}$ are the moments associated with translating these forces from the panel to the beam axis, i.e. $\mathbf{m} = \mathbf{r} \times \mathbf{n}$. Note that these conjugate forces and moments are not the same as those used in (12). Using the principles of consistency and conservativeness the conjugate forces are derived as

$$\mathbf{n} = q_\infty C_P J_l w \hat{\boldsymbol{n}} \tag{20}$$

where q_∞ is the dynamic pressure, w the panel width, $\hat{\boldsymbol{n}}$ is the panel's normal vector, and J_l is a mapping function to account for differences in panel length and beam element length (refer to [21]).

IV. Results

The results section is divided into two subsections. The first subsection presents comparisons between designs achieved with linear and nonlinear beam finite element models and the second presents studies on aeroelastic optimization of non-planar wings. Each optimization problem is solved using the method of moving asymptotes [35] where gradients are calculated analytically using the adjoint formulation given in Appendix C.

A. Aeroelastic Shape Optimization with Nonlinear Deformations

The first study seeks to optimize a deformable wing using a linear or nonlinear finite element (FE) models. Consider the following optimization problem where the objective is to minimize drag with respect to a constraint on lift-weight equilibrium, where the weight, W, is defined as the combined weight of the wing and a payload.

$$\begin{aligned} \min_{\mathbf{d}\,\in\,\mathbb{R}^{N_\mathrm{d}}} \quad &: \; D(\mathbf{d}, \mathbf{u}, \boldsymbol{\mu}) \\ \text{subject to} \quad &: \; L(\mathbf{d}, \mathbf{u}, \boldsymbol{\mu}) = W(\mathbf{d}) \\ & \quad \underline{d} \le d_i \le \bar{d} \qquad \text{for} \;\; i = 1, \dots, N_\mathrm{d} \end{aligned} \tag{21}$$

Because it is induced drag that is to be minimized, the optimizer will seek to reduce lift in order to reduce drag. The lift-weight equilibrium constraint is not only a physical consideration, it also gives a minimum bound to the lift which prevents the optimizer from creating zero lift as this would give zero drag. The problem is solved for a fixed span planar wing using only symmetric airfoils where chord, thickness, and twist can vary at each spanwise section, i.e. $\mathbf{d} = \{\delta\boldsymbol{c}, \boldsymbol{t}, \boldsymbol{\alpha}\}$. Optimized designs from both FE models are shown in Fig. 4.

With a linear FE model the design converges to a rectangular wing with a very large deflection. Deformations like this are certainly unphysical as they violate the assumption made by the linear FE model (small deflections) and the design would likely fail under the large stresses produced. But for the purpose of this discussion, we will consider these results as they are. When the deformations are this large, the coupled problem is prone to divergence as a small change in the displacements can cause a large change in the loading [7, 21]. Because the optimizer wants to create a very compliant wing, the minimum allowable chord length was increased in order to achieve a converged solution. The design converges with this minimum chord length and a maximum twist at each airfoil section, which gives the

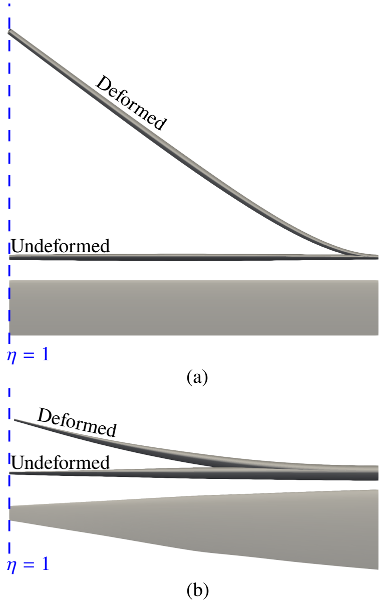

Fig. 4 Optimized results with (a) linear and (b) nonlinear finite element models. η markers are included at the wingtip.

rectangular planform and large displacements.

When the nonlinear FE model is used the optimizer converges to a tapered wing with moderate deflections. This design is closer to what one would naturally expect from this optimization problem, where chord and thickness is reduced towards the tip to reduce weight and increased towards the root to reduce deflections. The differences in these designs are related to the degrees of freedom (DOF) of the model. With a linear FE model, DOFs are defined to allow transverse deflections due to bending, but there is no coupling between axial and bending deformations. This means displacements in the spanwise direction are only affected by axial loading, and in pure bending the deformations will only be in the transverse direction. With respect to a wing model, this means the wingtip is displaced vertically where the wingspan does not change, but the curve length of the wing has increased which is clearly unphysical (refer to Fig. 4a). This is not the case in the co-rotating formulation because the constitutive relations are satisfied in a local reference frame that updates as the beam deforms. This allows the nonlinear FE model to capture the apparent shortening of the wingspan due to bending, which means there will be a large loss in lift as the beam deforms. It should also be noted that the weight is calculated in the undeformed configuration, meaning the artificial increase in the curved length of the linear wing is not considered in the weight calculation.

It is easier to demonstrate the shortening effect of the wingspan when there is more control over the deflection. A similar optimization problem is defined where an additional constraint on the tip deflection of the wing, u_t, is introduced.

$$\begin{aligned} \min_{\mathbf{d} \in \mathbb{R}^{N_\mathrm{d}}} \quad &: \; D(\mathbf{d}, \mathbf{u}, \boldsymbol{\mu}) \\ \text{subject to} \quad &: \; L(\mathbf{d}, \mathbf{u}, \boldsymbol{\mu}) = W(\mathbf{d}) \\ & \; u_t(\mathbf{u}) \leq \bar{u}_t \\ & \; \underline{d} \leq d_i \leq \bar{d} \qquad \text{for } i = 1, \ldots, N_\mathrm{d} \end{aligned} \tag{22}$$

Results are shown in Fig. 5 for both linear and nonlinear FE models with varying values of $\bar{u}_t$. Lift-to-drag ratios and tip displacements are presented in Table 1. Each design converges to a tapered wing, and in general, the nonlinear designs have a slightly larger aspect ratio which is likely due to the increased stiffness that comes from the geometric terms. In each case with a linear FE model the tip displacement constraint is active. For the nonlinear FE model the tip displacement constraint is only active when a strict constraint is imposed. In these cases both wings converge to designs that predict similar lift-to-drag ratios, as shown in Table 1. When the constraints are relaxed and a linear FE model is used, the optimizer tends to stiffen the inboard portion of the wing towards the root and increase the compliance towards the tip to create unrealistic large deformations (e.g. Fig. 5d). These unrealistic deformations allow the linear wings to achieve large increases in $\frac{L}{D}$ for a relaxed $\bar{u}_t$ constraint, whereas the nonlinear wings do not see much change when the constraint is relaxed. Because the tip constraint is inactive with a nonlinear FE model when $\bar{u}_t$ set to $0.2\frac{b}{2}$ or $0.3\frac{b}{2}$, the optimizer converges to the same design shown in Fig. 4b. Note also that the model predicts large $\frac{L}{D}$ values for each design because only the induced drag is considered.

$\bar{u}_t \frac{2}{b}$	$\frac{L}{D}$		$\frac{u_t}{\bar{u}_t}$	
	Linear	Nonlinear	Linear	Nonlinear
0.05	63.8	63.7	1.00	1.00
0.1	65.0	64.1	1.00	1.00
0.2	67.5	64.4	1.00	0.71
0.3	70.4	64.4	1.00	0.47

Table 1 Lift-to-drag ratios and tip deflection for the converged designs shown in Fig. 5

For designs with a nonlinear FE model and a relaxed tip constraint, large deflections lead to a loss in aerodynamic performance and the optimizer has created trade-offs between reducing the weight and reducing deflections. With a linear FE model the wing can still maintain a good aerodynamic performance for large deformations. As discussed previously, this is due to the ability of the nonlinear FE model to capture the effect of a shortening wingspan as the wing deforms. The details in Figs 5 shows the deflections at the wingtip where this effect is clearly visible. For induced drag minimization problems small changes to the wingspan can have a large impact on performance [20]. Because the linear FE model is unable to capture the shortening wingspan due to large deflections, the model predicts high lift-to-drag

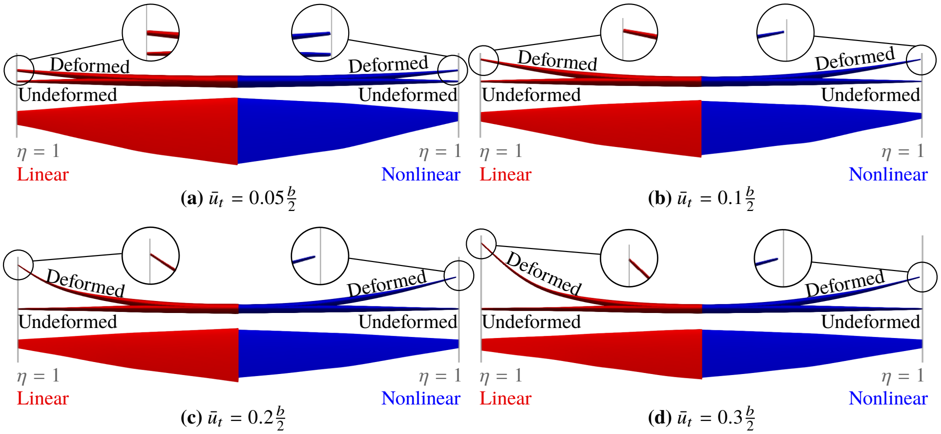

(a) $\bar{u}_t = 0.05\frac{b}{2}$ **(b)** $\bar{u}_t = 0.1\frac{b}{2}$

(c) $\bar{u}_t = 0.2\frac{b}{2}$ **(d)** $\bar{u}_t = 0.3\frac{b}{2}$

Fig. 5 Shape optimization results for linear (left) and nonlinear (right) finite element models with different tip displacement constraints. Each figure shows an elevation view with undeformed and deformed wings above, a planform view below, and markers at $\eta = 1$. Details magnify the deflection at the wingtip.

ratios at large deformations.

B. Aeroelastic Shape Optimization of Non-Planar Wings

Given the findings of previous studies, the remaining problems will only be solved using the nonlinear FE model. These studies will explore the differences in performance for flexible non-planar unswept wings where the out-of-plane geometry is controlled by $\hat{z}$ which is defined in the undeformed configuration, refer to Fig. 1. Consider the following optimization problem to minimize drag subject to lift-weight equilibrium and root bending moment constraints. The problem is solved for both raised ($\hat{z} > \mathbf{0}$) and drooped ($\hat{z} < \mathbf{0}$) wings. By enforcing a constraint on the root bending moment, raised and drooped wings are more comparable to one another as increases in aerodynamic performance may also lead to an increased bending moment. To make the non-planar designs comparable to previous examples the maximum bound on M_r is defined in terms of a scalar M_0 which is equal to the root bending moment produced by the design in Fig. 4b. The final constraint is a geometry constraint imposed on the value of $\hat{z}$ at the wingtip, where $\bar{\hat{z}}_t = 0.1\frac{b}{2}$.

$$\begin{aligned} \min_{\mathbf{d}\in\mathbb{R}^{N_\mathrm{d}}} \quad &: D(\mathbf{d},\mathbf{u},\boldsymbol{\mu}) \\ \text{subject to} \quad &: L(\mathbf{d},\mathbf{u},\boldsymbol{\mu}) = W(\mathbf{d}) \\ & \quad M_r(\mathbf{d},\mathbf{u},\boldsymbol{\mu}) \leq \bar{M}_r \\ & \quad |\hat{z}_t(\mathbf{d})| \leq \bar{\hat{z}}_t \\ & \quad \underline{d} \leq d_i \leq \bar{d} \qquad \text{for } i = 1,\dots,N_\mathrm{d} \end{aligned} \tag{23}$$

Converged designs are shown in Fig. 6 for upper bounds on root bending moment, $\bar{M}_r = \{M_0, 0.95M_0, 0.9M_0, 0.85M_0\}$, and their lift-to-drag ratios are presented in Table 2. In each case the designs converge to similar planform geometries irrespective of whether the wings are raised or drooped. The constraint on $\hat{z}_t$ is active when the bending moment constraint is relaxed, and is inactive for a drooped wing with $\bar{M}_r = 0.9M_0$ and both cases with $\bar{M}_r = 0.85M_0$. In fact, when $\bar{M}_r = 0.85M_0$ (Fig. 6d) neither raised or drooped wings form and both problems converge to a similar planar wing. Because of the strict bending moment constant in this case, the design has converged to a straight tapered wing with a high aspect and taper ratio. Comparing this design to the wing in Fig. 4b, we can see a higher aspect ratio and much smaller chord length at the tip which helps to reduce the bending moment. For the other designs there is a larger chord length in the outer regions towards the wingtip when the geometry goes out-of-plane, and the aspect ratio reduces as the constraint is relaxed.

$\frac{\bar{M}_r}{M_0}$	$\frac{L}{D}$	
	Raised	Drooped
1.0	68.9	71.0
0.95	66.7	68.6
0.9	62.4	63.5
0.85	56.8	56.8

Table 2 Lift-to-drag ratios for the raised and drooped wings shown in Fig. 6.

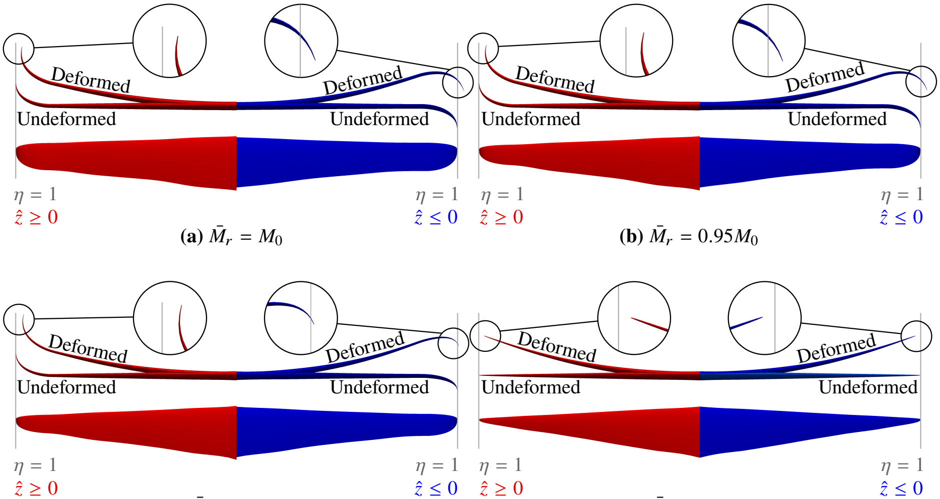

(a) $\bar{M}_r = M_0$

(b) $\bar{M}_r = 0.95M_0$

(c) $\bar{M}_r = 0.9M_0$

(d) $\bar{M}_r = 0.85M_0$

Fig. 6 Shape optimization results for raised (left) and drooped (right) wings with different bending moment constraints. Each figure shows an elevation view with undeformed and deformed wings above, a planform view below, and markers at $\eta = 1$. Details magnify the deflection at the wingtip.

Previous work has demonstrated that for a rigid wing both drooped and raised designs should be capable of achieving the same performance [22]. Now that the deformations are included in the model, the drooped wings consistently out perform raised wings, as shown in Table 2. When the bending moment constraint is gradually tightened, the lift-to-drag ratios are reduced and performance of raised and drooped wings start to converge. This is not surprising as both converge to a similar planar wing for $\bar{M}_r = 0.85$. The additional benefit of drooped wings is due to the way the wings deform. Because the wingtips are drooped there is an effective increase in the wingspan as the wing deforms, e.g. refer to detail in Fig. 6a. But with raised wing designs the effective wingspan is shortened as wing deforms, which is also seen in details in Fig. 6a. The induced drag is inversely proportional the wingspan squared, and as such increasing the effective wingspan leads to large reductions in drag. For a constant lift, a larger wingspan will also allow the chord length to be reduced which is why the planforms of the drooped wings have slightly higher aspect ratios in Fig. 6. Comparing the details of each wing in Fig. 6, it is easy to see that the effective wingspan is reduced for stricter constraint on M_r, as a shorter wingspan will reduce the root bending moment. By reducing $\hat{z}$ the effective wingspan is also reduced for cases where $\bar{M}_r$ is equal to $0.9M_0$ and $0.85M_0$.

Fig. 7 plots lift and root bending moment distributions for raised and drooped wings in terms of the product of local lift/root moment coefficients and the chord length, i.e. $C_l c = \frac{l}{q_\infty}$ and $C_{m_r} c = \frac{m_r}{q_\infty b}$. Figs 7a and 7b show lift and root moment distributions for each of the raised wing designs. When the bending moment constraint becomes more restrictive the lift distribution tends close to a inverse-linear distribution for the tapered wing design in Fig. 6d, which is what would be expected from a triangular planform wing. This would correspond to a parabolic root moment distribution, and as shown in Fig. 7b the distributions become close to parabolic. When the bending moment constraint is relaxed, less of the total lift is produced towards the root and more is produced towards the tip (as seen in Fig 7a). This in turn will lead to a larger contribution to the bending moment being produced in the outer regions of the wing (as seen in Fig 7b).

Although distributions in Figs 7a and 7b are only shown for raised wings, the drooped wing designs vary in a similar way when $\bar{M}_r$ is varied. Figs 7c and 7d compare distributions for raised and drooped wings with $\bar{M}_r = 0.85M_0$ and $\bar{M}_r = M_0$. Here, the x-axis plots $\hat{\eta}$ which represents the y locations in the deformed configuration normalized with the undeformed wingspan. This gives values that are not equal to 1 at the wingtip. For $\bar{M}_r = M_0$ similar trends are seen between raised and drooped wings, where the maximum lift and bending moment is larger for the raised wing because the effective wingspan is shorter, whereas negligible differences are seen when $\bar{M}_r = 0.85M_0$ since both cases converged to similar designs without planar geometry.

The optimization studies presented here have minimized the induced drag where viscous effects are neglected. It is important to note that previous studies in the literature have demonstrated that drooped wings are not as efficient as raised when viscous effects are included, e.g. [22, 36]. However, these conclusions were based only on aerodynamic modeling where deformations were not accounted for. It is still yet to be investigated whether the advantage the drooped

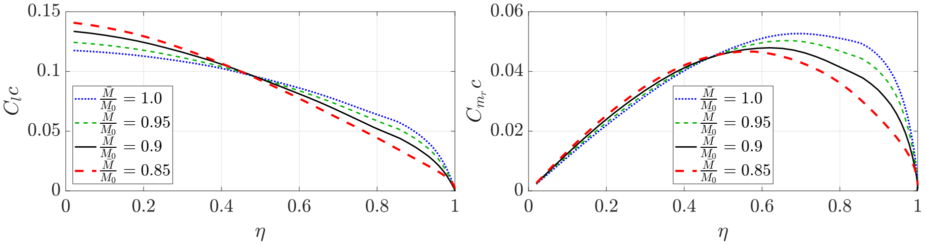

(a) Lift distributions, $\hat{z} > 0$ **(b) Root moment distributions, $\hat{z} > 0$**

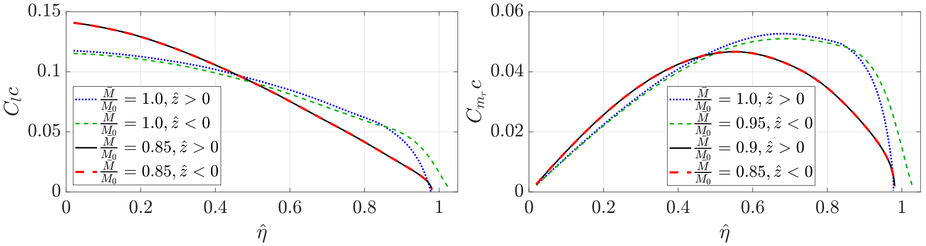

(c) Lift distributions, $\hat{z} > 0$ & $\hat{z} < 0$ **(d) Root moment distributions, $\hat{z} > 0$ & $\hat{z} < 0$**

Fig. 7 Lift and bending root moment distributions for converged designs shown in Fig. 6. η values in (a) and (b) represent undeformed configurations, whereas in (c) and (d) $\hat{\eta}$ represents deformed configurations.

wings achieve from increasing the effective wingspan is enough to make drooped wings beneficial when viscous effects are included.

V. Conclusions

A nonlinear co-rotating beam formulation has been applied to aeroelastic shape optimization of aircraft wings with solid isotropic cross sections. Cross sectional properties are calculated using derived analytic expressions or approximations, where a new approximation method is introduced to find the shear center of the airfoil. The method allows the stiffness matrix to be calculated for airfoil sections without the need for numerical integration methods over the cross section. Comparisons have been presented on optimized designs achieved using linear and nonlinear finite element models. Results have found that capturing nonlinear deformations can be crucial for induced drag minimization problems as the model is capable of predicting the change in wingspan as the wing deforms. Because linear models are unable to capture this effect, the wingspan remains constant leading to inaccurate predictions of aerodynamic performance and unphysical deformations for compliant wings. Flexible raised and drooped wings have been compared based on their aerodynamic performance where it was found that drooped wings will achieve larger lift-to-drag ratios. This is directly due to differences in geometry, where for a drooped wing the effective wingspan is increased as the wing deforms, whereas the effective wingspan of the raised wing is decreased as the wing deforms.

Appendices

A. Local orientation in 3D space

The local orientation of the beam can be expressed in 3 forms: a rotation matrix which is used throughout the finite element analysis, Euler angles which describes the degrees of freedom in the finite element analysis, and quaternions which are represented as a scalar $\bar{q}$ and vector $\boldsymbol{q}$. Quaternions are introduced because rotations in the first two forms are non-additive in 3D space [3, 27]. The following procedure is adopted to calculate the current orientation, $\mathbf{T}$, from an initial configuration, $\mathbf{T}_0$, having undergone the Euler rotations $\boldsymbol{\theta}$. For more details on the theory of this procedure readers are referred to [27], Chapter 16.

1) Convert initial configuration, $\mathbf{T}_0$, to a quaternion representation, $\bar{q}_0, \boldsymbol{q}_0$.

   If $\max(\mathrm{Tr}(\mathbf{T}_0), T_{0,11}, T_{0,22}, T_{0,33}) = \mathrm{Tr}(\mathbf{T}_0)$ then

$$\bar{q}_0 = \frac{1}{2}\sqrt{1 + \mathrm{Tr}(\mathbf{T}_0)} \tag{24a}$$

$$q_{0,i} = \frac{T_{0,kj} - T_{0,jk}}{4\bar{q}} \qquad \text{for } i = 1, 2, 3 \tag{24b}$$

   with i, j, k as the cyclic combination of 1,2,3.

   If $\max(\mathrm{Tr}(\mathbf{T}_0), T_{0,11}, T_{0,22}, T_{0,33}) \neq \mathrm{Tr}(\mathbf{T}_0)$ but instead $= T_{0,ii}$

$$q_{0,i} = \sqrt{\frac{1}{2}T_{0,ii} + \frac{1}{4}(1 - \mathrm{Tr}(\mathbf{T}_0))} \tag{25a}$$

$$\bar{q}_0 = \frac{T_{0,kj} - T_{0,jk}}{4q_i} \tag{25b}$$

$$q_{0,l} = \frac{T_{0,li} - T_{0,il}}{4q_i} \qquad \text{for } l = j, k \tag{25c}$$

   where the opertation $\mathrm{Tr}(\mathbf{T}_0)$ represents the trace of $\mathbf{T}_0$.

2) Convert the Euler rotations $\boldsymbol{\theta}$ to a quaternion representation, $\bar{q}_r, \boldsymbol{q}_r$.

$$\bar{q}_r = c_1c_2c_3 + s_1s_2s_3 \tag{26a}$$

$$q_{r,1} = s_1c_2c_3 - c_1s_2s_3 \tag{26b}$$

$$q_{r,2} = c_1s_2c_3 + s_1c_2s_3 \tag{26c}$$

$$q_{r,3} = c_1c_2s_3 - s_1s_2c_3 \tag{26d}$$

where $c_i = \cos\left(\frac{\theta_i}{2}\right)$ and $s_i = \sin\left(\frac{\theta_i}{2}\right)$.

3) Calculate the quaternion representation of the current orientation as the quaternion sum of the initial orientation and the rotation

$$\bar{q} = \bar{q}_0\bar{q}_r - \boldsymbol{q}_0 \cdot \boldsymbol{q}_r \tag{27a}$$

$$\boldsymbol{q} = \bar{q}_0\boldsymbol{q}_r + \bar{q}_r\boldsymbol{q}_0 - \boldsymbol{q}_0 \times \boldsymbol{q}_r \tag{27b}$$

4) Convert back to the rotation matrix representation

$$\mathbf{T} = (\bar{q}^2 - \boldsymbol{q}^{\mathrm{T}}\boldsymbol{q})\mathbf{I} + 2(\boldsymbol{q}\boldsymbol{q}^{\mathrm{T}}) + 2\bar{q}\mathbf{S}(\boldsymbol{q}) \tag{28}$$

where $\mathbf{I}$ is the identity matrix and $\mathbf{S}(\boldsymbol{q})$ is a skew matrix defined in (10).

B. Cross sectional properties

This work assumes a solid isotropic cross section whose geometry is defined by the airfoil parameterization represented in Fig. 2. The parameterization is based on the equations for NACA 4-digit airfoils which define thickness and camber distributions as [23]

$$\tilde{z}_t = 5tc\left(0.2969\sqrt{\frac{\tilde{x}}{c}} - 0.1260\frac{\tilde{x}}{c} - 0.3516\left(\frac{\tilde{x}}{c}\right)^2 + 0.2843\left(\frac{\tilde{x}}{c}\right)^3 - 0.1036\left(\frac{\tilde{x}}{c}\right)^4\right) \tag{29}$$

$$\tilde{z}_m = \begin{cases} \dfrac{mc}{p^2}\left(2p\dfrac{\tilde{x}}{c} - \left(\dfrac{\tilde{x}}{c}\right)^2\right), & \text{if } 0 \leq \dfrac{\tilde{x}}{c} \leq p \\ \dfrac{mc}{(1-p)^2}\left(1 - 2p + 2p\dfrac{\tilde{x}}{c} - \left(\dfrac{\tilde{x}}{c}\right)^2\right), & \text{if } p \leq \dfrac{\tilde{x}}{c} \leq 1 \end{cases} \tag{30}$$

NACA 4-digit airfoils define the thickness as normal to the camber line. The current parameterization modifies this definition such that thickness is measured normal to the chord line which ensures the derivatives are continuous [20]. The upper and lower surface of the airfoil are then be defined as

$$\tilde{z}_u = \tilde{z}_m + \tilde{z}_t \tag{31a}$$

$$\tilde{z}_l = \tilde{z}_m - \tilde{z}_t \tag{31b}$$

where the origin is at the leading edge, and subscripts u and l represent upper and lower surfaces, respectively. Now that there are analytic expressions for the airfoil, the following cross sectional properties can be derived through evaluating the integrals provided in [37]

$$A = \int_0^c (\tilde{z}_u - \tilde{z}_l) d\tilde{x} = \frac{40853}{60000} t c^2 \tag{32}$$

$$\tilde{e}_x = \frac{1}{A} \int_0^c \tilde{x} (\tilde{z}_u - \tilde{z}_l) d\tilde{x} = \frac{17072}{40853} c \tag{33}$$

$$\begin{aligned} \tilde{e}_z = \frac{1}{2A} \int_0^c (\tilde{z}_u^2 - \tilde{z}_l^2) d\tilde{x} = & \frac{30000cm}{40853(p-1)^2} \Big[-0.904838096 p^{\frac{3}{2}} + 1.80967619 p^{\frac{5}{2}} - 0.03946666699 p^6 \\ & + 0.209266666968018 p^5 - 0.563566667023105 p^4 - 0.18559999995126 p^3 \\ & + 0.209999999949106 p^2 - 1.58539999956691 p + 1.0499285706036 \Big] \end{aligned} \tag{34}$$

$$\begin{aligned} \tilde{I}_{xx} = \frac{1}{3} \int_0^c (\tilde{z}_u^3 - \tilde{z}_l^3) d\tilde{x} = & \frac{c^{\frac{4}{3}}}{(p-1)^4} \Big[-2.056450216 p^{\frac{3}{2}} m^2 t + 8.22580086 p^{\frac{5}{2}} m^2 t - 9.62418701 p^{\frac{7}{2}} m^2 t \\ & - t(-0.1176566644 t^2 - 1.310524784 m^2 + 4.066219048 m^2 p + 0.4706266577 p t^2 \\ & - 0.7059399865 t^2 p^2 - 2.79677229 p^{\frac{9}{2}} m^2 - 3.716828571 p^2 m^2 + 1.413257143 m^2 p^3 \\ & + 0.098666667 m^2 p^8 - 0.11765666 t^2 p^4 + 0.470626658 t^2 p^3 + 0.27081072 p^4 m^2 \\ & - 3.22688095 p^5 m^2 + 2.46037382 p^6 m^2 - 0.713157141 p^7 m^2) \Big] \end{aligned} \tag{35}$$

$$\begin{aligned} \tilde{I}_{xz} = \frac{1}{2} \int_0^c \tilde{x} (\tilde{z}_u^2 - \tilde{z}_l^2) d\tilde{x} = & -0.0123333335 \frac{c^4 t m}{(p-1)^2} \Big[12.22754164 p^{\frac{5}{2}} - 24.45508329 p^{\frac{7}{2}} + p^7 \\ & - 4.8907335151639 p^6 + 11.698069340392 p^5 + 2.05945943106902 p^4 \\ & - 3.40540535911413 p^3 + 20.856370370699 p - 15.0902185805057 \Big] \end{aligned} \tag{36}$$

$$\tilde{I}_{zz} = \int_0^c \tilde{x}^2 (\tilde{z}_u - \tilde{z}_l) d\tilde{x} = \frac{32743}{210000} c^4 t \tag{37}$$

Properties notated with a tilde are defined with respect to the airfoil's leading edge, but cross sectional properties in (16) are defined with respect to the beam center and therefore properties in equations (33)-(37) need to be corrected e.g. using the parallel axis theorem.

Cross sectional properties that cannot be calculated analytically include the location of the shear center and the torsional stiffness. The torsional stiffness is calculated using a technique in [32] where J about the quarter chord point is approximated as $J \simeq 0.15 t^3 c$. A similar approximation was formed for the location of the shear center in terms of the elastic center, by stating that

$$(\tilde{s}_x, \tilde{s}_z) \simeq (k_x \tilde{e}_x, k_z \tilde{e}_z) \tag{38}$$

where k_x and k_z are coefficients that are constant for all airfoils defined by the parameterization above. BECAS [31] was used to evaluate k_x and k_z for a selection of airfoils with different values of m, t, and p. Based on average values, k_x and k_z were found to be 0.89 and 1.45, respectively. Table 3 compares the difference in these approximations to the values calculated via BECAS. The approximation of the shear center was shown to be accurate to within 2% and 0.7% of the chord length for $\tilde{x}$ and $\tilde{z}$ locations, receptively. The torsional stiffness approximation had a maximum relative error of 6%.

NACA 4-digit	0006	0012	0018	2506	2512	2518	4506	4512	4518
Δs_x [% c]	-0.647	-0.426	-0.511	0.074	-0.208	-0.399	1.82	0.411	-0.115
Δs_z [% c]	0	0	0	0.026	0.010	-0.013	0.073	0.0235	-0.146
ΔJ [%]	0.691	-0.347	-4.01	5.93	-0.464	-4.13	5.65	-0.801	-3.69

Table 3 Comparison of cross sectional properties calculated via BECAS and the approximations presented in the current work. Difference in shear centers is presented as percentage difference in chord length, and torsional stiffness as relative difference.

C. Sensitivity analysis

Gradients are calculated using a discrete adjoint method, where the total derivative of an objective/constraint function Ψ can be calculated as

$$\frac{d\Psi}{d\mathbf{d}} = \frac{\partial\Psi}{\partial\mathbf{d}} + \boldsymbol{\lambda}_a^{\mathrm{T}}\left[\frac{\partial\mathbf{A}_\mu}{\partial\mathbf{d}}\boldsymbol{\mu} + \frac{\partial\mathbf{A}_\sigma}{\partial\mathbf{d}}\boldsymbol{\sigma} + \mathbf{A}_\sigma\frac{\partial\boldsymbol{\sigma}}{\partial\mathbf{d}}\right] + \boldsymbol{\lambda}_b^{\mathrm{T}}\left[\frac{\partial\mathbf{p}}{\partial\mathbf{d}} - \frac{\partial\mathbf{f}}{\partial\mathbf{d}}\right] \tag{39}$$

where partial derivatives capture only the explicit dependence without solving the governing equations. The terms $\boldsymbol{\lambda}_a$ and $\boldsymbol{\lambda}_b$ are Langragian multipliers whose length is equal to that of $\boldsymbol{\mu}$ and $\mathbf{u}$ respectively, and are calculated through solving the following adjoint problem

$$\begin{bmatrix} \mathbf{A}_\mu & \left[\frac{\partial\mathbf{A}_\mu}{\partial\mathbf{u}}\boldsymbol{\mu} + \frac{\partial\mathbf{A}_\sigma}{\partial\mathbf{u}}\boldsymbol{\sigma} + \mathbf{A}_\sigma\frac{\partial\boldsymbol{\sigma}}{\partial\mathbf{u}}\right] \\ -\frac{\partial\mathbf{f}}{\partial\boldsymbol{\mu}} & \left[\mathbf{K} - \frac{\partial\mathbf{f}}{\partial\mathbf{u}}\right] \end{bmatrix}^{\mathrm{T}} \begin{bmatrix} \boldsymbol{\lambda}_a \\ \boldsymbol{\lambda}_b \end{bmatrix} = - \begin{bmatrix} \frac{\partial\Psi}{\partial\boldsymbol{\mu}} \\ \frac{\partial\Psi}{\partial\mathbf{u}} \end{bmatrix} \tag{40}$$

Acknowledgments

This work was funded the Villum Foundation under the InnoTop Villum Investigator project.

References

[1] Kroo, I., "Nonplanar Wing Concepts for Increased Aircraft Efficiency," *VKI lecture series on innovative configurations and advance concepts for future civil aircraft*, 2005.

[2] Crisfield, M. A., “A consistent co-rotational formulation for non-linear, three-dimensional, beam-elements,” *Computer Methods in Applied Mechanics and Engineering*, Vol. 81, No. 2, 1990, pp. 131–50. doi:https://doi.org/10.1016/0045-7825(90)90106-V.

[3] Krenk, S., *Non-linear modelling and analysis of solids and structures*, Cambridge University Press, 2009.

[4] Larsen, T. J., and Hansen, A. M., *How 2 HAWC2, the user’s manual*, Risø National Laboratory, 2007.

[5] HODGES, D., “A mixed variational formulation based on exact intrinsic equations for dynamics of moving beams,” *International Journal of Solids and Structures*, Vol. 26, No. 11, 1990, pp. 1253–1273. doi:https://doi.org/10.1016/0020-7683(90)90060-9.

[6] Patil, M. J., Hodges, D. H., and Cesnik, C. E., “Nonlinear aeroelasticity and flight dynamics of high-altitude long-endurance aircraft,” *Journal of Aircraft*, Vol. 38, No. 1, 2001, pp. 88–94. doi:https://doi.org/10.2514/2.2738.

[7] Jasa, J. P., Hwang, J. T., and Martins, J. R., “Open-source coupled aerostructural optimization using Python,” *Structural and Multidisciplinary Optimization*, Vol. 57, No. 4, 2018, pp. 1815–1827. doi:https://doi.org/10.1007/s00158-018-1912-8.

[8] Jansen, P. W., Perez, R. E., and Martins, J. R., “Aerostructural optimization of nonplanar lifting surfaces,” *Journal of Aircraft*, Vol. 47, No. 5, 2010, pp. 1490–1503. doi:https://doi.org/10.2514/1.44727.

[9] Xie, C., Meng, Y., Wang, F., and Wan, Z., “Aeroelastic Optimization Design for High-Aspect-Ratio Wings with Large Deformation,” *Shock and Vibration*, Vol. 2017, No. 2564314, 2017. doi:https://doi.org/10.1155/2017/2564314.

[10] Kennedy, G. J., and Martins, J. R. R. A., “A Comparison of Metallic and Composite Aircraft Wings using Aerostructural Design Optimization,” *12th AIAA Aviation Technology, Integration and Operations (ATIO) Conference and 14th AIAA/ISSMO Multidisciplinary Analysis and Optimization Conference*, American Institute of Aeronautics and Astronautics Inc., 2012. doi:https://doi.org/10.2514/6.2012-5475.

[11] Burdette, D. A., Kenway, G. K., and Martins, J. R., “Aerostructural design optimization of a continuous morphing trailing edge aircraft for improved mission performance,” *17th AIAA/ISSMO Multidisciplinary Analysis and Optimization Conference*, 2016. doi:https://doi.org/10.2514/6.2016-3209.

[12] Mieloszyk, J., and Goetzendorf-Grabowski, T., “Introduction of Full Flight Dynamic Stability Constraints in Aircraft Multidisciplinary Optimization,” *Aerospace Science and Technology*, Vol. 68, 2017, pp. 252–260. doi:https://doi.org/10.1016/j.ast.2017.05.024.

[13] James, K. A., Kennedy, G. J., and Martins, J. R. R. A., “Concurrent Aerostructural Topology Optimization of a Wing Box,” *Computers and Structures*, Vol. 134, 2014, pp. 1–17. doi:https://doi.org/10.1016/j.compstruc.2013.12.007.

[14] Khosravi, S., and Zingg, D. W., “Aerostructural optimization of drooped wings,” *Journal of Aircraft*, Vol. 55, No. 3, 2018, pp. 1261–1268. doi:https://10.2514/1.C034605.

[15] Kenway, G. K., Kennedy, G. J., and Martins, J. R., “Scalable parallel approach for high-fidelity steady-state aeroelastic analysis and adjoint derivative computations,” *AIAA Journal*, Vol. 52, No. 5, 2014, pp. 935–951. doi:https://doi.org/10.2514/1.J052255.

[16] Kenway, G. K., and Martins, J. R., "Multipoint high-fidelity aerostructural optimization of a transport aircraft configuration," *Journal of Aircraft*, Vol. 51, No. 1, 2014, pp. 144–160. doi:https://doi.org/10.2514/1.C032150.

[17] Vassberg, J., DeHaan, M., Rivers, S., and Wahls, R., "Development of a common research model for applied CFD validation studies," *Collection of Technical Papers - AIAA Applied Aerodynamics Conference*, 2008. doi:https://doi.org/10.2514/6.2008-6919.

[18] Maute, K., and Allen, M., "Conceptual design of aeroelastic structures by topology optimization," *Structural and Multidisciplinary Optimization*, Vol. 27, No. 1-2, 2004, pp. 27–42. doi:https://doi.org/10.1007/s00158-003-0362-z.

[19] Gori, R., Bernardini, G., and Cesnik, C. E., "Flapping wing aeroelasticity using corotational fem and 3D panel method," *IFSAD 2013 - International Forum on Aeroelasticity and Structural Dynamics*, 2013.

[20] Conlan-Smith, C., Ramos-García, N., Sigmund, O., and Andreasen, C. S., "Aerodynamic Shape Optimization of Aircraft Wings Using Panel Methods," *AIAA Journal*, Vol. 58, No. 9, 2020, pp. 3765–3776. doi:https://doi.org/10.2514/1.J058979.

[21] Conlan-Smith, C., and Schousboe Andreasen, C., "A coupled 3D panel-beam model for aeroelastic optimization of aircraft wings," *AIAA Journal*, 2020. Accepted/In Press.

[22] Conlan-Smith, C., Ramos-García, N., and Schousboe Andreasen, C., "Aerodynamic shape optimization of non-planar wings," *Journal of Aircraft*, 2020. Under review.

[23] Abbott, I., and von Doenhoff, A., *Theory of Wing Sections: Including a Summary of Airfoil Data*, Dover Books on Aeronautical Engineering, Dover Publications, 2012.

[24] Ramos García, N., Sørensen, J., and Shen, W., "Three-Dimensional Viscous-Inviscid Coupling Method for Wind Turbine Computations," *Wind Energy*, Vol. 19, No. 1, 2016, p. 67–93. doi:https://doi.org/10.1002/we.1821.

[25] Smith, S. C., *A Computational and Experimental Study of Nonlinear Aspects of Induced Drag*, Technical Paper 3598, National Aeronautics and Space Administration, 1996.

[26] Drela, M., *Flight Vehicle Aerodynamics*, The MIT Press, 2014.

[27] Crisfield, M., *Non-linear Finite element analysis of solids and structures. Volume 2: advanced topics*, John Wiley and sons,, 1997.

[28] Simo, J. C., and Vu-Quoc, L., "A three-dimensional finite-strain rod model. II. Computational aspects," *Computer Methods in Applied Mechanics and Engineering*, Vol. 58, No. 1, 1986, pp. 79–116. doi:https://doi.org/10.1016/0045-7825(86)90079-4.

[29] Hodges, D. H., *Nonlinear composite beam theory*, Vol. 213, American Institute of Aeronautics and Astronautics, 2006.

[30] Yu, W., Volovoi, V. V., Hodges, D. H., and Hong, X., "Validation of the variational asymptotic beam sectional analysis," *AIAA Journal*, Vol. 40, No. 10, 2002, pp. 2105–2112. doi:https://doi.org/10.2514/2.1545.

[31] Blasques, J. P. A. A., *User's Manual for BECAS: A cross section analysis tool for anisotropic and inhomogeneous beam sections of arbitrary geometry*, Risø DTU - National Laboratory for Sustainable Energy, 2012.

[32] Kosmatka, J. B., *The use of cross-section warping functions in composite rotor blade analysis*, Report no. SSRP-92/11, National Aeronautics and Space Administration, 1992.

[33] Kuettler, U., and Wall, W. A., "Fixed-point fluid-structure interaction solvers with dynamic relaxation," *Computational Mechanics*, Vol. 43, No. 1, 2008, pp. 61–72. doi:https://doi.org/10.1007/s00466-008-0255-5.

[34] Gray, J. S., Hwang, J. T., Martins, J. R. R. A., Moore, K. T., and Naylor, B. A., "OpenMDAO: an open-source framework for multidisciplinary design, analysis, and optimization," *Structural and Multidisciplinary Optimization*, Vol. 59, No. 4, 2019, pp. 1075–1104. doi:https://doi.org/10.1007/s00158-019-02211-z.

[35] Svanberg, K., "The Method of Moving Asymptotes - a New Method for Structural Optimization," *International Journal for Numerical Methods in Engineering*, Vol. 24, No. 2, 1987, pp. 359–373. doi:https://doi.org/10.1002/nme.1620240207.

[36] Ranjan, P., Ansell, P. J., and James, K. A., "Optimal hyperelliptic cambered span configurations for minimum drag," *Journal of Aircraft*, Vol. 56, No. 1, 2019, pp. 356–368. doi:https://doi.org/110.2514/1.C034992.

[37] Johnson, D. F., and Gendler, S., *Determination of minimum moments of inertia of arbitrarily shaped areas, such as hollow turbine blades*, NACA RM E9H10, National Aeronautics and Space Administration, 1950.

DTU Mechanical Engineering
Section of Solid Mechanics
Technical University of Denmark

Nils Koppels Allé, Bld. 404
DK-2800 Kgs. Lyngby
Denmark
Tlf.: +45 4525 4250
Fax: +45 4525 1961

www.mek.dtu.dk

November 2020

ISBN: 978-87-7475-628-6

DCAMM
Danish Center for Applied Mathematics and Mechanics

Nils Koppels Allé, Bld. 404
DK-2800 Kgs. Lyngby
Denmark
Phone (+45) 4525 4250
Fax (+45) 4525 1961

www.dcamm.dk

DCAMM Special Report No. S282

ISSN: 0903-1685